UCLouvain
Institute for Information
and Communication Technologies,
Electronics and Applied Mathematics

Optical and Electrical Properties of Highly Strained Silicon towards Extended Infrared Photodetection

Nicolas Roisin

Thesis submitted in partial fulfillment of the requirements for the Degree of Doctor in Applied Sciences

January 2025

Thesis Committee:

Pr. Laurent **Francis** (Chair)	UCLouvain, Belgium
Pr. Denis **Flandre** (Advisor)	UCLouvain, Belgium
Pr. Jean-Pierre **Raskin** (Advisor)	UCLouvain, Belgium
Pr. Samuel **Poncé**	UCLouvain, Belgium
Pr. Andrea **Fiore**	TU/e, the Netherlands
Pr. Beata **Kardynal**	FZ Jülich, Germany

Optical and Electrical Properties of Highly Strained Silicon towards Extended Infrared Photodetection

by Nicolas Roisin

© Nicolas Roisin 2025

ICTEAM
Université catholique de Louvain
Place du Levant, 3
1348 Louvain-la-Neuve
Belgium

It doesn't matter how beautiful your theory is, it doesn't matter how smart you are. If it doesn't agree with experiment, it's wrong.

RICHARD P. FEYNMAN

Remerciements

Je tiens à exprimer ma profonde gratitude envers mes deux promoteurs, les professeurs **Denis Flandre** et **Jean-Pierre Raskin**, pour leur encadrement de grande qualité tout au long de cette thèse. Ils se distinguent non seulement par leur excellence scientifique, mais également par leurs remarquables qualités humaines. Merci pour leur soutien indéfectible, la confiance qu'ils m'ont témoignée, et la grande liberté qu'ils m'ont accordée, allant jusqu'à me laisser explorer des simulations théoriques, domaine pour lequel aucun des deux n'avait d'affinité particulière. Je remercie particulièrement Denis pour sa rigueur et son exigence scientifique, ses nombreux conseils pédagogiques, et ses relectures approfondies de chacun de mes articles. Merci à Jean-Pierre pour sa bonne humeur quotidienne, ses encouragements et son enthousiasme pour mes recherches.

Un grand merci à l'équipe de simulation théorique du département MODL, en particulier à **Gian-Marco Rignanese** et **Guillaume Brunin**, de m'avoir fait découvrir ce domaine. Merci à tous les deux pour leur accompagnement et bienveillance lors de mes premières recherches théoriques. Merci également à **Samuel Poncé** d'avoir pris la relève ces dernières années et **Matteo Giantomassi** pour les nombreux échanges techniques à propos d'ABINIT. Leur rigueur et leur patience m'ont permis de progresser et d'affiner mes compétences.

Je tiens à remercier **Pascal Simon** et **Valeriya Kilchytska** pour leur gestion de WELCOME et leur précieux soutien, ainsi que **Benoît Hubert**, **Souley Djadjandi**, et **Pierre Gérard** pour leur aide quotidienne, sans laquelle de nombreuses mesures n'auraient pu aboutir.

Merci à **Alex Bertholet** pour nos discussions toujours enrichissantes et agréables à propos des jauges de déformation.

Je tiens à exprimer une reconnaissance particulière à **Marie-Stéphane Colla** pour notre collaboration scientifique et la fabrication des échantillons au sein de WinFAB. Malgré des difficultés et quelques déceptions, ce fut un réel plaisir d'échanger et de travailler ensemble tout au long de cette thèse.

Un grand merci à **Romain Scaffidi** pour avoir co-construit et encadré avec moi les séances d'exercices du cours LELEC2330. Ce fut un réel plaisir de travailler à ses côtés. Merci également pour son aide précieuse dans les mesures de photoluminescence réalisées à IMMOMEC, à Genk.

Je remercie tout le personnel administratif et technique qui nous permet d'évoluer avec confiance et sérénité dans la complexité administrative de l'UCLouvain. Et plus particulièrement, **Viviane Sauvage**,**Anne Gillet**, **Isabelle Dargent**, **Christel Derzelle**, **Brigitte Dupont** et **Rémi Dekimpe**.

J'ai une pensée toute particulière pour mes premiers collègues de bureau, à savoir **Sedki Amor** avec son calme et sa gentillesse; **Nicolas André** pour sa bonne humeur permanente et les nombreuses collaborations scientifiques; et enfin **Thibault Delhaye** pour les parties de ping-pong, notre franche complicité, et nos échanges scientifiques et personnels. Après leur départ, j'ai eu la chance de croiser la route de **Loïc Lahaye**, d'abord en tant que mémorant, puis comme collègue et finalement comme ami. Merci à lui pour les rires partagés, les moments de complicité, et son enthousiasme permanent.

Merci à mes nombreux collègues de bureau (ou sympathisants) qui ont égayé mes journées à l'UCLouvain: **Eléonore Masarweh**, **Jérémy Trips**, **Roselien Vercauteren**, **Ottilie Bonfanti**, **Tom Klauner**, **Anne-sophie Collin** et **Clémentine Gevers**.

Merci à tous ces collègues devenus amis, dont certains ont été jusqu'à participer à notre chorale de mariage, à savoir **Adrian Kneip**, **Martin Lefebvre** et **Noémie Bidoul**. Merci notamment pour les riches moments passés ensemble en conférence à Lisbonne.

Je suis reconnaissant envers les membres des collectifs que j'ai eu le privilège d'intégrer, tels que l'*IEEE Student Branch* et l'*ACSEP*. Un merci tout particulier aux premiers membres d'*Ingés en Transition*, pour avoir porté et développé ce projet avec moi, et à tous ceux qui continuent de le faire vivre.

Une reconnaissance toute particulière pour **Karim El Khoury** avec qui j'ai tissé une amitié rare et précieuse depuis notre rencontre en première master. Merci à lui pour sa présence permanente, sa bienveillance, sa gentillesse, et toutes ses qualités qui en font une personne exceptionelle.

J'ai également une pensée pour un autre ami cher, **Thibault Pirson**.

Merci à lui pour son énergie débordante, sa gaieté naturelle et sa bienveillance permanente.

En dehors de l'UCLouvain, je remercie ma famille et tout particulièrement mes parents, **Patrick Roisin** et **Catherine Debouvrie**, mon frère et son épouse, **Arnaud Roisin** et **Candy Sonveaux**, et ma grand-mère, **Béatrice Bintein**, pour leur soutien et bienveillance quotidienne; et sans qui je ne serais pas la personne épanouie que je suis aujourd'hui.

Enfin, et surtout, je remercie mon épouse, **Mélanie Lechien**. Merci pour ta présence inébranlable, ta capacité à donner du sens à tout ce que j'entreprends, et ton soutien constant qui me poussent à donner le meilleur de moi-même. Merci pour tout le bonheur que nous partageons au quotidien. Cette thèse aurait bien peu de valeur sans toi à mes cotés.

Abstract

Silicon photodetectors are commonly used for visible and near-infrared photodetection. They are relatively easy to manufacture and can be produced in large quantities at relatively low cost, making them well suited for use in a wide range of devices. However, the ability of silicon-based photodetectors to detect infrared radiation beyond 1.1 µm is limited by their indirect band gap of 1.12 eV. Strain engineering has been proven to reduce the band gap of semiconductors, but its application to improve optoelectronic performance has been lacking. In this work, a thorough study of the optical and electrical properties of highly strained silicon is proposed to evaluate its potential for infrared photodetectors. First-principles calculations using density functional theory is performed to obtain the strain-induced changes in the silicon band structure for all major strain configurations. Uniaxial strain along the [110] direction is found to be promising for reducing the band gap, with a reduction of about 200 meV at 2%-strain, while being compatible with high-strain fabrication schemes. The band gap reduction is experimentally validated by photoluminescence measurements on silicon beams strained up to 1% with silicon nitride actuators.

In the second chapter, the variations in electron mobility in n-type silicon resistors have first been studied experimentally for uniaxial strain along [001] using a four-point bending scheme. The experimental results highlight the important increase in the longitudinal resistivity, with a 50% increase at 1%-strain, while showing the limitations of existing theories to predict the mobility of strained silicon. First-principles calculations are performed to retrieve the mobilities of strained silicon by solving the Boltzmann transport equation, considering electron-phonon interactions. The method is used for [001] and [110] uniaxial strains. The theoretical calculations show the limitation of existing theories for the electron mobil-

ity while calculating, for the first time with this level of theory, the hole mobility of strained silicon. A significant increase in hole mobility up to 1340 $cm^2V^{-1}s^{-1}$ and 1761 $cm^2V^{-1}s^{-1}$ as been found for uniaxial strain of 2% along [001] and [110], respectively. The electron mobility shows an increase up to 2200 $cm^2V^{-1}s^{-1}$ for uniaxial strain along [001] of 2%, but is negatively impacted by [110] uniaxial strain with a longitudinal and transverse mobilities of 1221 $cm^2V^{-1}s^{-1}$ and 168 $cm^2V^{-1}s^{-1}$, respectively.

The Bethe-Salpeter equation and the EPW code is used to predict fully theoretically the complex refractive index and absorption coefficient of highly strained silicon, taking into account the electron-phonon interactions, without the need for a semi-empirical model containing experimental biases. The results for the absorption coefficient show a significant increase with [110] uniaxial strain, following the band gap reduction. As the band gap is reduced to 0.66 eV at 4%-strain, the wavelength of light that can be absorbed is extended to 1.88 µm. The absorption coefficient calculated theoretically at 1.2 µm goes from 1.5×10^{-2} cm^{-1} to 168 cm^{-1} at 4%-strain. The absorption results are compared with the absorption coefficient of conventional infrared materials such as Ge, SiGe and InGaAs, showing the potential of strained silicon to compete with them.

Finally, the first-principles results are used in combination with technology computer aided design (TCAD) simulation to investigate the potential of strained silicon for infrared photodetection, showing equivalent performances to standard infrared materials but with the necessity of achieving high levels of strain. The increase of the absorption coefficient for [110] uniaxial strains is found to directly enhance the infrared sensitivity of the device, while the mobility variations impact the time response of the detector. A sensitivity of 0.8 AW^{-1} at 1400 nm is finally predicted theoretically for a 100µm-long photodiode strained up to 4%.

This work demonstrates for the first time the potential of using strained silicon for near and shortwave infrared applications, although the fabrication of such devices remains a challenge.

Author's publication list

Conference Proceedings

1. Delhaye, T. P., **Roisin, N.**, Andre, N., Francis, L. A., Flandre, D. "Improving MOSFET Piezoresistive Strain Gauges Limit of Detection Using Lock-In Principle". In: *2021 IEEE Sensors*. IEEE, Oct. 2021, pp. 1–4. ISBN: 978-1-7281-9501-8. DOI: 10.1109/SENSORS47087.2021.9639730.
2. Klauner, T., Alirezaei, I., **Roisin, N.**, Andre, N., Flandre, D. "SPICE Model of SPAD Transient Intrinsic Response Validated using Mixed-Mode TCAD Simulations". In: *European Solid-State Device Research Conference*. 2023. ISBN: 9798350304237. DOI: 10.1109/ESSDERC59256.2023.10268486.
3. **Roisin, N.**, Raskin, J.-P., Flandre, D. "Near-IR response of highly-strained Si photodetector linking first principles and TCAD". in: *European Solid-State Device Research Conference*. 2023. ISBN: 9798350304237. DOI: 10.1109/ESSDERC59256.2023.10268568.

Articles in Periodicals

1. **Roisin, N.**, Brunin, G., Rignanese, G.-M., Flandre, D., Raskin, J.-P. "Indirect light absorption model for highly strained silicon infrared sensors". In: *Journal of Applied Physics* 130 (2021). ISSN: 10897550. DOI: 10.1063/5.0057350.
2. **Roisin, N.**, Delhaye, T., André, N., Raskin, J.-P., Flandre, D. "Low-power silicon strain sensor based on CMOS current reference topology". In: *Sensors and Actuators A: Physical* 339 (2022). ISSN: 09244247. DOI: 10.1016/j.sna.2022.113491.

3. **Roisin, N.**, Colla, M.-S., Raskin, J.-P., Flandre, D. "Raman strain–shift measurements and prediction from first-principles in highly strained silicon". In: *Journal of Materials Science: Materials in Electronics* 34 (2023). ISSN: 1573482X. DOI: 10.1007/s10854-022-09769-3.
4. **Roisin, N.**, Colla, M.-S., Scaffidi, R., Pardoen, T., Flandre, D., Raskin, J.-P. "Band gap reduction in highly-strained silicon beams predicted by first-principles theory and validated using photoluminescence spectroscopy". In: *Optical Materials* 144 (2023). ISSN: 09253467. DOI: 10.1016/j.optmat.2023.114347.
5. Bidoul, N., **Roisin, N.**, Flandre, D. "Tuning the Intrinsic Stochasticity of Resistive Switching in VO2 Microresistors". In: *Nano Letters* 24 (2024), pp. 6201–6209. ISSN: 1530-6984. DOI: 10.1021/acs.nanolett.4c00184.
6. **Roisin, N.**, Brunin, G., Rignanese, G.-M., Flandre, D., Raskin, J.-P., Poncé, S. "Phonon-limited mobility for electrons and holes in highly-strained silicon". In: *npj Computational Materials* 10.242 (2024). ISSN: 2057-3960. DOI: 10.1038/s41524-024-01425-0.

Patents

1. **Roisin, N.**, Flandre, D., André, N., Delhaye, T. "Strain sensor". WO2022023571A1. 2022.

Contents

Remerciements i

Abstract v

Author's publication list vii

Table of Contents ix

List of Acronyms xiii

Introduction 1

1 Fundamental properties of strained silicon 13
1.1 Computation scheme 14
1.1.1 Relaxed silicon 14
1.1.2 Calculation parameters 17
1.1.3 Primitive cell of strained silicon 18
1.2 First-principles results 21
1.2.1 Band gap reduction 22
1.2.2 Effective mass 30
1.2.3 Phonon energy 39
1.3 Experimental validation of the band gap reduction 44
1.3.1 Fabrication of deformed silicon microbeams 44
1.3.2 Description of the samples 47
1.3.3 Strain determination by Raman spectroscopy 48
1.3.4 Photoluminescence measurements 51
1.4 Chapter Summary 57

2 Phonon-limited mobility in strained silicon 59
2.1 Piezoresistive measurements 60
2.1.1 Semi-empirical models 60
2.1.2 Experimental observation 66
2.2 First-principles computations 70
2.2.1 Boltzmann transport equation 70
2.2.2 Scattering rate and velocity 77
2.2.3 Phonon-limited mobility 81
2.2.4 Piezoresistive coefficients 90
2.2.5 Impact of the doping 92
2.2.6 Mobility for uniaxial strain along [110] direction 95
2.3 Chapter Summary 98

3 Optical properties of strained silicon 101
3.1 First-principles computation scheme 102
3.1.1 Description of the optical properties 102
3.1.2 BSE method for direct transitions 104
3.1.3 EPW method for indirect transitions 106
3.1.4 Analytical model for the absorption coefficient 107
3.1.5 Computation scheme 112
3.2 First-principles results 113
3.2.1 Refractive index and direct absorption 114
3.2.2 Indirect absorption 117
3.3 Chapter Summary 125

4 Infrared performances of strained silicon photodiode 127
4.1 Optical absorption in a semiconductor layer 127
4.1.1 Absorption in a single layer 130
4.1.2 Absorption with antireflective coating 131
4.2 Photodetector theory 134
4.2.1 Photogenerated current in a photoconductor 134
4.2.2 Photogenerated current in a photodiode under transverse illumination 136
4.2.3 Photogenerated current in a photodiode under longitudinal illumination 139
4.2.4 Responsivity 142
4.3 TCAD simulation of a photodiode 144
4.3.1 Photodiode design 145
4.3.2 Strained photodiode under normal illumination 148

4.3.3 Strained photodiode under longitudinal and lateral illumination 151
4.3.4 Strained photodiode with antireflective coating 157
4.4 Chapter Summary 162

Conclusion **165**

Appendix **173**
A Convergence study 173

Bibliography **179**

List of Acronyms

ARC antireflective coating 128

BSE Bethe-Salpeter equation 101

BTE Boltzmann transport equation 59

CCD charge-coupled device 49

CMOS complementary metal-oxide-semiconductor 7

DFPT density-functional perturbation theory 17

DFT density-functional theory 1

DOS density of states 74

EPM empirical pseudopotential method 15

EPW electron-phonon wannier 70

FIR far infrared 2

FCC face-centered cubic 14

GGA generalised gradient approximation 16

HH heavy hole 25

IR infrared 1

KS Kohn-Sham 17

LA longitudinal accoustic 39

LDA local density approximation 16
LH light hole 25
LO longitudinal optical 39
LWIR longwave infrared 2
MBPT Many-body perturbation theory 16
MRTA momentum relaxation time approximation 72
MWIR midwave infrared 2
NIR near infrared 2
NSCF non-self-consistent field 17
PBE Perdew-Burke-Ernzerhof 17
PDP phonon deformation potential 41
PL photoluminescence 14
QNR quasi-neutral region 137
SCF self-consistent field 17
SEM scanning electron microscopy 46
SERTA self-energy relaxation time approximation 72
SO spin orbit 25
SOC spin orbit coupling 73
SWIR shortwave infrared 2
TA transverse accoustic 39
TB tight-binding 15
TCAD technology computer-aided design 2
TMM transfer matrix method 128
TO transverse optical 39

Introduction

Silicon has long been a key material in the electronics industry, playing a critical role in the development of efficient and reliable electronic devices. Its dominance in semiconductor technology is due to its good electronic properties, as well as its abundance, low cost and compatibility with large-scale manufacturing processes [1]. Silicon photodetectors benefit from these advantages while having a relatively low environmental impact compared to other materials such as germanium (Ge) [2] or indium gallium arsenide ($In_xGa_{1-x}As$) [3]. However, the performance of silicon-based photodetectors is fundamentally limited by their indirect band gap of 1.12 eV at room temperature, which restricts their ability to efficiently detect light beyond wavelength of 1.1 µm [4]. This poses a significant challenge to extend the use of silicon detectors into the infrared (IR) region, which is critical for applications such as telecommunications [5], chemical sensing [6] or atmospheric observation [7]. To overcome these limitations, a promising approach is the use of strain engineering to modify the electronic band structure of silicon and thereby enhance its optical and electrical properties.

The aim of this thesis is to carry out a comprehensive study of the optical and electrical properties of strained silicon in order to assess its potential for IR photodetection. Theoretical and experimental approaches are used in this work. First-principles calculations based on density-functional theory (DFT) are used to investigate the strain-induced changes in the band structure, carrier mobility and absorption properties of silicon. Where possible, experimental validation is provided to validate the theoretical re-

For the sake of English correction only, an AI writing tool (DeepL) has been used in this thesis.

sults. Finally, technology computer-aided design (TCAD) simulations are used to investigate the improvement of a photodetector using strained silicon.

Photodetector for infrared applications

IR wavelengths are defined from 0.7 µm to 1000 µm and cover applications from optical communications at lower wavelengths to thermal imaging at higher wavelengths. The first IR region, defined between 0.7 µm and 1.4 µm, is called the near infrared (NIR) and typical applications are optical communications in the O-band at 1310 nm [8], night vision [9] and gas detection such as carbon dioxide [10]. Beyond this range, the shortwave infrared (SWIR) from 1.4 µm to 3 µm includes optical communications in the C-band at 1550 nm [11], chemical observation for industrial or food monitoring [12], and atmospheric observation [13]. Thermal imaging [14] at high temperatures begins in the midwave infrared (MWIR), between 3 µm and 8 µm, which includes military applications such as missile guidance [15]. Longwave infrared (LWIR) from 8 µm to 15 µm and far infrared (FIR) from 15 µm to 1000 µm are mainly used for thermal imaging. LWIR includes room temperature measurements such as human body monitoring around 10 µm [16] or industrial monitoring such as gas leak detection [17], e.g., NH_3 monitoring at 9 µm [18]. FIR sensors are used for thermal observation below 200 K, for example in astronomical observation [19]. This range is also used for chemical and biomedical characterisation as the energy levels are typically those of molecular vibrations [20]. Table 1 summarises the infrared regions, typical applications and materials used for intrinsic photon detectors.

There are two main types of IR detector. Thermal IR sensors detect radiation by absorbing heat, which causes a temperature change in the sensor material. These sensors typically operate in the MWIR and LWIR ranges. They have slower response times because they rely on gradual heating but do not require external cooling. Although less sensitive than photon sensors, thermal IR sensors are widely used in thermal imaging cameras [22]. In contrast, photon IR sensors work by directly detecting infrared photons by optoelectronic absorption in the material. These sensors are faster and more sensitive, but often require cooling to reduce noise, especially at higher wavelengths where the thermal energy becomes similar

Infrared	Range	Material	Typical applications
Near (**NIR**)	0.75 - 1.4 µm	Si, Ge, $In_{0.53}Ga_{0.47}As$	*Optical communication* *Gas sensing (CO_2)* *Night vision*
Shortwave (**SWIR**)	1.4 - 3 µm	InAs, GaSb $In_{0.79}Ga_{0.21}As$	*Optical communication* *Chemical observation* *Atmospheric observation*
Midwave (**MWIR**)	3 - 8 µm	PbSe, InSb	*High-temperature imaging* *Defense and military*
Longwave (**LWIR**)	8 - 15 µm	$InAs_{1-x}Sb_x$, $Pb_{1-x}Sn_xTe$	*Room-temperature imaging* *Industrial monitoring*
Far (**FIR**)	15 - 1000 µm	$Hg_{1-x}Cd_xTe$	*Chemical characterization* *Low-temperature imaging*

Table 1 Infrared spectrum definitions in terms of wavelength [21] and most widely used materials for IR intrinsic photon detector.

to the band gap. This work focuses on photon sensors operating mainly at lower wavelengths, *i.e.*, NIR and SWIR, as strain engineering allows silicon absorption to be extended in these regions. Different types of IR photon detectors can be designed such as intrinsic, extrinsic, free carrier and quantum (dots and wells). These detection mechanisms are illustrated in Fig. 1. Intrinsic photodetectors rely on band-to-band transitions where photons excite electrons from the valence band to the conduction band [23, 24]. These detectors operate primarily in the NIR and SWIR regions. They offer high sensitivity and fast response times. Extrinsic photodetectors use doped semiconductors in which impurities introduce energy levels within the band gap, allowing detection at longer wavelengths than intrinsic detectors [25, 26]. These detectors typically operate in the LWIR range using doped silicon. Free-carrier photodetectors work by interacting with free electrons or holes in a material, causing a change in conductivity [27, 28]. These detectors are most effective in the FIR range, typically using highly doped semiconductors or metals. They are less sensitive than other types, but offer a wide detection range. Quantum photodetectors, includ-

ing quantum dots and quantum wells, exploit the quantum confinement effect, where the dimensions of the semiconductor structures control the energy levels, typically from the SWIR to the LWIR range [29, 30].

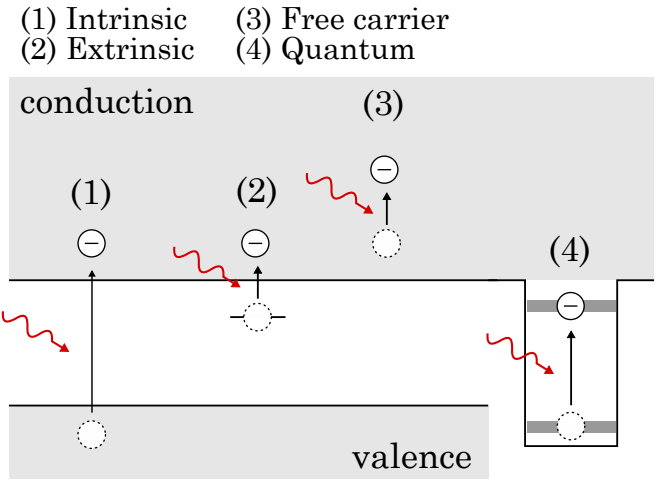


Fig. 1 Illustration of the detection mechanisms for photon-type IR detector. The mechanisms of carrier generation due to incident photon (red arrow) are (1) intrinsic detection based on band-to-band transition, (2) extrinsic detection based on impurity-to-band transition, (3) free carriers and (4) quantum detections.

Typical materials used for intrinsic photodetection are indicated in table 1. Silicon is the most commonly used material in the NIR , but only up to 1.1 µm [31], making it unsuitable for optical communications or CO_2 sensing. To reach higher wavelengths, $In_{1-x}Ga_xAs$ is widely used [32]. An equal proportion of indium and gallium allows the detector to detect up to 1.6 µm light, while a larger proportion of indium, *e.g.*, 80%, can lead to absorption up to 2.6 µm [33, 34]. Cooling is required at higher wavelengths to avoid thermal generation leading to high noise. Compounds with antimony (Sb) such as $InAs_{1-x}Sb_x$ are used for MWIR and LWIR [35, 36], the higher the Sb content the lower the band gap of the alloy. For even higher wavelengths, tellurium (Te) compounds are preferred, especially $Hg_{1-x}Cd_xTe$ for FIR [37]. Ge and $In_{1-x}Ga_xAs$, while offering an extended wavelength range for NIR and SWIR applications, rely on scarce materials that require environmentally damaging extraction processes [38, 39, 40]. In contrast, silicon is abundant, less toxic and benefits from established pro-

duction methods, making it a more sustainable and economical option for many applications despite its limited wavelength range [4]. The microfabrication process still has a significant environmental impact, but the cost of extracting rare materials is avoided [41, 42, 43].

Strained silicon as promising material for IR detection

Since the discovery of the piezoresistive effect in 1925 in metals [44] and in 1954 for silicon and germanium [45], strain has been widely used to increase the mobility of silicon devices in today's technology [46]. Despite this knowledge, the studies on strained silicon have remained stuck at low stress levels due to the brittleness of silicon wafer, which struggle to tolerate stress above 500 MPa [47, 48]. These low strains, below 0.3%, have been found to be sufficient to obtain a significant increase in the mobility of the silicon, but too low to observe the optical enhancement of interest for infrared detection. The potential to tune the band structure with strain, thereby reducing the band gap and increasing infrared detection, was first highlighted by theoretical studies. However, theoretical studies [49] at the end of the nineties were based on parameters obtained experimentally at low strains, leading to large errors at higher strains. It was not until the end of the 2000s that a fully theoretical model based on DFT [50, 51] was able to treat the strain-induced change in band structure with precision [52, 53]. At the same time, the first experimental work was done to show the band gap reduction with strain in silicon using photoluminescence measurements [54, 55]. Only recently, Katiyar *et al.* [56, 57] has demonstrated the change in IR absorption in a silicon using thin devices of tens of nanometers but without any explanation or exploitation of this phenomenon for photodetection. All these previous works have shown the potential for extending light absorption into the infrared, although accurate prediction of the change in the material properties at large strain and demonstrations of strained silicon devices are still lacking. Evidences from previous work leads us to think that with sufficient strain, it should be possible to develop a new generation of silicon-based photodetectors that could operate at higher wavelengths where expensive materials such as Ge and $In_{1-x}Ga_xAs$ are usually preferred. The main objective of this work is to investigate the feasibility of such solution, first by looking at the impact in optoelectronic properties with strain, then by studying the sen-

sitivity improvement we could expect for a photodetector using strained silicon.

Reaching high strain in silicon

To tune the optoelectronic properties of silicon, high strains up to a few percents are required [49, 58, 54]. In recent decades, many improvements have been made to achieve significant strain levels thanks to advanced microfabrication schemes [59, 60, 61, 62]. Several experimental methods for stressing semiconductor-based devices have been proposed in the literature. We group all these methods into four types as shown in Fig. 2.

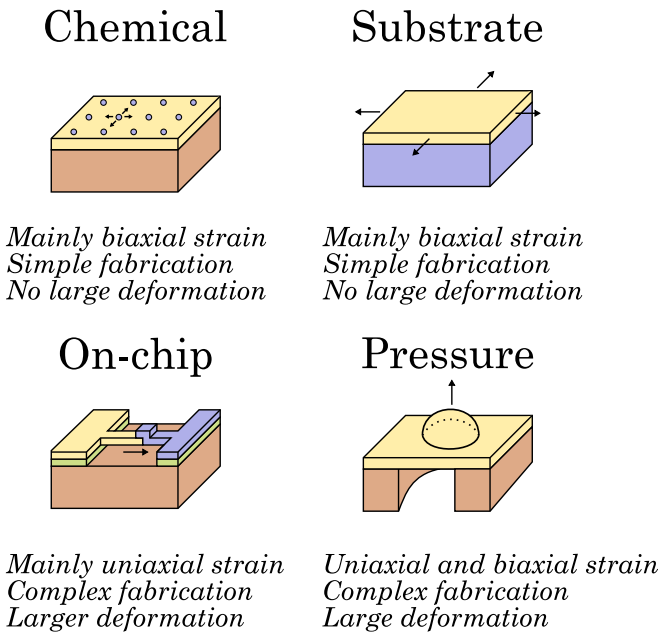


Fig. 2 Illustration and specification of the different types of strain techniques existing. The straining system, strained material and substrate are shown in purple, yellow and brown, respectively. The specificity of each solution is written in italic.

Chemical strain is mostly based on ion implantation inside a thin-film material layer to form strain clusters due to the addition of an external specimen in the material lattice [63, 64, 65]. This technique allows strain

up to 1%, but tends to introduce a large number of defects incompatible with photodetection applications [66, 67]. Substrate-induced strain allows wafer-scale deformation using the mismatch between the lattices of two materials [68, 69]. Devices can also be directly strained by bending the substrate using external actuation. On-chip techniques rely on stressors that use the internal stress of the deposited material to strain the device [60, 70]. Finally, pressure can be applied to a membrane to strain devices, but this requires external control of the environment [71, 72]. Substrate-induced strain techniques show the advantages of a simple fabrication scheme, but are only used for biaxial strain and smaller deformations have been reported in the literature. Pressure-based setup allows fine control of the strain applied to the material, with significant strain being achieved (up to 4% biaxial strain [56]). Both uniaxial and biaxial strains can be generated by positioning devices at the side or centre of the membrane. However, the need for external actuation by a pressure system and the complex fabrication process limit its applicability for long-term strained devices. This solution is then more commonly used for test or research purposes. The most promising techniques to achieve high strain are on-chip tensile techniques using stressors or electrically actuated [73, 74, 40], which can achieve fracture strain in silicon of about 17 % [61, 75], close to the theoretical limit [76]. However, it requires a complex fabrication process and no electronic devices have yet been demonstrated at this high level. On-chip techniques at lower strain are now being used with silicon nitride strainers to achieve high-mobility transistors in complementary metal-oxide-semiconductor (CMOS) technology [77, 78, 79], but the achievable strain using simple strainers without free-standing structure is limited.

The nanoscale dimensions are key to reducing the number of defects in the strained structures and thus allowing higher strains to be achieved without failure. As shown in Fig. 3, there is a trend of increasing fracture stress and strain as the volume of the sample decreases. It has been shown that the defect and the quality of the interface are critical to avoid crack propagation which can lead to fracture [80]. The reduction in volume leads to a reduction in the size of the defect, but also to better control of the sample fabrication using microfabrication techniques. The higher fracture strain is obtained with silicon nanowires that have a small volume [73, 74, 81, 75, 82, 83]. As shown by Zhang *et al.* [61], nanowires grown using a bottom-up approach have better quality and can withstand much higher strain than samples made using etching techniques. Bottom-up fabricated samples are thus able to approach the fundamental limit of silicon, pre-

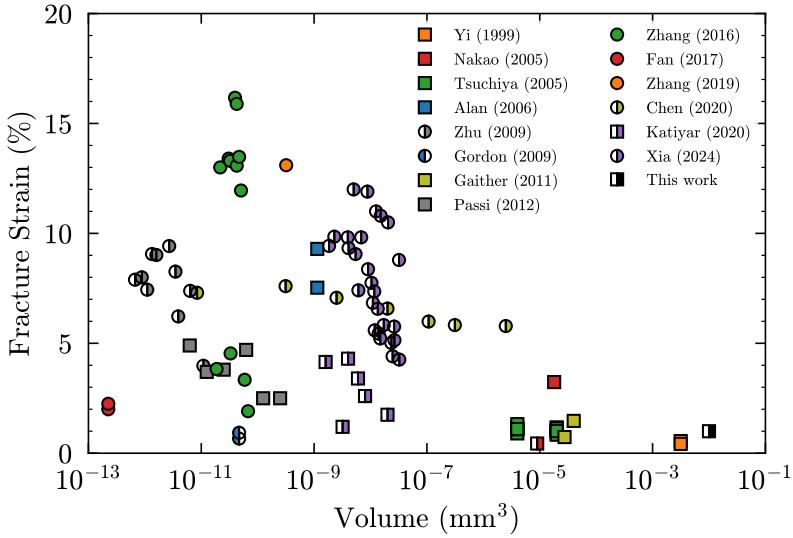


Fig. 3 Literature comparison of the fracture strain obtained in microfabricated samples with regards to the silicon volume. Fracture strain of silicon nanowires are indicated with colored circles while the one obtained from thin-films samples are shown with square. Loading has been done along [110] (full colored marker), [100] (right colored marker) and [111] (left colored marker) crystal directions.

dicted to be between 17% and 23% [84, 76]. Although the fracture strain of thin-film samples is typically lower [85, 86, 87, 88], they still manage to reach a few percent deformation [60, 59]. In addition, Katiyar *et al.* [56] has recently shown the potential of thin-film silicon to achieve high strain levels. All reported studies that achieve high fracture strains are based on a uniaxial strain configuration, with the exception of work by Katiyar *et al.* [56] that compresses a polyimide membrane to achieve 4% biaxial strain.

In this work, lab-on-chip samples following the fabrication scheme of Passi *et al.* [60] are processed to study the band gap reduction in strained silicon with photoluminescence measurements. The fabrication was done by Dr. Marie-Stéphane Colla in UCLouvain cleanroom (Winfab). Unfortunately, only 1% of strain has been achieved due to the failure of the silicon nitride stressors. In addition, silicon strain gauges from *Kyowa* company are employed to retrieve the variation of the electron mobility with strain. The samples were able to withstand up to 1%-strain before fracture despite the large volume of silicon.

Research objectives and outline of the work

The main objective of this work is to evaluate the potential of strain engineering to improve the optoelectronic performance of silicon photodetectors for IR detection. The motivation behind this is the substitution of materials used in NIR and SWIR detectors, such as Ge and $In_xGa_{1-x}As$, with strained silicon. Indeed, silicon has a reduced environmental impact while being low cost and compatible with the current CMOS fabrication scheme. We focus on the theoretical study of material properties and device performance, while validating the theoretical results experimentally where possible. A graphical summary of the outline of the thesis with the associated research questions for each chapter is given in Fig. 4.

In order to answer the main research question of how to improve the IR sensitivty of photodetector using strained silicon, three secondary research questions about the material properties need to be answered. The first is to know the effect of strain on the fundamental properties of silicon and which strain configuration would be best for optical absorption. The **first chapter** gives the answer by performing first-principles simulations to find the strain configuration that leads to the lower band gap, which is the most important property when talking about light absorption. In addition to these important results, the effect of strain on effective masses and phonon energy is also calculated for the following chapters. Both uniaxial and biaxial strain are considered in the three main crystal orientations of silicon, *i.e.*, $\langle 100 \rangle$, $\langle 110 \rangle$ and $\langle 111 \rangle$. This work intend to fill the gap in the literature of the lack of non-exhaustive study of the fundamental properties of strained silicon. Uniaxial tensile strain along the [110] direction is chosen as the best strain configuration. Indeed, uniaxial tensile strains are the best for achieving high strain levels, while the [110] direction is the one that leads to the most significant band gap reduction under uniaxial strain. An experimental validation of the band gap reduction for this strain direction is then carried out using photoluminescence measurements on samples that have been strained with silicon nitride actuators.

As strain has a significant effect on both electrical and optical properties, they are investigated in the second and third chapters respectively. The **second chapter** answers the question of the changes in electron and hole mobilities due to strain. It is the first time that *ab initio* theory has been used to predict the phonon-limited mobilities in strained silicon without any semi-empirical parameters. The theoretical calculations allow us

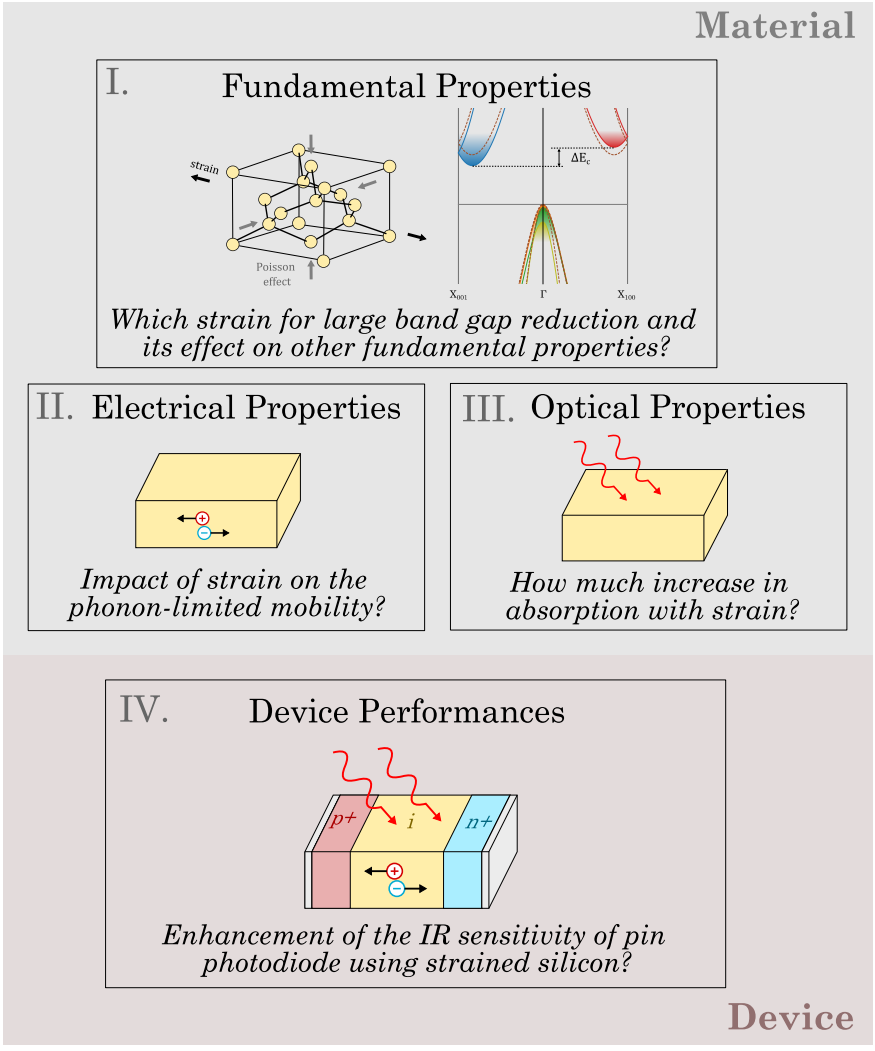


Fig. 4 Graphical summary of the outline of the thesis. The fundamental properties of strained silicon are studied in first chapter (I). The second (II) and third (III) chapters analysed the electrical and optical properties of silicon under uniaxial tensile strain, respectively. The device performances of an IR photodetector using strained silicon is finally studied in the fourth chapter (IV). The principal research question of each chapter is indicated in italic.

to accurately explain the effect of strain on the scattering mechanism, such as inter- and intravalley scattering for the electrons and inter- and intraband scattering for the holes. The results are confirmed experimentally for the electrons using n-doped silicon samples measured under a four-point bending scheme.

The **third chapter** answers the question of how the optical properties of silicon change with strain. The complex refractive index is the key parameter to be studied, describing both the propagation and absorption of light in the material. The Bethe-Salpeter equation (BSE), which takes into account the electron-hole interaction, is used to obtain the real part of the refractive index, which describes the propagation of light. It also gives the absorption coefficient through its imaginary part, but only for direct absorption. Indirect absorption, which is responsible for infrared absorption, is then calculated using the EPW code that takes into account the electron-phonon interactions. The first-principles results are compared with a semi-empirical model, which has the advantage of fast calculation but lacks accuracy due to the use of inaccurate semi-empirical parameters.

The **fourth and final chapter** answers the main research question of this thesis by predicting the sensitivity enhancement of IR sensors using strained silicon. In practice, the optical and electrical properties calculated for highly strained silicon are used in TCAD finite element software to study detectors based on pin photodiode configurations. Different light couplings such as normal, transverse and longitudinal to the photodiode structure are analysed. The importance of sufficient thickness to absorb IR light and maximise the effect of strain is highlighted. In particular, the sensitivity of such strained devices is studied as a fundamental parameter that depends on the strain. Finally, our results are compared with typical detectors using other infrared sensing materials such as $In_xGa_{1-x}As$ and Ge, showing the potential but also the necessity of high strain to achieve efficient IR photodetectors in silicon.

1

Fundamental properties of strained silicon

Silicon is a well-known material that has been used in the electronic and optoelectronic industries for decades. The relatively high mobility of the carriers, its ability to be produced with few defects and its ability to be doped to tune its properties, together with its abundance and low cost, make silicon the basis of semiconductor chips. Its fundamental electronic properties, such as the band structure (with band gaps and effective masses), have been carefully studied both theoretically [49, 51, 89] and experimentally [90, 91]. However, studies of the effect of strain on these properties, especially at high strain levels, remain scarce. This is due to the complexity of preparing and observing highly strained samples. In addition, semi-empirical models with fitting parameters struggle to accurately predict the effect of strain, and more advanced theoretical simulations such as DFT without fitting parameters are then required. The aim of this chapter is to analyse the fundamental properties of highly strained silicon by considering the most common strain configuration, *i.e.*, uniaxial and biaxial strain along the [001], [110] and [111] crystal directions. Indeed, the literature lacks a systematic approach to calculate the band structure properties in strained silicon for all strain configurations of interest. Theoretical calculations are used to predict the band gap reduction in order to find the most promising strain configuration for IR detection.

Additional analysis of effective masses and phonon energy are also carried out. Uniaxial tensile strain is the most promising way to achieve very high strain levels, and among these configurations, strain along the [110] crystal directions shows the highest band gap reduction. This strain was then chosen as the study case for the remainder of this work, which is aimed at improving IR photodetection. Finally, the band gap reduction for uniaxial strain along the [110] crystal direction is experimentally investigated with photoluminescence (PL) measurements on silicon beams strained with silicon nitride actuators.

1.1 Computation scheme

This section explains the computational scheme used to carry out the theoretical analysis. The basic crystal structure of silicon is recalled and we explain how to compute the new silicon lattice under six strain configurations, *i.e.*, uniaxial or biaxial along the [001], [110] and [111] crystal directions.

1.1.1 Relaxed silicon

The silicon unit cell is made of two inter-penetrating face-centered cubic (FCC) crystal structure with a two-atom primitive cell as displayed in Fig. 1.1. The three Bravais lattice vectors are given by

$$\mathbf{a} = \frac{a_0}{2}\begin{pmatrix} 0 \\ 1 \\ 1 \end{pmatrix}, \mathbf{b} = \frac{a_0}{2}\begin{pmatrix} 1 \\ 0 \\ 1 \end{pmatrix}, \mathbf{c} = \frac{a_0}{2}\begin{pmatrix} 1 \\ 1 \\ 0 \end{pmatrix}, \tag{1.1}$$

where $a_0 = 0.543$ nm is the experimental lattice parameter [92].

The two atoms of the primitive cells are located at positions $\mathbf{x}_1$ and $\mathbf{x}_2$:

$$\mathbf{x}_1 = \begin{pmatrix} 0 \\ 0 \\ 0 \end{pmatrix}, \qquad \mathbf{x}_2 = \begin{pmatrix} 0.25 \\ 0.25 \\ 0.25 \end{pmatrix}. \tag{1.2}$$

The reciprocal space containing all possible electron states in silicon has a body-centered cubic (BCC) lattice. Since experimental observation of the full electronic states is difficult, numerous theoretical frameworks

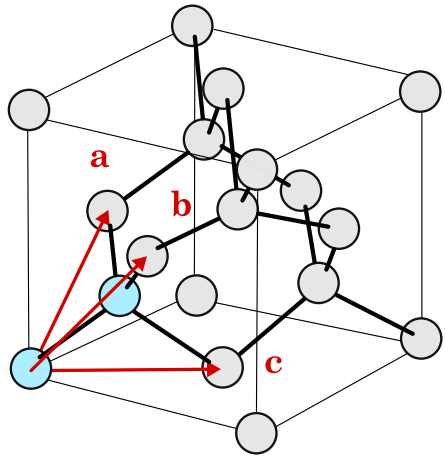


Fig. 1.1 Representation of FCC crystal structure of silicon. The lattice vectors of the primitive cell are indicated as well as the two atoms (in blue) of the primitive cell.

have been developed to study the electronic properties of semiconductors. Most of these computation schemes are semi-empirical, meaning that some tuning parameters are needed that are often deducted from experimental observation. The most popular methods are the $\mathbf{k}\cdot\mathbf{p}$ method [90, 93], the empirical pseudopotential method (EPM) [94, 49] and the tight-binding (TB) method [95, 96].

In order to avoid fitting parameters and the associated uncertainty, DFT [97, 98] has been extensively used to calculate the band structure of materials in a reliable way, but with additional computational cost. The idea behind DFT is the use of the simple three-dimensional electron density to describe the electron interactions in a system. It allows efficient calculations most of the time but still suffer from the approximation of the exchange-correlation functional. This causes large delocalization error that leads to an important underestimation of the band gap and static correlation error that prevents a correct calculation for degenerated or near-degenerate states such as in strongly correlated material [99].

Figure 1.2 shows the TB band structure calculated for silicon using the parameters from Ref. [100], considering sp^3-bonded atoms. In this model the valence bands are in good agreement, while the introduction of an excited state s^* allows the lowest energy conduction bands to be described. This rough model uses seven empirical parameters to fit the band struc-

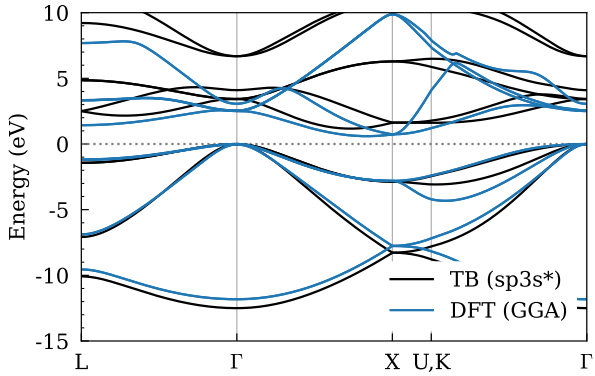


Fig. 1.2 Band structure obtained using first-principles computations. The DFT using generalised gradient approximation (GGA) (blue curves) is compared to the sp^3s^* TB theory (black curves).

ture. The method gives a satisfactory shape for the valence bands and the lower part of the conduction band, but lacks precision for advanced calculations. More recent models that include *d*-orbitals give better results but increase the number of fitting parameters [101]. This method was then extended to predict the band structure variations of strained group IV semiconductors such as silicon and germanium [102]. Additional semi-empirical parameters were introduced to deal with the band structure variations with strain. Semi-empirical methods are useful to avoid computational costs, but they lack the ability to predict the evolution in an unstudied case, as they always need to be calibrated against experimental or *ab initio* data.

For this reason, DFT calculations are preferred, although basic implementations using the local density approximation (LDA) or the GGA underestimate the band gap of the material as they do not feature the discontinuity in the derivative of the exchange correlation energy [103, 104]. Many-body perturbation theory (MBPT), based on the Green's functions formalism (GW) [105, 106], is used to correct the band gap underestimation in GGA.

As shown in Tab. 1.1, the 0.61 eV band gap predicted using DFT with the parameters discussed in section 1.1.2, between the maximum of valence bands at Γ and the minimum of conduction bands along Δ-path, is

corrected close to the experimental value of 1.12 eV using single-shot GW calculations (G_0W_0). The direct band gap at those position are respectively going from 2.55 eV and 3.30 eV up to 3.17 and 3.89 eV.

	DFT	G_0W_0	Exp. [107]
$E_{g,\Gamma\Delta}$	0.61	1.13	1.12
$E_{g,\Gamma}$	2.55	3.17	3.2
$E_{g,\Delta}$	3.30	3.89	4.0

Table 1.1 Relevant band gaps of silicon, obtained with DFT and corrected with GW calculation. Experimental data are also provided. All the values are expressed in eV.

1.1.2 Calculation parameters

In this work, the band structure is calculated from first principles using DFT, the band gap correction using single-shot GW, and the phonon energies using density-functional perturbation theory (DFPT), as implemented in ABINIT [108, 109]. Scalar-relativistic norm-conserving pseudopotential with non-linear core correction from PSEUDO DOJO [110] in the GGA of Perdew-Burke-Ernzerhof (PBE) [111] is used.

Convergence results are shown in appendix A, starting with the lattice parameter a_0 for which a value of 0.5469 nm was found with a planewave cutoff of 20 Ha and a $\mathbf{k}$ grid of $12 \times 12 \times 12$. The calculated lattice parameter is a bit higher than the experimental value of 0.543 nm [92]. The calculation parameters are kept to study the atomic relaxation in the strained structure.

For the band parameters calculated using DFT, the Kohn-Sham (KS) wavefunctions are obtained by performing a self-consistent field (SCF) calculation on a coarse $12 \times 12 \times 12$ $\mathbf{k}$ grid using a Monkhorst-Pack grid [112] with a planewave cutoff of 20 Ha. A non-self-consistent field (NSCF) calculation is then performed along the important paths of the reciprocal space with fine resolution to retrieve the band gaps and effective masses. This leads to a convergence below 0.1 meV for the fundamental band gap, as shown in appendix A. The same grid of $12 \times 12 \times 12$ $\mathbf{k}$ points with a planewave of 20 Ha provides convergence below 0.05 meV for the phonon energy calculating with DFPT.

MBPT, based on the Green's functions (GW) formalism, is used to correct the well-known band gap underestimation in GGA. In practice, quasi-

particle energies and amplitudes are computed on a $12 \times 12 \times 12$ **k**-point grid, the same as DFT calculations. Convergence study for the G_0W_0 have been done by looking at the quasi-particle correction at Γ. As shown in appendix A, a planewave cutoff of 8 Ha is sufficient while a cutoff of 6 Ha and 100 bands for the calculation of the screening interactions lead to convergence below 10 meV.

1.1.3 Primitive cell of strained silicon

Considering elastic deformation, the relation between the stress components σ_{ij} and the strain ones ε_{kl} can be described using the components C_{ijkl} of the compliance tensor:

$$\sigma_{ij} = C_{ijkl}\varepsilon_{kl}. \tag{1.3}$$

In silicon, only three distinct components are used for the 81 terms of the fourth rank tensor and the compliance matrix **C** in Voigt notation becomes [113]

$$\mathbf{C} = \begin{pmatrix} C_{11} & C_{12} & C_{12} & & & \\ C_{12} & C_{11} & C_{12} & & & \\ C_{12} & C_{12} & C_{11} & & & \\ & & & C_{44} & & \\ & & & & C_{44} & \\ & & & & & C_{44} \end{pmatrix}, \tag{1.4}$$

where $C_{11} = 165.77$ GPa, $C_{12} = 63.93$ GPa, and $C_{44} = 79.62$ GPa [114].

In order to calculate the stress-strain relationships in an arbitrary direction, it is then necessary to rotate the tensor so that one of the axes is aligned with the crystal direction of interest. In this work the stress conditions along three crystal directions ([001], [110] and [111]) are studied.

The Young's modulus Y_{ijk} defines the relationship between the stress applied in a particular direction $[ijk]$ and the deformation caused in that direction. It can be expressed in terms of the C_{ijkl} components. This leads to the following expressions for the moduli in the three directions stud-

ied [115]:

$$\begin{aligned} Y_{001} &= \frac{(C_{11}-C_{12})(C_{11}+2C_{12})}{(C_{11}+C_{12})}, \\ Y_{110} &= 2\left(\frac{C_{11}}{C_{11}^2+C_{11}C_{12}-2C_{12}^2}+\frac{1}{2C_{44}}\right)^{-1}, \\ Y_{111} &= 3\left(\frac{C_{11}-C_{12}}{C_{11}^2+C_{11}C_{12}-2C_{12}^2}+\frac{1}{C_{44}}\right)^{-1}. \end{aligned} \tag{1.5}$$

The strain tensors under stress applied in the three main crystal directions are given by

$$\begin{aligned} \mathbf{E}_{001} &= \begin{pmatrix} \varepsilon_{\parallel} & & \\ & \varepsilon_{\parallel} & \\ & & \varepsilon_{\perp} \end{pmatrix}, \\ \mathbf{E}_{110} &= \frac{1}{2}\begin{pmatrix} (\varepsilon_{\perp}+\varepsilon_{\parallel}) & (\varepsilon_{\perp}-\varepsilon_{\parallel}) & \\ (\varepsilon_{\perp}-\varepsilon_{\parallel}) & (\varepsilon_{\perp}+\varepsilon_{\parallel}) & \\ & & 2\varepsilon_{\perp} \end{pmatrix}, \\ \mathbf{E}_{111} &= \frac{1}{3}\begin{pmatrix} (\varepsilon_{\perp}+2\varepsilon_{\parallel}) & (\varepsilon_{\perp}-\varepsilon_{\parallel}) & (\varepsilon_{\perp}-\varepsilon_{\parallel}) \\ (\varepsilon_{\perp}-\varepsilon_{\parallel}) & (\varepsilon_{\perp}+2\varepsilon_{\parallel}) & (\varepsilon_{\perp}-\varepsilon_{\parallel}) \\ (\varepsilon_{\perp}-\varepsilon_{\parallel}) & (\varepsilon_{\perp}-\varepsilon_{\parallel}) & (\varepsilon_{\perp}+2\varepsilon_{\parallel}) \end{pmatrix}, \end{aligned} \tag{1.6}$$

where $\mathbf{E}_{ijk}$ is the strain tensor for biaxial or uniaxial stress applied in the $[ijk]$ crystal direction. $\varepsilon_{\perp}$ stands for the strain component oriented perpendicularly to the crystal plane (ijk) while $\varepsilon_{\parallel}$ is the associated transverse strain, *i.e.*, parallel to the crystal plane (ijk).

The Poisson ratio describes the relationship between the perpendicular and parallel strain components:

$$\varepsilon_{\parallel} = -\nu_{ijk}\,\varepsilon_{\perp}, \tag{1.7}$$

where ν_{ijk} is the Poisson ratio for the stress applied in the $[ijk]$ direction. For uniaxial configuration, the stress is applied perpendicular to the crystal interface, *i.e.*, in the direction of the $\varepsilon_{\perp}$ component. Conversely, for biaxial stress, the stress is applied parallel to the crystal interface, *i.e.*, in the direction of the $\varepsilon_{\parallel}$ component.

The Poisson ratios for uniaxial stress are given by [115]

$$\begin{aligned} \nu_{001}^{uni} &= \frac{C_{11}+C_{12}}{C_{12}}, \\ \nu_{110}^{uni} &= \frac{2C_{11}C_{44}+(C_{11}+2C_{12})(C_{11}-C_{12})}{4C_{12}C_{44}}, \\ \nu_{111}^{uni} &= \frac{C_{11}+2C_{12}+2C_{44}}{C_{11}+2C_{12}-2C_{44}}, \end{aligned} \tag{1.8}$$

while the ratios for biaxial stress are given by

$$\begin{aligned} \nu_{001}^{bi} &= \frac{2C_{12}}{C_{11}}, \\ \nu_{110}^{bi} &= \frac{C_{11}+3C_{12}-2C_{44}}{C_{11}+C_{12}+2C_{44}}, \\ \nu_{111}^{bi} &= \frac{2(C_{11}+2C_{12}-2C_{44})}{C_{11}+2C_{12}+4C_{44}}. \end{aligned} \tag{1.9}$$

In a deformed crystal, the new set of lattice vectors ($\mathbf{a}'$, $\mathbf{b}'$ is $\mathbf{c}'$) are given by

$$(\mathbf{a}'\ \mathbf{b}'\ \mathbf{c}') = (\mathbf{I} + \mathbf{E}_{ijk}) \cdot (\mathbf{a}\ \mathbf{b}\ \mathbf{c}), \tag{1.10}$$

where $\mathbf{I}$ is the unit matrix.

In addition to the deformation of the crystal structure, the displacement of the two silicon atoms in the strained cell must be taken into account. Indeed, the positions of the two Si atoms must be recalculated to find the new equilibrium that minimises the total energy of the strained system. An internal structural relaxation for the two atoms of the strained unit cell is performed for each strain level, finding the positions that minimise the total energy of the cell.

The results of atomistic relaxation are shown in Fig. 1.3a and Fig. 1.3b for uniaxial and biaxial loading respectively. Only the atomic displacements corresponding to a stress applied in the [110] and [111] directions are calculated. In the [001] case, no internal relaxation occurs due to the absence of shear strain [116]. Both atoms have the same absolute displacement with respect to their relaxed positions, but in opposite directions. For uniaxial strain along [110], the structural displacement is directed along the lattice vector $\mathbf{c}$, giving an atomic displacement along this vector of about 0.087 % per unit strain (in percent) (negative for $\mathbf{x}_1$ and positive for $\mathbf{x}_2$). The components for the other lattice vectors involve the same displacement but in the opposite direction. In the case of [111] the displacement is 0.051 % per unit strain (in percent) and is similar along the three vectors (positive for $\mathbf{x}_1$ and negative for $\mathbf{x}_2$).

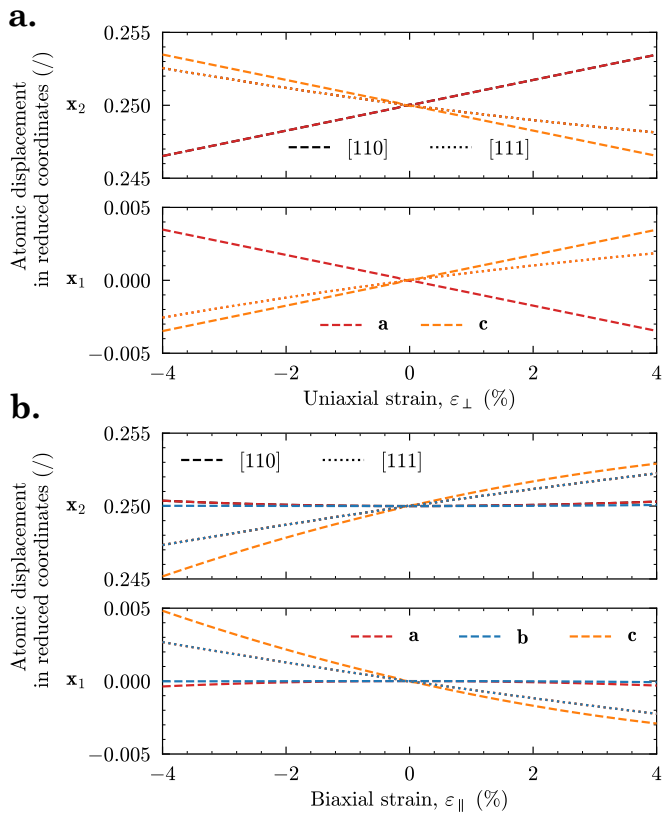


Fig. 1.3 Positions of the atoms $\mathbf{x}_1$ and $\mathbf{x}_2$ in relative coordinates inside the primitive cell under (a) uniaxial and (b) biaxial strain applied in the [110] (dashed lines) and [111] (dotted lines) crystal direction. The indices **a**, **b** and **c** refer to the lattice vectors.

1.2 First-principles results

In this section, the effect of strain on the band structure (energy and effective masses) and the phonon energy is studied with DFT for uniaxial and biaxial strain along the [001], [110] and [111] crystal directions.

1.2.1 Band gap reduction

One of the most important effects of strain on the band structure is the change in band edge energy, resulting in a reduction in the fundamental band gap. In silicon, the electron valleys, written Δ-valley, are defined at the minima of the conduction bands and are six-fold degenerated along the ⟨001⟩ directions. When strain is applied to the crystal, the degeneracy of the six electron valleys is lifted for uniaxial and biaxial strain applied along the [001] and [110] directions, as shown in Fig. 1.4, while strain applied

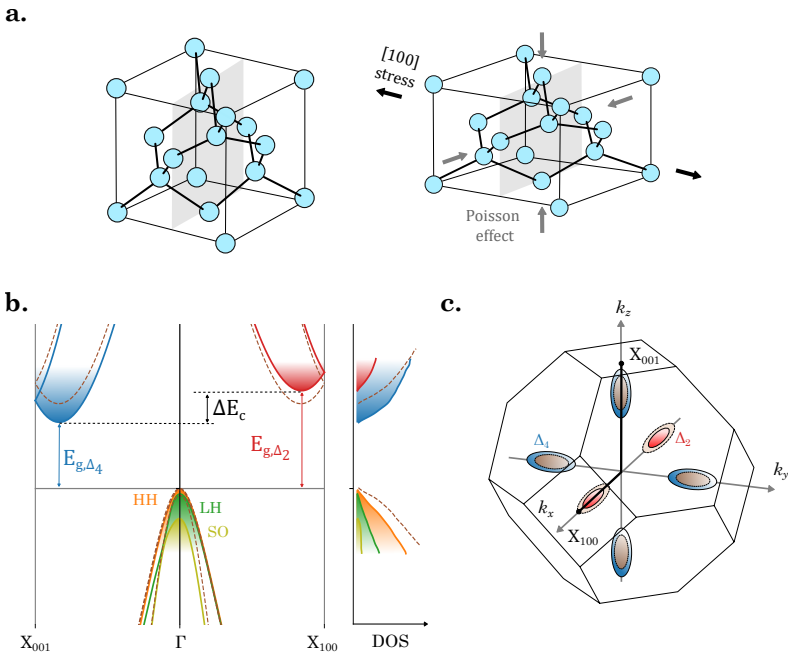


Fig. 1.4 (a) Illustration of the deformation of the silicon conventional cell under a strain along the [100] crystal direction and (b) its impact on the extrema of the valence bands (HH in orange, LH in dark green and SO in light green) and conduction bands (blue for the Δ_4-valleys and red for the Δ_2-valleys). The DOS of the three conduction bands and the two valleys are indicated next to the band structure. Dashed brown curves are used for the unstrained case. (c) Equipotential surface of the six electron-valleys and the lift of the degeneracy between the Δ_2-valleys (in red) along the [100] symmetry direction and the Δ_4-valleys (in blue) oriented in the transverse directions.

along the [111] direction maintains the degeneracy. The band structure is calculated from first principles using DFT for relaxed and strained silicon as implemented in ABINIT [108, 109]. A NSCF is then performed along a specific path in the Brillouin zone for fine resolution of the electron valley position and energy.

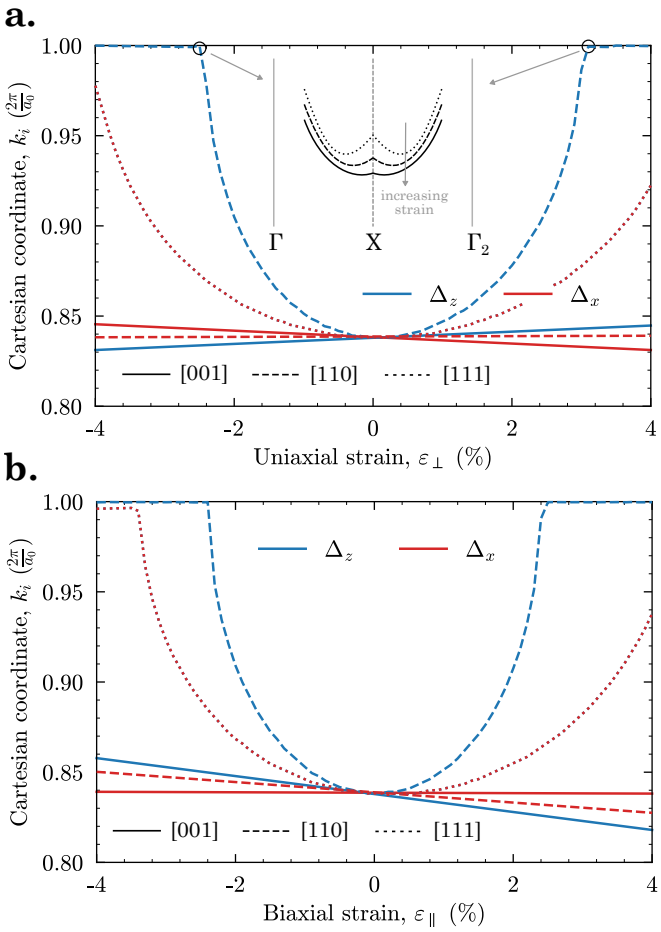


Fig. 1.5 Valley displacement along its longidutinal direction for (a) uniaxial and (b) biaxial strain along the [001] (continuous lines), [110] (dashed lines) and [111] (dotted lines) crystal directions. The position of the valley located towards the [100] (Δ_x) and [001] (Δ_z) symmetry point are shown in red and blue, respectively.

Before we can determine the different band gaps and effective masses

for each strained structure, we need to accurately calculate the position of the Δ-valleys when strain is applied [52, 117]. In fact, the strain caused the electron valleys to move in the reciprocal space. In the absence of strain, the six valleys are located at about 84% in the Γ-X symmetry path. Figures 1.5a and 1.5b show the valley displacement along its longitudinal axes for uniaxial and biaxial strain, respectively. The [001] strain configuration caused a limited change in the valley position, resulting in less than a few percent displacement even at high strain. On the other hand, the Δ_z-valleys, defined as the Δ-valleys along the [001] path, reach the limit of the reciprocal space for an uniaxial strain of 3.1% along the [110] direction, while a biaxial strain of 2.4% is sufficient. As shown in the inset of Fig. 1.5a, the position of the valley, defined as the minimum of the conduction bands, reaches the limit of the first Brillouin zone with increasing strain along the [110] and [111] crystal directions.

The variations of the band edges are shown in Fig. 1.6a and Fig. 1.6b for uniaxial and biaxial strain, respectively. For tensile strain, the maximum of the valence bands shows little variation and the spin-orbit band is shifted away from the HH and LH bands. The minimum of the conduction bands shows a higher rate of reduction, especially for uniaxial strain along the [110] direction or biaxial strain along the [001] direction. Conversely, compressive strain leads to a significant increase in the valence band maximum, while showing less variations for the conduction band minimum. Biaxial strain tends to cause a greater reduction in the band gap, especially for biaxial compressive strain along [110] and biaxial tensile strain along [001]. Uniaxial tensile strain is the most promising strain configuration to achieve high fracture strain, as seen in the introduction. For strain along [001], Δ_z-valleys show a reduced gap of 0.36 eV at 4%-strain, while the gap of Δ_x-valleys increases by 0.36 eV. The opposite behaviour is observed for [110] strain with a lower gap energy down to 0.12 eV at 4%-strain for the Δ_z-valleys and 0.54 eV for the Δ_x-valleys. In addition to the reduction of the band gap, a splitting between the HH and LH valence bands up to 72 meV can be observed for a strain of 4% oriented along the [110] direction. The degeneracy is maintained under [111] strain and the Δ_6-valleys show the smaller energy variations with respect to strain with 0.38 eV at 4%.

It is worth mentioning that the accuracy of DFT remains uncertain when the band gap starts to be small or negative (semi-metal) due to the stronger electron interactions that are not treated properly in standard DFT [99]. The accuracy of the effective masses can be greatly affected by

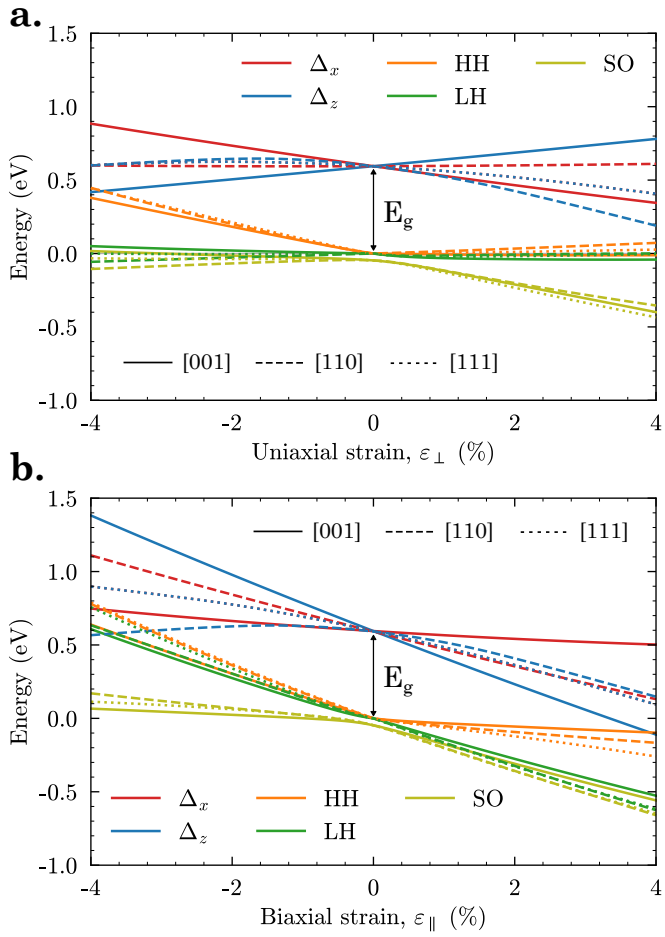


Fig. 1.6 Band edge variations for (a) uniaxial and (b) biaxial strain along the [001] (continuous lines), [110] (dashed lines) and [111] (dotted lines) crystal directions. The energy of the valley located towards the [100] (Δ_x) and [001] (Δ_z) symmetry point are shown in red and blue, respectively. The energy of the maximum of the heavy hole (HH), light hole (LH) and spin orbit (SO) bands located at Γ are shown in orange, dark green and light green, respectively. The fundamental band gap of silicon E_g can be computed by taking the difference between the band edges of lower energy among the conduction bands and the one with higher energy among the valence bands.

the small band gap and the resulting strong interactions.

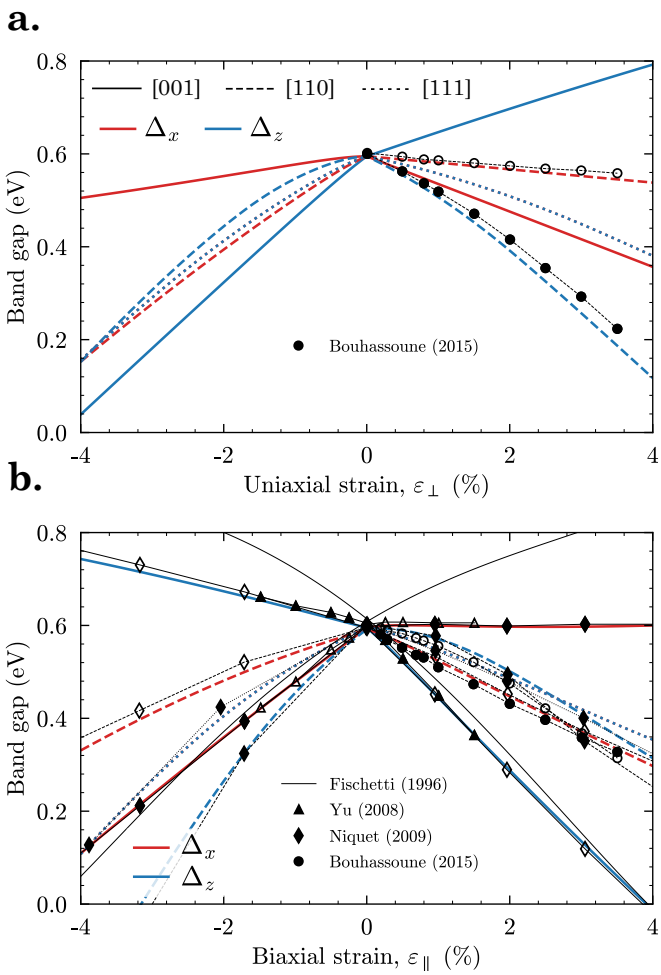


Fig. 1.7 Indirect band gap variations of silicon under (a) uniaxial and (b) biaxial strain along [001] (continuous line), [110] (dashed line), and [111] (dotted line) crystal directions. The results are obtained using DFT and are compared to literature for which the data have been offset to match the 0.61 eV band gap found in our calculations.

Figure 1.7 shows the evolution of the band gaps, defined as the difference between the minimum energy of the electron valleys and the maximum of the valence bands at Γ. The band gaps are calculated with respect

to the valley along [100] and [001], *i.e.*, Δ_x and Δ_z, which are no more degenerated for strain applied in the [001] and [110] directions.

		Uniaxial		Biaxial	
(meV)		-2%	2%	-2%	2%
Δ_x	[001]	−42.5	−119.0	**−235.6**	2.6
	[110]	**−200.7**	−28.0	−110.2	**−144.1**
	[111]	−182.0	**−86.0**	−189.8	−109.1
Δ_z	[001]	**-271.5**	102.3	78.8	**−306.6**
	[110]	−150.8	**−202.9**	**−326.5**	−90.0
	[111]	−182.0	−86.0	−189.8	−109.1

Table 1.2 Band gap shift in meV due to strain of the Δ_x-valley (along [100]) and Δ_z-valley (along [001]). The results are shown for a tensile and compressive strain of 2%. The largest shifts for each valley type are given in bold.

Table 1.2 summarises the band gap reduction of the Δ_x- and Δ_z-valleys for all strain configurations studied for compressive and tensile strains of 2%. For uniaxial strain, the highest reduction of −271.5 meV is achieved for the Δ_z-valleys under compressive strain, while tensile strain along the [110] direction only leads to a reduction of −202.9 meV at 2% strain. Biaxial strain of 2% shows higher strain reduction of −326.5 meV and −306.6 meV for compressive strain along [110] and tensile strain along [001], respectively. The calculation of the band structure of strained silicon with respect to strain is not new, but most of past works have focused on biaxial strain, as easily achieved using SiGe substrate [118]. Theoretical works based on EPM of Fischetti and Laux [49] are shown for biaxial strain along [001] direction. This method relies on perturbation coefficients determined experimentally at lower strain levels, resulting in an inaccurate prediction of the band gap variations. Later, Niquet *et al.* [102] used TB methods to predict the evolution for strain applied in three directions, *i.e.*, [001], [110] and [111], and validated their predictions using DFT. Other works, such as those by Yu *et al.* [53] and Bouhassoune *et al.* [117], obtained similar results using DFT for biaxial strain along the [001] and [110] crystal directions, respectively. Furthermore, Bouhassoune predicts the evolution of band gaps for uniaxial tensile strain along the [110] direction. Results based on, or calibrated with, DFT are in good agreement with ours, but we can see that the results of Fischetti and Laux [49] show a significant deviation, demon-

strating the limitations of the method used with inaccurate parameters.

Figure 1.8 shows the few experimental results of band gap reduction in highly strained silicon available in literature. They have all been obtained using PL measurements for which the luminescence peaks can be related to the band gaps of the material [119]. Munguía *et al.* [58, 120, 121, 122] studied [001] biaxial strain using a SiGe substrate to stress the top silicon layer. On the other hand, Wang *et al.* [54, 55, 123] have studied uniaxial compressive strain using silicon beams along [001] and [110] crystal directions encapsulated in silicon nitride stressors. Similarly, the strain was measured using Raman spectroscopy, while the band gap was determined using PL measurements. These experimental works show good agreement with the trend obtained from our DFT calculations. However, the variability between samples (at different strain levels) makes it difficult to obtain a clear trend experimentally.

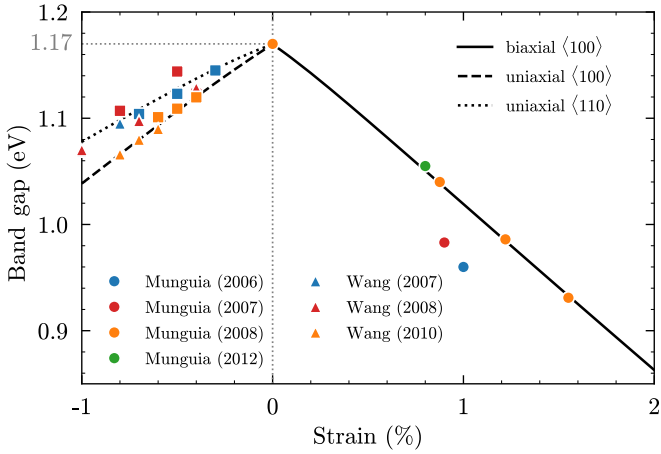


Fig. 1.8 Band gap reduction obtained experimentally using photoluminescence measurements. DFT results are indicated for tensile biaxial strain along [001] crystal direction (continuous line) and for compressive uniaxial strain along [001] (dashed line) and [110] (dotted line) directions. The theoretical results are offset to match the zero-strain band gap of silicon at 1.17 eV refered in the experimental works.

It is clear from the results in Fig. 1.7 that the highest reduction of the band gap, which is critical to enhance the absorption in the infrared region, is obtained for biaxial compressive strain along [110]. For tensile loading, uniaxial strain along [110] and biaxial along [001] lead to the most

important reduction. In this work, the band gap reduction are not the only concern and the ability to develop a manufacturing process capable of achieving high strain is critical for further development. For this reason, compressive strain, which can lead to bulking or delamination of the sample, is avoided [124]. Biaxial tensile strain is more easily achieved using membrane fabrication [56] or SiGe substrate [52]. However, the highest strain levels achieved in microfabricated specimens were obtained in uniaxial tensile loading using silicon nanowires [61, 75] or thin-film technology [60]. For this reason, tensile uniaxial strain has mainly been investigated in this work, and [110] shows the highest reduction.

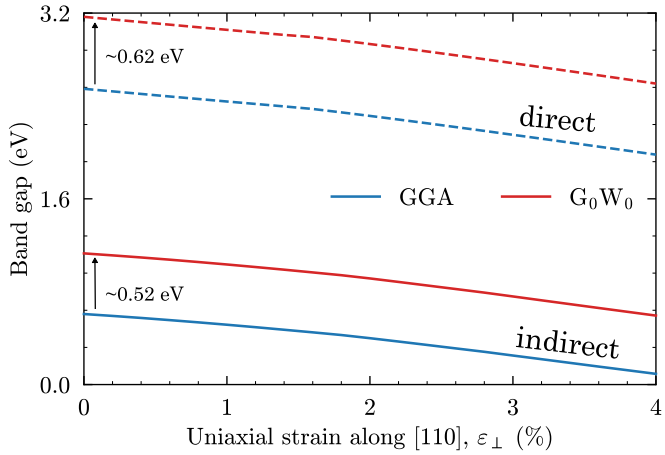


Fig. 1.9 Comparison of the indirect band gap (continuous lines) and the direct band gap located at Γ (dashed lines) computed using PBE functional (blue) and corrected by G_0W_0 (red) calculations for uniaxial strain applied in the [110] direction.

LDA and GGA are well known to underestimate the band gap of semiconductors [125], leading to a zero-strain band gap of 0.61 eV for silicon. MBPT based on GW is then used to correct the KS calculations. Since MBPT calculations are more expensive than DFT, single-shot quasi-particle correction G_0W_0 is performed only for uniaxial strain along the [110] direction. The 0.52 eV correction obtained in the relaxed case was found to be hardly insensitive to strain, as shown in Fig. 1.9. The slight change in the primitive cell due to strain does not significantly affect the quasi-particle correction.

1.2.2 Effective mass

The curvature at the band edges is important for macroscopic properties such as absorption or mobility. To analyse this curvature, the directional effective mass has been calculated for the valence and conduction bands for uniaxial and biaxial strain along the [001], [110] and [111] crystal directions. As a reminder, the effective mass is calculated by taking the inverse of the second derivative of the eigenenergies along a given direction [126], *i.e.*,

$$m^*_{n,ijk} = \hbar \left(\frac{\partial^2 E_n(k_{ijk})}{\partial k^2_{ijk}} \right)^{-1}, \tag{1.11}$$

where $\hbar$ is the reduced Planck constant, n is the band indice, k_{ijk} is the norm of the wavevector along direction $[ijk]$ and E_n is the energy of band n at that $\mathbf{k}$ point.

The calculation scheme is similar to that used to find the band gap reduction with strain. The band structure is first calculated from first principles using DFT for relaxed and strained silicon as implemented in ABINIT [108, 109]. A NSCF is then performed along a specific path in the Brillouin zone for fine resolution of the electron valley position and energy. Fine resolution is essential to obtain accurate second derivatives. The effective masses of the electrons are calculated at the minima of the Δ-valley, while those of the holes are calculated at the maximum of the valence bands in the centre of the reciprocal space, *i.e.*, at Γ. For the electrons, only two components need to be calculated as the shape of the valley is ellipsoidal. In the absence of strain, the transverse and longitudinal effective masses are calculated to be 0.200 m_e and 0.969 m_e respectively. For the holes, the HH band is highly anisotropic as we found effective masses of 0.269 m_e, 0.539 m_e and 0.678 m_e in the [100], [110] and [111] directions, respectively. The LH band has smaller effective masses in the different directions with values of 0.184 m_e, 0.137 m_e and 0.130 m_e in the [100], [110] and [111] directions, respectively. Finally, the SO band has a round and isotropic shape with the same effective mass of 0.224 m_e in all directions.

In Table 1.3, we compare our calculated effective masses with previous literature in the absence of strain. Both theoretical and experimental works are summarised. Experimental results have been obtained by cyclotron resonance from p-doped silicon for the valence effective masses [91, 90, 128] and n-doped silicon for the conduction ones [127, 90]. Theoret-

ical results have been obtained using first-principles calculations such as DFPT [132] or DFT [53, 130, 131, 133]. The theoretical calculations show good agreement with the experimental values, except in the [100] direction of the HH band.

The variations of the longitudinal and transverse effective masses for the valleys oriented along [100] (Δ_x) and [001] (Δ_z) are calculated for uniaxial and biaxial strain in the [001], [110] and [111] crystal directions and are shown in Fig. 1.10. Under uniaxial and biaxial strain along the [001] direction, the variations of the electron effective masses show a linear trend for both the longitudinal and transverse components. The increase (resp. decrease) of the longitudinal component and the decrease (resp. increase) of the transverse component lead to an elongation (resp. compression) of the ellipsoid equipotential surface of the Δ-valleys. The longitudinal component of the Δ_z-valleys shows highly non-linear variations for [110] and [111] strain. For [111] strain, the six Δ-valleys are equally affected. The evolution of the effective masses under uniaxial (resp. biaxial) strain is more important for [110] (resp. [111]) strain. A non-linear trend is also visible to a lesser extent for the transverse component. The large increase in the longitudinal component of the Δ_z-valleys for [110] and [111] strain can be explained by the movement of the electron valleys. Indeed, as the strain increases, the valleys move close to the edge of the first Brillouin zone. By symmetry, the valleys of the second Brillouin zone also moves, but in the opposite direction. At higher strains, the valleys from the first and second Brillouin zones start to overlap, resulting in an almost flat band curvature, leading to a high effective mass.

The calculation of the effective masses is much more sensitive to the theoretical method chosen. For example, the values obtained by Fischetti and Laux [49] using EPM show significant difference to the values we obtained using DFT. The semi-empirical method first used parameters to fit the band structure and then extrapolated with additional parameters to account for the effect of structural deformation induced by strain. The determination of this second set of parameters is much more precarious as there is very little data available to validate it. Bouhassoune *et al.* [117] use DFT calculations to find the effective electron mass under [110] uniaxial and biaxial strain. The trend of the evolution of the effective masses is in good agreement with our calculations. The main difference is the zero-strain effective mass, which is slightly higher in our calculations. This can be related to the range of **k** points used to perform the effective mass calculations. Indeed, as the bands are not perfectly parabolic, taking a larger

range to perform the second derivative tends to reduce the calculated effective mass. Although the use of DFT or DFPT to calculate it is well known and is proven to give accurate results. No work has been found with an exhaustive calculation of the effective masses in strained silicon for all major configurations as done here.

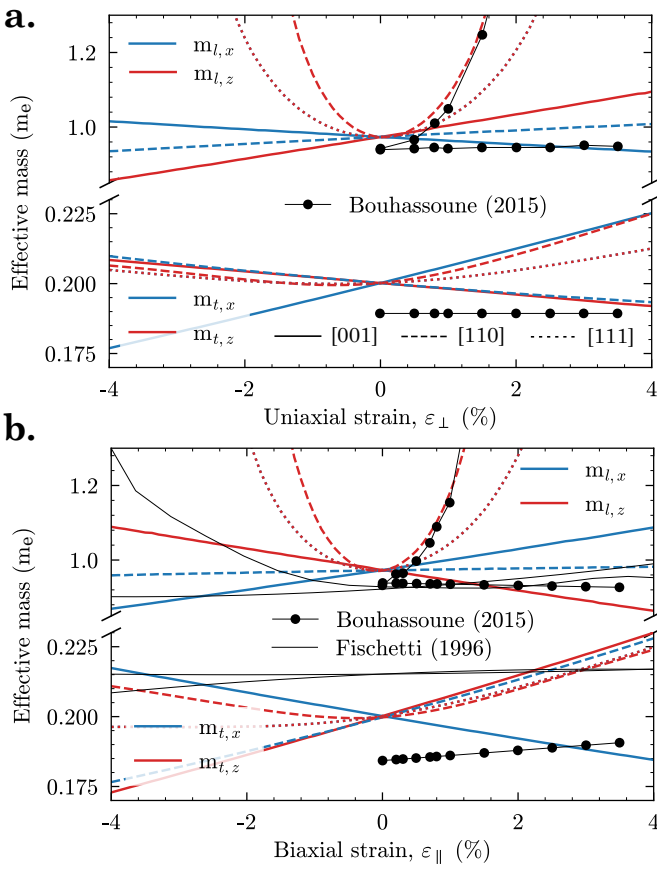


Fig. 1.10 Effective masses variations of the electron valleys with (a) uniaxial and (b) biaxial strains along the [001] (continuous lines), [110] (dashed lines) and [111] (dotted lines) crystal directions. The transverse effective masses ($m_{t,x/z}$) and longitudinal effective masses ($m_{l,x/z}$) for valleys located towards the [100] (Δ_x in blue) and [001] (Δ_z in red) symmetry path.

	HH			LH			SO			Δ_x	
	[100]	[110]	[111]	[100]	[110]	[111]	[100]	[110]	[111]	[100]	[001]
Dexter and Lax [91] (exp.)	0.46	0.53	0.56	0.171	0.163	0.160					
Dresselhaus *et al.* [90] (exp.)	0.459	0.532	0.555	0.160	0.156	0.157				0.97	0.19
Hensel *et al.* [127] (exp.)										0.916	0.191
Stradling and Zhukov [128] (exp.)	0.43			0.202							
Ohyama *et al.* [129] (exp.)							0.29	0.29	0.29		
Ramos *et al.* [130] (th.)	0.26	0.54	0.67	0.18	0.14	0.13	0.22	0.22	0.22	0.96	0.16
Yu *et al.* [53] (th.)	0.22	0.36	0.66	0.22	0.17	0.13	0.22	0.22		0.95	0.19
Inaoka *et al.* [131] (th.)	0.26	0.55									
Laflamme *et al.* [132] (th.)	0.254	0.517	0.648	0.188	0.137	0.130	0.222	0.222	0.222	0.946	0.188
Poncé *et al.* [133] (th.)	0.256	0.521	0.654	0.189	0.140	0.131	0.224	0.227	0.227	0.824	0.190
This work (th.)	0.269	0.539	0.678	0.184	0.137	0.130	0.224	0.224	0.224	0.969	0.200

Table 1.3 Literature comparison of the effective masses computed experimentally (exp.) or theoretically (th.) for the three valence bands (HH, LH and SO) in the [100],[001],[110] and the [111] directions, and the conduction band at the electron Δ-valley in the longitudinal ([100]) and transverse ([001]) directions. The masses are expressed in the unit of the free electron mass m_e.

Under strain conditions, the curvature of the HH and LH bands shows sharp variations due to the broken symmetries of the crystal. Figure 1.11 shows the discontinuity with an illustration of the wave function density at the centre of the band between a strain free structure and one strained at 0.03% under uniaxial strain along the [001] direction.

The HH effective mass goes from 0.539 m_e to 0.203 m_e in the [110] direction, while that calculated along the [111] direction goes from 0.678 m_e to 0.223 m_e. The effective mass of the LH band goes from 0.137 m_e to 0.235 m_e in the [110] direction and from 0.130 m_e to 0.214 m_e for the one calculated in the [111] direction. The discontinuity is also found in the electronic density, with a high density located between the silicon atoms in the relaxed structure.

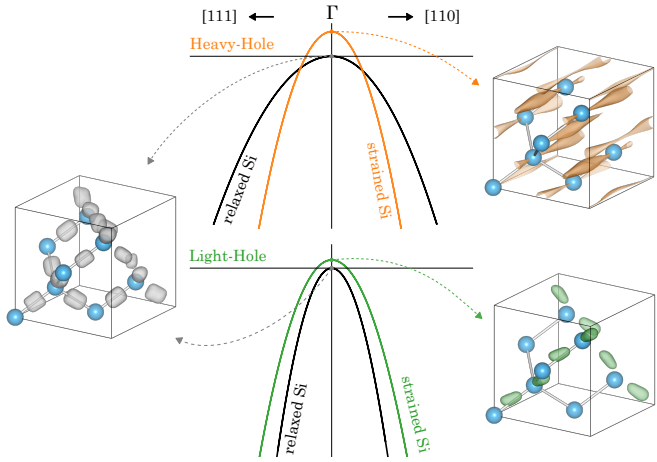


Fig. 1.11 Band curvature of the heavy-hole and light-hole valence bands for the relaxed silicon structure and for the uniaxially strained at 0.03% in the [100] direction. The electronic density at Γ is represented in the conventional cell next to the curve for the relaxed case (black) and for the strained case for the heavy-hole (orange) and light-hole (green).

Figures 1.12, 1.13 and 1.14 show the hole effective masses for HH, LH and SO bands, respectively, under uniaxial and biaxial strain along the [001], [110] and [111] crystal directions, respectively. Contrary to the electron effective masses, the strain causes a significant variation in the shape of the valence bands, as shown by the significant change observed in the effective masses calculated in different directions. Uniaxial strain along [110] and [111] causes the shape of the HH band to align with the strain

direction, as indicated by the dominance of the [110] and [111] effective masses, respectively. It is important to note that very fine **k**-point resolution is required to observe the discontinuity and sharp variations caused by the broken symmetry due to strain. In fact, taking a coarse **k**-point grid leads to an averaging effect as observed in other works [134, 49, 135]. Since the valence bands are not parabolic, using a large range to calculate the effective mass leads to an overestimation of it, which explains why our results are lower than those obtained in the literature. Zhang *et al.* [135] used the $\mathbf{k} \cdot \mathbf{p}$ method to compute the effective masses for biaxial strain in the [001] and [110] directions. While their results are close to ours in the [001] case, the values obtained for [110] strain are much higher. The EPM used by Fischetti and Laux [49] for biaxial strain in the [001] directions achieved good agreement with our results, but with a small overestimation. Theoretical values from Inaoka *et al.* [131] for the HH band are available for silicon undergoing high strain in the [100] direction. Similar to our results, they found a significant reduction from 0.55 m_e to 0.24 m_e for the effective mass along the [110] direction when silicon is strained at 1%. The effective masses of the LH band show less variation than the HH band, but can still reach about 0.8 m_e under [111] uniaxial or [110] biaxial strain. Ohyama and Otsuka [129] show experimentally the important difference between the effective masses of the LH band in the [100] and [001] directions of 0.199 m_e and 0.256 m_e respectively under 0.1% strain. Ma *et al.* [134] calculate the effective masses for the HH and LH bands using $\mathbf{k} \cdot \mathbf{p}$ theory for uniaxial strain along [110], but their results differ significantly from those obtained using DFT. Again the $\mathbf{k} \cdot \mathbf{p}$ methods have been used by Hu *et al.* [136] for the HH and LH under biaxial strain along [110]. Their results are in better agreement with ours.

Finally, there are only a few works in the literature using DFT that provide reliable calculations of the effective masses of the valence bands. The situation is even more critical for the SO band, for which no results have been found. However, this band has little effect on the macroscopic properties such as mobility or absorption due to spin-orbit splitting. The effective masses of the SO are degenerate in the absence of strain, *i.e.*, the shape of the band is spherical. Under [001] strain, the degeneracy is lifted and the shape of the band is compressed (resp. stretched) following the strain directions for uniaxial (resp. biaxial) tensile strain, as evidenced by the decrease (resp. increase) of the [001] effective mass and the increase (resp. decrease) of the [100] one. A similar but larger trend is seen under [110] and [111] strain conditions, able to reach 0.8 m_e in [110] direction.

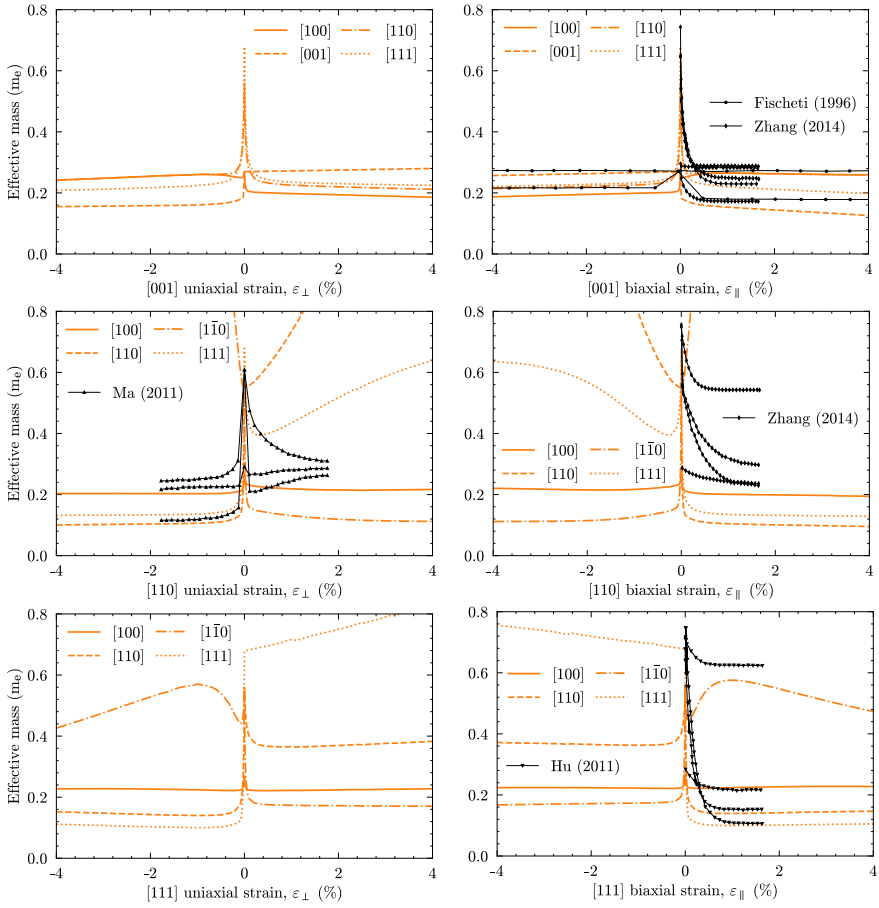


Fig. 1.12 Effective masses as a function of uniaxial and biaxial strain computed at the maxima of the HH band. Theoretical results from Refs. [49], [134], [136] and [135] are indicated with black dots, up triangles, down triangles and diamonds, respectively.

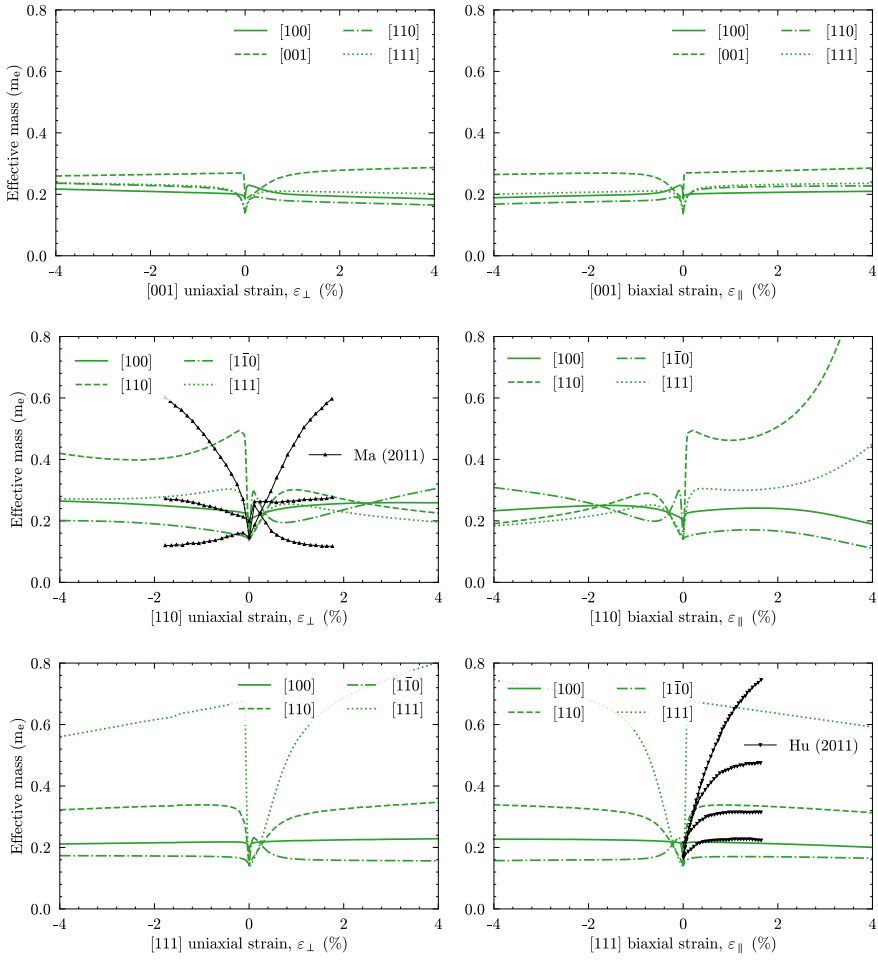


Fig. 1.13 Effective masses as a function of uniaxial and biaxial strain computed at the maxima of the LH band. Theoretical results from Refs. [134] and [136] are indicated with black up and down triangles, respectively.

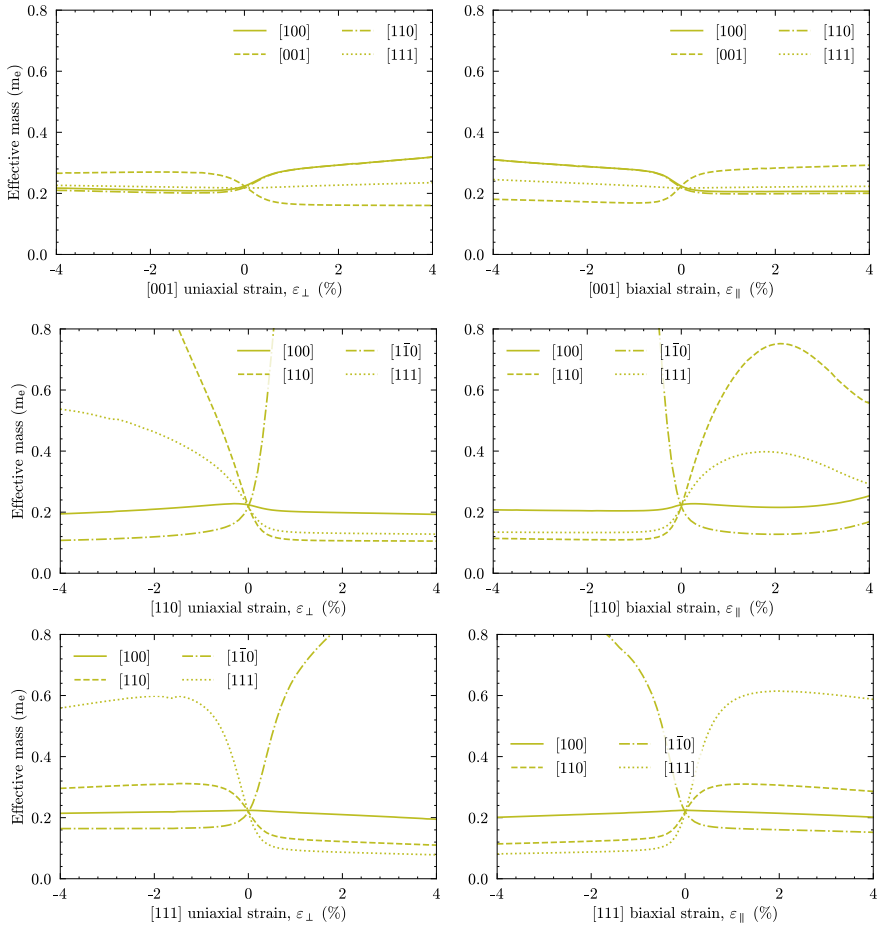


Fig. 1.14 Effective masses as a function of uniaxial and biaxial strain computed at the maxima of the SO band.

1.2.3 Phonon energy

The change in the crystal cell due to strain affects the lattice vibrations of silicon, *i.e.*, the phonons. It is then important to calculate the variations of the phonon modes with strain, especially since the mobility and absorption depend on the electron-phonon interactions. In addition, the energy variations of the optical modes in silicon are used to determine the strain of samples using Raman spectroscopy.

In the harmonic approximation, the frequencies $\omega_{\nu\mathbf{q}}$ of the phonon mode ν with wavevector $\mathbf{q}$ associated with the displacement $\mathrm{u}_\alpha(l\kappa)$ in direction α of the atom κ with mass M_κ in unit cell l are obtained by solving the following eigenvalue problem:

$$\sum_{\kappa'\beta} D_{\mathbf{q},\alpha\beta}(\kappa\kappa')\ \gamma_{\nu\mathbf{q}}(\kappa'\beta) = \omega^2_{\nu\mathbf{q}}\ \gamma_{\nu\mathbf{q}}(\kappa\alpha), \tag{1.12}$$

where $\gamma_{\nu\mathbf{q}}(\kappa\alpha)$ are the phonon eigenvectors [137] and the dynamical matrix $D_{\mathbf{q},\alpha\beta}(\kappa\kappa')$ is given by the second derivative of the potential energy U with respect to the displacement $\mathbf{u}_\alpha(l\kappa)$ of the atoms κ in unit cell l and κ' in unit cell l' for perturbation along the Cartesian directions α and β:

$$D_{\mathbf{q},\alpha\beta}(\kappa\kappa') = \frac{1}{\sqrt{M_\kappa M_{\kappa'}}} \sum_l \frac{\partial^2 U}{\partial \mathrm{u}_\alpha(l\kappa)\ \partial \mathrm{u}_\beta(l'\kappa')} e^{i\mathbf{q}\cdot(\mathbf{x}(l\kappa)-\mathbf{x}(l'\kappa'))}, \tag{1.13}$$

where $\mathbf{x}(l\kappa)$ is the equilibrium position of the atom κ in unit cell l.

In this work, DFPT as implemented in ABINIT [108, 109] is used to compute the eigenvalues corresponding to the energy of the phonon modes in strained silicon. A $12 \times 12 \times 12$ Monkhorst-Pack $\mathbf{k}$-point grid is used to perform the SCF calculation of the total energy, which is used as the starting point for the perturbation calculation.

Figure 1.15 illustrates the effect of strain on the phonon bands. The two-atom lattice of silicon gives rise to six phonon modes. There are three optical modes, one longitudinal optical (LO) and two transverse optical (TO), with maximum energy at Γ and three acoustic modes, one longitudinal accoustic (LA) and two transverse accoustic (TA), with zero energy at Γ due to the acoustic sum rule [138]. The phonon dispersion under uniaxial strain along the [001] direction has been calculated for 0%-, 1%- and 2%-strain. A first observation is the low dependence of the dispersion curves with strain. Indeed, hardly any variations are seen for the acoustic modes, where the maximum changes for longitudinal and transverse modes occur

at the symmetry point X. The energy of the optical modes shows higher variations but remain small.

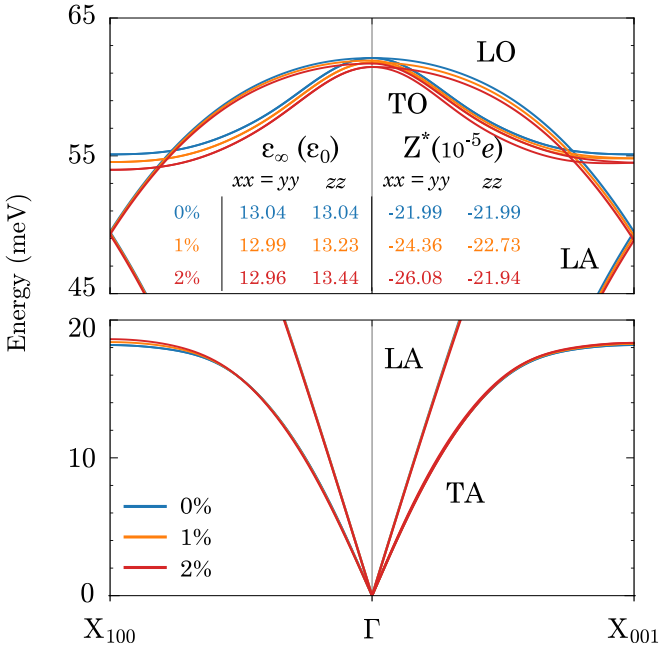


Fig. 1.15 Phonon band structures for [001] uniaxial strain of 0% (blue), 1% (orange) and 2% (red). Each band structure is represented between the X_{100} symmetry point along the [100] direction, *i.e.*, the same as the strain direction, and the X_{001} symmetry point along the [001] direction. The LO and TO modes are shown in the upper panel while the LA and TA modes are shown in the lower panel. The components of the dielectric tensor ε_∞ and Born effective charge Z^* are indicated for each strain level.

Figure 1.16 shows the variations at the edge of the Brillouin zone in the [100] (X_{100}) and [001] (X_{001}) directions. In the absence of strain, the energy of the LA and LO modes is 50.7 meV, while that of the TA and TO modes is 17.5 meV and 57.2 meV, respectively. Limited variations with respect to the Γ position are observed, especially for the TA modes at lower energies. Higher variations of nearly 1 meV/% are observed at X_{001} under [001], [110] and [111] uniaxial and biaxial strain.

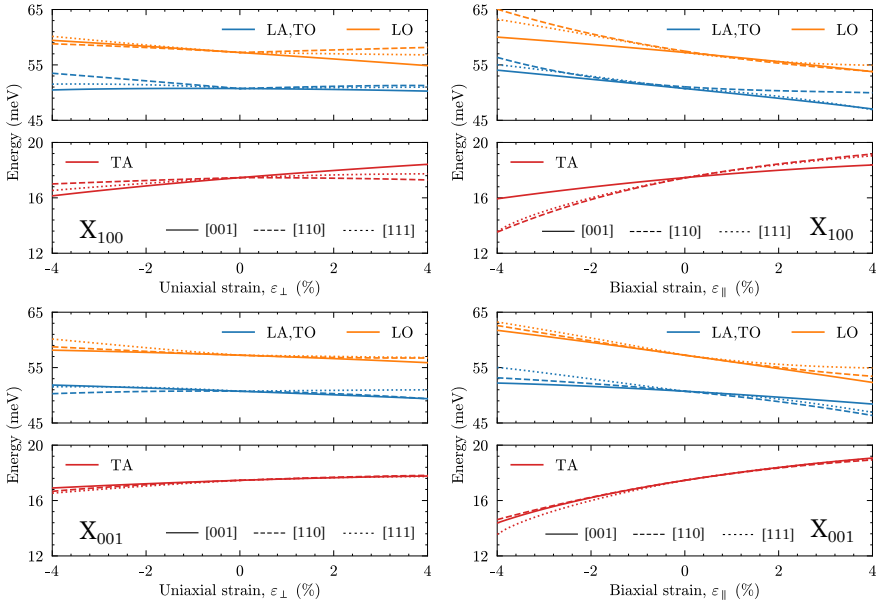


Fig. 1.16 Variations of the energies of the phonon modes at X_{100} and X_{001} for uniaxial and biaxial strain along [001] (continuous line), [110] (dashed line) and [111] (dotted line) crystal directions. At these symmetry points, the transverse modes are degenerated and the energy of the LA mode is equal to the TO modes. The energy of the TA, TO and LO modes are shown in red, blue and orange, respectively.

The three optical modes are degenerated at Γ in the absence of strain at an energy of 63.7 meV. Under strain, the degeneracy is lifted by breaking the crystal symmetries. Ganesan *et al.* [139] provide a theoretical model to predict the strain shift of the frequencies of the triply degenerated optical modes in crystals with a diamond structure. In this phonon deformation potential (PDP) theory, the first-order perturbation of the dynamical matrix is calculated as :

$$D_{I\alpha,J\beta} = D^{(0)}_{I\alpha,J\beta} + \sum_{ij} \frac{\partial D_{I\alpha,J\beta}}{\partial \varepsilon_{ij}} \varepsilon_{ij} + ..., \tag{1.14}$$

where ε_{ij} are the components of the strain tensor. For silicon, it has been shown that only three parameters (p, q and r) are needed for the first

derivatives:

$$\frac{\partial D_{xx}}{\partial \varepsilon_{xx}} = p, \quad \frac{\partial D_{xx}}{\partial \varepsilon_{yy}} = q, \quad \frac{\partial D_{xy}}{\partial \varepsilon_{xy}} = r, \tag{1.15}$$

while the other derivatives are zero. The frequency shifts can then be computed by solving the following characteristic equation:

$$\begin{vmatrix} p\varepsilon_{xx} + q(\varepsilon_{yy} + \varepsilon_{zz}) - \lambda_{\mathbf{q}\nu} & 2r\varepsilon_{xy} & 2r\varepsilon_{xz} \\ 2r\varepsilon_{yx} & p\varepsilon_{yy} + q(\varepsilon_{xx} + \varepsilon_{zz}) - \lambda_{\mathbf{q}\nu} & 2r\varepsilon_{yz} \\ 2r\varepsilon_{zx} & 2r\varepsilon_{zy} & p\varepsilon_{zz} + q(\varepsilon_{xx} + \varepsilon_{yy}) - \lambda_{\mathbf{q}\nu} \end{vmatrix} = 0, \tag{1.16}$$

with $\lambda_{\mathbf{q}\nu} = \hbar\omega_{\mathbf{q}\nu}^2 - \hbar\omega_0^2$ where $\hbar\omega_i$ is the energy of phonon mode ν and $\hbar\omega_0$ is the energy in the absence of strain at Γ.

Table 1.4 summarises the sets of PDP parameters found in the literature. The discrepancy between the parameters is usually due to the strain configuration and the samples used to determine the coefficients. For example, loading along the [001] crystal directions is insensitive to the coefficient r, which deals with the shear component of the strain tensor. The values found in the table have been obtained experimentally by Raman spectroscopy [140, 141, 142, 143] for silicon uniaxially strained along the [001] direction to determine p and q, while [111] uniaxial strain is then used to determine r. Only the values from Peng *et al.* [144] have been calculated by fitting results for uniaxial strain along the [001], [110] and [111] crystal directions.

	$p/\hbar\omega_0^2$	$q/\hbar\omega_0^2$	$r/\hbar\omega_0^2$
Anastassakis *et al.* [140]	−1.25	−1.87	−0.66
Chandrasekhar *et al.* [141]	−1.49	−1.97	−0.61
Nielsen *et al.* [142]	−1.63	−1.89	−0.6
Anastassakis *et al.* [143]	−1.85	−2.31	−0.71
Peng *et al.* [144]	−1.56	−1.98	−0.96

Table 1.4 Silicon phonon deformation potentials in relative units reported in the literature and obtained experimentally.

Figure 1.17 shows the energy variations of the optical modes at Γ under biaxial and uniaxial strains along [001], [110] and [111] crystal directions. The results obtained using the PDP model with coefficients from Peng *et al.* [144] are shown. These coefficients have been chosen for comparison as they have been fitted simultaneously to the experimental measurements with [001], [110] and [111] loading. Measurements have only been per-

formed for uniaxial strain, leading to correct agreement at low uniaxial strain, but failing at higher strains due to the non-linear evolution. The discrepancy is worse for biaxial strain, showing the limitations of using a single set of coefficients for all strain configurations.

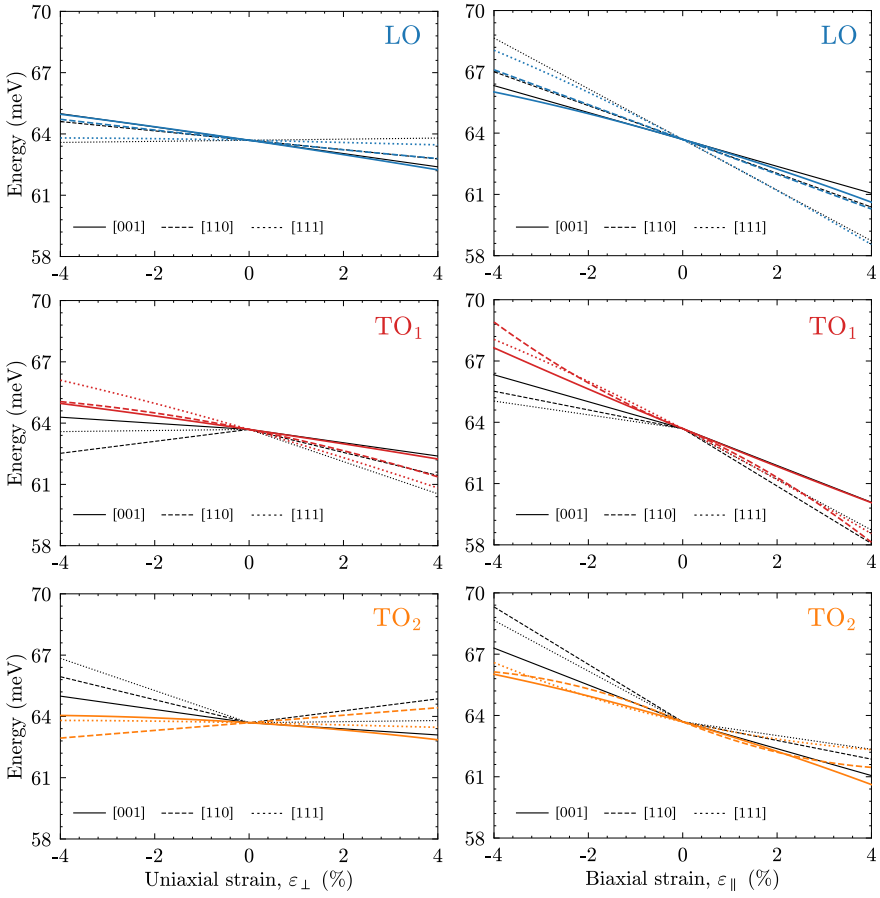


Fig. 1.17 Variations of the phonon energies of the optical modes at Γ for uniaxial and biaxial strain along [001] (continuous line), [110] (dashed line) and [111] (dotted line) crystal directions. The two transverse optical modes, denoted TO_1 and TO_2, are shown in red and orange, respectively. The longitudinal mode, denoted LO, is shown in blue. The black lines represent the linear model using phonon deformation potential theory with coefficients calculated by Peng *et al.* [144].

1.3 Experimental validation of the band gap reduction

As shown in the introduction, uniaxial tensile strain is the most promising candidate to achieve high strain while limiting the fracture probability. Among the uniaxial tensile strains, the one along the [110] crystal direction shows the highest band gap reduction. In this section, PL measurements are therefore performed to validate the first-principles prediction for the band gap reduction under uniaxial strain along the [110] direction.

1.3.1 Fabrication of deformed silicon microbeams

An on-chip tensile testing technique has been used to stretch silicon microbeams without external actuation [145, 62]. The concept of this technique is to use the high internal stress present in silicon nitride to pull on the silicon microbeam [60, 146, 70, 147, 148]. The illustration of the fabrication process of the on-chip tensile testing is shown in Fig. 1.18.

The samples used in this work have been manufactured in UCLouvain cleanroom (Winfab) by Dr. Marie-Stéphane Colla. The fabrication process starts with a p-type 700µm-thick silicon-on-insulator (SOI) substrate with a 685nm-thick top Si layer n-doped about 10^{15} cm^{-3} and a 1µm-thick buried oxide (BOX) that will serve as a sacrificial layer. First, the top Si layer is patterned thanks to a photolithography step followed by a CHF_3/SF_6 plasma etching to shape to the microbeam specimens (Figs. 1.18 a to c). A 20nm-thick dry thermal oxide layer is then grown at 950°C on the patterned top-Si and locally etched away after photolithography using BHF solution in order to open area where the actuator is in contact with the top Si microbeams (Figs. 1.18 d to e). Finally, the actuator layer made of low pressure chemical vapour deposited (LPCVD) silicon nitride film is deposited at 800°C on top of the partly oxidized top-Si and patterned using CHF_3/O_2 dry etching (Figs. 1.18 f to h). The 20nm-thick oxide on the top Si serves as an etch stop layer during this processing step, thus avoiding the degradation of the Si beams. For characterization purposes, as in this work, it is needed to remove the bulk Si substrate under the microbeams of interest using deep reactive ion etching following a previous study[149].

The back-etching step begins with a thinning of the whole substrate by mechanical polishing to reduce the substrate thickness down to 250 µm. Then, a 300nm-thick Al layer is evaporated and patterned using pho-

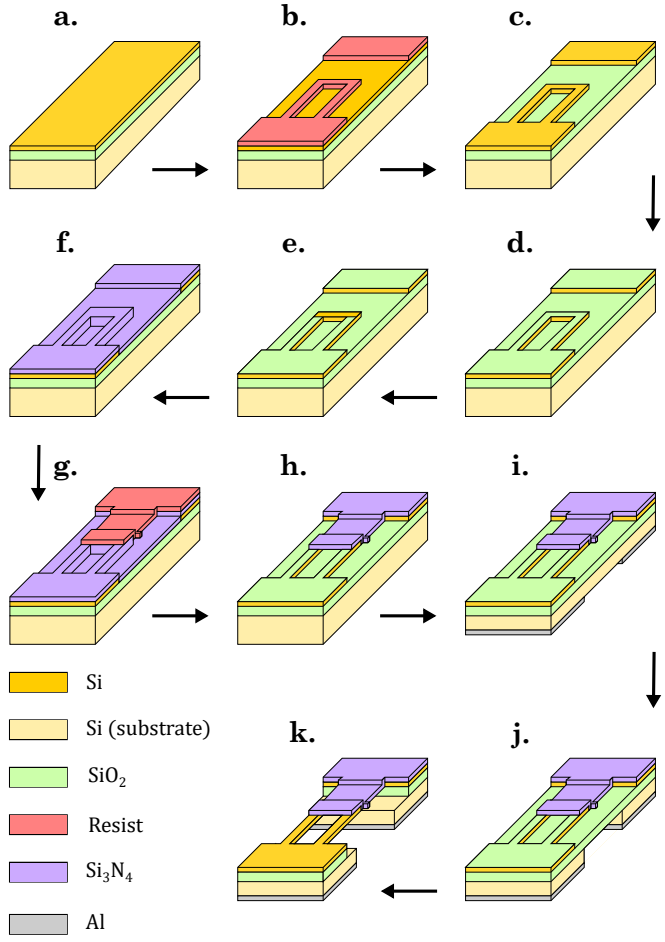


Fig. 1.18 Overview of the fabrication process of strained silicon microbeams. The silicon beams are patterned first (a→c), followed by the silicon nitride patterning (d→h). The back etching and release of the structures are performed at the end of the process (i→k).

tolithography followed by H_3PO_4 etching. This Al layer acts as a hard mask during deep reactive ion etching (Fig. 1.18 i). The front face of the wafer containing the microbeams is protected by a resin AZ 502 D from *Merck*. The Bosch process [150] is used for the deep Si etching. The cyclic etching is performed by alternating 12 seconds-long SF_6 etching steps and 13 seconds-long C_4F_8 deposition steps. 500 cycles have been applied to

fully open the windows in the substrate. The buried oxide sacrificial layer is acting as an etch-stop layer and ensures that the microbeams are not affected by the back-etching process (Fig. 1.18 j).

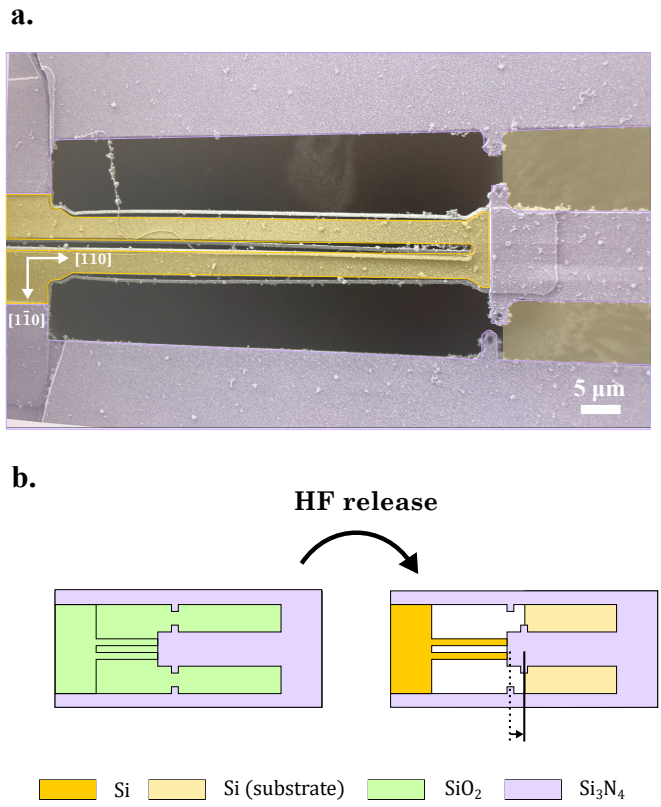


Fig. 1.19 Scanning electron microscopy (SEM) micrograph of a deformed microbeams structure (a). Stress is applied after the silicon oxide (SiO_2) etching with a hydrofluoric acid (HF) solution concentrated at 49% (b). The silicon beams are pulled under tension due to the internal stress in the silicon nitride (Si_3N_4) actuator.

The last step is the release of the entire structure using hydrofluoric acid (HF) concentrated at 49% in order to remove the sacrificial buried oxide lying under the specimen and actuator beams (Figs. 1.18 k). After the release, the Si_3N_4 beam is pulling on the Si microbeam that is deformed under tension. The strain in each Si beam can be calculated from the relative displacement of the freestanding structure thanks to a series of fixed

and moving cursors [145] or by Raman spectroscopy as in this work.

1.3.2 Description of the samples

Hundreds of elementary strained structures with varying dimensions can be produced on one die. The length of the silicon nitride actuator beams is varied from 50 to 500 µm to access to different strain levels inside the Si microbeams that have a constant length of 50 µm. The width of the actuator beams is equal to 10 µm while the Si microbeams are 2µm-wide.

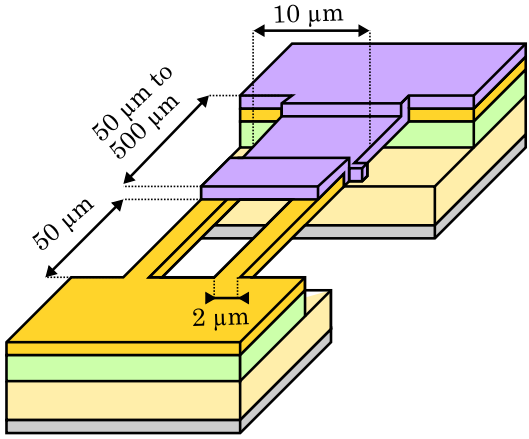


Fig. 1.20 Illustration of the silicon microbeams strained with silicon nitride actuators with a width of 10 µm and lengths ranging from 50 µm to 500 µm. The thickness, width and length of the silicon beams are 0.685 µm, 2 µm and 50 µm, respectively.

An illustration of the final structures is shown in Fig. 1.20 while the measured structures are listed in Tab. 1.5. The length of the silicon nitride actuator and the strain are indicated for each sample. The strain is measured through Raman spectroscopy. Eleven measurements are taken along the silicon beams to increase the accuracy and calculate the standard deviation of the measurements. The method is explained in section 1.3.3.

Number (/)	Actuator length (µm)	Raman peak (cm^{-1})	Standard deviation (cm^{-1})	Strain %
0	0	519.65	0.007	0.22
1	50	518.42	0.048	0.47
2	75	518.08	0.068	0.54
3	100	518.91	0.012	0.37
4	125	518.56	0.012	0.44
6	175	517.79	0.036	0.6
7	200	519.04	0.015	0.34
8	225	516.79	0.074	0.81
13	375	516.82	0.043	0.8
14	400	516.33	0.022	0.9
15	425	516.26	0.036	0.92
16	450	516.06	0.047	0.96
18	500	516.17	0.026	0.93

Table 1.5 List of the measured samples with the strain determined through Raman spectroscopy. The ratio between the Raman shift and strain is -485 cm^{-1} [70]. The standard deviation is calculated with 11 measurements points along the strained silicon beams.

1.3.3 Strain determination by Raman spectroscopy

Strain could be determined with SEM imaging by measuring the displacement of the cursors, as shown in Fig. 1.19. However, the microfabrication process lead to various cracks in the silicon nitride layer and at the anchor of the structure. This caused a displacement of the cursor unrelated to the strain of the samples. For this reason Raman spectroscopy is preferred to determine the intensity of the strain field in our samples.

Raman spectroscopy is a well-known non-invasive method to extract the magnitude of the elastic strain field in a semiconductor from the vibrational modes of the crystal [151]. In silicon, the degeneracy of the three optical phonon peaks (about 520.7 cm^{-1}) is lifted under strain. The intensity of the strain field can then be determined directly from the peak positions if the correct relations between strain and peak shifts are known, as discussed in section 1.2.3. The labRAM HR system from *Horiba* with a 514 nm-laser is used to perform backscattered Raman spectroscopy. The system is shown in Fig. 1.21 and is based on a confocal microscope with a filter and an attenuator in the incident light path, while a spectrographic grating coupled with mirrors to spatially discriminates the energy of the

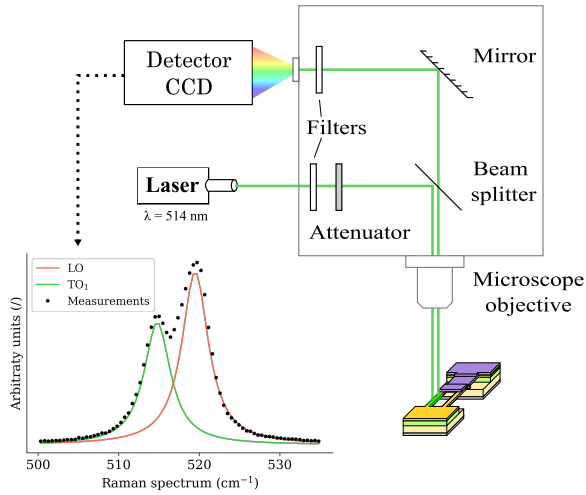


Fig. 1.21 Raman spectroscopy set-up to determine the intensity of the strain field in the deformed silicon samples. A 514 nm laser is guided onto the sample and the scattered signal is collected through a beamsplitter and diffraction grating to be analyzed on a charge-coupled device (CCD). The spectrum is then analyzed by fitting Lorentzian peaks to extract the position of the LO and TO phonon modes that depend on the magnitude of the elastic strain.

scattered light on a CCD. The measurements are done in the WELCOME facilities from UCLouvain. According to the Raman selection rule, only the LO mode should be excited with the laser polarised in the [110] direction above the (001) crystal plane [152]. However, the high numerical aperture (NA) of the microscope objective (MPLAPON100x from *Olympus*) leads to the observation of the TO mode thanks to the tilted components of the light beam hitting the material. In fact, with a numerical aperture of 0.95, it is possible to collect incident light with an angle of incidence of up to 70°. The spectrum can then be fitted with Lorentzian functions to obtain the positions of the Raman peaks [153]. Fig. 1.22 shows the Raman spectra of five samples strained from 0.22% to 0.80%. The Lorentzian fit representing the two phonon modes (TO and LO) is highlighted, while the vertical position is set according to the strain of the samples. The strain level has been calculated from the position of the TO peaks with a strain shift coefficient of -485 cm^{-1} [154]. Eleven measurement points are taken along

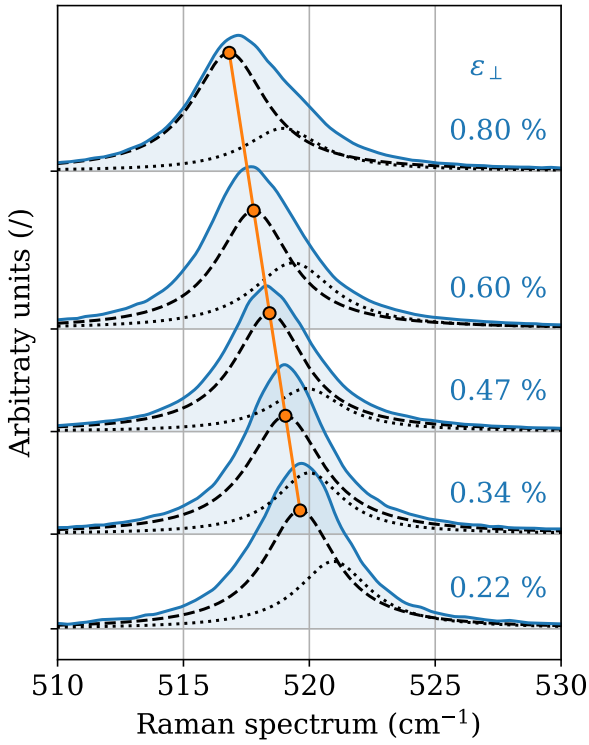


Fig. 1.22 Raman spectrum of several deformed microbeams. The measurement data (continuous blue lines) are fitted using two Lorentzian functions representing the contribution of the TO mode (dashed lines) and LO mode (dotted lines). The spectra are normalized with regards to the intensity of the TO peaks while the vertical position of each spectrum is related to the strain of the sample. This strain level has been determined using the linear relationship (continuous orange line) between the peak position of the TO modes (oranges dots) and the strain.

each silicon beam to determine the uncertainty of the measurements. Figure 1.23 shows the histogram of the Raman peaks from which the standard deviations are resumed in Tab. 1.5.

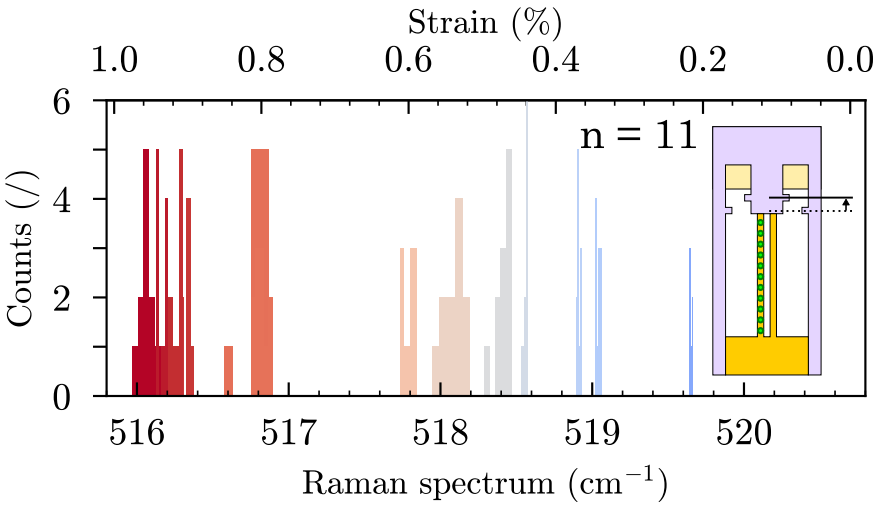


Fig. 1.23 Histogram of the position of the Raman peaks for eleven measurement points along the silicon microbeams for each strained sample. The inset on the right shows the position of the Raman measurements along the beam (green dots).

1.3.4 Photoluminescence measurements

Transmission/reflection measurements are usually preferred to determine the absorption and the band gap of a material [155]. However, due to the microscopic dimensions of our samples, standard equipment are unable to perform accurate measurement on a micrometric spot. For this reason, PL measurements through microscope objective have been chosen to retrieve the band gap of our samples.

The FluoMic and FluoTime 300 from *Picoquant* are used to generate the luminescence spectrum of the strained samples as shown in Fig. 1.24. A 532 nm pulsed laser passing through an attenuator is focused on the sample with an MPLN50x objective from *Olympus*. The spot size of about 20 µm diameter results in almost complete illumination of the deformed samples. The pulse duration is 25 ps with a repetition rate of 3 MHz. The

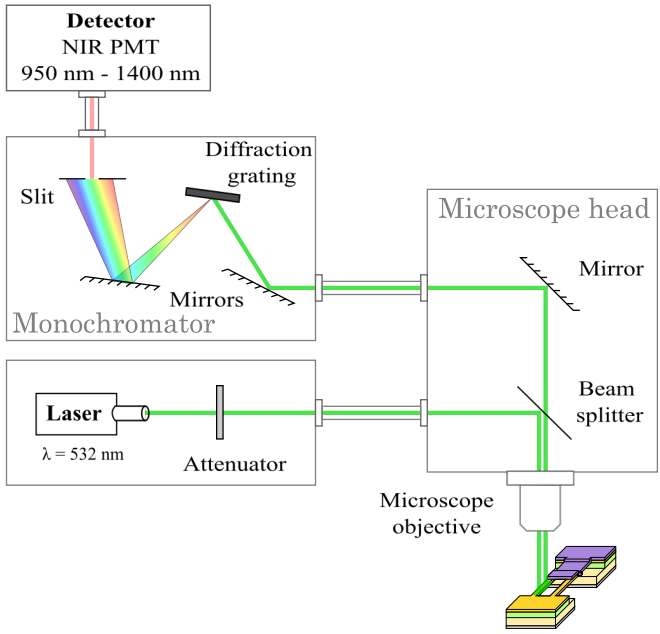


Fig. 1.24 Diagram of the PL set-up used to determine the band gap of the deformed microbeams. A 532 nm laser has been used with confocal backscattering configuration. The signal emitted by the sample is collected through the same objective as the input laser beam. A monochromator coupled to a NIR photodetector is used at the end to retrieve the luminescence spectrum.

backscatter system collects the emitted light through the same objective. A beam splitter separates the input laser line from the emitted spectrum, which is directed to a monochromator. The monochromatic output light is finally analysed by a NIR photodetector with a photomultiplier tube (MPT). The full spectrum is then obtained by tuning the monochromator between 900 nm and 1300 nm with 1 nm steps. The integration time for each point of the spectrum is set to 15 s. The photoluminescence measurements are done at IMO-IMOMEC, the joint department of imec and UHasselt, on the site of EnergyVille in Genk with the help of researchers Mr. Romain Scaffidi and Dr. Guy Brammertz.

The luminescence spectrum $\Phi_L(E)$ is fitted and calibrated using the

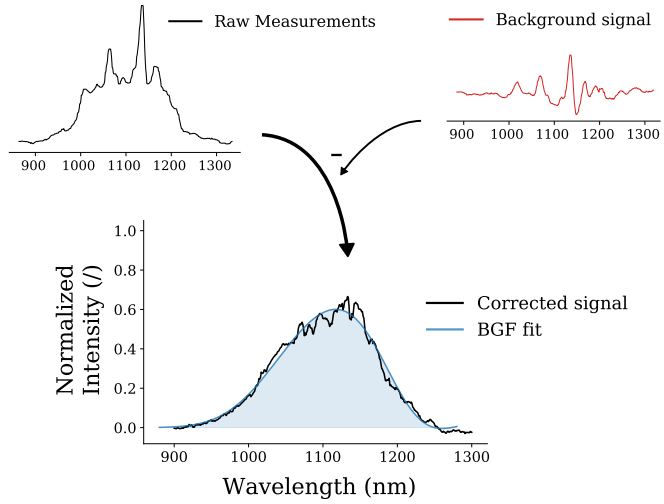


Fig. 1.25 Data processing scheme to remove the background signal (red) from the raw measurements (black) before the fit with the PL model (blue).

band gap fluctuation model [156, 157]:

$$\Phi_L(E) \propto \mathrm{erfc}\left(\frac{\bar{E}_g - E}{\sqrt{2}\sigma_g}\right) E^2 \exp\left(-\frac{E-\mu}{k_B T}\right), \tag{1.17}$$

where E is the photon energy, μ is the chemical potential, k_B is the thermal energy, σ_g is the band gap fluctuation, $\bar{E}_g$ is the mean band gap. This model allows to tackle the band gap fluctuation that originates from local disorder in the crystal coming from doping, interfaces, defects, and so on [158].

A first fit is performed on the sample to separate the background signal from the luminescence signal. A second fit is then made on the signal from which the background have been subtracted to obtain the final band gap value. The correction and fitting steps are shown in Figure 1.25. The back-etched configuration of the microfabricated samples avoids a background signal from the silicon substrate and thus improves the quality of the measurements. Thirteen beams were characterised with strain levels between 0.2% and 0.95%, resulting in a band gap reduction between 22 meV and 91 meV.

In order to estimate the uncertainty due to the data processing, a statistical approach is chosen where corrections were made on each of the

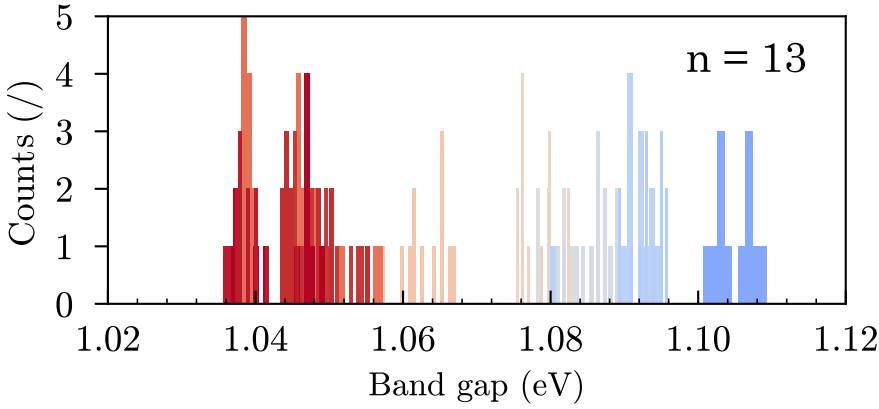


Fig. 1.26 Histogram of the band gap evaluation comparing the effect of background correction on each of the thirteen silicon beams against the background signal of the others.

thirteen Si beams with the background signal from the other. For each deformed beam, the PL measurements are thus fitted after removing the background signal from the other beams. Indeed, important uncertainty is induced by the large diameter (20 µm) of the laser spot and the displacement of the microscope objective between the measurements of each samples. Figure 1.26 shows the histogram of the band gap evaluation to compare the effect of the background correction.

The results of the data processing are shown in Fig. 1.27. The coordinates of each point refer to the mean value of the band gap and strain level determined for each Si beam. The vertical bars represent the PL uncertainty of the band gap due to the background corrections. The size of the bars is equal to three times the standard deviation of the extracted band gap values after the background corrections. The Raman shift at eleven points along each beam is extracted to calculate the uncertainty in the strain represented by the horizontal bars. The width of the bars is equal to three times the standard deviation coming from the strain calculated at each point of the test beams. The values of the standard deviations are resumed in Tab. 1.5. The inset of Fig. 1.27 shows normalised luminescence spectra with the peak position highlighted for several deformation levels and compared with the theoretical results. The first-principles results for the tensile strain applied along the [110] directions have been presented and show good agreement with the experimental results. The largest band

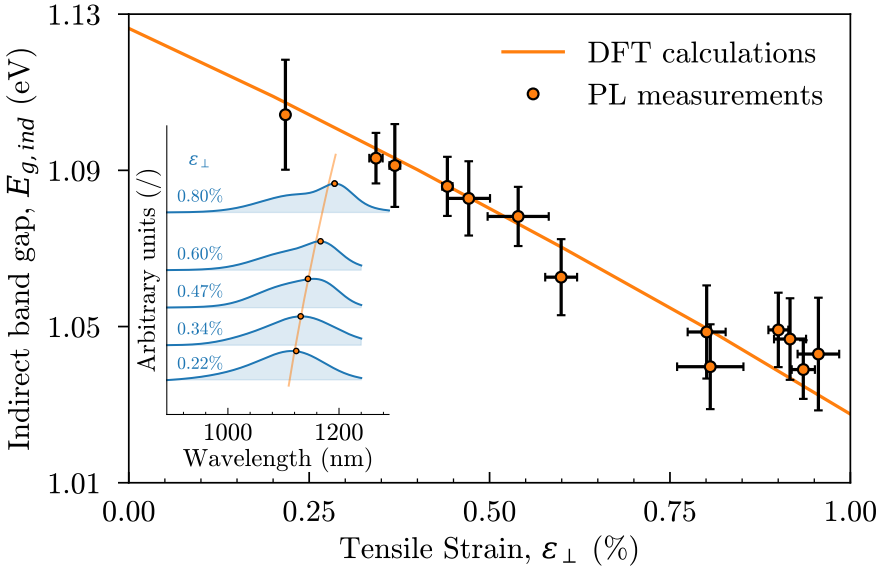


Fig. 1.27 Results of the band gap determination from Raman and PL measurements (orange dots). The vertical and horizontal bars around the experimental results are the strain and band gap uncertainties coming from the Raman and the luminescence measurements, respectively. Data are compared to the calculation results obtained by DFT (orange line). The inset represents the PL spectrum fitted on experimental data after the post-processed step to remove the interference signal. The band gap position for different strain levels is indicated on the spectrum (orange dot) as well as the first-principles prediction (orange line).

gap reduction found experimentally is about 91 meV at 0.95 %, whereas a reduction of 93 meV was predicted at this level of deformation. The results extend a previous experimental determination using PL spectroscopy [55], where a band gap reduction of 100 meV was found for a compressive strain of about 1% along the [001] direction. A previous study showed a band gap reduction of 69 meV for a compressive strain of ∼0.6% applied in the [110] crystal direction [123]. A higher band gap reduction of 239 meV was obtained with a biaxial strain of 1.54% applied to a (001) silicon layer using the Si_xGe_{1-x} stressor [120, 121].

This demonstrates experimentally the physical insight given by the first-principles simulations to characterise the band gap reduction in highly strained silicon. In addition, the results of PL and Raman measure-

ments confirm the use of strain engineering to tune the optical behaviour of deformed materials.

1.4 Chapter Summary

The fundamental properties of silicon have been studied in this chapter considering all major strain configurations. DFT allows accurate predictions of the band structure variations, especially with respect to the band gap and effective masses. The theoretical calculations provide, for the first time, an exhaustive study of biaxial and uniaxial strain along the [001], [110] and [111] directions and show the potential of uniaxial tensile strain along [110] to achieve a band gap reduction of -202.9 meV at 2% strain.

Biaxial compressive strain along [110] and tensile strain along [001] show -326.5 meV and -306.6 meV respectively at 2%-strain. However, uniaxial tensile strain is the preferred strain mode to achieve high strain without fracture. The results of the effective masses for the conduction band and the three valence bands fill the existing gap in the literature while demonstrating the important variations of the band shape with strain. In addition, the effect of strain on the phonon energy has been demonstrated, with important implications for Raman spectroscopy. The first-principles approach has the ability to account for the nonlinearity of the strain effect without being restricted to any strain configuration, in contrast to the existing phonon deformation potential (PDP) theory. Finally, photoluminescence (PL) measurements were performed on silicon beams strained up to 1% along [110] using silicon nitride stressors to experimentally study the band gap reduction and validate the theoretical calculations. By combining the results of the first-principles study with the experiments, this work confirms the theoretical understanding of band structure tailoring under stress conditions, making silicon an interesting material for infrared applications.

Key messages of the chapter

- Density-functional theory (DFT) allows in-depth study of the effect of strain on the band structure of silicon and related parameters without semi-empirical bias. This allows a complete study in any strain configuration of interest, bypassing the experimental complexity of having and observing large strained samples.
- Except for small bandgap materials, simple approximations such as generalised gradient approximation (GGA) and local density approximation (LDA) are sufficient to study band gap variations theoretically, without the need for more complex calculations such as GW.
- Density-functional perturbation theory (DFPT) allows the calculation of the phonon band structure and the calculation of the energy variations used in Raman spectroscopy to determine strain in silicon samples. The theoretical results highlight the non-linearity of the variations at larger strains, showing the limits of the standard PDP theory traditionally used.
- Biaxial strain along [110] in compression and along [001] in tension are the strain configurations that give the highest band gap reduction, but are more difficult to achieve in practice than uniaxial tensile strain.
- Tensile uniaxial strain along [110] crystal directions leads to a band gap reduction of -96 meV at 1%- strain, which we have confirmed experimentally using photoluminescence (PL) measurements on strained silicon beams that show a reduction of -91 meV at 0.95%.

2

Phonon-limited mobility in strained silicon

The relatively low mobility of silicon compared to other semiconductors such as GaN [159, 160], InGaAs [161, 162] and Ge [163] limits its use in high-speed devices essential for optical [164, 165] and microwave [166, 167] communications. Strain engineering is a proven technique to enhance the performance of semiconductors, in particular to increase the mobility of their charge carriers at low additional cost [168]. Mobility enhancement in strained devices is a well-known mechanism that has already been exploited to develop semiconductor strain gauges or high mobility silicon transistors [169, 170]. Although several theoretical methods have been developed to predict the improvement or degradation of mobility at high strain [49, 171, 172], none of them has been experimentally validated.

In this chapter, piezoresistive measurements of electron mobility up to 1% have been performed on n-doped silicon samples uniaxially strained in the [001] crystal direction. The experimental data are used to discuss the existing theoretical models. Due to the lack of accuracy of the semi-empirical models and the difficulty of observing the hole mobility experimentally, we have then calculated theoretically the phonon-limited electron and hole mobilities of highly strained silicon. The first-principles calculations explicitly account for the electron-phonon scattering, including momentum and phonon modes, and solve the Boltzmann transport equa-

tion (BTE) to find the phonon-limited mobility. The method is demonstrated for uniaxial strain along the [001] crystal direction, before being used to calculate the mobility components for uniaxial strain along the [110] directions.

2.1 Piezoresistive measurements

Various theoretical models have been developed to predict the mobility, starting with an empirical linear model [45] valid at low strain, and later based on semi-empirical analysis using the calculated band structure of strained silicon [49]. Experimental work observing the mobility enhancement at high strain remains scarce [173, 174]. Therefore, advanced theoretical models for high uniaxial strain have rarely been experimentally validated [171, 175, 172, 53]. In this section, we review the existing semi-empirical models and measure the electron mobility variations up to 1%-strain in the [001] direction using n-doped silicon samples.

2.1.1 Semi-empirical models

The first model developed to tackle the change in resistivity of silicon under strain condition is the linear empirical one from Smith [45]. It allows to predict the variations under any low-strain field based on a tensor representation. The piezoresistive tensor $[\pi_{ij}]$ links two second-order tensors : the stress tensor $[\sigma_i]$ and the relative resistivity variation tensor $[\frac{\Delta\rho_i}{\rho_0}]$. This makes $[\pi_{ij}]$ a four-order tensor such as

$$\begin{pmatrix} \frac{\Delta\rho_1}{\rho_0} \\ \frac{\Delta\rho_2}{\rho_0} \\ \frac{\Delta\rho_3}{\rho_0} \\ \frac{\Delta\rho_4}{\rho_0} \\ \frac{\Delta\rho_5}{\rho_0} \\ \frac{\Delta\rho_6}{\rho_0} \end{pmatrix} = \begin{pmatrix} \pi_{11} & \pi_{12} & \pi_{13} & \pi_{14} & \pi_{15} & \pi_{16} \\ \pi_{21} & \pi_{22} & \pi_{23} & \pi_{24} & \pi_{25} & \pi_{26} \\ \pi_{31} & \pi_{32} & \pi_{33} & \pi_{34} & \pi_{35} & \pi_{36} \\ \pi_{41} & \pi_{42} & \pi_{43} & \pi_{44} & \pi_{45} & \pi_{46} \\ \pi_{51} & \pi_{52} & \pi_{53} & \pi_{54} & \pi_{55} & \pi_{56} \\ \pi_{61} & \pi_{62} & \pi_{63} & \pi_{64} & \pi_{65} & \pi_{66} \end{pmatrix} \begin{pmatrix} \sigma_1 \\ \sigma_2 \\ \sigma_3 \\ \sigma_4 \\ \sigma_5 \\ \sigma_6 \end{pmatrix}. \tag{2.1}$$

The Voigt [113] notation is used to express the four-order piezoresistive system as a second-order one.

The basic unit of the silicon structure is a FCC cell. By its symmetric operations, it can be verified that there are only three non-zero independent components for the piezoresistive coefficient tensor [45]. They are $\pi_{11} = \pi_{22} = \pi_{33}$, $\pi_{12} = \pi_{21} = \pi_{13} = \pi_{31} = \pi_{23} = \pi_{32}$ and $\pi_{44} = \pi_{55} = \pi_{66}$ The piezoresistive tensor in the crystallographic coordinate system of the crystal can then be expressed as

$$[\pi_{\alpha\beta}] = \begin{pmatrix} \pi_{11} & \pi_{12} & \pi_{12} & & & \\ \pi_{12} & \pi_{11} & \pi_{12} & & & \\ \pi_{12} & \pi_{12} & \pi_{11} & & & \\ & & & \pi_{44} & & \\ & & & & \pi_{44} & \\ & & & & & \pi_{44} \end{pmatrix}, \tag{2.2}$$

with $\pi_{11} = -1022$ TPa^{-1}, $\pi_{12} = 534$ TPa^{-1} and $\pi_{44} = -136$ TPa^{-1} for n-type silicon and $\pi_{11} = 66$ TPa^{-1}, $\pi_{12} = -11$ TPa^{-1} and $\pi_{44} = -1381$ TPa^{-1} for p-type silicon [45].

The change in resistivity $\frac{\Delta\rho}{\rho_0}$ for a conductor oriented in direction $(i\ j\ k)$ can be expressed as

$$\begin{aligned} \frac{\Delta\rho}{\rho_0} &= \begin{pmatrix} i & j & k \end{pmatrix} \begin{pmatrix} \frac{\Delta\rho_1}{\rho_0} & \frac{\Delta\rho_6}{\rho_0} & \frac{\Delta\rho_5}{\rho_0} \\ \frac{\Delta\rho_6}{\rho_0} & \frac{\Delta\rho_2}{\rho_0} & \frac{\Delta\rho_4}{\rho_0} \\ \frac{\Delta\rho_5}{\rho_0} & \frac{\Delta\rho_4}{\rho_0} & \frac{\Delta\rho_3}{\rho_0} \end{pmatrix} \begin{pmatrix} i \\ j \\ k \end{pmatrix}, \\ &= \begin{pmatrix} i^2 & j^2 & k^2 & jk & ik & ij \end{pmatrix} \begin{pmatrix} \frac{\Delta\rho_1}{\rho_0} \\ \frac{\Delta\rho_2}{\rho_0} \\ \frac{\Delta\rho_3}{\rho_0} \\ \frac{\Delta\rho_4}{\rho_0} \\ \frac{\Delta\rho_5}{\rho_0} \\ \frac{\Delta\rho_6}{\rho_0} \end{pmatrix}. \end{aligned} \tag{2.3}$$

The change of resistivity in a particular $[ijk]$ direction is finally given by

$$\begin{aligned} \frac{\Delta\rho}{\rho_0} = {} & [\pi_{11}\sigma_1 + \pi_{12}(\sigma_2 + \sigma_3)]\, i^2 + [\pi_{11}\sigma_2 + \pi_{12}(\sigma_1 + \sigma_3)]\, j^2 \\ & + [\pi_{11}\sigma_3 + \pi_{12}(\sigma_1 + \sigma_2)]\, k^2 + 2\pi_{44}[\sigma_6\, ij + \sigma_5\, ik + \sigma_4\, jk] \end{aligned}. \tag{2.4}$$

For specific strain direction, the resistivity variations is usually expressed as

$$\frac{\Delta\rho}{\rho_0} = \pi_l\sigma_l + \pi_t\sigma_t, \tag{2.5}$$

where σ_l and σ_t are the arbitrary stresses applied along the conductor or transverse to it, respectively. π_l and π_t are the effective piezoresistive coefficient in the longitudinal and transverse directions, respectively. Table 2.1 gives the expression of the coefficients for stress applied in the [001], [110] and [111] crystal directions.

	[001]	[110]	[111]
π_l	π_{11}	$\frac{\pi_{11}+\pi_{12}+\pi_{44}}{2}$	$\frac{\pi_{11}+2\pi_{12}+2\pi_{44}}{3}$
π_t	π_{12}	$\frac{\pi_{11}+\pi_{12}-\pi_{44}}{2}$	$\frac{\pi_{11}+2\pi_{12}-\pi_{44}}{3}$

Table 2.1 Longitudinal and transverse piezoresistive coefficients for stress applied in the [001], [110] and [111] crystal directions. The transverse directions considered are respectively the [100], [$\bar{1}$10] and [$\bar{1}$10] ones.

Later, semi-empirical models were developed taking into account the scattering mechanism, but mainly for the electron. In fact, the calculation of hole scattering rates in the valence bands is more tedious due to the proximity between the LH and HH bands, while exhibiting important shape variations under stress conditions. Conversely, the electron valley in the conduction band retains its shape for [001] strain. Analytical expressions for the intra- and interscattering rates are easier to develop for conduction bands with ellipsoid shape.

In these models the electron mobility tensor μ_n is the weighted sum of the mobility of each electron valley μ_{n,Δ_i}:

$$\mu_n = \sum_i p_{\Delta_i}\mu_{n,\Delta_i}, \tag{2.6}$$

where p_{Δ_i} is the occupancy of the valley Δ_i.

Figure 2.1 shows the occupancy of the valley under [001] uniaxial strain. As the valley splits, the electron population migrates from the Δ_2-valleys (along [001]) to the Δ_4-valleys (along [100] and [010]). At 1%-strain, hardly any of the electron population remains in the Δ_2-valleys, leading to saturation of the mobility enhancement. The occupancy of the

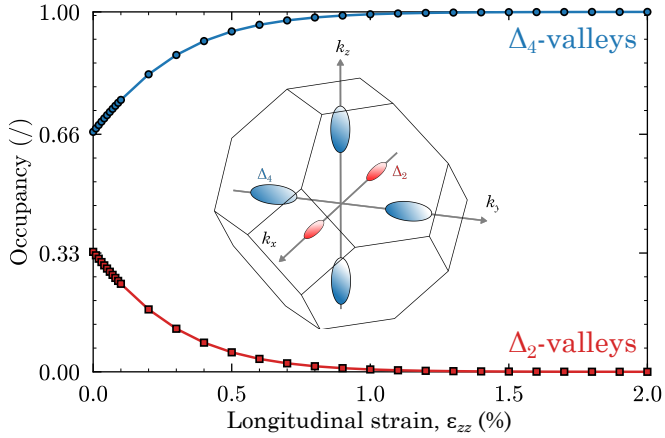


Fig. 2.1 Occupancy of the Δ_2-valleys (red) and Δ_4-valleys (blue) under uniaxial strain along [001] crystal direction. The reciprocal space with the equipotential surface of the valleys is also shown.

lower energy n_{Δ_4} valleys is given by [171]

$$n_{\Delta_4} = \frac{2\, N_{C,\Delta_4} \exp(\Delta E_C / k_B T)}{N_{C,\Delta_2} + 2\, N_{C,\Delta_4} \exp(\Delta E_C / k_B T)}, \tag{2.7}$$

where N_{C,Δ_i} is the density of states in the valley Δ_i, ΔE_C is the energy split between the valleys, k_B is the Boltzmann constant and T is the temperature.

The valley mobility can be computed as [176]

$$\mu_{n,\Delta_i} = e \left\langle \tau_{n,\Delta_i} \right\rangle m_{\Delta_i}^{-1}, \tag{2.8}$$

where e is the electron charge, $\left\langle \tau_{n,\Delta_i} \right\rangle$ is the mean time between collision and $m_{\Delta_i}^{-1}$ is the inverse of the effective mass tensor of the valley Δ_i. The effect of strain affects the effective masses as seen in chapter 1, but also the scattering rate. The intravalley scattering shows little strain dependence, as the strain only slightly changes the shape of the valley. On the contrary, most of the effect is seen on the scattering between different valleys (intervalley scattering). Fischetti and Laux [49] calculated the electron and hole mobility for silicon and germanium under [001] biaxial strain using EPM for the band structure and an analytical model for the mobility and scattering rates up to 5%. More recently, Ma *et al.* [172] performed a similar analysis for uniaxial strain along the [001] direction using the **k**·**p** method

and Boltzmann transport theory. Both of these works used first principles to calculate the scattering rates as a function of electron state (and hence energy) before calculating the mean scattering rates. In contrast, Dhar *et al.* [171] provides a simpler model based on analytical relations and fitting parameters to model the evolution of electron mobility with strain.

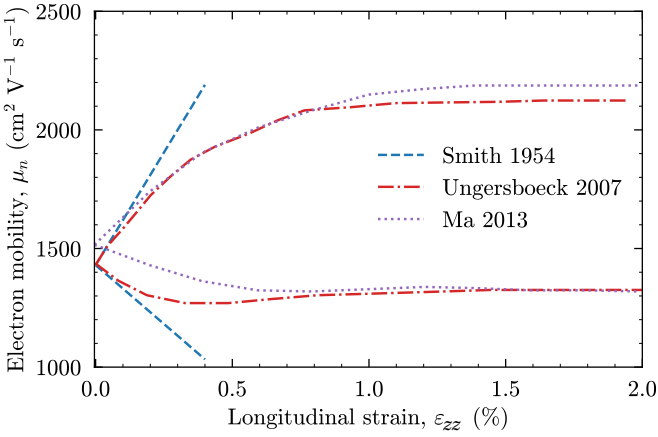


Fig. 2.2 Literature comparison of the theoretical computation of the electron mobility under uniaxial strain along [001] crystal direction.

Figure 2.2 shows the results of the work found in the literature for uniaxial strain along [001] direction. The linear low strain model of Smith [45] is in good agreement for strains below 0.1% with the results of Ungersboeck *et al.* [175], which extends the model developed by Dhar *et al.* [171].

In their model, the mean scattering rate $\langle \tau_{n,\Delta_i} \rangle$ is expressed as

$$\langle \tau_{n,\Delta_i} \rangle = \langle \tau^{-1}_{n,equiv} \rangle + \langle \tau^{-1}_{n,neq,\Delta_i} \rangle + \langle \tau^{-1}_{n,I} \rangle \tag{2.9}$$

where $\langle \tau^{-1}_{n,equiv} \rangle$ is the mean scattering rate due to intravalley scattering and intervalley scattering between equivalent electron valleys, $\langle \tau^{-1}_{n,neq} \rangle$ is the mean scattering rate for intervalley scattering for non-equivalent valley that depends on the energy split between valleys due to strain $\Delta E_{C,\Delta_i}$, and $\langle \tau^{-1}_{n,I} \rangle$ is the mean scattering rates due to impurity scattering.

A mobility enhancement factor f is introduced to link the scattering

rates from equivalent and non-equivalent valleys:

$$f = \frac{m_c}{m_t}\left(1 + \frac{\langle \tau_{n,neq,\Delta_i}^{-1} \rangle}{\langle \tau_{n,equiv}^{-1} \rangle}\right), \tag{2.10}$$

where m_c and m_t are the conductivity and transverse effective mass of silicon in the absence of strain. This mobility enhancement is used as a semi-empirical parameter to fit our measurements in section 2.1.2.

In the semi-empirical model, the strain only impact the scattering rates of non-equivalent valleys $\langle \tau_{n,neq,\Delta_i}^{-1} \rangle$ due to the energy splitting between Δ_2 and Δ_4-valleys. The change in the scattering rates is calculated as

$$\langle \tau_{n,neq,\Delta_i}^{-1} \rangle = h_{\Delta_i} \left\langle \tau_{n,neq,\Delta_i}^{-1} \right\rangle \Big|_{\varepsilon_{zz}=0}, \tag{2.11}$$

with

$$h_{\Delta_i} = \frac{g(\frac{\Delta_{ij}^-}{k_B T}) + g(\frac{\Delta_{il}^-}{k_B T}) + \exp(\frac{\hbar\omega_{opt}}{k_B T})[g(\frac{\Delta_{ij}^+}{k_B T}) + g(\frac{\Delta_{il}^+}{k_B T})]}{2[g(\frac{-\hbar\omega_{opt}}{k_B T}) + \Gamma(\frac{3}{2})]}, \tag{2.12}$$

where $\Delta_{ij}^{\pm} = \Delta E_C^{ij} \pm \hbar\omega_{opt}$, ΔE_C^{ij} is the energy split between valleys Δ_i and Δ_j, $\hbar\omega_{opt}$ is the energy of the phonon involves in the scattering. The plus (+) and minus (−) signs stand for the absorption or emission of the phonon.

The function $g(z)$ is defined as

$$g(z) = \begin{cases} \exp(-z)\ \frac{\sqrt{\pi}}{2} & z > 0, \\ \exp(-z)\ \Gamma(\frac{3}{2}, -z) & z \leq 0, \end{cases} \tag{2.13}$$

where $\Gamma(\frac{3}{2}, -z)$ is the incomplete Gamma function.

The valley mobility is finally expressed as

$$\mu_{n,\Delta_i} = \frac{\beta\mu_{n,l}}{1 + (\beta+1)h_{\Delta_i} + \beta(\frac{\mu_{n,l}}{\mu_{n,li}} - 1)} m_{\Delta_i}^{-1}, \tag{2.14}$$

where $\beta = f\ m_t/m_c$, $\mu_{n,l}$ is the electron mobility without impurity scattering and $\mu_{n,li}$ with it.

2.1.2 Experimental observation

Reliable experimental observations of mobility variations at high uniaxial strains remain scarce. To fill this gap, n-type silicon strain gauges oriented along the [001] crystal direction have been tested to their limits, reaching almost 1%-strain before fracture. The gauges comes from the commercial KSNB series provided by *Kyowa* with a length of 2 mm oriented along [001], a width of 250 µm and thickness of 20 µm. The sensing silicon beam is encapsulated in polyimide while gold wires are used to connect the gauge to metallic pads.

Figure 2.3a illustrates the experimental setup used to obtain the resistance variations with strain. The four-point bending machine shown in Fig. 2.3c is used to strain the silicon gauge up to 1%. The four point scheme allows an accurate and constant strain between the two lower bars where the samples are placed. An image of the polyimide-encapsulated silicon resistor is shown in Fig. 2.3b. Strain is measured using a reference strain

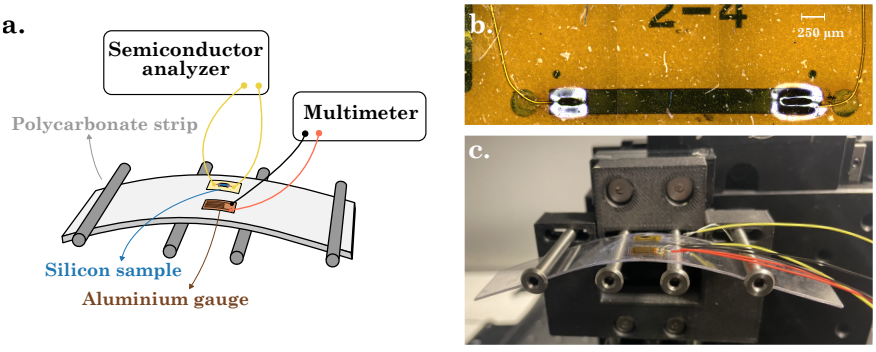


Fig. 2.3 (a) Illustration of the experimental set-up made of a four-point bending machine used to apply tensile strain on the silicon sample glued on a polycarbonate strip. The silicon resistance is retrieved using a semiconductor analyzer while an aluminium strain gauge, measured with a digital multimeter, is used to determine the strain applied to the samples. (b) Microscope picture of the silicon sample (dark) encapsulated in polyimide (orange) and connected with gold wire-bonding. The silicon beam is 2 mm in length, 250 µm wide and 20 µm in thickness. (c) Picture of the experimental set-up for strain about 0.2%.

gauge from *Micro-Measurements* and a DMM7510 from *Keithley*. The aluminium reference strain gauge and the silicon devices are bonded to the same side of a 1mm thick polycarbonate strip. The polymer allows high

levels of strain while retaining elastic properties that limit plastic deformation of the substrate. The current of the silicon rods is measured over a voltage range of -0.5 V to 0.5 V with steps of 20 mV using a *HP 4145B* semiconductor analyser. Two different samples are bent perpendicular and parallel to the current measurements to obtain the transverse and longitudinal mobility evolutions respectively.

The resistance variations are corrected with the dimensional variations to obtain only the resistivity:

$$\rho_n = R_n \frac{wt}{l}, \tag{2.15}$$

where R_n is the measured resistance, ρ_n is the resistivity, l is the length, w is the width and t is the thickness of the device. The zero-strain resistance at room temperature is 126.8 Ω, leading to a resistivity of 0.0315 Ω cm. A doping concentration about 5×10^{17} cm^{-3} is calculated using the relation between resistivity and doping developed by Masetti *et al.* [177].

Under the assumption of constant ionization of the dopant at room-temperature [178], the resistivity variations is directly proportional to the mobility variations:

$$\frac{\Delta\rho_n}{\rho_{n,0}} = -\frac{\Delta\mu_n}{\mu_n}, \tag{2.16}$$

where $\rho_{n,0}$ is the resistivity in the absence of strain.

Finally, the longitudinal (long.) and transverse (trans.) variations of the electron mobility are given by

$$\begin{aligned} \left(\frac{\Delta\mu_n}{\mu_n}\right)_{long.} &= -\frac{\Delta R_n}{R_n} + (1 + 2\nu_{001}^{uni})\,\varepsilon_{zz}, \\ \left(\frac{\Delta\mu_n}{\mu_n}\right)_{trans.} &= -\frac{\Delta R_n}{R_n} - \varepsilon_{zz}, \end{aligned} \tag{2.17}$$

with the longitudinal strain ε_{zz} and the Poisson's ratio $\nu_{001}^{uni} = 0.28$ [115].

As explained in chapter 1, the uniaxial stress applied along the [001] crystal direction lifts the degeneracies of the six electron valleys. The energy of the two Δ_2-valleys oriented along the strain direction increases by 91.7 meV at 2%-strain. The energy of the other four, called Δ_4-valleys, decreases with strain by 129.5 meV at 2%-strain. On the other hand, the maximum of the valence bands located at the Γ symmetry point shows little variation, decreasing by 10.6 meV at 2%-strain.

In Fig. 2.4, we show our measured change in transverse and longitudinal resistances, calculated by linear regression from the slopes of the

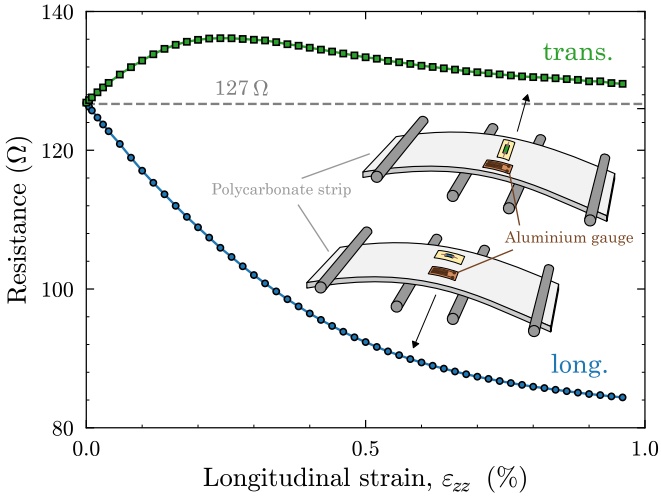


Fig. 2.4 Resistance of the n-doped silicon beam oriented perpendicular (green squares) and parallel (blue dots) to the bending. The pictures show the configuration of the two samples on the four-point bending machine used to strain the devices. The unstrained resistance is about 127 Ω for both samples (126.87 Ω for the transverse configuration and 126.80 Ω for the longitudinal one).

current-voltage measurements.

The longitudinal component shows a monotonic decrease but saturates at higher strain. At low strain, the occupancy variations between the Δ_2 and Δ_4-valleys play an important role, but as strain increases, most of the electron population is already in the lower energy valleys, *i.e.*, the Δ_4-valleys. In the longitudinal direction, only the small transverse effective mass plays a role in the mobility, leading to the strong enhancement of the mobility. The transverse component shows non-monotonic variations, starting with an increase in resistance up to 0.15%, to finally decrease close to the initial value of the resistance. In this case, both the longitudinal and transverse effective masses are important and lead to a mobility value at higher strain close to the relaxed one. As shown with Eq. (2.16), the relative mobility variations are directly related to the relative resistivity variations. The relative variations are then scaled by the electron mobility for undoped silicon in the absence of strain, *i.e.*, 1420 $cm^2V^{-1}s^{-1}$ [177], to obtain the results shown in Fig. 2.5. The use of the zero-strain mobility as scaling factor allows to compare the experimental results with the theoretical

ones although the impurity concentrations are different. Indeed, the relative mobility variations with strain are much less affected by the doping concentration when below 10^{19} cm^{-3}, as explained by Kanda [179], even though the impurity concentration reduces significantly the mobility [180, 181].

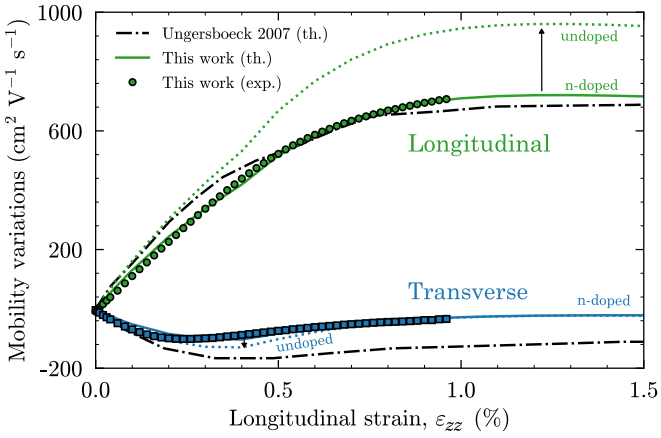


Fig. 2.5 Mobility variations computed from the resistance measurements for the longitudinal (green dots) and transverse (orange squares) components. The figure displays the analytical model from Ungersboeck *et al.* [175] for undoped silicon as a dash-dotted line. The continuous and dotted lines represent the fitted model for doped (5×10^{17} cm^{-3}) and undoped silicon, respectively.

The variations are compared with the analytical model developed by Dhar *et al.* [171] and used by Ungersboeck *et al.* [175]. This semi-empirical model is explained in section 2.1.1. As parameter, they considered a transverse mobility factor f of 70%, also known as enhancement factor, which resulted in a greater reduction in the transverse component than that observed experimentally. We used the model of Dhar *et al.* [171] (see Eq. (2.14)) with the enhancement factor as a fitted parameter. We found a factor of 110% which is close to previous experimental work [182]. The analytical model is then used to determine the undoped behaviour as shown in Fig. 2.5. A significant improvement up to almost 1000 cm^{2}V^{-1}s^{-1} in the longitudinal component is observed at high strain, which was underestimated in the previous study.

2.2 First-principles computations

Only recently have first-principles calculations of the BTE become available within the electron-phonon wannier (EPW) code [183, 184], PERTURBO [185], PHOEBE [186] or ABINIT [187, 108], which made it possible to predict mobility in semiconductors fully theoretically [188]. These new techniques can now be used to calculate the mobility variation in a deformed crystal from first principles, without the empirical bias. In this section, the mobility for holes and electrons is calculated from first principles for silicon strained up to 2 % in the [100] direction. The mobility for uniaxial strain along [110] is then calculated based on the same methodology. The method presented is general and can be used for any strain type and direction for any semiconductor where the mobilities are limited by electron-phonon scattering. In particular, the use of *ab initio* calculations proves to be particularly important for holes, for which the proximity of the valence bands and the important modification of their shapes under strain conditions limit the accuracy that can be obtained by an analytical approach. In addition, the calculations allow the study of intrinsic phenomena at large strains, which cannot be achieved experimentally due to the challenge of obtaining low-doped [189] or highly strained samples.

2.2.1 Boltzmann transport equation

In the low-field limit, the carrier mobility $\mu_{\alpha\beta}$ is defined as the ratio between the electrical conductivity $\sigma_{\alpha\beta}$ and the product of the electron charge e by the carrier density n_c:

$$\mu_{\alpha\beta} = \left| \frac{\sigma_{\alpha\beta}}{e\, n_c} \right|, \tag{2.18}$$

where α and β are Cartesian directions. The conductivity is obtained by iteratively solving the BTE [188], which involves directly calculating the scattering rates $\tau^{-1}_{n\mathbf{k}}$ and the electronic velocity $\mathbf{v}_{n\mathbf{k}}$ of a state with band index n and electron momentum $\mathbf{k}$.

The mobility in Eq. (2.18) depends on the carrier density n_c and the electric conductivity at low electric field $\sigma_{\alpha\beta} = \left(\partial J_\alpha / \partial E_\beta\right)|_{\mathbf{E}=\mathbf{0}}$, defined as the ratio between the mean current density J_α in the Cartesian direction

α and the electric field E_β in the Cartesian direction β [190]. The carrier density n_c for the electron or hole can be computed as [188]

$$n_{e,h} = \frac{1}{V_{cell}} \sum_n \int \frac{d^3k}{\Omega_{\mathrm{BZ}}} \left[f^0_{n\mathbf{k}}(\mu, T) - f^0_{n\mathbf{k}}(\varepsilon_{\mathrm{F}}, 0) \right], \tag{2.19}$$

where the band index n runs over the valence bands for the holes and over the conduction bands for the electrons, Ω_{BZ} is the volume of the Brillouin zone, μ is the chemical potential, T is the temperature, ε_{F} is the Fermi energy, $f^0_{n\mathbf{k}}(\mu, T) = 1/\{(\exp[(\varepsilon_{n\mathbf{k}} - \mu)/k_{\mathrm{B}}T] + 1\}$ is the Fermi-Dirac distribution evaluated at the band energy $\varepsilon_{n\mathbf{k}}$ in the absence of electric field.

The conductivity can be expressed as

$$\sigma_{\alpha\beta} = -\frac{e}{V_{cell}} \sum_n \int \frac{d^3k}{\Omega_{\mathrm{BZ}}} v_{n\mathbf{k},\alpha} \partial_{E_\beta} f_{n\mathbf{k}}, \tag{2.20}$$

with V_{cell} the volume of the primitive cell, $v_{n\mathbf{k},\alpha} = \hbar^{-1} \partial \varepsilon_{n\mathbf{k}} / \partial k_\alpha$ the component of the band velocity with crystalline moment $\mathbf{k}$ and band index n and $\partial_{E_\beta} f_{n\mathbf{k}} = \left(\partial f_{n\mathbf{k}} / \partial E_\beta \right)\big|_{\mathbf{E}=0}$ where $f_{n\mathbf{k}}$ is the electronic occupation distribution at the band energy $\varepsilon_{n\mathbf{k}}$.

This last term can be computed recursively solving iteratively the BTE [133, 191]:

$$\begin{aligned} \partial_{E_\beta} f_{n\mathbf{k}} = e v_{n\mathbf{k},\beta} \frac{\partial f^0_{n\mathbf{k}}}{\partial \varepsilon_{n\mathbf{k}}} \tau_{n\mathbf{k}} + \frac{2\pi\tau_{n\mathbf{k}}}{\hbar} \sum_{m\nu} \int \frac{d^3q}{\Omega_{\mathrm{BZ}}} \\ \times |g_{mn\nu}(\mathbf{k}, \mathbf{q})|^2 \Big[(n_{\mathbf{q}\nu} + 1 - f^0_{n\mathbf{k}}) \delta(\varepsilon_{n\mathbf{k}} - \varepsilon_{m\mathbf{k}+\mathbf{q}} + \hbar\omega_{\mathbf{q}\nu}) \\ + (n_{\mathbf{q}\nu} + f^0_{n\mathbf{k}}) \delta(\varepsilon_{n\mathbf{k}} - \varepsilon_{m\mathbf{k}+\mathbf{q}} - \hbar\omega_{\mathbf{q}\nu}) \Big] \partial_{E_\beta} f_{m\mathbf{k}+\mathbf{q}}, \end{aligned} \tag{2.21}$$

with the scattering rate

$$\begin{aligned} \tau^{-1}_{n\mathbf{k}} = \frac{2\pi}{\hbar} \sum_{m\nu} \int \frac{d^3q}{\Omega_{\mathrm{BZ}}} |g_{mn\nu}(\mathbf{k}, \mathbf{q})|^2 \\ \Big[(n_{\mathbf{q}\nu} + 1 - f^0_{m\mathbf{k}+\mathbf{q}}) \delta(\varepsilon_{n\mathbf{k}} - \varepsilon_{m\mathbf{k}+\mathbf{q}} - \hbar\omega_{\mathbf{q}\nu}) \\ + (n_{\mathbf{q}\nu} + f^0_{m\mathbf{k}+\mathbf{q}}) \delta(\varepsilon_{n\mathbf{k}} - \varepsilon_{m\mathbf{k}+\mathbf{q}} + \hbar\omega_{\mathbf{q}\nu}) \Big], \end{aligned} \tag{2.22}$$

where $n_{\mathbf{q}\nu} = 1/\left[\exp(\hbar\omega_{\mathbf{q}\nu}/k_{\mathrm{B}}T) - 1\right]$ is the Bose-Einstein distribution evaluated at the phonon energy $\hbar\omega_{\mathbf{q}\nu}$ and $g_{mn\nu}(\mathbf{k}, \mathbf{q})$ is the e-ph matrix el-

ement for the scattering of an electron from state $\psi_{n\mathbf{k}}$ into state $\psi_{m\mathbf{k}+\mathbf{q}}$ with a phonon of mode ν and wavevector $\mathbf{q}$. The matrix elements are given by [192]

$$g_{mn\nu}(\mathbf{k},\mathbf{q}) = \left\langle \psi_{m\mathbf{k}+\mathbf{q}} \right| \Delta_{\mathbf{q}\nu} V^{\mathrm{KS}} \left| \psi_{n\mathbf{k}} \right\rangle, \tag{2.23}$$

where $\psi_{n\mathbf{k}}$ is the KS Bloch state and $\Delta_{\mathbf{q}\nu} V^{\mathrm{KS}}$ is the first-order variation of the self-consistent KS potential defined as [193]

$$\Delta_{\mathbf{q}\nu} V^{\mathrm{KS}} = \frac{1}{\sqrt{2\omega_{\mathbf{q}\nu}}} \sum_{p\kappa\alpha} \frac{\partial V^{\mathrm{KS}}}{\partial \tau_{\kappa\alpha}} \frac{e_{\kappa\alpha,\nu}(\mathbf{q})}{\sqrt{M_\kappa}} e^{i\mathbf{q}\cdot\mathbf{R}_p}, \tag{2.24}$$

where $e_{\kappa\alpha,\nu}(\mathbf{q})$ is the α-th Cartesian component of the phonon eigenvector for the atom κ in the unit cell, M_κ its atomic mass, $\mathbf{R}_p$ are lattice vectors identifying the unit cell p, and $\tau_{\kappa\alpha}$ the ion position in the unit cell.

The main source of complexity is the resolution of Eq. (2.21) with the dependence between the linear response $\partial_{E_\beta} f_{n\mathbf{k}}$ of state $|n\mathbf{k}\rangle$ with the ones of states $|m\mathbf{k}+\mathbf{q}\rangle$. The momentum relaxation time approximation (MRTA) assumes only a component of the linear response in the direction of the band velocity and partially incorporates the effect of scattering. It leads to

$$\partial_{E_\beta} f_{n\mathbf{k}}\Big|_{\mathrm{MRTA}} \approx e v_{n\mathbf{k},\beta} \frac{\partial f^0_{n\mathbf{k}}}{\partial \varepsilon_{n\mathbf{k}}} \widetilde{\tau}_{n\mathbf{k}} \tag{2.25}$$

where $\widetilde{\tau}_{n\mathbf{k}}$ can be explicitely calculated as [194]

$$\widetilde{\tau}_{n\mathbf{k}} = \sum_m \int \frac{d^3q}{\Omega_{\mathrm{BZ}}} \left(1 - \frac{\mathbf{v}_{n\mathbf{k}} \cdot \mathbf{v}_{m\mathbf{k}+\mathbf{q}}}{|\mathbf{v}_{n\mathbf{k}}|^2}\right) \tau^{-1}_{n\mathbf{k}\to m\mathbf{k}+\mathbf{q}}. \tag{2.26}$$

The self-energy relaxation time approximation (SERTA) completely neglects the rate for backscattering so that $\partial_{E_\beta} f_{n\mathbf{k}}$ can be calculated as [133]:

$$\partial_{E_\beta} f_{n\mathbf{k}}\Big|_{\mathrm{SERTA}} \approx e v_{n\mathbf{k},\beta} \frac{\partial f^0_{n\mathbf{k}}}{\partial \varepsilon_{n\mathbf{k}}} \tau_{n\mathbf{k}} \tag{2.27}$$

The calculation parameters followed the ones used by Brunin *et al.* [187] who developed the electron-phonon code to calculate the phonon-limited mobility within ABINIT [108]. In practice, the scattering potentials were first computed from DFPT on a coarse $9 \times 9 \times 9$ $\mathbf{q}$-grid. They were then Fourier interpolated onto a fine $150 \times 150 \times 150$ $\mathbf{q}$-grid using dielectric tensors [195] and quadrupoles [187, 196] for the long-range electrostatic contributions. The KS wavefunctions are obtained by performing a SCF

on a coarse 18 × 18 × 18 **k**-grid before a NSCF calculations on a fine 150 × 150 × 150 **k**-grid. To reduce the computational cost, the e-ph calculation is performed only at the **k** points with energies within a window of 200 meV above or below the band edges, *i.e.*, close to the extrema of the valence and conduction bands. The spin orbit coupling (SOC) was taken into account in the calculation of the electronic properties, but neglected for the vibrational properties, dynamical quadrupoles and e-ph scattering potentials [197].

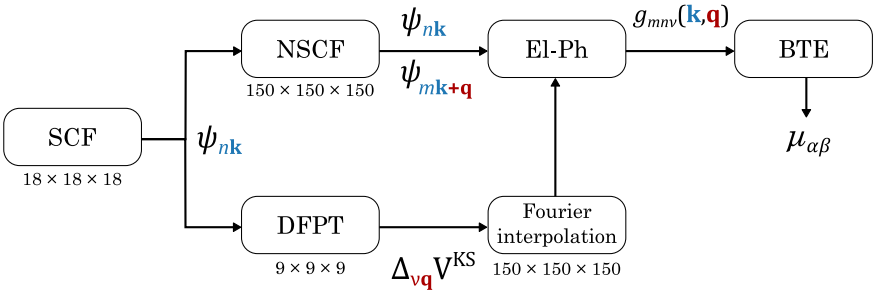


Fig. 2.6 Scheme to obtain the phonon-limited mobility based on DFT and DFPT to calculate the mobility by solving the BTE. The grid for each calculation step is indicated.

As a reminder, a direct effect of crystal deformation under uniaxial tensile strain is the modification of the band structure, in particular the variation of the band edges. In silicon, the six electron valleys are located along the symmetry path from Γ towards X, while the top of the valence bands is located at Γ. The SO valence band is slightly separated (∼47 meV) from the HH and LH valence bands due to SOC. Under uniaxial stress in the [001] direction the degeneracy of the conduction band minima is lifted and the two valleys (Δ_2) along the symmetry path longitudinal to the stress direction increase in energy while the four others (Δ_4) decrease, as shown in Fig. 2.7a. This effect increases the electron population at the conduction minima and decreases it in the higher energy valleys. The variations of the band edges due to stress applied in the [001] direction with and without SOC taken into account are shown in Fig. 2.7b. In the case of the valence bands, the strain slightly separates the HH and LH bands up to 28 meV at 2%, while pushing the SO band down by 200 meV at 2% deformation. Apart from a reduction in the band gap of 17 meV, the edge variations of the electron valleys are not strongly affected by the inclusion of SOC in the calculation.

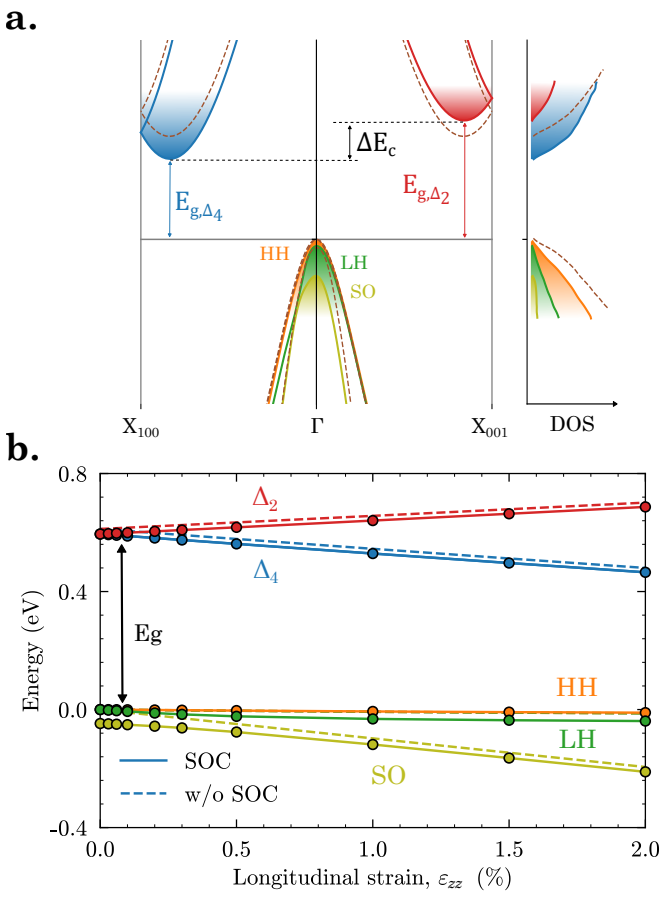


Fig. 2.7 (a) Impact of stress along the [100] crystal direction on the extrema of the valence bands and conduction bands. The lift of the degeneracy between the Δ_2-valleys (red) and the Δ_4-valleys (blue) is shown. The density of states (DOS) of the three valence bands and the two valleys are indicated next to the band structure. Dashed brown curves are used for the unstrained case. (b) Band edges variations of the Δ_4-valleys (blue), Δ_2-valleys (red), HH band (orange), LH band (dark green) and SO band (light green) with the strain with spin-orbit coupling taken into account (continuous line) and without (dashed line). The energy is scaled to the valence band maximum at zero strain while the band gap (E_g) is obtained from the energy difference between the band edges.

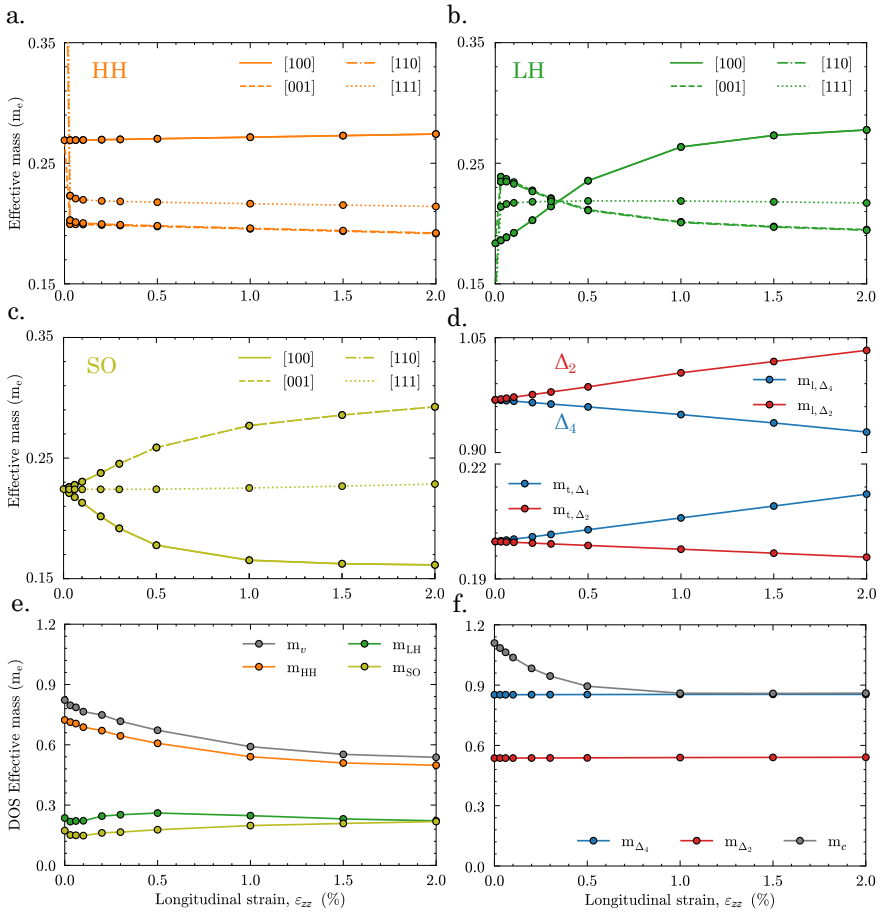


Fig. 2.8 Effective masses as a function of strain computed at the maxima of the valence bands along the [100], [001], [110] and [111] crystal directions for (a) the HH band (orange), (b) the LH band (dark green), and (c) the SO band (light green) with SOC included. (d) Effective masses computed at the minima of the conduction bands along the longitudinal and transverse directions for the Δ_4-valleys (blue) and Δ_2-valleys (red). (e) Valence DOS effective mass with the contribution of the three valence bands and (f) the conduction DOS effective mass with the contribution of the two types of valleys. The values in the absence of strain are discontinuous for the effective masses in the [001], [110], and [111] directions of the HH and LH bands and are not shown here.

The directional effective masses for the three valence bands (HH, LH and SO) have been calculated using the second derivatives of the band energy along the [100], [001], [110] and [111] crystal directions and are shown in Figs. 2.8a, 2.8b and 2.8c, respectively. The high anisotropy of the HH band is reduced under uniaxial tensile strain as the effective masses in the [110] (resp. [111]) direction show a strong reduction from 0.539 m_e (resp. 0.678 m_e) to 0.203 m_e (resp. 0.223 m_e) at 0.03%-strain. The LH band shows a sharp increase in the presence of strain, going from 0.137 m_e to 0.235 m_e for the masses calculated in the [110] direction and from 0.130 m_e to 0.214 m_e for those calculated in the [111] direction. The values in the absence of strain are discontinuous for the effective masses in the [001], [110] and [111] directions of the HH and LH bands due to the removal of band degeneracy. The strain breaks the isotropy of the effective masses calculated for the SO band, which has the same value of 0.224 m_e in the absence of strain. The electron effective masses are calculated only along the [100] and [001] directions, as the electron valleys have a regular ellipsoidal shape which is preserved under this strain condition. The directional effective masses for the Δ_2- and Δ_4-valleys show small linear variations with strain compared to the hole effective masses, as shown in Fig. 2.8d. The decrease (resp. increase) of the longitudinal component and the increase (resp. decrease) of the transverse component of the Δ_4-valleys (resp. Δ_2-valleys) are the sign of an elongation (resp. compression) of the ellipsoid shape formed by the equipotential surfaces, as shown in Fig. 1.4a.

The DOS effective mass of a band is computed by integrating the DOS and is defined as the one giving the same density of states as if the band was parabolic. In the case of the valence band, it is obtained through [198, 199]

$$\frac{\sqrt{\pi}}{2}\frac{1}{2\pi^2}\left(\frac{2\,m_v}{\hbar^2}k_B T\right)^{3/2} = \int_{-\infty}^{E_v} g(E) e^{-\frac{E_v - E}{k_B T}} dE, \tag{2.28}$$

where E_v is the energy of the valence band maximum and $g(E)$ is the density of states integrated on a dense $150 \times 150 \times 150$ **k**-grid for each strained configuration. The energy integral allows the degeneracy lift due to strain to be taken into account to obtain a global DOS effective mass. The evolution of the DOS effective masses is shown in Fig. 2.8e for the holes and Fig. 2.8f for the electrons. In silicon, the DOS effective mass of the holes is dominated by the top band (HH) with the largest mass, which decreases from 0.723 m_e to 0.498 m_e at 2%-strain, while the other two valence bands are pushed away by strain. In the case of the electrons, the conduction

band is almost perfectly parabolic, and this is held under uniaxial strain along [001], so that m_c is very close to the geometric mean of the transverse and longitudinal components of the electron effective mass tensor, m_t and m_l, respectively [200],

$$m_{c,\Delta_i} = (m_{l,\Delta_i} m_{t1,\Delta_i} m_{t2,\Delta_i})^{1/3}, \tag{2.29}$$

where Δ_i denotes a single electron valley. These longitudinal and transverse electron effective masses can be determined as second-order derivatives of the electronic energies obtained from NSCF calculations of the band structure on a dense mesh. As strain increases, the Δ_2-valleys become higher in energy than the Δ_4-ones and their contribution to the global DOS effective mass decreases. In the absence of strain, the global conduction effective mass gathers contributions from all 6 valleys equally and is 1.116 m_e. At 1%-strain the global DOS effective mass is equal to that of the Δ_4-valleys, *i.e.*, 0.860 m_e.

2.2.2 Scattering rate and velocity

Figure 2.9a shows the phonon-limited scattering rates $\tau_{n\mathbf{k}}^{-1}$ calculated for all $\mathbf{k}$ points with energy states near the minimum of the conduction band or the maximum of the valence band for a 0%-, 0.3%- and 1%-strain and for a temperature of 200 K, 300 K and 400 K. As the temperature increases from 200 K to 400 K, the maximum scattering rates in the absence of strain increase by 72% for the electrons and 52% for the holes with increasing temperature. The phonon band structure is only slightly altered by strain, resulting in a negligible effect on the scattering variations. An increase of 76% for the electrons and 54% for the holes is observed at 1%-strain as the temperature increases from 200 K to 400 K. This means that the increase in scattering with temperature is strain independent. In silicon, electron scattering can be divided into two categories: intravalley scattering, where long-wavelength phonons ($\mathbf{q} \rightarrow 0$) scatter the electrons within a single valley (Δ_2- or Δ_4-valleys), and intervalley scattering, where electrons scatter from one valley to another due to short-wavelength phonons (large $\mathbf{q}$). Similarly, hole scattering is described by intraband scattering, where phonons scatter a hole within a single band (LH, HH or SO), and interband scattering, where holes are scattered from one band to another. Figure 2.9b shows the scattering rates at 300 K for the different strain levels.

For a deeper understanding, the intravalley scattering contributions

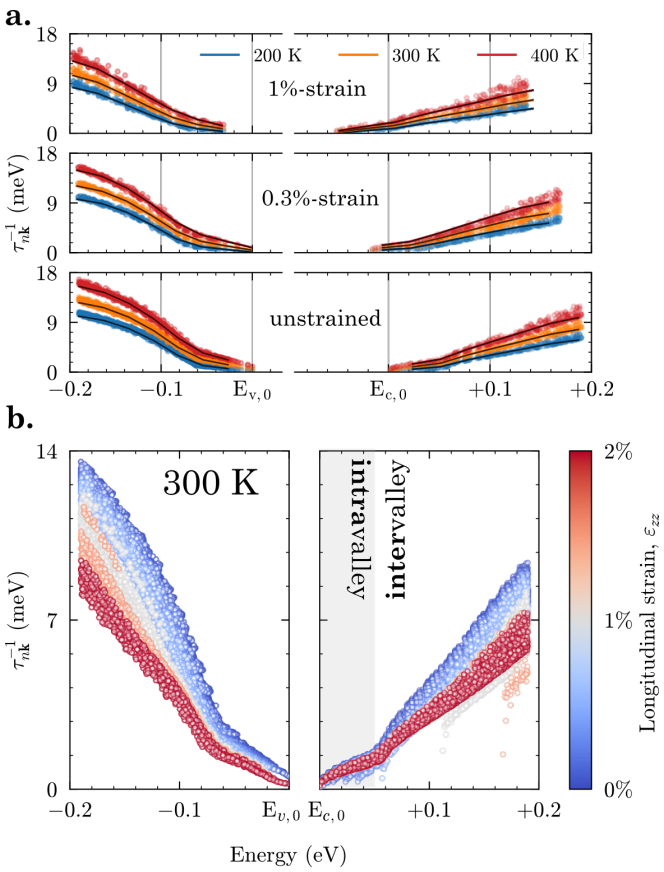


Fig. 2.9 (a) Scattering rates for **k** points with an energy within 0.2 eV of the band edges under 0%, 0.3%, and 1%-strain along [001] at 200 K (blue dots), 300 K (orange dots) and 400 K (red dots). The black lines are the scattering rates density at the three temperatures. (b) Scattering rates for all relevant **k** points at 300 K under strain ranging from 0% (blue) to 2% (red). The panels show the hole (left) and electron (right) scattering rates. The intravalley contribution of the electron scattering rates at 0%-strain dominates for energy below 53 meV (see Fig. 2.10) and is highlighted (grey area), while the intervalley scattering is seen at higher energies. The minimum and maximum of the conduction and valence bands are indicated by $E_{c,0}$ and $E_{v,0}$, respectively.

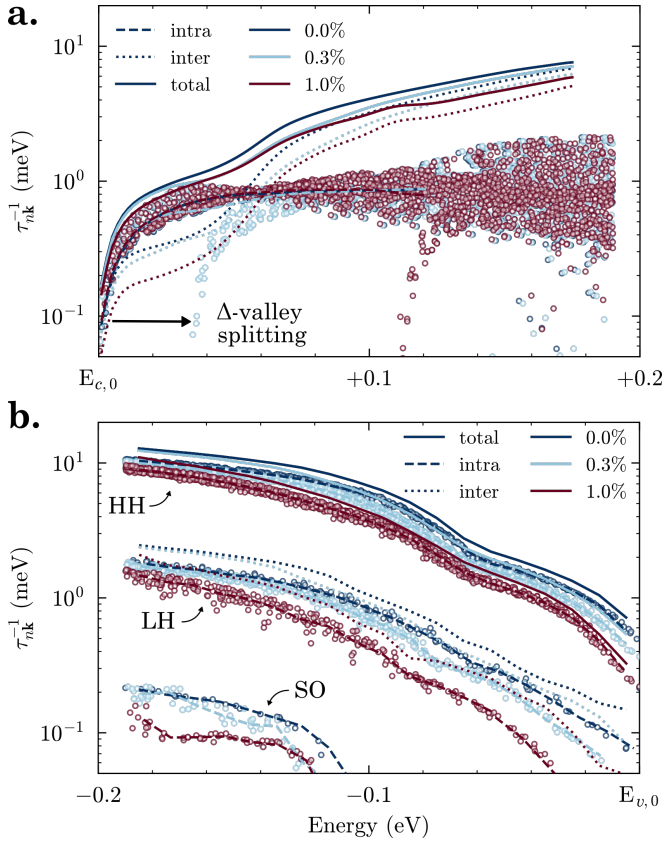


Fig. 2.10 (a) Electron intravalley scattering rates for **k** points with an energy within 0.2 eV of the band edges under 0% (dark blue), 0.3% (light blue) and 1%-strain (red) along [001] at 300 K. The strain-induced valley splitting between the Δ_4 and Δ_2-valleys is indicated. (b) Hole intraband scattering rates for all relevant **k** points under 0% (dark blue), 0.3% (light blue) and 1%-strain (red) at 300 K. The scattering rates for the HH, LH and SO bands have been computed. The mean intravalley and intraband scattering rates using 2 meV energy bins are shown with dashed lines, while the intervalley curves are obtained by subtracting the intravalley contribution from the total scattering rate. The minimum and maximum of the conduction and valence bands are indicated by $E_{c,0}$ and $E_{v,0}$, respectively.

have also been calculated explicitly by considering only higher wavelength phonon modes with a norm of $|\mathbf{q}| < 0.06$ bohr^{-1}. Figure 2.10a shows the intravalley scattering rate for electrons. The mean scattering rate has been calculated by averaging over 2 meV energy bins. The intervalley scattering rate is calculated by subtracting the intravalley contribution from the total scattering rate previously obtained. The intravalley contribution is dominant below 53 meV for 0%-strain, in agreement with the results of Yang *et al.* [3]. In particular, the calculations show the independence of intravalley scattering with strain, as both the phonon band structure and the shape of the valley do not change significantly. In contrast, for energies above 53 meV, intervalley scattering becomes the dominant process, but it is reduced by the splitting of the electron valleys with strain. Therefore, the energy limit between intra- and intervalley scattering increases linearly with strain and reaches 63 meV at 1%-strain. At higher strains, all electrons occupy the Δ_4-valleys, reducing the intervalley scattering by about a third. For the holes, the scattering rate is dominated by the intraband scattering of the HH band as shown in Fig. 2.10b. Additionally, the interband contribution has been calculated by subtracting the intraband scattering from the previously calculated total scattering. It is evident that the intraband scattering of the HH band significantly exceeds the LH and SO contributions at all energies. It can be observed that the intraband scattering at low strain is significantly affected by the variations of the band shapes around the Γ-point. Furthermore, the splitting between the HH and LH bands, which reaches a separation of 28 meV at 1%-strain, causes a reduction in the interband scattering. However, this has only a limited effect on the total scattering rate.

The components of the electronic velocity $v_{n\mathbf{k},\alpha}$ are shown in Fig. 2.11 as a function of state energy for different strain configurations. The separation of the Δ_4-valleys and the Δ_2-valleys leads to a separation of the longitudinal component of the velocity $v_{n\mathbf{k},z}$ (oriented along the direction of the applied stress) and the transverse components $v_{n\mathbf{k},x}$ and $v_{n\mathbf{k},y}$.

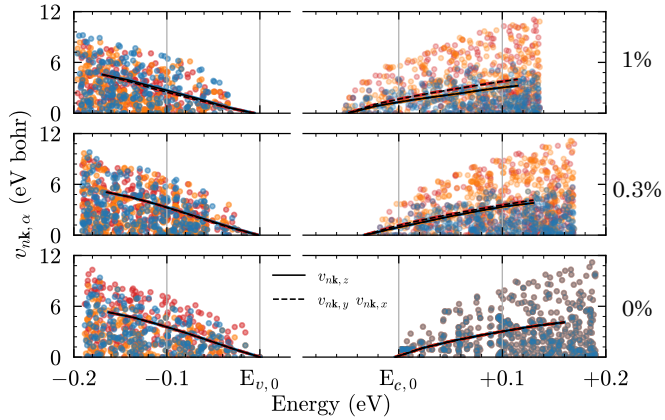


Fig. 2.11 Band velocities along the three Cartesian directions for all relevant **k** points under 0%-, 0.3%- and 1%-strain along [001] direction. The velocities in the x, y, and z directions are indicated with blue, orange, and red dots, respectively. The minimum and maximum of the zero-strain conduction and valence bands are indicated by $E_{c,0}$ and $E_{v,0}$, respectively. The continuous and dashed lines represent the velocity density of the longitudinal ($v_{n\mathbf{k},x}$) and transverse ($v_{n\mathbf{k},y}$, $v_{n\mathbf{k},z}$) components, respectively. They have been computed using linear-tetrahedron method [201] with steps of 25 meV.

2.2.3 Phonon-limited mobility

The room-temperature electron and hole mobilities attained at longitudinal strain levels up to 2% are shown in Fig. 2.12. Under the applied strain conditions, the mobility tensor is no longer isotropic and gives rise to longitudinal and transverse mobilities. As can be seen, first-principles calculations are able to reproduce the non-linear behaviour of the mobility with increasing strain, especially at larger strain levels for the electron mobility which saturates around 1%-strain at 2249 $cm^2V^{-1}s^{-1}$ for the longitudinal and 1321 $cm^2V^{-1}s^{-1}$ for the transverse component, while the zero-strain mobility is 1366 $cm^2V^{-1}s^{-1}$. We find a minimum in the transverse electron mobility at 0.3%-strain with a value of 1195 $cm^2V^{-1}s^{-1}$. In relaxed silicon the longitudinal and transverse components are identical and the six electron valleys contribute to the mobility. For mobility in a given Cartesian direction, the two valleys along that direction contribute with their low longitudinal curvature and velocity, while the other four contribute with their high longitudinal curvature and velocity. The reduction at low strain

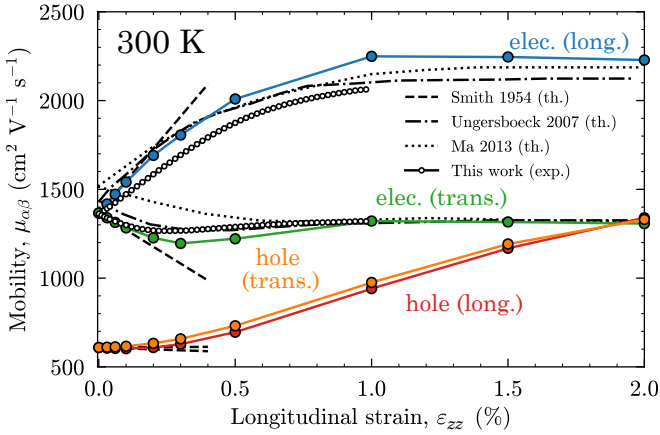


Fig. 2.12 Phonon-limited mobilities calculated theoretically as a function of the longitudinal strain in the transverse (green for the electrons and orange for the holes) and longitudinal (blue for the electrons and red for the holes) directions of the applied stress in the [001] crystal direction. The mobility variations for the electrons obtained experimentally in this work are shown with white dots. The relative variations of the resistivity of n-doped silicon samples have been scaled by the zero-strain mobility to retrieve the mobility variations, *i.e.*, 1366 $cm^2V^{-1}s^{-1}$. The linear model using the piezoresistive coefficients from Smith [45] is indicated with the dashed black lines while the computation of the electron mobilities from Ma *et al.* [172] and Ungersboeck *et al.* [175] are represented by dotted and dash-dotted lines.

is explained by the significant depletion of electrons from the Δ_2- to the Δ_4-valleys due to energy splitting. The difference in valley occupancy leads to the distinction between the longitudinal and transverse components. In addition, the longitudinal mobility is oriented along the transverse axis of the Δ_4-valleys, with low curvature resulting in a significant increase in mobility. On the other hand, the two equivalent transverse mobilities are oriented both longitudinally to two Δ_4-valleys and transversely to the other two. The calculation of this component combines both low curvature from the transverse axis and high curvature from the longitudinal axis, resulting in a pronounced reduction in mobility, particularly at lower strain levels. This is in contrast to the relaxed value, which includes two transverse curvatures and a longitudinal valley curvature oriented along the transport direction. The reduction in the intervalley scattering tends to increase the

mobility. However, at lower strains this is masked by the depletion of electrons in the lower energy valleys. At about 0.3%, more than 80% of the electron population is found in the Δ_4-valleys, and the increase due to the reduced scattering rates begins to be visible for the transverse mobility. At levels above 1%, the vast majority of the electrons are localised in the Δ_4-valleys and no longer interact with the Δ_2-valleys, resulting in stable intervalley scattering with strain.

We measured the change in resistivity of the transverse and longitudinal components on an n-doped (about 5×10^{17} cm^{-3} doping) sample in section 2.1 and found excellent agreement, see white circles in Fig. 2.12. As a reminder, the strain was applied to the devices using a four-point bending set-up which produces a constant strain field on the sample [189]. Strain levels up to 1% were accurately measured using an aluminium strain gauge as a reference, bonded next to the silicon sample. The experimental results show the same trend as the first-principles calculations, with saturation of the electron mobility for the longitudinal component starting at about 0.5%, but with reduced intensity. The transverse mobility decreases similarly to the calculations but reaches a minimum just before the 0.3%-strain minimum to finally reach a reduction of about -3.4% at a strain of 1%. The enhancement (resp. reduction) found experimentally is 51% at 1%-strain (resp. -7% at 0.3%-strain) for the longitudinal (resp. transverse) component. The doped sample shows smaller variations compared to the theoretical values of 65% and -12.5% for the longitudinal and transverse mobilities, respectively. Since the carrier mobility decreases with increasing doping [202], we expect a greater increase in mobility with strain when using a less doped sample, even closer to the theoretical prediction. The calculated hole mobility at zero strain is about 609 cm^{2}V^{-1}s^{-1}, in agreement with previous calculations [187, 203], and shows little enhancement initially, but increases strongly for strains above 0.4% to reach 1340 cm^{2}V^{-1}s^{-1} and 1330 cm^{2}V^{-1}s^{-1} for the longitudinal and transverse components respectively at 2%.

Table 2.2 compares the results of our theoretical calculations with other semiconductor materials such as Ge [204] and $In_{0.53}Ga_{0.47}As$ [205, 206]. It can be seen that strain along [001] direction significantly improves the hole mobility, bringing it closer to that of Ge at 1840 cm^{2}V^{-1}s^{-1}. For the electrons, the important improvement in mobility up to 2230 cm^{2}V^{-1}s^{-1} at 2%-strain remains small compared to Ge mobility of 3780 cm^{2}V^{-1}s^{-1} or $In_{0.53}Ga_{0.47}As$ mobility of 13800 cm^{2}V^{-1}s^{-1}.

Theoretical calculations by Ungersboeck *et al.* [175] and Ma *et al.* [172]

	s-Si	Si	Ge	$In_{0.53}Ga_{0.47}As$
electron	2230	1450 [180]	3780 [204]	13800 [205]
hole	1340	450 [181]	1840 [204]	220 [206]

Table 2.2 Electron and hole mobility in $cm^2V^{-1}s^{-1}$ for typical semiconductor material. The values of strained silicon (s-Si) has been taken from our theoretical calculations for the longitudinal component at 2%-strain along the [001] crystal direction.

for the electron mobility were able to predict the non-linear behaviour as shown in Fig. 2.12, but failed to predict the hole mobility due to the triple contributions of the valence bands (HH, LH and SO) in addition to the high variations of the effective masses of these bands with strain [207, 208]. For these reasons, a first-principles scheme such as the one presented here is essential.

The effect of SOC on the mobility enhancement for the holes at 300 K is shown in Fig. 2.13. The zero-strain value initially shows a deviation of around −5% between calculations with and without SOC taken into account. Rhe longitudinal component reaches a minimum value around 0%

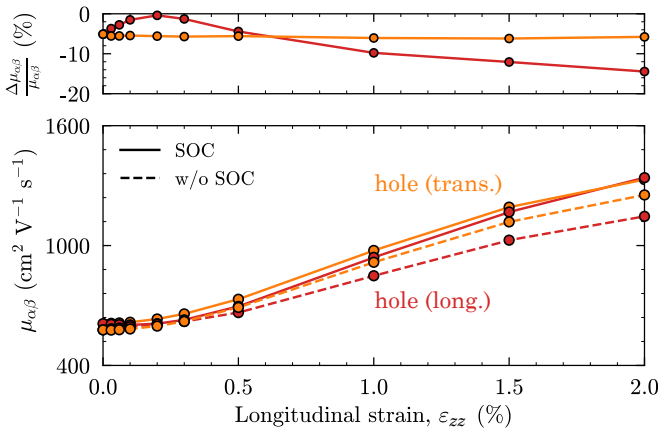


Fig. 2.13 Mobilities with longitudinal strain at 300 K (bottom panel) for the holes in the longitudinal (red) and transverse (orange) components with (continuous lines) and without (dashed lines) the SOC taken into account, and the relative difference induced by the coupling (top panel).

to finally decrease to -15% as the strain increases at 2%. A deviation of about -6% is observed for the transverse component when the SOC is not taken into account. The curves for the transverse mobility are similar with and without taking the coupling into account, but with an deviation factor, while the discrepancy between the longitudinal mobilities varies with strain. Taking coupling into account first removes the degeneracy of the SO band, as shown in Fig. 1.4c. Furthermore, the linear strain dependence in the absence of SOC of the SO and LH bands, -97 meV/% and -7 meV/% respectively, shows a non-linear trend at low strain when SOC is considered. The variations of these bands with SOC eventually reach the same linear variations at high strain as without SOC. The variations of the HH bands do not show significant differences and maintain a linear variation of about -7 meV/% with and without SOC. The calculations with and without SOC showed no significant difference for the electron mobilities, since the coupling does not affect the shape and the splitting of the electron valleys [133]. In addition, the strain dependence of the valley minima around -66 meV/% for the Δ_4-valleys and 44 meV/% for the Δ_2-valleys remain unchanged when the coupling is taken into account, as shown in Fig. 1.4c.

Solving the BTE instead of using an empirical model gives more confidence in the evolution of electron mobility with strain. In fact, the studies of Ungersboeck *et al.* [175] and Ma *et al.* [172] seem to underestimate the enhancement factor at high strain for the longitudinal component, but we find the same mobility for the transverse component, as shown in Fig. 2.12. In addition, the low strain variations predicted from first principles show excellent agreement with the linear model from Smith [45]. The analytical prediction of the electron mobility can be achieved because the variation comes mainly from the energies of a conduction band. In fact, the band curvature and hence the effective masses do not change significantly with strain. The main phenomenon to be considered is the energy shift between the Δ_4- and Δ_2-valleys, which can be easily calculated using DFT. Once all the electrons are in the lower energy valley, the mobility components stabilise. The difference in the mobility shift of the longitudinal and transverse components is due to the difference in the longitudinal and transverse effective masses of the lower-energy valleys [172]. Other strain configurations with four-fold degenerated valleys lead to similar plateaus for both components. Strain configurations such as uniaxial compressive and biaxial tensile strain in the [001] direction or uniaxial tensile and biaxial compressive strain in the [110] direction show only double degenerated

lower energy valleys which lead to larger mobility shifts, especially for the transverse component [175, 171, 53].

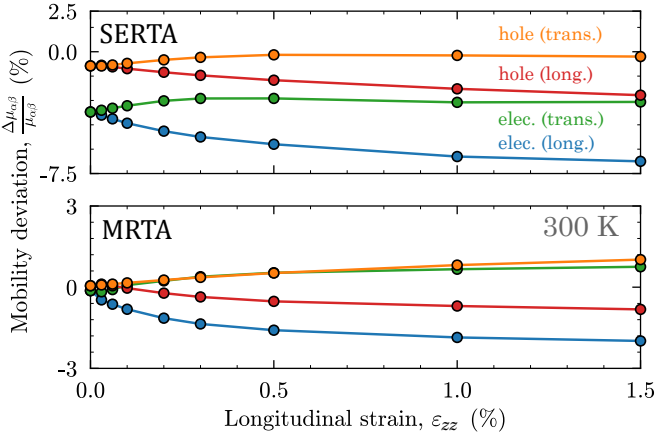


Fig. 2.14 Relative difference of the phonon-limited mobility computed under SERTA (top) and MRTA (bottom) compared to the iterative Boltzmann transport equation for the electrons (blue for the longitudinal component and green for the transverse one) and the holes (red for the longitudinal component and orange for the transverse one).

The mobilities obtained by solving iteratively the BTE can be compared to the MRTA or the SERTA [209, 210]. The comparison between the SERTA, MRTA and BTE results is shown in Fig. 2.14. As expected, MRTA shows a globally lower deviation (below 3%) compared to SERTA, which shows a deviation of up to 7% (resp. 3%) for the electron (resp. hole) mobility in the longitudinal direction. The deviation with respect to the BTE results is more important for the electrons under SERTA, especially for the longitudinal contribution. The SERTA results for the hole mobility remain closer to the BTE results, especially for the transverse contribution. At low strain, the MRTA shows very small variations which increase with strain but remain below 1% for the transverse components and below 3% for the longitudinal components. We note that this is specific to non-polar silicon, but much larger differences between SERTA, MRTA and BTE can be observed in other systems [210, 203, 193].

The temperature dependence of the mobilities at low strain is shown in Fig. 2.15. The mobility variations show a typical $T^{-1.5}$ decrease [211], going from 3562 $cm^2V^{-1}s^{-1}$ (resp. 1780 $cm^2V^{-1}s^{-1}$) at 200 K to 601 $cm^2V^{-1}s^{-1}$ (resp. 261 $cm^2V^{-1}s^{-1}$) at 400 K for the electrons (resp. holes). We have

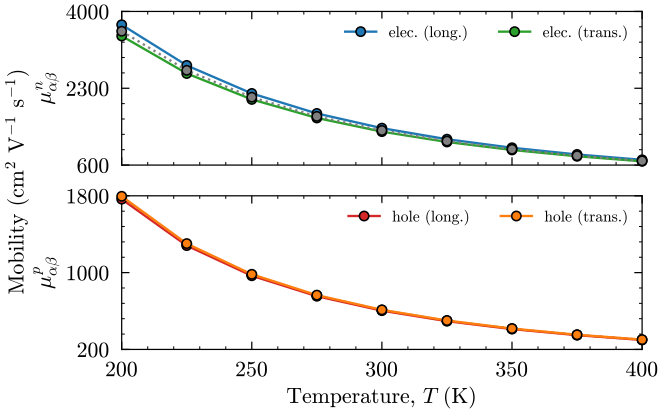


Fig. 2.15 Phonon-limited mobilities as a function of temperature. The the results at zero strain and 0.03% are shown in the longitudinal direction (blue for the electrons and red for the holes) and transverse direction (green for the electrons and orange for the holes).

studied the effect of temperature together with the different strain levels as shown in Fig. 2.16.

The effect is quite weak, but we find that lower temperature samples show a smaller variation of longitudinal electron mobility with strain. The maximum value at 2%-strain of the longitudinal mobility increases by 50.3%, 63.1% and 70.1% and the transverse mobility decreases by 12.5%, 4.3% and 0.3% at 200 K, 300 K and 400 K respectively. Nevertheless, the electron mobilities still show a saturation effect for strains greater than 1%, and this limit is mainly related to the valley splitting. As strain increases, the electron population spreads over a larger energy range. The valley splitting required to have all carriers in the lower energy valleys therefore increases with temperature. In contrast to the electrons, the strain decreases the hole mobility with temperature, from an enhancement at 2%-strain of 155.7% at 200 K to 98.7% at 400 K for the longitudinal component and from 118.4% at 200 K to 107.2% at 400 K for the transverse component. With decreasing temperature, the hole population decreases in the upper HH band and partially in the LH band, which remain close to each other even at higher strains, as shown in Fig. 2.7. An important parameter for the increase (resp. decrease) of the high strain mobilities for the electrons (resp. holes) with temperature is the increase (resp. decrease) of the scattering rate variations with strain. The scattering rates to be

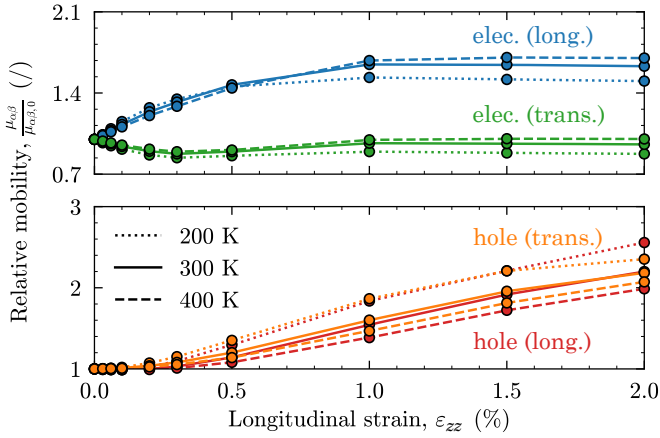


Fig. 2.16 Relative variations of the phonon-limited mobilities with respect to the longitudinal strain for the electrons (blue for the longitudinal component and green for the transverse one) and the holes (red for the longitudinal component and orange for the transverse one) for a temperature of 200 K (dotted lines), 300 K (continuous lines), and 400 K (dashed lines). The zero-strain mobility is taken as a reference to compute the relative variations.

considered are only those near the band edge where the carriers remain. With increasing temperature, the scattering rates further away from the band edges start to contribute to the mobility. Figure 2.17 shows the maps of electron and hole mobility as a function of temperature and uniaxial strain applied along the [001] crystal direction. The mobility curves in steps of 500 $cm^2V^{-1}s^{-1}$ clearly show the non-monotonic evolution for the transverse mobility and the saturation of the longitudinal component. Both hole mobility components show similar maps with small variations at low strain followed by a significant increase. The maps confirm that the relative mobility evolution with strain is almost independent of temperature for all components.

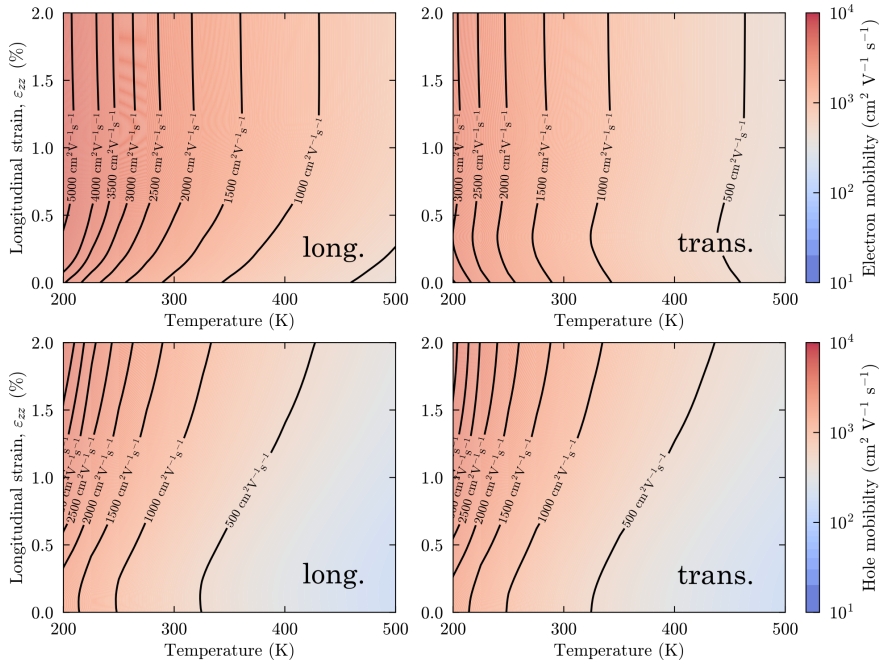


Fig. 2.17 Maps of the electron (top panels) and hole (bottom panels) mobility according to the temperature and the uniaxial strain applied along the [001] crystal direction. The longitudinal (long.) mobility, *i.e.*, along the [001] direction, and the transverse (trans.) mobility, *i.e.*, along the [010] direction, are shown in the left and right panels, respectively. A logarithmic color scale is used while contours every 500 $cm^2V^{-1}s^{-1}$ are shown with black solid lines.

2.2.4 Piezoresistive coefficients

Importantly, the linear behaviour of the mobility at low strain gives direct access to the piezoresistive coefficients. In the case of silicon, the π_{44} piezoresistive coefficient determines the resistivity variations under shear strain. The shear coefficient is important for the holes and has been well studied with values ranging from 1018 TPa^{-1} to 1381 TPa^{-1} at 300 K for lightly doped samples [45, 212, 213, 207, 214]. The π_{44} coefficients for the electron are less important than π_{11} and π_{12} with values ranging from -123 TPa^{-1} to -200 TPa^{-1} at 300 K for lightly doped samples [215, 45, 213]. Here this coefficient is not accessible with uniaxial strain along the [100] crystal direction. The two piezoresistive coefficients π_{11} and π_{12} for the holes have been much less studied, while few works [45, 213, 215] manage to obtain the coefficients for the electrons at low impurity concentration due to the challenge of producing low-doped samples. They can be calculated from the slope of the longitudinal and transverse mobility variations for holes and electrons respectively at low strain levels. In practice, the slope has been calculated from the mobility variations between 0%-strain and 0.03%-strain. The values of the hole (or electron) coefficient are 148 TPa^{-1} (resp. -989 TPa^{-1}) for π_{11} and -72 TPa^{-1} (resp. 502 TPa^{-1}) for π_{12}. The electron coefficients calculated from the experimental results are -632 TPa^{-1} and 403 TPa^{-1} for the longitudinal and transverse contributions, respectively.

The piezoresistive coefficients are less sensitive to temperature than the mobility, as shown in Fig. 2.18. They decrease from -1265 TPa^{-1} (resp. 170 TPa^{-1}) at 200 K to -816 TPa^{-1} (resp. 128 TPa^{-1}) at 400 K for the longitudinal coefficient and from 676 TPa^{-1} (resp. -84 TPa^{-1}) at 200 K to 411 TPa^{-1} (resp. -55 TPa^{-1}) at 400 K for the transverse coefficient for the electrons (resp. holes). Up to now the prediction of the temperature dependence of π_{11} and π_{12} has only been done relatively [179], *i.e.*, without calculating the exact value of the coefficients.

Previous experimental measurements of the piezoresistive coefficients for p-type and n-type silicon at low strain levels, *i.e.*, below 0.1%, are summarised in Table 2.3. Th first ones applied strain by hanging a weight directly on a silicon sample [45, 215] or on a cantilever with silicon resistance [213]. The stress applied on the samples (below 170 MPa) is then calculated from mechanical relation between the weight and the deformed structure. Later, four-point bending has been preferred [216] and strain has been measured with metallic strain gauge, as done in this work. The coef-

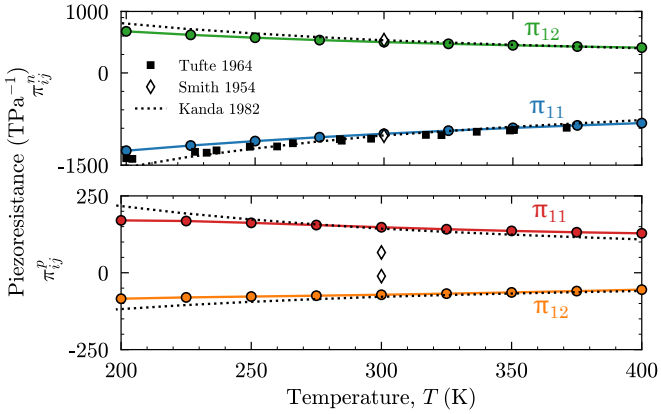


Fig. 2.18 Piezoresistive coefficients as a function of temperature. The coefficients are computed by finite difference between the results at zero strain and 0.03% in the longitudinal direction (blue for the electrons and red for the holes) and transverse direction (green for the electrons and orange for the holes). Experiments by Smith [45] and Tufte and Stelzer [215] are indicated with white diamonds and black squares, respectively. The theoretical model from Kanda [179] has been scaled using the piezoresistive values computed at 300 K, and is indicated with dotted lines.

ficients extracted from the first-principles results are in good agreement for electrons, but differ slightly for holes. We suspect that the impurity scattering resulting from the fabrication and doping processes introduces a bias to the experimental measurements [218, 219] in addition to the reduction of the measured coefficients [215, 213] as shown in Table 2.3. It has been shown that, despite the significant effect of doping on the zero-strain mobility [178, 180, 181, 177], the relative changes due to strain are much less sensitive to the level of doping when it is maintained at low or moderate levels [215, 179]. In addition, the small variations associated with the nonlinear behaviour of the hole mobility introduce greater uncertainty into the experimental measurements at low strain [213].

	n-Si		p-Si		Doping
	π_{11}	π_{12}	π_{11}	π_{12}	(cm^{-3})
Smith [45] (exp.)	−1022	534	66	−11	$5 \cdot 10^{14}$
Matsuda *et al.* [213] (exp.)	−840	430	-	-	$4 \cdot 10^{16}$
Tufte and Stelzer [215] (exp.)	−1077	-	-	-	$5 \cdot 10^{16}$
Cho *et al.* [216] (exp.)	−691	390	29	−6	10^{18}
This work (exp.)	−632	403	-	-	$5 \cdot 10^{17}$
Matsuda *et al.* [213] (th.)	−970	480	-	-	undoped
Dorey and Maddern [217] (th.)	-	-	213	−108	undoped
This work (th.)	−989	502	148	−72	undoped

Table 2.3 Piezoresistive coefficients for the holes (p-Si) and electrons (n-Si) of silicon determined experimentally (exp.) or theoretically (th.) in TPa^{-1}.

2.2.5 Impact of the doping

The semi-empirical model from Masetti *et al.* [177], that extends the work from Caughey and Thomas [220], is used to study the impact of impurities concentration on the phonon-limited mobility, and so the piezoresistive coefficient:

$$\mu_{li} = \mu_1 + \frac{\mu_l - \mu_1}{1 + (N_i/C_1)^{\gamma_1}} - \frac{\mu_2}{1 + (N_i/C_2)^{\gamma_2}}, \tag{2.30}$$

where μ_{li} is the mobility taking into account the impurity scattering, μ_l are the phonon-limited mobility computing using first principles and N_i is the impurity density. μ_k, C_k and γ_k are fitting parameters where $k = 1$ stands for moderated doping and $k = 2$ is for high-doping dependence. The values of the parameters from Masetti *et al.* [177] that are used in this work are summarised in Tab. 2.4.

Using Eq. (2.30) the electron and hole mobilities have been calculated taking into account the impurity densities N_i and the results are shown in Fig. 2.19. The phonon-limited mobility at 300 K in the absence of strain calculated from first principles has been used, *i.e.*, 1366 $cm^2V^{-1}s^{-1}$ for the electrons and 609 $cm^2V^{-1}s^{-1}$ for the holes. The hole mobility at zero strain

	μ_l (cm^2/Vs)	μ_1 (cm^2/Vs)	μ_2 (cm^2/Vs)	C_1 (cm^{-3})	C_2 (cm^{-3})	γ_1 (-)	γ_2 (-)
n-Si	1417	52.2	43.4	9.68e16	3.43e20	0.68	2.00
p-Si	470.5	44.9	29.0	2.23e17	6.10e20	0.719	2.00

Table 2.4 Semi-empirical parameters at 300 K used by Masetti *et al.* [177] to compute the mobility taking into account the impurity scattering in n-doped and p-doped silicon.

is overestimated by the theoretical calculation in this work, similarly to previous study [133]. The mobility results are compared with those of Masetti *et al.* [177], which assumes an undoped mobility μ_l of 1417 $cm^2V^{-1}s^{-1}$ for the electrons and 470.5 $cm^2V^{-1}s^{-1}$ for the holes. Experimental measurements from Irvin [221], Mousty *et al.* [222] and Thurber *et al.* [180, 181] are shown with dark and white markers for p-type and n-type silicon, respectively. These experimental results were used by Masetti *et al.* [177] to determine the parameters of the semi-empirical model at moderate doping.

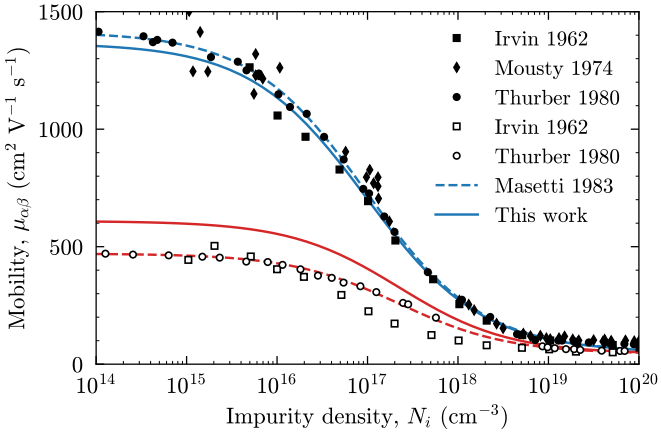


Fig. 2.19 Electron (blue) and hole (red) mobility according to the impurity density. The continuous and dashed curves are respectively computed analytically based on the model developed by Masetti *et al.* [177] and adapted with the lattice mobility μ_l of 1366 $cm^2V^{-1}s^{-1}$ for the electrons and 609 $cm^2V^{-1}s^{-1}$ for the holes, calculated theoretically at 300 K. The experimental results from Irvin [221], Mousty *et al.* [222] and Thurber *et al.* [180, 181] are shown with dark and white markers for p-type and n-type silicon, respectively.

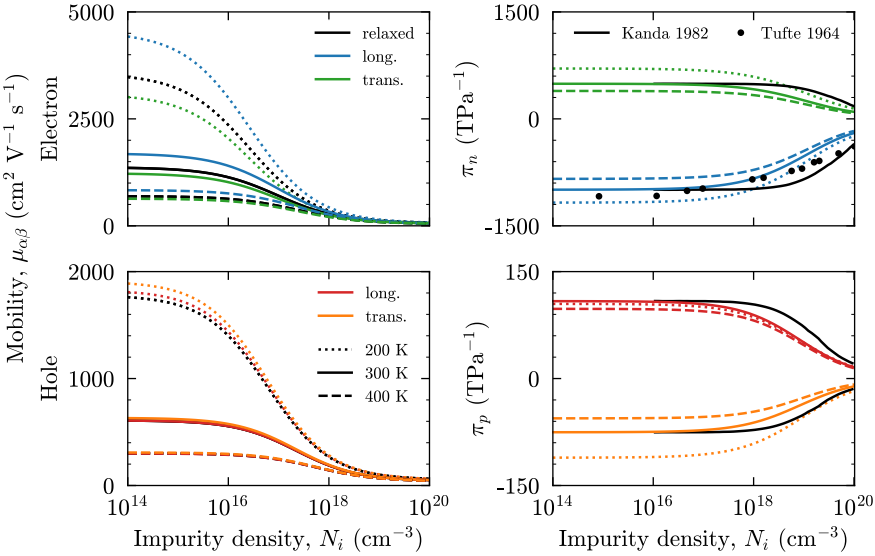


Fig. 2.20 Electron and hole mobility (left panels) according to the impurity density and the piezoresistive coefficients (right panels). The mobility results are shown for 0.2% uniaxial strain along the [001] direction (color curves) and without strain (grey curves). The piezoresistive coefficients have been computed by taking the finite difference between the mobility at 0% and 0.03%-strain. The longitudinal mobility and coefficient for the electrons (resp. holes) are shown in blue (resp. red) while the transverse ones are shown in green (resp. orange). The results are computed at 200 K (dotted lines), 300 K (solid lines) and 400 K (dashed lines). The theoretical results for the piezoresistive factor from Kanda [179] scaled by the coefficients at zero impurity are shown, as well as the experimental results from Tufte *et al.* [215] for the longitudinal coefficient of the electron mobility.

The results of the mobility and the piezoresistive coefficient with the impurity density at 200 K, 300 K and 400 K are shown in Fig. 2.20. The mobility results are shown for 0.2% uniaxial strain along the [001] direction. The piezoresistive coefficients have been calculated by taking the finite difference between the mobility at 0% and 0.03%-strain. They are found to be independent of the impurity concentration up to 10^{17} cm^{-3}, while the mobility starts to decrease at much lower densities. The theoretical results for the piezoresistive factor from Kanda [179] scaled by the coefficients at zero impurity are shown. They show a variation for the piezoresistive coefficient at even higher impurity densities, in contrast to the experimental re-

sults of Tufte *et al.* [215] for the longitudinal coefficient of electron mobility. Our results show good agreement with the experimental data at low and moderate impurity concentration, but the experiments still show a higher longitudinal coefficient at high doping.

The impact of doping can also be directly integrated in the Eph4mob [187] calculations from ABINIT [108] within the rigid band approximation. However, semi-empirical model has been preferred here to avoid additional calculation cost (each doping level bring a new set of calculations) and also to maintain coherence with TCAD software that uses model from Masetti *et al.* [177].

2.2.6 Mobility for uniaxial strain along [110] direction

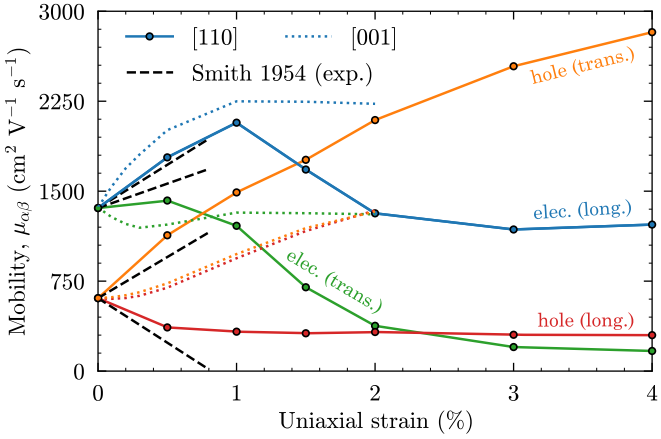


Fig. 2.21 Phonon-limited mobilities at 300 K as a function of the [110] uniaxial strain in the transverse (green for the electrons and orange for the holes) and longitudinal (blue for the electrons and red for the holes) directions of the applied stress. The results for uniaxial strain along [001] from section 2.2.3 are shown with dotted lines. The experimental linear model using the piezoresistive coefficients from Smith [45] for [110] strain is indicated with the dashed black lines.

The method calculating theoretically the phonon-limited mobility has been used to retrieve the electron and hole mobilities under uniaxial strain along [110] for undoped silicon. Indeed, this strain configuration leads to the highest band gap reduction among the uniaxial strain directions stud-

ied. It has therefore been chosen to improve the optical properties of silicon for the detection of IR light.

Figure 2.21 shows the results obtained for [110] uniaxial strain up to 4%. The longitudinal and transverse direction are respectively along the [110] and [$\bar{1}$10] crystal directions. The results for the hole mobilities are monotonic with an important increase for the transverse component and a decrease for the longitudinal one. The zero-strain mobility of 608 $cm^2V^{-1}s^{-1}$ decreases and stabilises down to 328 $cm^2V^{-1}s^{-1}$ at 1%-strain for the longitudinal component. On the opposite, the transverse component increase up to 1490 $cm^2V^{-1}s^{-1}$ at 1% and even reaches 2825 $cm^2V^{-1}s^{-1}$ at 4%. The longitudinal component for the electron mobility shows a non-monotonic trend, reaching a maximal value of 2071 $cm^2V^{-1}s^{-1}$ at 1%-strain, while the transverse one show first small changes before dropping down to 168 $cm^2V^{-1}s^{-1}$ at 4%-strain. The mobility variations obtained for uniaxial strain along [110] is significantly different than the variations calculated in section 2.2.3 for [001] uniaxial strain, as shown in Fig. 2.21.

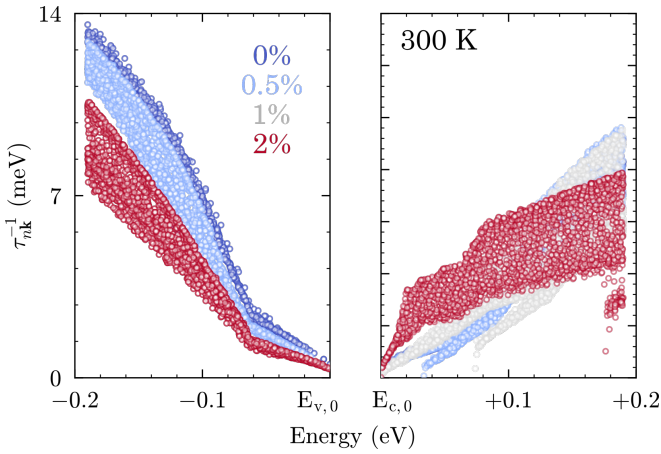


Fig. 2.22 Scattering rates for all relevant **k** points at 300 K under strain ranging from 0% (blue) to 2% (red). The panels show the hole (left) and electron (right) scattering rates. The minimum and maximum of the conduction and valence bands are indicated by $E_{c,0}$ and $E_{v,0}$, respectively.

Figure 2.22 shows the results for the scattering rates $\tau_{n\mathbf{k}}$ calculated on a $150 \times 150 \times 150$ grid at each **k** point 200 meV away from the band edges. For the holes, it has been shown previously that the scattering is dominated

by the intraband HH. With increasing strain, this scattering decreases, leading to an increase of the transverse component for the hole mobility. This is enhanced by the increase in effective mass along [$\bar{1}$10] due to strain, as shown in chapter 1. On the contrary, the longitudinal component decreases due to the large reduction of the effective mass along [110], which counteracts the scattering reduction.

For the electrons, the scattering and especially the intravalley scattering, which dominates at lower strain, increases with strain. Figure 2.23 shows the band structure under [110] uniaxial strain, showing the flattening of the Δ_2-valleys with strain that increases the intravalley scattering. Furthermore, the valleys move closer to the edge of the Brillouin zone, increasing intervalley scattering between equivalent Δ_2-valleys. This tends to decrease the mobility. The Δ_2-valleys along [001] decrease with strain, while the Δ_4-valleys along [100] and [010] increase. This causes the electrons to migrate to the lower energy Δ_2-valleys, so that the transport mechanism along [110] (longitudinal) and [$\bar{1}$10] is mainly influenced by the transverse mobility. The initial increase or plateau in the electron mobility can thus be explained by the reduction in the influence of the Δ_4-valleys and the associated large longitudinal effective mass.

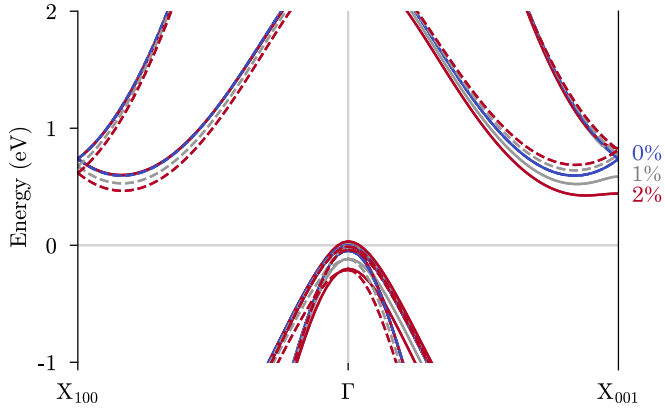


Fig. 2.23 Band structure for silicon strained at 0% (blue), 1% (grey) and 2% (red) along [110] (solid lines) and [001] (dashed lines).

2.3 Chapter Summary

In this chapter the mobility variations due to strain have been studied both experimentally and theoretically in silicon. The lack of experimental work on electron mobility under [001] uniaxial strain was filled by measurements on an n-type silicon resistor using a four-point bending scheme to obtain the resistance variations with strain up to 1%. The results showed the limitations of the linear model of Smith [45] to describe the mobility evolution at high strain, while demonstrating the underestimation and lack of accuracy of recent models which take the non-linearity into account. A detailed study of the effect of strain on the phonon-limited mobility was then carried out using state-of-the-art first-principles calculations. They take into account the electron-phonon interactions and solve iteratively the Boltzmann transport equation (BTE) to retrieve the mobility. This allows an in-depth understanding of the effect of strain by looking at the band structure variations and scattering rates. Under uniaxial strain along [001], the mobility is no longer isotropic and the longitudinal component of the electron mobility shows an important increase up to 2249 $cm^2V^{-1}s^{-1}$ at 1%-strain, mainly due to the reduction of the intervalley scattering. On the contrary, the transverse component first shows a decrease due to the migration of the electrons in the lower energy valley, as the reduction of the intervalley scattering causes the increase of the mobility starting from 0.3%-strain to finally stabilise at 1321 $cm^2V^{-1}s^{-1}$ at 1%-strain. Our results show for the first time the important increase of the hole mobility, which contradicts the intuition given by the small variations observed at low [001] strain. The longitudinal and transverse components even reach 1340 $cm^2V^{-1}s^{-1}$ and 1330 $cm^2V^{-1}s^{-1}$, respectively, close to the zero-strain mobility of the electrons. For [110] strain, the transverse component for the hole mobility shows a strong increase of 1761 $cm^2V^{-1}s^{-1}$ at 2%-strain, while the longitudinal one decrease down to 328 $cm^2V^{-1}s^{-1}$ at 1%-strain with little evolution beyond this point. The increase in intravalley scattering tends to reduce the electron mobility at high strain, giving 1221 $cm^2V^{-1}s^{-1}$ and 168 $cm^2V^{-1}s^{-1}$ for the longitudinal and transverse components at 2%-strain, respectively. The theoretical method using first principles could be easily generalised to any semiconductor material and for any strain configuration, allowing a more fundamental understanding of the mobility.

Key messages of the chapter

- Four-point bending measurements up to 1%-strain on n-type silicon beams show the limitations of the linear model, which can only describe the mobility at low strain, while other semi-empirical models underestimate the electron enhancement obtained with strain. Furthermore, such models exist only for the electron mobility and not for the holes.
- Modern first-principles approaches are now capable of accurately predicting the phonon-limited mobility in strained silicon. Although the computational cost is still high, the calculations could lead to new discoveries in strain engineering, such as the strong enhancement of the hole mobility for uniaxial strain along [001] and the dominance of heavy hole (HH) intraband scattering.
- The origin of the piezoresistive effect is a combination of several phenomena. At low strain, the migration of electrons in the lower energy valleys and their respective effective masses dominate the mobility variations with strain. At higher strains, the evolution of the intravalley scattering plays an important role, but is kept constant under uniaxial strain along [001], since no variations in the valley shapes are induced. On the other hand, uniaxial strain along [110] significantly increases the intravalley scattering due to the important change in the valley shapes, reducing the electron mobility.
- Even though the impurity density strongly reduces the mobility, the relative sensitivity to strain is maintained at low and moderate doping levels, *i.e.*, below 10^{17} cm^{-3}.

3

Optical properties of strained silicon

The optical absorption of silicon and bulk materials has been extensively studied, particularly in the field of photovoltaic cells [223, 224]. However, the effect of strain on optical properties remains largely unexplored, especially at higher strains. Only recently have first-principle studies for phonon-assisted absorption succeeded in accurately predicting the indirect absorption in silicon [225, 226]. The reason for the lack of theoretical work is mainly due to the high complexity of the electron-phonon interactions. The computational cost is high due to the double sum in the first Brillouin zone to predict all possible transitions between the initial and final states. Semi-empirical work has the advantage of being much cheaper than *ab initio* methods, but lacks the physical consistency and robustness to predict complex behaviour [227, 228, 229]. In this chapter, a complete set of first-principles calculations is performed to obtain the optical properties of highly strained silicon in the [110] crystal direction. The dielectric function and refractive index are first studied under the Bethe-Salpeter equation (BSE) formalism, taking into account the electron-hole interactions. The EPW code is then used to obtain the absorption coefficient of strained silicon by explicit calculation of the electron-phonon interactions. Finally, the results are compared with the semi-empirical model developed by Tsai [230], which uses the fundamental parameters calculated in chap-

ter 1.

3.1 First-principles computation scheme

The theory behind the first-principles calculation is summarised in this section. We begin by describing the optical properties to be calculated, *i.e.*, the dielectric function, the complex refractive index and the absorption coefficient. The BSE method used for the refractive index and the dielectric function is described in detail, taking into account the electron-hole interaction. Finally, the theoretical calculations for indirect absorption that takes into account the electron-phonon interaction using the EPW code and the analytical model of Tsai [230] are explained.

3.1.1 Description of the optical properties

The explanation to describe the dielectric function are explained in details by Onida *et al.* [105], including the BSE formalism. Only the main relations of interest for understanding the theoretical background are included here.

Standard KS ground-state calculations only consider single-particle system that can not predict correctly the response to perturbations such as light. To consider it, many-particle interactions have to be considered with electron-hole interactions, caused by the electron-hole pairs created by the light excitation. The response of the crystal system to an external potential can be expressed using the dielectric matrix $\varepsilon(\mathbf{r}, \mathbf{r}'; \omega)$ such as

$$V_{tot}(\mathbf{r}; \omega) = \int d\mathbf{r}' \varepsilon^{-1}(\mathbf{r}, \mathbf{r}'; \omega) V_{ext}(\mathbf{r}'; \omega), \tag{3.1}$$

with $V_{tot}(\mathbf{r}; \omega)$ the screened (total) potential modified according to the external potential $V_{ext}(\mathbf{r}; \omega)$. The total potential is thus the sum of the external potential and the one due to the polarization of the system under the external stimulus (light). The dielectric function $\varepsilon(\mathbf{r}, \mathbf{r}'; \omega)$ is thus used to analyse the response of the material to an external potential of angular frequency ω. The dielectric function in real space for an electron system can be expressed as [231]:

$$\varepsilon(\mathbf{r}, \mathbf{r}'; \omega) = \delta(\mathbf{r}, \mathbf{r}') - \int d\mathbf{r}'' v(\mathbf{r} - \mathbf{r}'') \Pi(\mathbf{r}'', \mathbf{r}'; \omega), \tag{3.2}$$

where v is the bare Coulomb interaction and $\Pi(\mathbf{r}'', \mathbf{r}'; \omega)$ is the polarizability operator introduced. A simple approximation of $\Pi(\mathbf{r}'', \mathbf{r}'; \omega)$ is the random-phase approximation for which independent particles are considered and their transition is independently added up [232].

In a solid, a macroscopic dielectric function $\varepsilon_M(\omega)$ has to be used for experimental observation and is defined in a periodic crystal as:

$$\varepsilon_M(\omega) \equiv \lim_{\boldsymbol{\lambda}\to 0} \frac{1}{\varepsilon^{-1}_{\mathbf{G}=0,\mathbf{G}'=0}(\boldsymbol{\lambda};\omega)}, \tag{3.3}$$

where $\varepsilon_{\mathbf{G},\mathbf{G}}(\boldsymbol{\lambda};\omega) = \varepsilon(\boldsymbol{\lambda}+\mathbf{G}, \boldsymbol{\lambda}+\mathbf{G}';\omega)$ is the Fourier transform to reciprocal space of $\varepsilon(\mathbf{r}, \mathbf{r}';\omega)$, $\mathbf{G}$ is a reciprocal lattice vector, and $\boldsymbol{\lambda}$ is the photon momentum.

The complex refractive index γ is defined as the square root of the dielectric function, *i.e.*, $\gamma = \sqrt{\varepsilon_M}$. The real part of the index, written n, describes the propagation of the wave in a medium, while the imaginary part, written κ, describes the absorption of the medium. Their expressions are given by

$$\begin{aligned} n(\omega) &= \sqrt{\frac{\sqrt{\varepsilon_1(\omega)^2+\varepsilon_2(\omega)^2}+\varepsilon_1(\omega)}{2}}, \\ \kappa(\omega) &= \sqrt{\frac{\sqrt{\varepsilon_1(\omega)^2+\varepsilon_2(\omega)^2}-\varepsilon_1(\omega)}{2}}, \end{aligned} \tag{3.4}$$

with $\varepsilon_1(\omega)$ and $\varepsilon_2(\omega)$ the real and imaginary part of the dielectric function $\varepsilon_M(\omega)$, respectively. $\varepsilon_1(\omega)$ and $\varepsilon_2(\omega)$ are given relatively to the vacuum permittivity ε_0. The refractive index $\gamma(\omega)$ describes the propagation and absorption in real space (x) of an electromagnetic field $\mathbf{E}(x,t)$ [233]:

$$\mathbf{E}(x,t) = \mathbf{E}_0 e^{i(\frac{2\pi\gamma(\omega)}{\lambda}x-\omega t)}, \tag{3.5}$$

where $\mathbf{E}_0$ is the amplitude of the wave, ω its frequency and λ its wavelength. By developing explicitly the expression with the real and imaginary part of the index, the attenuation part is clearly visible in the shape of a real exponential terms:

$$\mathbf{E}(x,t) = \mathbf{E}_0 e^{-\frac{\alpha(\omega)}{2}x} e^{i(\frac{2\pi n(\omega)}{\lambda}x-\omega t)}. \tag{3.6}$$

In which the absorption coefficient α can finally be described as:

$$\alpha(\omega) = \frac{4\pi}{\lambda}\kappa(\omega). \tag{3.7}$$

3.1.2 BSE method for direct transitions

A two-particle equation is needed to account for electron-hole interactions in the response function, such as the BSE, which is found using Green's function theory [234]. It requires first the calculation of quasi-particle correction and screened interactions W from the many-body interaction (via GW). Then, the kernel K mixing the independent transitions [235, 105] is calculated. Formally, this is described by the two-particle Hamiltonian $H^{2p}_{(n_1n_2),(n_3n_4)}$ for particles going from states (n_1n_2) to states (n_3n_4) due to light excitation:

$$H^{2p}_{(n_1n_2),(n_3n_4)} = (\varepsilon_{n_2} - \varepsilon_{n_1})\delta_{n_1n_3}\delta_{n_2n_4} + (f_{n_1} - f_{n_2})K_{(n_1n_2),(n_3n_4)}, \tag{3.8}$$

where $K_{(n_1n_2),(n_3n_4)}$ is the Kernel describing the two-particles interactions, ε_{n_i} is the energy of state n_i, and f_{n_i} is Fermi occupation numbers. For the sake of clarity, the indices $n\mathbf{k}_i$, describing a possible state, are indicated with indices n_i. Furthermore, the double states (n_in_j) are always composed of one empty and one occupied states.

The Kernel $K_{(n_1n_2),(n_3n_4)}$ is expressed as

$$K_{(n_1n_2),(n_3n_4)} = \delta_{n_1n_2}\delta_{n_3n_4}\overline{v}_{n_1n_3} - \delta_{n_1n_3}\delta_{n_2n_4}W_{n_1n_2} \tag{3.9}$$

where $W_{n_1n_2}$ is the screened interactions calculated using MBPT (GW). The exchange term taking into account the screened electron-hole interaction is associated to the modified Coulomb interaction $\overline{v}_{n_1n_3}$ defined as

$$\overline{v}(\boldsymbol{\lambda}) = \begin{cases} 0 & \text{if } \boldsymbol{\lambda} = 0, \\ \frac{4\pi}{|\boldsymbol{\lambda}+\mathbf{G}|^2} & \text{otherwise} \end{cases} \tag{3.10}$$

The macroscopic dielectric function is then given by

$$\varepsilon_M(\omega) = 1 - \lim_{\boldsymbol{\lambda}\to 0} v(\boldsymbol{\lambda}) \sum_{(n_1n_2)} \sum_{(n_3n_4)} \langle n_1|e^{-i\boldsymbol{\lambda}\cdot\mathbf{r}}|n_2\rangle \left[H^{2p} - I\omega\right]^{-1}_{(n_1n_2),(n_3n_4)} \times (f_{n_4} - f_{n_3}) \langle n_4|e^{i\boldsymbol{\lambda}\cdot\mathbf{r}'}|n_3\rangle., \tag{3.11}$$

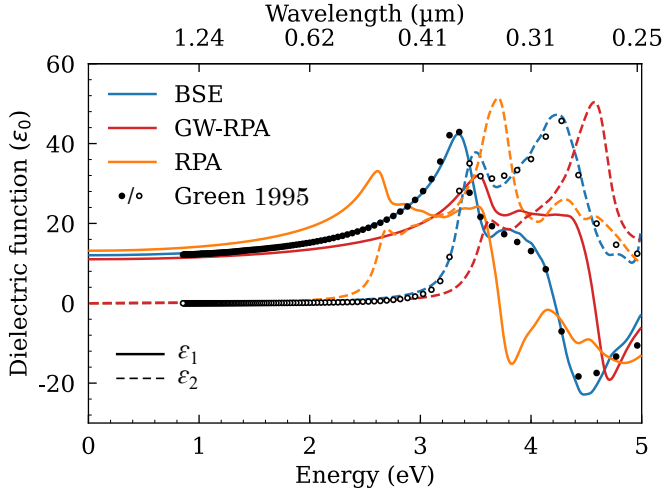


Fig. 3.1 Dielectric function in unit of vacuum permittivity ε_0 computed theoretically with random-phase approximation (RPA), random-phase approximation with quasiparticle correction using GW (GW-RPA), and considering electron-hole interaction with BSE. The real and imaginary parts of the dielectric function are shown with solid and dashed lines, respectively. Experimental data from Green and Keevers [236] for the real and imaginary components are indicated with black and white dots, respectively.

In practice, the first-principles scheme to calculate the dielectric function starts by a ground-state DFT calculation. Then a GW calculation is performed to correct the eigenvalues. Finally, we solve the Bethe-Salpeter equation (BSE) using GW eigenvalues, KS orbitals and static RPA screening for the electron-hole interactions, as implemented in ABINIT [108]. Figure 3.1 shows the results of the first-principles calculation of the dielectric function under the different approximations for silicon in the absence of strain. As expected, the RPA calculation underestimates the optical threshold due to the underestimation of the band gap in the DFT calculation. The quasi-particle correction using GW addresses this problem, but does not improve anything further. In contrast, the BSE calculations show an important correction of the optical spectrum, especially for the imaginary part, showing the strong excitonic character of the silicon spectrum. Excellent agreement was obtained with experimental data from Green and

Keevers [236]. A common problem using BSE is the difficulty in achieving global convergence to the full spectrum, leading to reduced accuracy beyond 4.5 eV [237].

3.1.3 EPW method for indirect transitions

The indirect band gap of silicon allows light to be absorbed by interband transitions for photon energies greater than the fundamental band gap of 1.13 eV at 300 K (wavelengths less than 1.1 μm) [238]. Such indirect transitions require additional momenta provided by lattice vibrations, *i.e.*, phonons [225]. This phonon-assisted process dominates the absorption spectrum of silicon in the energy region between the fundamental and direct band gaps. For energies larger than the direct band gap, the absorption increases rapidly and is dominated by direct interband transitions. Despite the importance of the subject, there are only few theoretical calculations of the indirect absorption spectrum of silicon [225, 226, 230, 239], mainly because of the complexity of the interactions between electrons and phonons [209]. Only recently, first-principles calculations of phonon-assisted absorption have been able to quantitatively describe the absorption spectrum of silicon [225, 226]. However, while these first-principles calculations give accurate results, the computational cost is very high.

While the BSE method correctly treats the electron-holes interactions, it is only valid for direct transitions and failed to correctly predict the absorption of indirect band gap semiconductors. The EPW code has been developed to calculate electron-phonon interactions and related properties, including optical properties [240, 183]. In EPW, Wannier functions are used to calculate the electron-phonon interactions on a dense mesh in the first Brillouin zone [241, 242]. The electronic properties are calculated using standard DFT calculations, while DFPT is used for the phonon properties. In practice, the imaginary part of the dielectric function is calculated for all possible phonon wavevectors $\mathbf{q}$ and electron wavevectors $\mathbf{k}$ as follows

$$\begin{aligned}\varepsilon_2(\omega) = 2\frac{4\pi e^2}{V_{cell}}\frac{1}{\omega^2} \\ \sum_{mn\nu,\beta=\pm1}\int\frac{d\mathbf{k}}{\Omega_{\mathrm{BZ}}}\int\frac{d\mathbf{q}}{\Omega_{\mathrm{BZ}}}\left|\boldsymbol{\lambda}\cdot\left[\mathbf{S}_{1,mn\nu}(\mathbf{k},\mathbf{q})+\mathbf{S}_{2,mn\nu\beta}(\mathbf{k},\mathbf{q})\right]\right|^2 \\ \times P_{nm\nu\beta}(\mathbf{k},\mathbf{q})\delta(\varepsilon_{m\mathbf{k}+\mathbf{q}}-\varepsilon_{n\mathbf{k}}-\hbar\omega+\beta\hbar\omega_{\mathbf{q}\nu}),\end{aligned} \quad (3.12)$$

where e is the electron charge, $\boldsymbol{\lambda}$ is the polarisation vector of light with photon energy $\hbar\omega$, and β is equal to 1 for phonon absorption and -1 for phonon emission. V_{cell} and Ω_{BZ} are the volume of the primitive cell and the first Brillouin zone, respectively. $\mathbf{S}_{1,mn\nu}$ and $\mathbf{S}_{2,mn\nu\beta}$ represent the two possible paths for the transition of an electron $\psi_{n\mathbf{k}}$ with energy $\varepsilon_{n\mathbf{k}}$ into the state $\psi_{m\mathbf{k}+\mathbf{q}}$ with energy $\varepsilon_{m\mathbf{k}+\mathbf{q}}$, with a phonon of mode ν and wavevector $\mathbf{q}$ of energy $\hbar\omega_{\mathbf{q}\nu}$. $\mathbf{S}_{1,mn\nu}$ considers a path starting with the excitation of the electron at the same wavevector $\mathbf{k}$, followed by a relaxation to the new position $\mathbf{k}+\mathbf{q}$. On the contrary, $\mathbf{S}_{2,mn\nu\beta}$ first considers the phonon interactions followed by the excitation at higher energy.

They are computed as

$$\begin{aligned}\mathbf{S}_{1,mn\nu}(\mathbf{k},\mathbf{q}) &= \sum_j \frac{g_{mj\nu}(\mathbf{k},\mathbf{q})p_{jn}(\mathbf{k})}{\varepsilon_{j\mathbf{k}}-\varepsilon_{n\mathbf{k}}-\hbar\omega+i\eta},\\ \mathbf{S}_{2,mn\nu\beta}(\mathbf{k},\mathbf{q}) &= \sum_j \frac{p_{mj}(\mathbf{k}+\mathbf{q})g_{jn\nu}(\mathbf{k},\mathbf{q})}{\varepsilon_{j\mathbf{k}+\mathbf{q}}-\varepsilon_{n\mathbf{k}}+\beta\hbar\omega_{\mathbf{q}\nu}+i\eta},\end{aligned} \tag{3.13}$$

where $g_{mn\nu}(\mathbf{k},\mathbf{q})$ is the electron-phonon matrix element, η is the broadening parameter, $p_{ij}(\mathbf{k})$ is the dipole matrix element.

The occupancy $P_{nm\nu\beta}(\mathbf{k},\mathbf{q})$ is given by

$$\begin{aligned}P_{nm\nu\beta}(\mathbf{k},\mathbf{q}) = &\left(n_{\mathbf{q}\nu}+\frac{1+\beta}{2}\right)f^0_{n\mathbf{k}}(1-f^0_{m\mathbf{k}+\mathbf{q}})\\ &-\left(n_{\mathbf{q}\nu}+\frac{1-\beta}{2}\right)(1-f^0_{n\mathbf{k}})f^0_{m\mathbf{k}+\mathbf{q}},\end{aligned} \tag{3.14}$$

where $n_{\mathbf{q}\nu} = 1/\left[\exp(\hbar\omega_{\mathbf{q}\nu}/k_{\mathrm{B}}T)-1\right]$ is the Bose-Einstein distribution evaluated at the phonon energy $\hbar\omega_{\mathbf{q}\nu}$ and $f^0_{n\mathbf{k}}$ is the electronic occupation distribution at the band energy $\varepsilon_{n\mathbf{k}}$.

Very recently, Tiwari *et al.* [243] has developed a new global framework to calculate both direct and indirect absorptions by including electron-phonon correlation via quasidegenerate MBPT.

3.1.4 Analytical model for the absorption coefficient

Tsai derived a theoretical model to calculate the indirect absorption coefficient based on the second-order time-dependent perturbation theory [230].

The model considers all possible types of intervalley scattering processes for the indirect transitions but is based on parabolic band approximation. These transitions are highlighted in Fig. 3.2 with the band structure of relaxed silicon. Such indirect light absorption occurs either by absorption of a photon (represented by blue arrows) followed by absorption or emission of a phonon (represented by red wavy arrows), or vice versa. For each

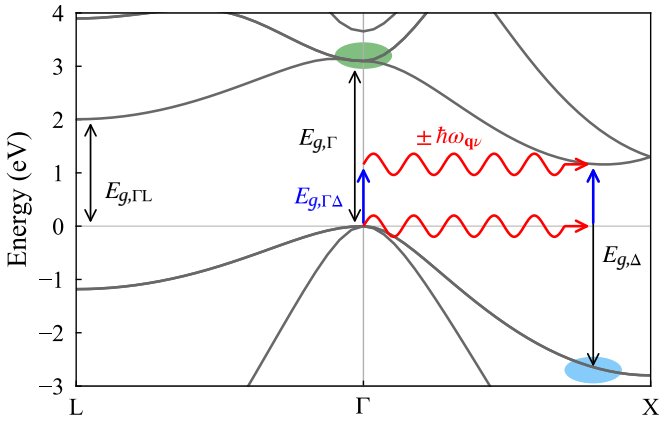


Fig. 3.2 Electronic band structure of silicon. Two possible absorption routes for the indirect light absorption are represented by blue (photon absorption) and red (phonon absorption or emission) arrows. The phonon energy is $\hbar\omega_{\mathbf{q}\nu}$. The intermediate states are highlighted by green and blue areas, and the important band gaps for indirect transitions between different $\mathbf{k}$ points are represented by vertical arrows. The zero energy is located at the valence band maximum.

valley of the conduction band where the electrons might be scattered, two intermediate states are considered. The first one (in green in Fig. 3.2) is located at Γ in the conduction band, and the second one (in blue in Fig. 3.2) is located in the valence band, at the high-symmetry $\mathbf{k}$-point (denoted by Δ in the following) where the minimum of the electron valley is located. For a given transition connecting two valleys through a phonon of wavevector $\mathbf{q}$ and mode ν, the absorption coefficient derived by Tsai is given by [230]

$$\alpha_{\mathbf{q}\nu}(\omega) = \frac{AN_{\text{val}}}{\hbar\omega\,\hbar\omega_{\mathbf{q}\nu}} \left[\frac{n_{\mathbf{q}\nu}(\hbar\omega - E_g + \hbar\omega_{\mathbf{q}\nu})^2}{|E_{g1} - \hbar\omega - i\eta|^2} H(\hbar\omega - E_g + \hbar\omega_{\mathbf{q}\nu}) \right.$$
$$+ \frac{(n_{\mathbf{q}\nu}+1)(\hbar\omega - E_g - \hbar\omega_{\mathbf{q}\nu})^2}{|E_{g1} - \hbar\omega - i\eta|^2} H(\hbar\omega - E_g - \hbar\omega_{\mathbf{q}\nu})$$
$$+ \frac{n_{\mathbf{q}\nu}(\hbar\omega - E_g + \hbar\omega_{\mathbf{q}\nu})^2}{|E_{g2} - \hbar\omega - i\eta|^2} H(\hbar\omega - E_g + \hbar\omega_{\mathbf{q}\nu})$$
$$\left. + \frac{(n_{\mathbf{q}\nu}+1)(\hbar\omega - E_g - \hbar\omega_{\mathbf{q}\nu})^2}{|E_{g2} - \hbar\omega - i\eta|^2} H(\hbar\omega - E_g - \hbar\omega_{\mathbf{q}\nu}) \right], \tag{3.15}$$

where N_{val} is the number of degenerate conduction valleys, E_g is the indirect band gap (fundamental or not, depending on the valley considered), E_{g1} and E_{g2} are the direct band gap energies providing intermediate states (e.g. $E_{g,\Gamma}$ and $E_{g,\Delta}$ in Fig. 3.2), η is a damping factor, and $n_{\mathbf{q}\nu} = 1/\left[\exp(\hbar\omega_{\mathbf{q}\nu}/k_{\text{B}}T) - 1\right]$ is the Bose-Einstein distribution evaluated at the phonon energy $\hbar\omega_{\mathbf{q}\nu}$. The material-dependent proportionality constant A is defined as

$$A = \frac{e^2 \text{m}_c^{3/2} \text{m}_v^{3/2} E_p D_{\mathbf{q}\nu}^2}{96\pi^2\hbar^3 \text{m}_{\text{e}} c\varepsilon_0 n_r \rho_L}, \tag{3.16}$$

where e is the electron charge, m_{e} is the free electron mass, c is the speed of light in vacuum, ρ_L is the material density, n_r is the refractive index, E_p is an energy parameter for the electron-photon interactions, $D_{\mathbf{q}\nu}^2$ is the phonon deformation potential, and m_c and m_v are the DOS effective masses of the conduction and valence bands, respectively.

There are different indirect transitions to consider in silicon, corresponding to different valleys of the conduction band. Each of them gives a different contribution to the total absorption coefficient,

$$\alpha_{tot} = \sum_{\nu} \alpha_{\nu}, \tag{3.17}$$

where α_ν is the absorption for each phonon mode ν. In relaxed silicon, the only contribution to the absorption of infrared light ($\lambda > 750$ nm) comes from the transitions in the Δ-valleys, where the conduction band minimum of silicon lies. The indirect band gap $E_{g,\Gamma\Delta}$ is 1.13 eV and the valleys are six-fold degenerate. In the case of relaxed silicon, only the contributions

Parameters	Value
n_r	3.42
ρ_L	2.328 g/cm^3
m_c	0.32 $\mathrm{m_e}$
m_v	0.89 $\mathrm{m_e}$
T	300 K
E_p	6 eV
η	1.1 eV
E_Γ	3.2 eV
$E_{\Gamma\Delta}$	1.13 eV
E_Δ	4 eV
D_{TA}	4.1×10^8 eV/cm
D_{TO}	1.2×10^9 eV/cm
D_{LO}	2.2×10^9 eV/cm

Table 3.1 Physical parameters used to compute the indirect absorption coefficient of relaxed silicon. Values of n_r is taken from [230] while the values for the deformation potential $D_{\mathbf{q}\nu}$ are taken from [245]. E_p and η are fitted parameters computed based on the zero-strain absorption coefficient.

from the six degenerate Δ-valleys need to be included, and only three gaps need to be considered in Eq. (3.15): the direct band gaps at Γ and Δ ($E_{g,\Gamma}$ and $E_{g,\Delta}$, respectively) and the fundamental gap $E_{g,\Gamma\Delta}$, see Fig. 3.2. For the indirect transitions different phonon modes ν have to be considered. In silicon there are 6 modes that should be considered. Following Ridley [244], Tsai [230] included only the TO and TA modes. However, it has been shown by Vandenberghe *et al.* [245] that the deformation potential for the LO mode is far from negligible, while the LA mode can be safely ignored. Therefore, we also include the contribution of the LO mode and use these deformation potentials, evaluated at the $\mathbf{q}$ point connecting the valence band maximum to the conduction band minimum ($\mathbf{q} = \Delta$), given in Tab. 3.1.

Figure 3.3 shows the absorption spectrum obtained for silicon in the absence of strain using the parameters from Tab. 3.1. E_p and η have been determined by fitting the zero-strain coefficient, giving values of 6 eV and 1.1 eV, respectively. Close to the band gap of 1.13 eV, the results show the importance of considering the contribution of the LO mode for a better description of the absorption shape. Indeed, this mode dominates the absorption coefficient spectrum close to the band gap and should not be neglected, especially in the region of interest for NIR applications. The

results are compared with those obtained from our EPW calculations and show good agreement with it. The analytical model has the advantage of reducing the computational cost compared to the EPW method, but requires semi-empirical parameters such as E_p and η, making it more difficult to accurately predict new configurations for which not all parameters are known. To evaluate this model, the data from Green and Keevers [236] for the absorption coefficient of silicon is also shown in Fig. 3.3. This data set is usually used as a reference for silicon absorption to compare and check the validity of different absorption models.

The DOS effective mass m_v for the valence bands is defined as the one which gives the same DOS as if the band were parabolic. In the case of the valence band it is obtained by [198, 199]

$$\frac{\sqrt{\pi}}{2}\frac{1}{2\pi^2}\left(\frac{2\mathrm{m}_v}{\hbar^2}\right)^{3/2}(k_\mathrm{B}T)^{3/2} = \int_{-\infty}^{E_v} g(E)\exp\left(-\frac{E_v - E}{k_\mathrm{B}T}\right)dE, \qquad (3.18)$$

where E_v is the energy of the valence band maximum and $g(E)$ is the den-

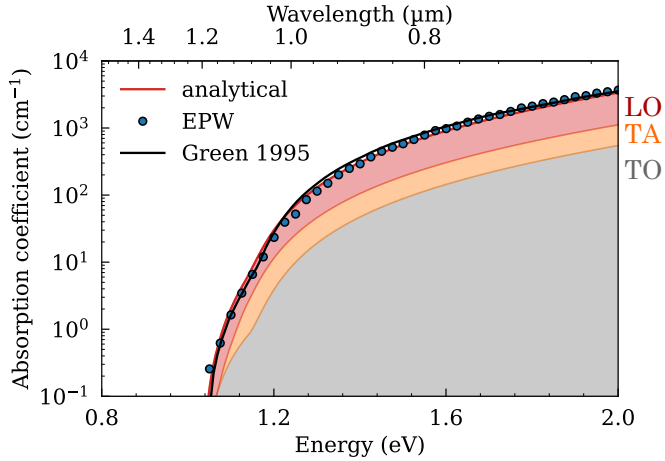


Fig. 3.3 Absorption coefficient computed analytically using parameters found by DFT (solid colored line) and coefficient computed theoretically using EPW code (blue dots). The contributions of the TO (grey), TA (orange) and LO (red) modes to the absorption coefficient are shown by filled area. The theoretical curves are compared with the absorption coefficient measured experimentally by Green and Keevers [236] (dark continuous line).

sity of states obtained on dense meshes for each strained configuration. A similar expression applies to the conduction band. Even for the electron, the DOS effective mass has to be calculated using the integrative method, since the valleys are no longer parabolic under high uniaxial strain along the [110] direction.

3.1.5 Computation scheme

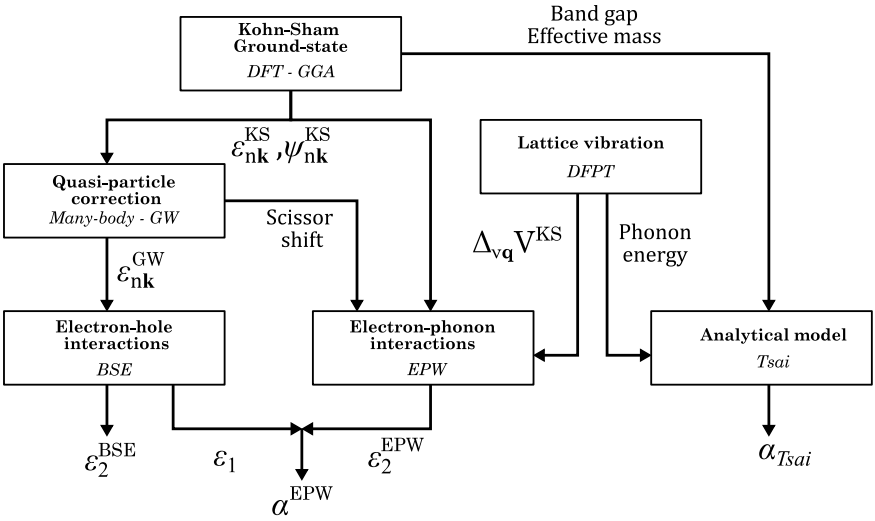


Fig. 3.4 Computation scheme for the real (ε_1) and imaginary (ε_2) part of the macroscopic dielectric function using first principles. KS wavefunctions ($\psi^{KS}_{n\mathbf{k}}$) and eigenvalues ($\varepsilon^{KS}_{n\mathbf{k}}$) are first computed and corrected using GW method before being used in BSE calculations, taking into account the electron-hole interaction for the dielectric function. The real part of the dielectric function is then used along KS eigenvalues corrected by a scissor shift (quasi-particle correction at band gap position) to find the imaginary part of the dielectric function with EPW code, taking into account the electron-phonon interactions.

Figure 3.4 shows the calculation scheme for the dielectric function. The KS wavefunction $\psi^{KS}_{n\mathbf{k}}$ with energy $\varepsilon^{KS}_{n\mathbf{k}}$ is computed using DFT ground-state calculations as implemented in ABINIT [108, 109]. We use norm-conserving pseudopotentials from PSEUDODOJO [110], in the GGA of PBE [98]. The results are then corrected using MBPT (GW), yielding

new set of energy $\varepsilon_{n\mathbf{k}}^{\mathrm{GW}}$. A first dielectric function taking into account the electron-hole interaction is calculated using the BSE, but only for the direct transition. The electron-phonon interactions are calculated with the EPW code to treat the indirect transition of the absorption. In practice, the phonon contribution is calculated using DFPT. The EPW code then computes the electron-phonon matrix $g_{mnv}(\mathbf{k}, \mathbf{q})$, which is used to calculate the imaginary part ε_2 of the dielectric function. The energy of the conduction bands from the ground-state calculation is shifted by a scissors shift calculated from the GW calculation to correct for the underestimation of the band gap with GGA.

The KS wavefunction and the quasi-particle correction are calculated on a $12 \times 12 \times 12$ **k**-grid with a cutoff energy of 20 Ha for the BSE calculation. The optical calculations were then performed considering the three higher occupied states and the first four conduction bands with an energy cutoff of 6 Ha for the dielectric matrix. Appendix A detailed the convergence study for the BSE calculations with regards to the number of **k** points, the energy cutoff for the screening matrix, the bands considered to calculate the possible transitions between the valence and conduction bands and the complex shift that mimics the experimental broadening of the absorption peaks.

For the EPW calculations, the parameters are taken based on the study from Noffsinger *et al.* [225] who developed the main framework for the absorption calculation in silicon considering electron-phonon interactions. The phonon calculations were performed on a $6 \times 6 \times 6$ **q**-grid. The electron-phonon interactions are finally calculated on a $30 \times 30 \times 30$ **k**-grid using Wannier-Fourier interpolation in the EPW code. The convergence study with regards to the number of **k**-point is shown in appendix A. The study is carried out for uniaxial strain along [110] crystal direction as uniaxial tensile strain is the most promising way to achieve high deformation and [110] is the direction that shows the highest band gap reduction to increase the light absorption.

3.2 First-principles results

The results of the first-principles calculations for uniaxial strain along [110] directions are described in this section. First, the refractive index and dielectric function calculated using the BSE method are discussed, followed

by the results of the absorption coefficient using the EPW code and the analytical model of Tsai [230].

3.2.1 Refractive index and direct absorption

The results of the dielectric function calculated using BSE are shown in Fig. 3.5.

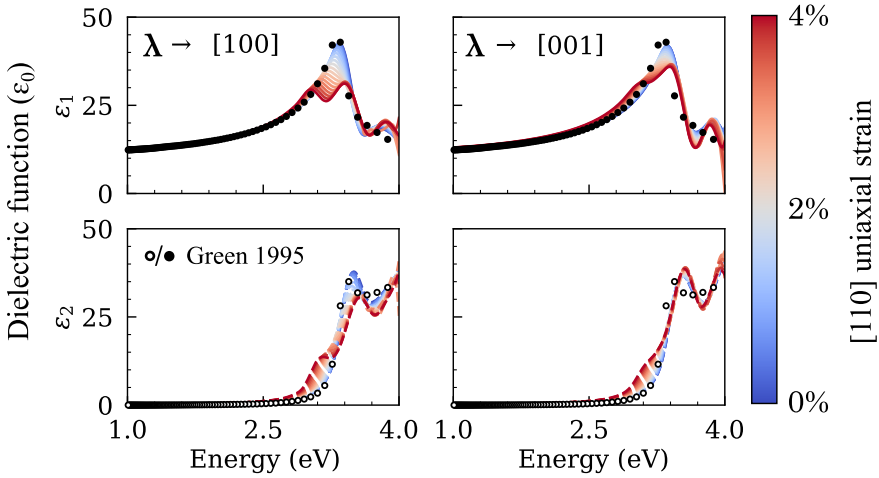


Fig. 3.5 Real (ε_1) and imaginary (ε_2) components of the dielectric function in unit of vacuum permittivity (ε_0) for uniaxial strain up to 4% along the [110] crystal direction. Results for computation with the light momentum $\boldsymbol{\lambda}$ along the [100] and [001] direction are shown.

In the absence of strain, the real part (ε_1) and the imaginary part (ε_2) are in excellent agreement with the experimental data of Green and Keevers [236]. For energies below the direct band gap (3.4 eV) the imaginary part of the dielectric function is close to zero, since no direct transitions from the valence to the conduction band are possible. Similarly, the excitonic peak in the real part of the dielectric function is maximal around 3.25 eV. It then decreases with energy to reach 11.9 ε_0 at zero energy, close to the experimental value [246]. According to Eq. (3.11), the macroscopic dielectric function is calculated for a certain light polarisation $\boldsymbol{\lambda}$. In the absence of strain, the functions computed for [100] and [001] polarisation are similar. As strain breaks the crystal symmetries, the calculations along these two directions give different results. For uniaxial strain along [110], the

calculations along [100] and [010] remain similar, but the one along [001] differs, as shown in Fig. 3.5. With increasing strain, the maximum value of ε_1 decreases from 42.25 ε_0 at 0%-strain to 30.66 ε_0 (resp. 35.46 ε_0) at 4%-strain for the calculation along [100] (resp. [001]). The zero energy value shows much smaller variations, going from 11.91 ε_0 at 0%-strain down to 11.83 ε_0 (resp. 12.51 ε_0) at 4%-strain for calculation along [100] (resp. [001]). The reduction of the direct band gap due to strain is clearly visible in the imaginary part ε_2, as the absorption edge is shifted to a lower energy. With increasing strain, the direct band gap in the centre of the Brillouin zone (Γ) is reduced from 3.17 eV at 0%-strain to 2.64 eV at 4%-strain, causing a shift of the excitonic peak at lower energy for the real part of the dielectric function and a shift at lower energy for the rising edge of the imaginary part.

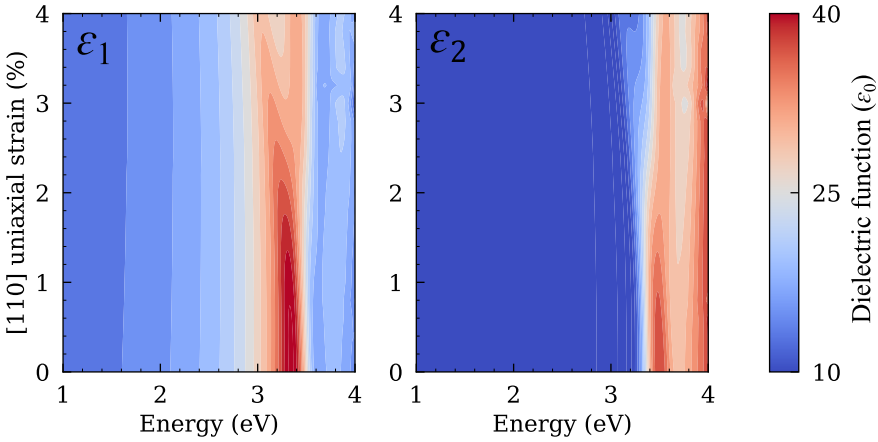


Fig. 3.6 Maps of the real ε_1 (left) and imaginary ε_2 (right) part of the macroscopic dielectric function computed with BSE method according to strain up to 4% along [110] crystal direction and the energy.

Figure 3.6 shows the maps of the components of the dielectric function with respect to strain and energy. The reduction of the amplitude of the excitonic peak and its position is clearly visible for ε_1. At lower energies, the vertical contour shows the low dependence of the permittivity on strain. For ε_2, the small variations at higher strain can be seen with the rising edge going from 3.25 eV down to 3.05 eV at 4%-strain. Furthermore, the reduction of the main peak at 3.45 eV is clearly visible, going from 39.21 ε_0 down to 31.31 ε_0 at 4%-strain.

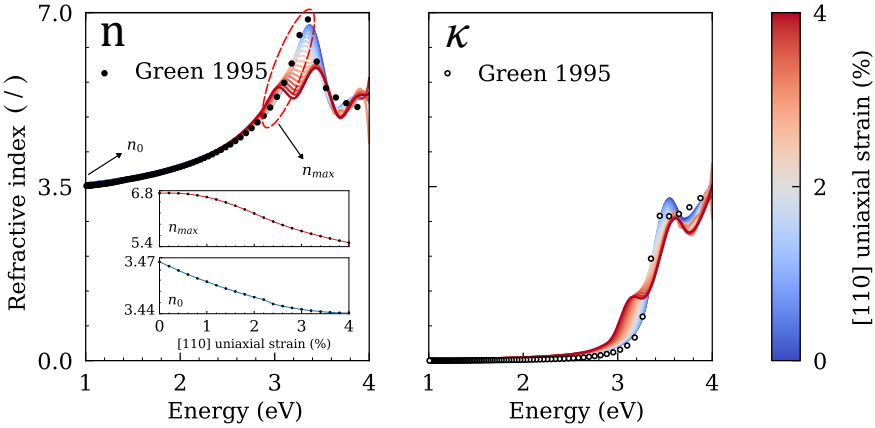


Fig. 3.7 Real n (left) and imaginary κ (right) part of the refractive index computed with BSE method for strain along [110] crystal direction. The real part of the refractive index with strain at zero-energy (n_0) and at maximum position (n_{max}) are shown in the insets of the left panel. The experimental results from Green and Keevers [236] are indicated.

The complex refractive index γ is then calculated using Eq. (3.4) to obtain the real part n and the imaginary part κ. The results of n and κ are shown in Fig. 3.7. Similar to the dielectric function, the excitonic peak is shown for the real part, with a maximum value n_{max} decreasing from 6.77 at 0%-strain to 5.55 at 4%-strain, and its position shifting from 3.4 eV to 3.06 eV. At lower energies the strain dependence is much smaller, with the zero-energy index decreasing from 3.47 at 0%-strain to 3.44 at 4%-strain. The imaginary part of the index shows an edge shift at lower energy due to the direct band gap reduction under strain, showing the increase in light absorption at lower energy.

Finally, the absorption coefficient α is calculated from the extinction coefficient κ using Eq. (3.7). The results of the absorption calculation with BSE method, *i.e.*, considering only direct transitions without electron-phonon interactions, are shown in Fig. 3.8. As expected, the lower energy limit of the direct absorption decreases with strain due to the reduction of the direct band gap. Conversely, a reduction in absorption is observed at higher energies. Experimental data from Green and Keevers [236] are shown as black dots. The higher energy data are in good agreement as the direct transition dominates the absorption, but at lower energy the indirect transition is not treated by the BSE calculation.

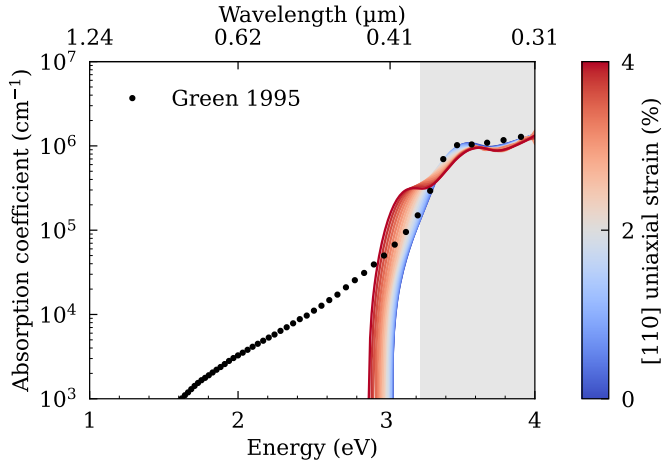


Fig. 3.8 Absorption coefficient for direct transition computed with BSE method for strain along [110] crystal direction. The experimental results from Green and Keevers [236], including indirect transitions, are indicated with black dots. The grey area highlight the region where direct absorption dominates.

3.2.2 Indirect absorption

The results of the band gaps and effective masses required for the analytical model from Tsai [230] are shown in Fig. 3.9. Under uniaxial strain along the [110] crystal direction, the broken symmetries lift the degeneracy of the Δ-valleys into the Δ_2-valleys (including the two valleys along [001]) and the Δ_4-valleys (including the four valleys along [100] and [010]). The lowest indirect band gap $E_{g,\Gamma\Delta_4}$ is significantly reduced by -202.9 meV at 2%-strain, while the reduction of the other indirect band gaps $E_{g,\Gamma\Delta_2}$ shows a reduction of only -28 meV at 2%. A similar trend is observed for the direct band gap at the Δ_x- and Δ_z-valleys, where the gap reduction is mainly due to the movement of the conduction band energy. The lowest direct gap is at Γ and shows a reduction down to 2.67 eV for a strain of 4%.

To calculate the DOS effective masses, the integrative method based on Eq. (3.18) is used. Indeed, the significant effect of strain on the band shape makes it difficult to use existing analytical models for the DOS. The valence DOS effective mass is reduced from 0.89 m_e at 0%-strain to 0.44 m_e at 4%-strain and is mainly influenced by the states of the HH band. The conduction DOS effective mass shows little variation for the higher energy

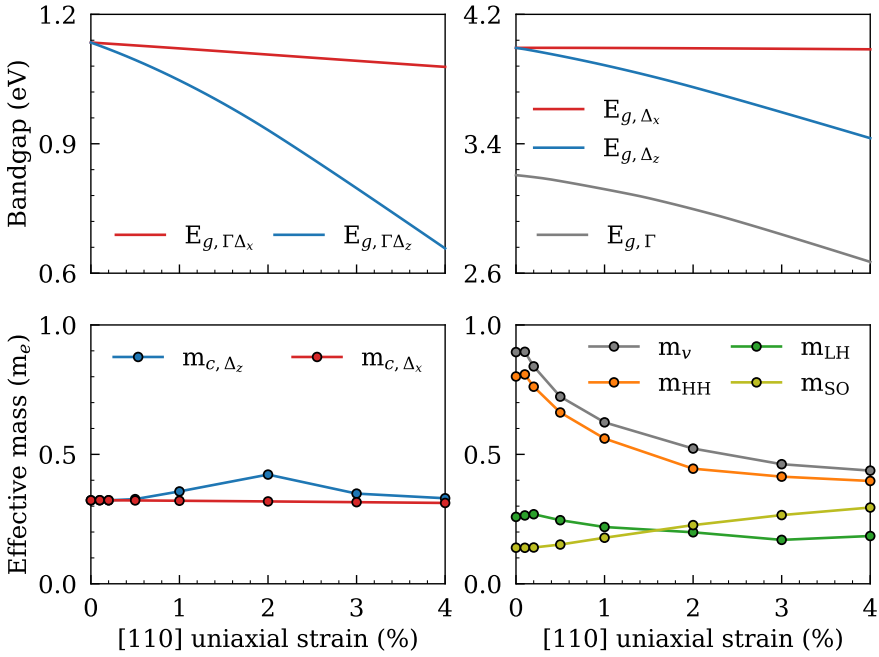


Fig. 3.9 Effective masses and band gaps calculated using DFT. The indirect and direct band gap under uniaxial strain along the [110] direction are shown in the top left and right panels, respectively. The gaps are computed for valleys along the [100] direction (Δ_x) and [001] direction (Δ_z) of the reciprocal space. The DOS effective masses for the two types of valleys (m_{c,Δ_x} and m_{c,Δ_z}) are shown in the bottom left panel as well as the global effective mass for the conduction bands (m_c). The DOS effective masses for the valence bands (m_v) are shown in the bottom right panel with the contribution of each valence band (HH, LH and SO).

valleys but increases from 0.32 m_e at 0%-strain to 0.42 m_e at 2%-strain for the lower energy valleys due to the valleys reaching the end of the Brillouin zone as explained in chapter 1.

Figure 3.10 shows the results of the phonon energies with strain, as needed to calculate the absorption using the analytical model of Tsai [230]. It has been shown that the TO, TA and LO modes show strong electron-phonon coupling for such interband transitions, while the LA mode plays a negligible role [245]. Only the phonons with a wavevector **q** connecting the valence band maximum at Γ to the conduction band minimum near X should be considered. At zero strain the energies found for the TO, LO,

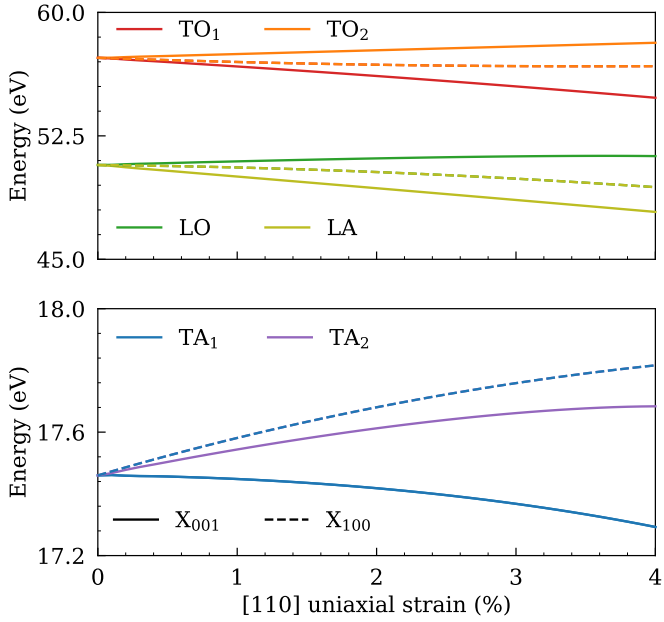


Fig. 3.10 Phonon energy under uniaxial strain along the [110] direction. The energies of the modes are calculated at the [100] (X_{100}) and [001] (X_{001}) position of the reciprocal space.

TA and LA modes are 57.24 meV, 50.73 meV, 17.46 meV and 50.73 meV, respectively. Under uniaxial strain along the [110] direction, the phonon modes at X symmetry points along the [100] and [010] paths show the same evolution with an energy increase up to 17.82 meV at 4%-strain for the two TA modes. The TO modes and the longitudinal modes (LO and LA) reach an energy of 56.73 meV and 49.38 meV at 4%-strain, respectively. For the X symmetry point along [001], the LO and LA modes split to reach 51.27 meV and 47.88 meV at 4%-strain, respectively. The TO_1 and TO_2 modes split to reach 54.82 meV and 58.16 meV at 4%-strain, respectively. Finally, the TA_1 and TA_2 modes split to reach 17.29 meV and 17.68 meV at 4%-strain, respectively. The changes in phonon frequencies are overall negligible compared to the band gap reduction, and these changes have only a small impact on the absorption coefficient of strained silicon.

The results of the absorption coefficient are shown in Fig. 3.11. As strain increases, the absorption curves are shifted towards lower energy, following the band gap reduction. Conversely, the reduction in the DOS caused

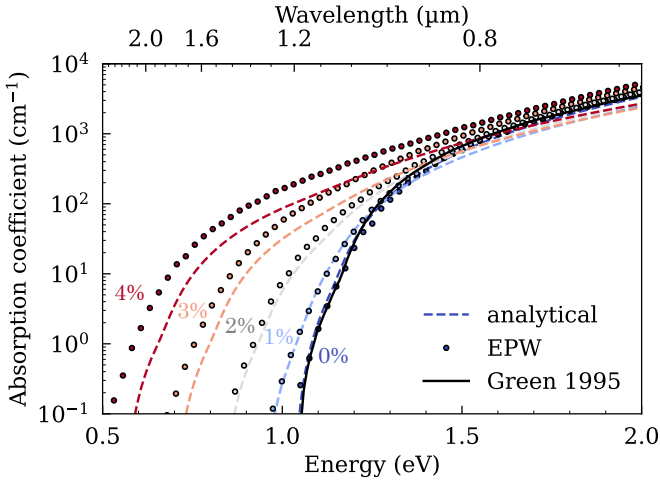


Fig. 3.11 Absorption coefficients computed analytically based on first-principles parameters (dashed lines) and computed theoretically using EPW (dots) for uniaxial strain along [110] direction at 300K. The results are compared with the absorption coefficient measured experimentally in absence of strain by Green and Keevers [236] (dark continuous line).

by the valley splitting leads to a reduction at higher energies. This makes the absorption enhancement much smaller for light with energy above 1.5 eV. The absorption results obtained by the analytical model and the EPW code are in good agreement for the lower absorption region (at lower energy), but the analytical model failed to correctly predict the strain effect at higher energy. This is mainly due to the limits of the parabolic band assumption used in the model, as well as the difficulty of accurately predicting the DOS effective masses involved in calculating the coefficient A in Eq. (3.16). At higher energies, the variations in the absorption coefficient are then much less pronounced and a greater discrepancy is observed between the analytical model and the EPW results.

Figure 3.12 shows the map of the absorption coefficient as a function of [110] uniaxial strain and light energy, calculated using the analytical model. The contour is shown at 1 cm^{-1}, 10 cm^{-1}, 100 cm^{-1} and 1000 cm^{-1}. At lower strains it can be observed that the increase in absorption due to the band gap reduction is counterbalanced by a reduction in the DOS, as indicated by the vertical evolution of the contours. This mechanism is more pronounced at higher energies. At higher strains, the DOS is stable and a

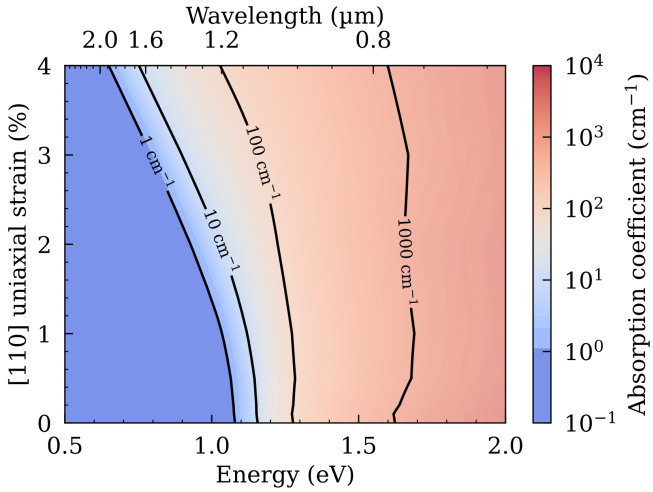


Fig. 3.12 Map of the absorption coefficient according to uniaxial strain along [110] crystal direction and the light energy using analytical model. Contour lines for absorption coefficient of 1, 10, 100 and 1000 cm^{-1} are shown in black.

clear dependence is observed, mainly due to the band gap reduction.

The evolution of the absorption coefficient with strain at a given photon energy is shown in Fig. 3.13a. These results clearly show that the increase in absorption is mainly observed at lower energies. Indeed, the absorption coefficients for 0.75 and 1.00 eV show a clear increase with strain, going from 5.44×10^{-3} cm^{-1} to 26 cm^{-1} and 1.5×10^{-2} cm^{-1} to 168 cm^{-1} from 0% to 4%-strain respectively. The coefficients for the 1.25 eV and 1.50 eV energies are much more stable, ranging from 52 cm^{-1} to 500 cm^{-1} at 0%-strain and from 582 cm^{-1} to 1241 cm^{-1} at 4%-strain.

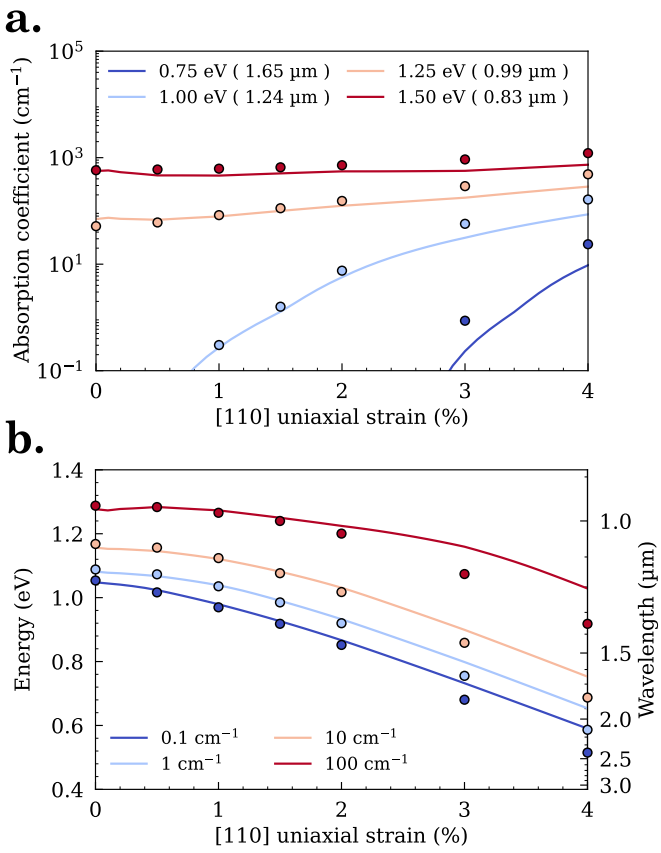


Fig. 3.13 (a) Absorption coefficient for uniaxial strain along [110] direction for photon energy of 0.75, 1, 1.25 and 1.5 eV. (b) Energy limit under uniaxial strain along [110] direction for absorption coefficient of 0.1, 1, 10 and 100 cm^{-1}. The continuous lines are the results from the analytical model while the dots have been computed using EPW code.

As an important metric, we conclude that strain can significantly improve the absorption only up to a certain level. The evolution of the energy cutoff at certain absorption coefficients is shown in Fig. 3.13b. For values up to 100 cm^{-1} the relative variation of the energy limit is similar regardless of the absorption value, with the limits decreasing with strain from 1.05 eV to 0.52 eV at 0.1 cm^{-1} and from 1.29 eV to 0.92 eV at 100 cm^{-1}. In both panels of Fig. 3.13 the analytical model is in good agreement with the EPW calculations.

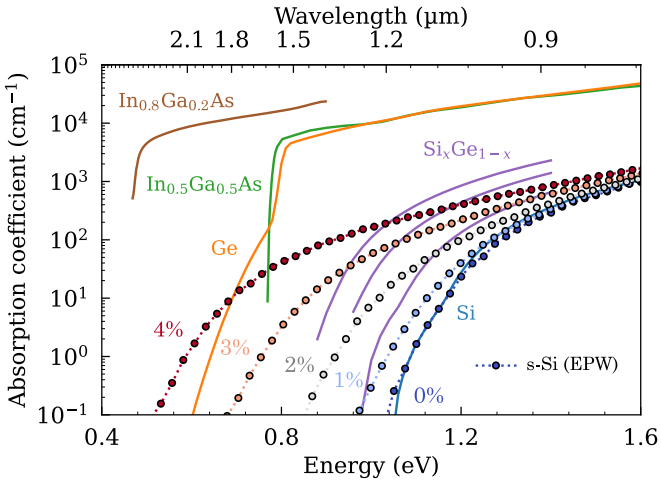


Fig. 3.14 Comparison of the absorption coefficient of strained silicon (dots) obtained with the EPW code and other semiconductor material such as relax silicon (Si) [236], germanium (Ge) [247], indium gallium arsenide ($In_{0.5}Ga_{0.5}As$ [248], $In_{0.8}Ga_{0.2}As$ [33]) and silicon-germanium alloy (Si_xGe_{1-x}) [249] with proportion x of 0.2, 0.5 and 0.8.

Figure 3.14 shows a comparison of the absorption coefficient obtained for strained silicon using the EPW code and typical semiconductors used in NIR and SWIR applications. Indium Gallium Arsenide ($In_{0.5}Ga_{0.5}As$) [248] has a band gap of 0.78 eV and can then absorb light up to 1.58 μm. It is also a direct band gap material, which leads to higher absorption as no phonon is needed to excite an electron from the valence band to the conduction band. By increasing the indium content, the band gap is reduced and the absorption in the infrared increases. $In_{0.8}Ga_{0.2}As$ is able to absorb light up to 2.5 μm due to its band gap of 0.5 eV [33]. Germanium (Ge) [247] has an indirect band gap of 0.66 eV and a direct band gap of 0.8 eV. The

indirect and direct absorption can be clearly observed, following typical square [224] and square-root [250] relationships, respectively. Finally, the silicon-germanium alloy (Si_xGe_{1-x}) [249] shows an increase in absorption with germanium content. It is clear from the curves in Fig. 3.14 that silicon suffers from indirect absorption. Although the absorption in strained silicon is much better than in relaxed silicon, a significant strain is required to achieve better absorption than the other semiconductor materials. 2%-strain is sufficient to match the performance of $Si_{0.7}Ge_{0.3}$, while at least 3%-strain is required to absorb beyond the $In_{0.53}Ga_{0.47}As$ limit. Finally, 4%-strain is required to exceed the performance of Ge in the low-absorption region.

3.3 Chapter Summary

The effect of uniaxial strain applied along [110] on the optical properties of silicon has been studied in detail using first principles. The Bethe-Salpeter equation (BSE) method allows the calculation of the refractive index taking into account the electron-hole interactions. The results for the real part of the index show the important variations of the excitonic peak around the 3.2 eV energy, while the zero-energy values show hardly any variations with strain. This method failed to predict the indirect absorption, as the phonon-assisted phenomena are not taken into account. The electron-phonon interactions and thus the indirect absorption are then calculated using the electron-phonon wannier (EPW) code. The results for the absorption coefficient show a significant increase with strain, following the band gap reduction. As the band gap is reduced from 1.13 eV to 0.66 eV at 4%-strain, the light wavelength that can be absorbed is extended to 1.88 µm. The absorption coefficient at 1.2 µm goes from 1.5e-2 cm^{-1} to 168 cm^{-1} at 4%-strain. The EPW results are then compared with an analytical model for which the parameters such as the band gap energies, the DOS effective masses and the phonon energies are calculated by DFT and DFPT. The model shows the advantage of fast computation compared to fully calculated results. It relies on fitting parameters that have to be determined from experimental or first-principles results, which limits the prediction of new configurations. Nevertheless, the analytical method provides a fast estimate of the absorption in strained silicon, although it tends to underestimate the absorption enhancement. The absorption results are finally compared with the absorption coefficient of conventional IR materials such as Ge, SiGe and InGaAs, showing the potential of strained silicon to compete with them, but mainly in the low-absorption range.

Key messages of the chapter

- The real part of the dielectric function and the refractive index can be accurately calculated with Bethe-Salpeter equation (BSE), taking into account the electron-hole interactions, while the imaginary part must be tackled with a calculation that takes into account the electron-phonon interactions, such as electron-phonon wannier (EPW). This first-principles calculation allows an accurate determination of the absorption coefficient of a new material or strain configuration without the need for semi-empirical bias.
- An analytical model can be used to describe the absorption coefficient of strained silicon, but it relies on the parabolic band assumption. However, semi-empirical values are required, usually determined by fitting the zero-strain coefficient, but this limits the use of the analytical model for new materials for which no clear experimental data are available.
- The strain has an important effect on the excitonic peak, around 3.4 eV, in the real part of the dielectric function and the refractive index, while showing a limited effect at lower energies. On the contrary, the enhancement of the absorption coefficient takes place mainly at lower energy, *i.e.*, below the zero-strain band gap energy at 1.12 eV.
- Strain is a promising technique for silicon to compete with traditional IR materials (Ge or InGaAs), but indirect absorption limits the enhancement for the low-absorption regime.

4

Infrared performances of strained silicon photodiode

Germanium (Ge) and Indium Gallium Arsenide ($In_xGa_{1-x}As$) photodetectors are the most commonly used devices to detect IR light beyond the range available for standard silicon detectors. This final chapter examines the benefits that highly strained silicon brings to IR photodiodes, focusing on the improvement of the device sensitivity. Previous chapters have shown the effect of strain on carrier transport and light absorption in silicon. The improvement in material properties still needs to be investigated in practical devices to confirm the potential of strained silicon for IR photodetectors. The first section recalls the important theory about the photodetector, including the effect of the dimensions on the light absorption and the working principles of a photoconductor and a photodiode. The second section performs a TCAD simulation to calculate the responsivity of a photodiode using strained silicon and discuss the performance we can expect with strain up to 4%.

4.1 Optical absorption in a semiconductor layer

The efficiency of light absorption is significantly influenced by the absorption coefficient of the material, which determines the required thickness

of the device. In particular, materials with lower absorption coefficients require thicker layers to absorb a sufficient amount of incident light. A typical light-absorbing device is composed of several layers, such as a substrate to provide mechanical support, an active layer where the photogenerated carriers are generated, metallic electrodes to collect these charges, an antireflective coating (ARC) to minimise the loss of light due to reflection at the surface, and so on. The transfer matrix method (TMM) [251] is widely used to analyse and optimise light propagation through these layers. This method provides a systematic approach to studying the transmission, reflection and absorption of light. This helps to select the dimensions and materials of photodetectors. The TMM method is explained in detail in Ref. [252]. For any interface m of the stack, a transfer matrix $\mathbf{M}_{m-1}$ is defined as the relation between the wave in layer $m-1$ and layer m, considering component of the wave moving forward E_m^+ and the component moving backward E_m^-:

$$\begin{pmatrix} E_{m-1}^+ \\ E_{m-1}^- \end{pmatrix} = \underbrace{\begin{pmatrix} 1 & r_m \\ r_m & 1 \end{pmatrix} \frac{1}{t_m} \begin{pmatrix} e^{i\phi_{m-1}} & 0 \\ 0 & e^{-i\phi_{m-1}} \end{pmatrix}}_{\mathbf{M}_{m-1}} \begin{pmatrix} E_m^+ \\ E_m^- \end{pmatrix} \tag{4.1}$$

where r_m is the Fresnel coefficient of interface m, t_m is the transmission coefficient.

The propagation constant ϕ_{m-1} is defined as

$$\phi_{m-1} = t_{m-1} \frac{2\pi}{\lambda} \gamma_{m-1} i, \tag{4.2}$$

where t_{m-1} is the thickness of layer $m-1$, γ_{m-1} is its complex refractive index and λ is the wavelength of the light.

The Fresnel coefficients for p- and s-polarised light are given by

$$r_{m,p} = \left| \frac{n_{m-1}\cos\theta_t - n_m \cos\theta_i}{n_{m-1}\cos\theta_t + n_m \cos\theta_i} \right|, \qquad r_{m,s} = \left| \frac{n_{m-1}\cos\theta_i - n_m \cos\theta_t}{n_{m-1}\cos\theta_i + n_m \cos\theta_t} \right|, \tag{4.3}$$

with θ_i and θ_t, the angles of incidence and transmitted light, respectively. For unpolarised light, the refractive coefficient r_m is taken as the average of the p- and s-polarised coefficients.

Figure 4.1 illustrates the multiple transmission and reflection happening in a 3-layers stack that can be handled by the TMM. The global trans-

mission and reflection of a N-layer stack is obtained by considering the transfer matrix of the full stack:

$$\begin{pmatrix} E_0^+ \\ E_0^- \end{pmatrix} = \underbrace{\mathbf{M}_0\mathbf{M}_1...\mathbf{M}_{N-1}\mathbf{M}_N}_{\mathbf{M}_{tot}} \begin{pmatrix} E_{N+1}^+ \\ E_{N+1}^- \end{pmatrix}, \tag{4.4}$$

where E_0^+ and E_0^- are the wave amplitudes of forward- and backward-propagating light in the initial medium (often considered as the air), respectively, and E_{N+1}^+ and E_{N+1}^- are the amplitudes in final medium.

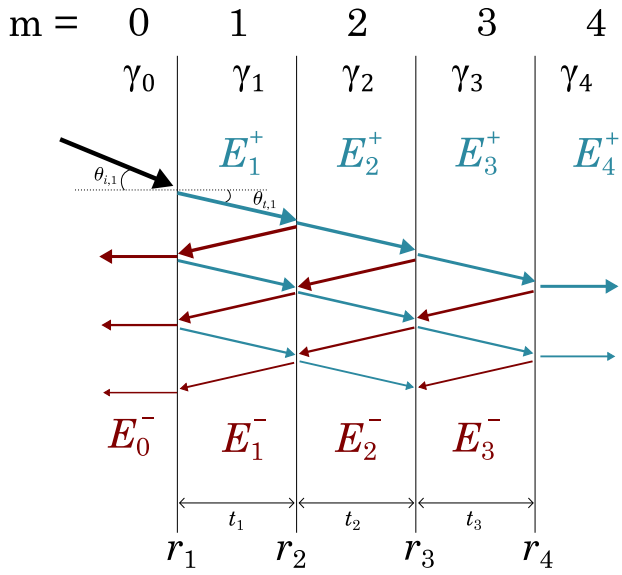


Fig. 4.1 Illustration of the light transmission and reflection in a stack of 3 layers. The first and last region ($m = 0$ and $m = 4$) are usually considered as air. Each layer is defined by its thickness t_m and its complex refractive index γ_m while r_{m+1} is the Fresnel coefficient at each interface between two layers. The component of the wave propagating forward (blue) and backward (red) in each layer are indicated by E_m^+ and E_m^-, respectively.

TMM shows high interference due to the consideration of perfectly flat interfaces and layers with coherent interface, leading to perturbations at higher wavelengths that are not observed experimentally [253]. To avoid this problem, a layer with incoherent interfaces can be defined using the squared norms instead of the complex amplitudes of the Fresnel coefficients and phase propagation terms [254]. The total transmission T is then

simply defined as the ratio between the amplitude of the forward propagating wave in the last medium E^+_{N+1} and in the initial medium E^+_0, while the total reflection R is defined as the ratio between the backward propagating wave in the initial medium E^-_0 and the forward propagating component E^+_0. The expressions for R and T are thus

$$R = \left| \frac{M_{tot,21}}{M_{tot,11}} \right|^2, \qquad T = \frac{n_{N+1}}{n_0} \frac{1}{|M_{tot,11}|^2}, \tag{4.5}$$

with n_0 and n_{N+1} the real part of the refractive index for the initial and last medium, respectively, $M_{tot,ij}$ the component of the transfer matrix.

The total fraction of the power absorbed in the stack, A, is then given by

$$A = 1 - R - T \tag{4.6}$$

4.1.1 Absorption in a single layer

Strain has been shown to increase the absorption coefficient of silicon, particularly in the infrared. Although the absorption coefficient increases, strained silicon still suffers from low indirect absorption and requires sufficient thickness to observe the benefit of straining the material. We first used the TMM to study the effect of strain on the absorption of a silicon layer with rough incoherent interfaces. The fraction of incident power absorbed in a single silicon layer is shown in Fig. 4.2 for thicknesses from 1 µm to 100 µm under uniaxial strain along the [110] direction of 0%, 1% and 2%. The complex refractive index values have been obtained using BSE methods and the EPW code as described in chapter 3. The fraction of absorbed power does not show a specific increase for a thickness of 1 µm, as most of the light absorbed is at lower wavelengths, for which the absorption coefficient does not show a significant improvement with strain. As the thickness increases, the layer begins to absorb light of higher wavelength and this absorption increases with strain. The fraction of absorbed power for a 1µm-wavelength goes from 4.5% to 12.4% for a 20µm-thick device under 2%-strain, while it goes from 19% to 41% for a 100µm-thick device. The inset of Fig. 4.2 shows the fraction of absorbed power with respect to the angle of incidence of unpolarised light at for a 50µm-thick device. The fraction is not affected by the angle as long as it remains below a certain threshold around 70°.

Figure 4.3 shows maps of the fraction of absorbed power at 0%- and 2%-

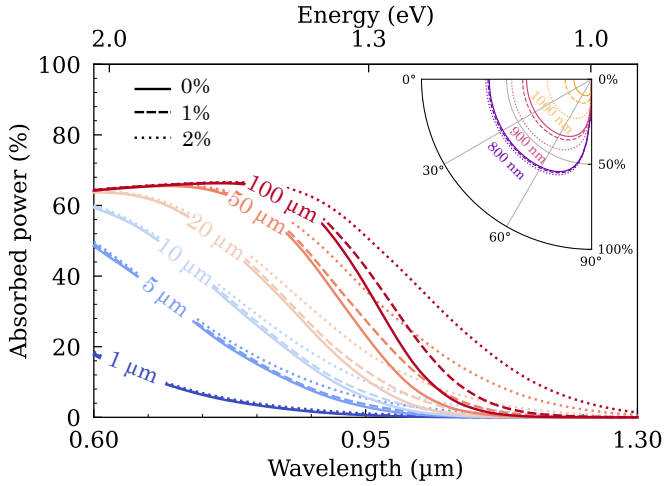


Fig. 4.2 Fraction of absorbed power in a single silicon layer with regards to the wavelength of a normal-incidence light with thicknesses from 1 µm to 100 µm. The results are shown for uniaxial strain along [110] crystal direction of 0% (solid line), 1% (dashed line) and 2% (dotted line). The inset shows the results for light with an incidence angle from 0° to 90° at wavelengths of 800 nm, 900 nm and 1000 nm for a 50µm-thick device.

strain as a function of the light wavelength and the thickness of a silicon layer surrounded by air. The contours of the maps show that sufficient thickness is required to absorb light in the IR region. The contours show no significant change at lower wavelengths, but shift at higher wavelengths as the thickness of the strained silicon layer increases.

4.1.2 Absorption with antireflective coating

To improve light absorption in an optoelectronic device, an ARC and a reflective layer can be used at the front and back interfaces, respectively. The first coating reduces reflective losses by matching the real part of the refractive index of the following layer, *i.e.*, silicon. The reflective layer at the back reduces transmission losses by reflecting the fraction of light that reaches the end of the absorbing layer.

The optimal single-layer ARC material should have a refractive index close to the geometric mean of the indexes of the first and second layers. For the air-silicon interface, this leads to a refractive index of about 2, for

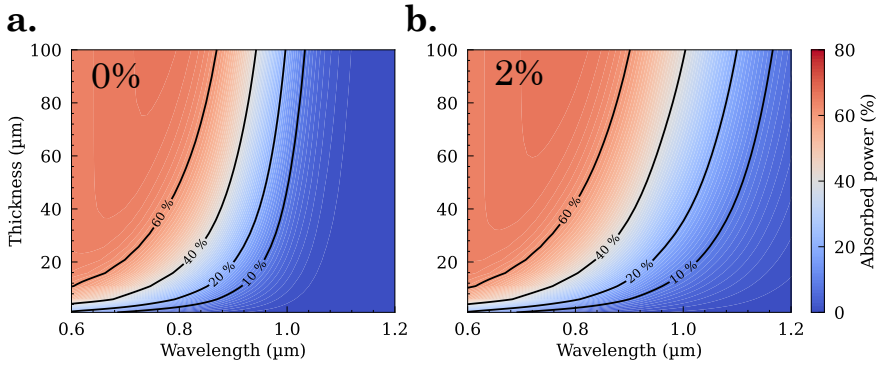


Fig. 4.3 Maps of the fraction of absorbed power for a single silicon layer with regards to the light wavelength and device thickness for (a) 0% and (b) 2% uniaxial strain along [110] crystal direction. The contours of 10%, 20%, 40% and 60% absorbed power are indicated with black lines.

which silicon nitride is a suitable material that can be easily processed in CMOS technology [255, 256]. In the case of an ARC layer, coherent interfaces are considered as this layer exploits the interferences to reduced the optical reflection. The thickness of the ARC (t_{ARC}) required to minimise reflection at a given wavelength (λ_{ARC}) is given by [257]

$$t_{ARC} = \frac{\lambda_{ARC}}{4n_{ARC}} \tag{4.7}$$

where n_{ARC} is the refractive index of the ARC.

In this work, a non-stoechiometric layer of silicon nitride (SiN_x) with a refractive index of 2 [258] is considered for the ARC. The target wavelength is 1000 nm, *i.e.*, around the absorption limit of relaxed silicon, resulting in an ARC thickness of 125 nm.

Figure 4.4 shows the fraction of absorbed power in a silicon layer coated with an ideal antireflective layer on the front and a reflective layer on the back. Results for thicknesses from 1 µm to 100 µm are shown for 0%, 1% and 2%-strain. The ideal ARC on the top surface allows the efficiency to be brought close to 100% for devices of sufficient thickness. In addition, the reflective coating reduces the transmission loss at the rear of the device. The effect is limited for thick devices at lower wavelengths as the light is absorbed before reaching the back, but it increases the absorption for thin devices or at higher wavelengths.

The fraction of absorbed power for a 1µm-wavelength of light goes

from 8.8% to 24.25% for a 20µm-thick device under 2%-strain, while it goes from 36.85% to 74.75% for a 100µm-thick device.

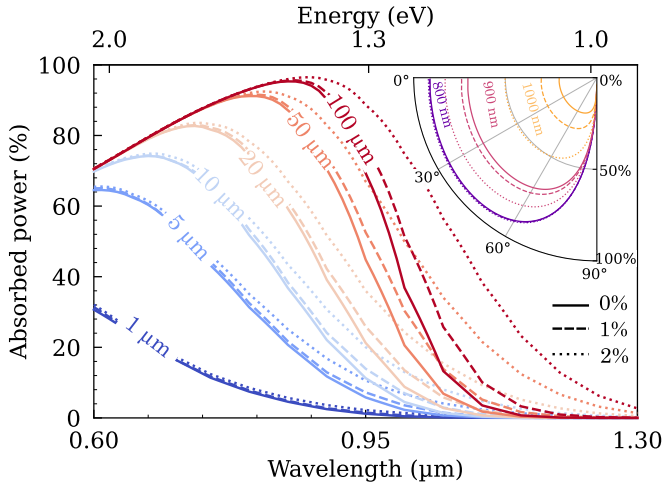


Fig. 4.4 Fraction of absorbed power in a silicon layer with ideal ARC at the front and reflective layer at the back with regards to the wavelength of a normal-incidence light with thicknesses from 1 µm to 100 µm. The results are shown for uniaxial strain along [110] crystal direction of 0% (solid line), 1% (dashed line) and 2% (dotted line). The inset shows the results for light with an incidence angle from 0° to 90° at wavelengths of 800 nm, 900 nm and 1000 nm for a 50µm-thick device.

4.2 Photodetector theory

This section reviews the relevant theory to understand the operation of a photodetector. This includes an explanation of the effect of the dimension on the light absorption, followed by theoretical modeling of the photogenerated current in a photoresistor and a pin photodiode. Responsivity and detectivity are then explained and a comparison is made between typical IR photodetector.

4.2.1 Photogenerated current in a photoconductor

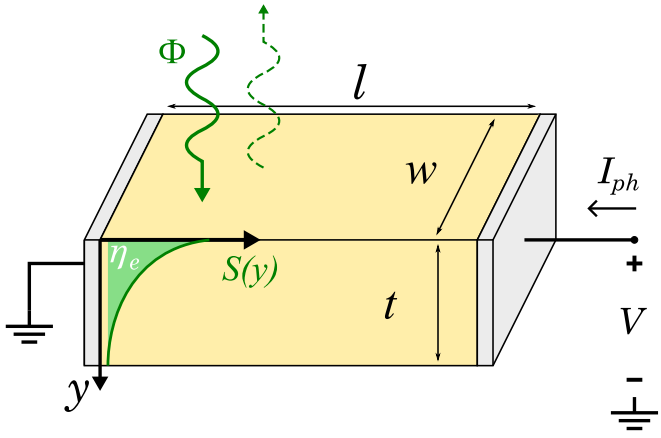


Fig. 4.5 Illustration of a photoresistor hit by an incoming photo flux Φ producing a photogenerated current I_{ph} under bias voltage V. The photogenerated charge profile $S(y)$ is indicated as well as the quantum efficiency η_e defined as the area under the photogenerated charge profile curve. The length, width and thickness of the device are respectively indicated by l, w and t.

The photogenerated current expresses the number of carriers generated by the incident light and collected at the electrodes. The general expression for the steady-state photocurrent is [259]

$$I_{ph} = e\eta_e A_{eff} \Phi g, \tag{4.8}$$

where e is the electron charge, A_{eff} is the effective area collecting the light,

Φ is the photon flux per unit area and g is the photoconductive gain depending on the configuration and type of photodetector.

The external quantum efficiency η_e is the first metric of importance in an optoelectronic device. It is defined as the ratio of the number of collected carriers to the number of incident photons. For a simple photoconductor, such as the resistor shown in Fig. 4.5, η_e can be calculated by integrating the photogenerated charge profile $S(y)$ along the dimension of light propagation. For a single layer device $S(y)$ is given by [260]

$$S(y;t) = \eta_i \frac{(1-r_1)\alpha}{1-r_1 r_2 e^{-2\alpha t}}(1+r_2 e^{-\alpha t})e^{-\alpha y}, \tag{4.9}$$

where η_i is the internal quantum efficiency, t is the thickness of the device along the direction of the light propagation, α is the absorption coefficient, r_1 and r_2 are the reflection coefficients at the first and second interfaces, respectively. The quantum efficiency η_e is then analytically expressed as

$$\eta_e = \int_0^d S(y;t)dy = \eta_i \frac{(1-r_1)}{1-r_1 r_2 e^{-2\alpha t}}(1+r_2 e^{-\alpha t})(1-e^{-\alpha t}). \tag{4.10}$$

In a photoconductor, the photogenerated current is written as [261]

$$I_{ph} = e(\Delta n \mu_n + \Delta p \mu_p)\frac{wt}{l}V, \tag{4.11}$$

where e is the electron charge, Δn and Δp are the excess electron and hole concentrations, μ_n and μ_p are the electron and hole mobilities, w is the width, t is the thickness, l is the length of the device and V is the applied voltage.

The excess carrier concentration can be found by solving the continuity equation under constant illumination [262]:

$$\frac{\partial \Delta n}{\partial t} = G_n - U_n, \qquad \frac{\partial \Delta p}{\partial t} = G_p - U_p, \tag{4.12}$$

where $U_n = \Delta n/\tau_n$ and $U_p = \Delta p/\tau_p$ are the electron and hole recombination rates per unit volume for radiative recombination [263] with excess carrier lifetime τ_n and τ_p, and $G_n = G_p = \Phi\eta_e/t$ is the generation rate per unit volume, uniform along the length of the photoresistor. In steady-state, the generation is equal to the recombination, and the excess carrier concentrations are then given by

$$\Delta n = \frac{\tau_n \eta_e \Phi}{t}, \qquad \Delta p = \frac{\tau_p \eta_e \Phi}{t}. \tag{4.13}$$

The photogenerated current in a photosensitive resistor is finally expressed as

$$I_{ph} = e\eta_e \Phi w l \left(\frac{\tau_n}{\tau_{tr,n}} + \frac{\tau_p}{\tau_{tr,p}} \right) \tag{4.14}$$

where $\tau_{tr,n/p} = \frac{l^2}{\mu_{n/p} V}$ is defined as the transit time of the electrons (n) and the holes (p).

The photoelectric gain in this case is expressed as

$$g = \left(\frac{\tau_n}{\tau_{tr,n}} + \frac{\tau_p}{\tau_{tr,p}} \right). \tag{4.15}$$

4.2.2 Photogenerated current in a photodiode under transverse illumination

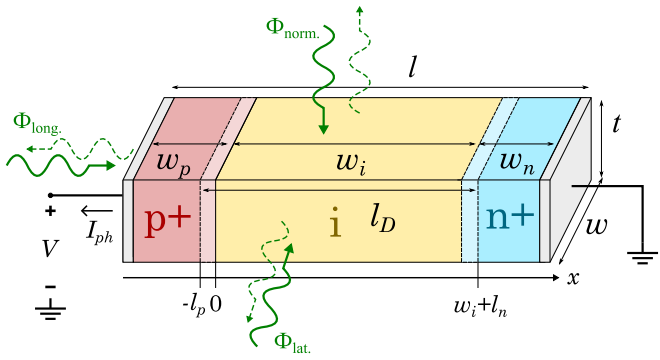


Fig. 4.6 Illustration of a pin photodiode hit normally (norm.), longitudinally (long.) and lateraly (lat.) by an incoming photon flux Φ, producing a photogenerated current I_{ph} under bias voltage V. The length, width and thickness of the device are respectively indicated by l, w and t. The length of the p-doped, intrinsic and n-doped regions are w_p, w_i and w_n. The length of the depletion region in the p-doped and n-doped regions are written by l_p and l_n, respectively. The total depletion length is written l_D.

The most popular photodetector is made of a pin diode, as shown in Fig. 4.6. The low dark current of the photodiode greatly improves its de-

tectivity for low-intensity light compared to a photoconductor. The detector is composed of p- and n-doped regions with a large intrinsic region in between, providing a large depleted area for collecting light. In addition, the large depletion region increases the speed of the detector by reducing the junction capacitance. In this case, the response time of the detector is mainly limited by the carrier transit time. Light can be collected longitudinally or transversly to the junction, but the device parameters must be adapted for each case. For transverse light, distincion is made between normal and lateral incidences, as shown in Fig. 4.6. The normal photodiode has the advantage of simple fabrication, but the small depth achievable of the depletion region limits its efficiency, especially for longer wavelengths. On the other hand, the longitudinal photodiode usually has a better efficiency, but a trade-off has to be made between a large length to collect most of the light, but not too large to avoid high response time. The lateral configuration eliminates this trade-off as the current flow is perpendicular to the light propagation.

In the three photodiode configurations, the photogenerated current can be calculated as the sum of the currents from the depletion and the two quasi-neutral region (QNR) [264]:

$$I_{ph} = (J_{QNR,n} + J_D + J_{QNR,p})wt, \tag{4.16}$$

where $J_{QNR,n}$ and $J_{QNR,p}$ are the minority carrier diffusion current densities in the n-doped and p-doped quasi-neutral regions, respectively, J_D is the drift current density from the depletion region, and w and t are the width and thickness of the device, respectively. The depletion and diffusion mechanisms in the diode are illustrated in Fig 4.7. The generation charge profiles are also given for transverse and longitudinal illuminations.

Under uniform illumination, *i.e.*, normal and lateral light configurations, and without recombination loss, J_D is similar to a photoresistor with unitary photoconductive gain:

$$J_D = \frac{e\Phi}{t} l_D \int_0^t S(y;t)dy, \tag{4.17}$$

with l_D the length of the depletion region.

$J_{QNR,n}$ and $J_{QNR,p}$ are obtained by computing the excess carriers at the edge of the depletion region using the ambipolar equation in the

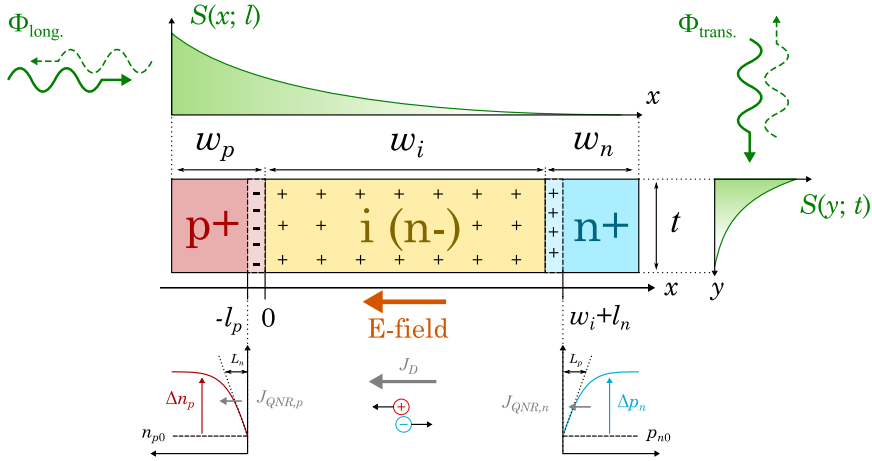


Fig. 4.7 Photodiode under transverse and longitudinal illumination, causing a photogenerated charge profile $S(y;t)$ and $S(x;l)$ along the y and x axis of the device, respectively. The profile of the excess minority carriers (Δn_p and Δp_n) in the two quasi-neutral region (QNR) are indicated in red and blue for the p-doped and n-doped region, respectively.

QNR [265]:

$$\begin{cases} \frac{\partial \Delta n}{\partial t} &= D_n \frac{\partial (\Delta n)^2}{\partial^2 x} - U_n + G_n \\ \frac{\partial \Delta p}{\partial t} &= D_p \frac{\partial (\Delta p)^2}{\partial^2 x} - U_p + G_p \end{cases} \tag{4.18}$$

where D_n and D_p are the diffusion coefficients, the recombination rates are given by $U_n = \Delta n/\tau_n$ and $U_p = \Delta p/\tau_p$, and the generation rates $G = G_n = G_p = \Phi\eta_e/t$.

These equations are solved by considering a long diode with only photogenerated excess carriers far in the QNR, *i.e.*, $\Delta n_p(-\infty) = G\tau_n$ and $\Delta p_n(\infty) = G\tau_p$, and no carriers at the edge of the depletion region, *i.e.*, $n_p(-l_p) = 0$ and $p_n(l_n + w_i) = 0$. In steady-state, the excess electron density in the p-doped region $\Delta n_p(x)$ and the excess hole density in the n-doped region $\Delta n_p(x)$ are given by

$$\begin{cases} \Delta n_p(x) &= G\tau_n - (G\tau_n + n_{p0})e^{(x-l_p)/L_n} \\ \Delta p_n(x) &= G\tau_p - (G\tau_p + p_{n0})e^{-(x-l_n-w_i)/L_p} \end{cases} \tag{4.19}$$

where $L_n = \sqrt{D_n\tau_n}$ and $L_p = \sqrt{D_p\tau_p}$ are the diffusion lengths for the electrons and holes, l_p and l_n are the depletion lengths, n_{p0} and p_{n0} are

the initial minority carrier densities in the p-doped and n-doped regions, respectively.

The diffusion current densities in the p-doped and n-doped regions are then given by

$$\begin{aligned} J_{QNR,p} &= eD_n \frac{d(\Delta n_p)^2}{d^2x}\Big|_{x=-l_p} \\ &= \frac{eD_n}{L_n}(G\tau_n + n_{p0}) \\ J_{QNR,n} &= eD_p \frac{d(\Delta p_n)^2}{d^2x}\Big|_{x=w_i+l_n} \\ &= \frac{eD_p}{L_p}(G\tau_p + p_{n0}) \end{aligned} \tag{4.20}$$

where n_{p0} and p_{n0} are the initial minority carriers density in the QNRs.

The total current, neglecting the dark current, is finally given by

$$I_{ph} = e\Phi\eta_e(L_p + l_D + L_n)w \tag{4.21}$$

4.2.3 Photogenerated current in a photodiode under longitudinal illumination

For the longitudinal pin diode, the generation is no longer uniform along the device length $G(x) = G_n(x) = G_p(x)$. In this case, the p-region of the photodetector must be much thinner than the penetration depth $1/\alpha$ to avoid photogeneration in the first QNR, which could reduce the efficiency.

To calculate the current density, the ambipolar equation (4.18) has to be solved with the generating term $G(x)$, expressed as

$$G(x) = \Phi S(x + w_p; l). \tag{4.22}$$

where $G(-w_p) = S(0; l)$ is the generation at the beginning of the photodetector.

The expression of the drift current density J_D in the depletion region is given by

$$\begin{aligned} J_D &= e\int_{-l_p}^{w_i+l_n} G(x;l)dx, \\ &= e\frac{G(-w_p)}{\alpha}e^{-\alpha(w_p-l_p)}\left(1 - e^{-\alpha l_D}\right). \end{aligned} \tag{4.23}$$

Note that the photogenerated charge profile $S(x; l)$ is now computed along the length l of the device, and no more along its thickness t. The amount of photogenerated carriers are obtained by integrating the profile

along the depletion region of length $l_D = l_p + l_n + w_i$ where l_p, l_n and w_i are the length of the depletion region in the p-doped, n-doped and the width of the intrinsic region, respectively.

For short diodes, the diffusion current $J_{QNR,p}$ in the p-type region can be computed by assuming no excess photogenerated carrier density at the electrode (ohmic contact) and no excess photogenerated carrier density at the edge of the depletion region [266], *i.e.*, $\Delta n_p(-w_p) = 0$ and $\Delta n_p(-l_p) = 0$. Furthermore, if the width w_p of the p-type region is much smaller than the diffusion length L_p, we can assume no recombination in the QNR, *i.e.*, $U_p = 0$ for $x < -l_p$. In this case, the excess carrier density Δn_p in the quasi-neutral p-doped region can be written as:

$$\Delta n_p(x) = \frac{G(-w_p)}{\alpha^2 D_n}\left(1 - \frac{x + w_p}{w_p - l_p}\left(1 - e^{-\alpha(w_p - l_p)}\right) - e^{-\alpha(x + w_p)}\right). \quad (4.24)$$

The diffusion current density in the p-region is then given by

$$J_{QNR,p} = e\frac{G(-w_p)}{\alpha^2(w_p - l_p)}\left(1 - (\alpha(w_p - l_p) + 1)e^{-\alpha(w_p - l_p)}\right). \quad (4.25)$$

For the diffusion current density $J_{QNR,n}$ in the n-type region, it is no longer necessary to assume a length w_n of the region much smaller than the diffusion length L_n. We can assume no excess carriers far into the QNR and no carriers at the edge of the depletion region, *i.e.*, $\Delta p_n(\infty) = 0$ and $p_n(w_i + l_n) = 0$.

The excess minority carrier concentration is then given by

$$\Delta p_n(x) = \frac{G(-w_p)\tau_p}{1 - \alpha^2 L_p^2} e^{-\alpha(x + w_p)} - \left(p_{n0} + \frac{G(-w_p)\tau_p}{1 - \alpha^2 L_p^2} e^{-\alpha(w_p + w_i + l_n)}\right) e^{-(x - w_i - l_n)/L_p}. \quad (4.26)$$

In this case, the diffusion photocurrent is

$$J_{QNR,n} = e\frac{G(-w_p)}{\alpha}\frac{\alpha L_p}{1 + \alpha L_p} e^{-\alpha(w_p + w_i + l_n)}. \quad (4.27)$$

The total photocurrent is finally calculated as the sum of the two diffu-

sion current of the QNR and the drift current from the depletion region:

$$I_{ph} = ewt\frac{G(-w_p)}{\alpha}\left(\frac{1-e^{-\alpha(w_p-l_p)}}{\alpha(w_p-l_p)} - \frac{e^{-\alpha(w_p-l_p)}e^{-\alpha l_D}}{1+\alpha L_p}\right). \tag{4.28}$$

The quantum efficiency is then expressed as

$$\eta_e = \eta_i\frac{(1-r_1)}{1-r_1r_2e^{-2\alpha l}}(1+r_2e^{-\alpha l})\left(\frac{1-e^{-\alpha(w_p-l_p)}}{\alpha(w_p-l_p)} - \frac{e^{-\alpha(w_p-l_p)}e^{-\alpha l_D}}{1+\alpha L_p}\right). \tag{4.29}$$

For low absorption coefficients, the light does not contribute to the current density of the p-type QNR and the photocurrent is expressed as

$$I_{ph} = ewd\frac{G(-w_p)}{\alpha}\left(1 - \frac{e^{-\alpha l_D}}{1+\alpha L_p}\right). \tag{4.30}$$

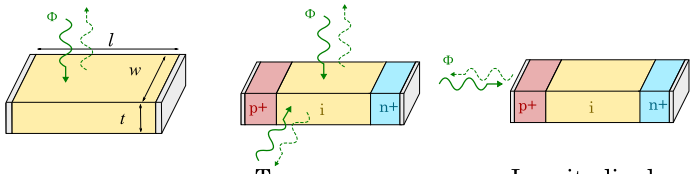
In addition, the photogenerated current becomes close to the ideal limit with a depletion length l_D long enough compared to the penetration depth $1/\alpha$:

$$I_{ph} = e\eta_i\Phi wt(1-r_1). \tag{4.31}$$

Figure 4.8 shows the comparison in quantum efficiency η_e, effective area A_{eff} and photoconductive gain g for the three types of devices: a photoresistor, a pin photodiode illuminated transversely (normal or lateral) and a pin photodiode illuminated longitudinally. A photoresistor is the simplest device, but suffers from a significant dark current, making it unsuitable for low light applications, although the sensitivity of the photogenerated current could be similar to that of a photodiode. On the other hand, a photodiode has a very low dark current, which makes light detection at low intensities much easier. In the normal or lateral configuration, the pin structure is uniformly illuminated and the effective area collecting light is defined by the depletion length and the diffusion length. In other words, the area deep in the QNR plays no part in the photogenerated current. Bringing light longitudinally into the pin structure does not suffer from this limitation, but requires careful design of the first QNR to avoid the generation of carriers that recombine before being collected. Due to fabrication constraints that limit the depth of the doped region, normal configurations are preferred for short wavelength detection, while transverse and longitudinal illumination are required for low absorption coefficient

at higher wavelengths.

$$I_{ph} = e\eta_e A_{eff} \Phi g$$



	Photoresistor	Transverse photodiode	Longitudinal photodiode
g	$\left(\frac{\tau_n}{\tau_{tr,n}} + \frac{\tau_p}{\tau_{tr,p}}\right)$	1	1
A_{eff}	$w\ l$	$w\ (L_n + l_D + L_p)$	$w\ t$
η_e	$\eta_i \frac{(1-r_1)}{1-r_1 r_2 e^{-2\alpha d}}(1+r_2 e^{-\alpha t})(1-e^{-\alpha t})$	$\eta_i \frac{(1-r_1)}{1-r_1 r_2 e^{-2\alpha l}}(1+r_2 e^{-\alpha l}) \times \left(\frac{1-e^{-\alpha(w_p-l_n)}}{\alpha(w_p-l_n)} - \frac{e^{-\alpha(w_p-l_n)} e^{-\alpha l_D}}{1+\alpha L_p}\right)$	

Fig. 4.8 Summary of the photoconductive gain g, the effective area A_{eff} and the quantum efficiency η_e used to calculate the photogenerated current I_{ph} for a photoresistor, a photodiode hit transversly by light and a photodiode hit longitudinally by light.

4.2.4 Responsivity

The responsivity R_i measures the effectiveness of a photodetector in converting incident optical power into an electrical signal. It is defined as the ratio between the photocurrent I_{ph} from the photodetector and the incident optical power P_{opt} and is expressed as

$$R_i = \frac{I_{ph}}{P_{opt}} = \frac{I_{ph}}{\Phi A_{eff} \hbar\omega}, \tag{4.32}$$

where Φ is the photon flux per unit area, $\hbar\omega$ is the photon energy and A_{eff} is the effective area collecting the incoming light. Higher values of responsivity indicate that the photodetector can generate more electrical

signal for a given amount of light, which translates into higher sensitivity. The link with quantum efficiency is easily made by considering the number of incident photons instead of the optical power, resulting in

$$\eta_e = R_i \hbar \omega \tag{4.33}$$

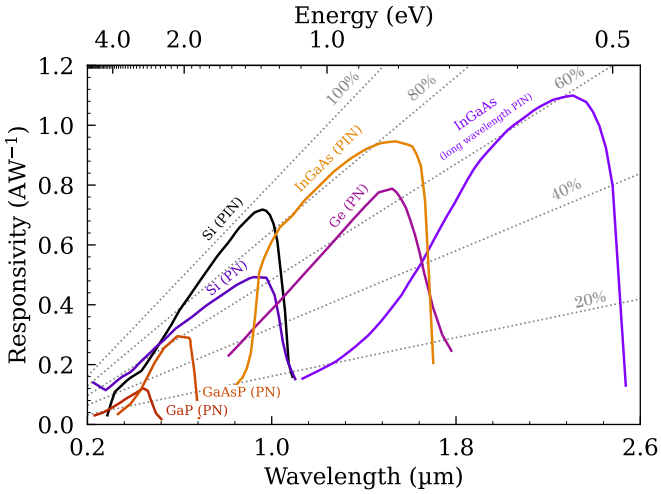


Fig. 4.9 Responsivity of typical semiconductor photodetectors at 300 K with regards to the light wavelength in visible and infrared region, adapted from [260]. The curves for the quantum efficiency levels are indicated with gray dotted lines every 20%.

Figure 4.9 shows the comparison of responsivity for photodiodes made from typical semiconductor materials for visible and near infrared applications. As expected, silicon performs well up to 1 µm. Above this wavelength, InGaAs or Ge photodiodes are commonly used. At even higher wavelengths, InGaAs detectors with higher indium content are chosen. In the visible, NIR and SWIR only photodiode or CCD detectors are used. Photoconductors are preferred at higher wavelengths where their lack of sensitivity is outweighed by their wide detection range and ease of fabrication. While responsivity measures the sensitivity of the photodetector, the detectivity D is a measure of the ability to detect weak signals in the presence of noise. It takes into account the noise that is inherent in any detector, whether it is thermal variation, shot noise or dark current. A higher value of the detectivity indicates that the photodetector is more effective at

distinguishing weak optical signals from the noise floor. Although other semiconductors can also achieve high quantum efficiency, silicon photodetectors offer competitive detectivity due to their low noise and optimised performance [267]. Their cost effectiveness and low dark current make them suitable for many applications. Figure 4.10 shows the detectivity of a typical photodetector, including InGaAs and Ge photodiodes at higher wavelengths.

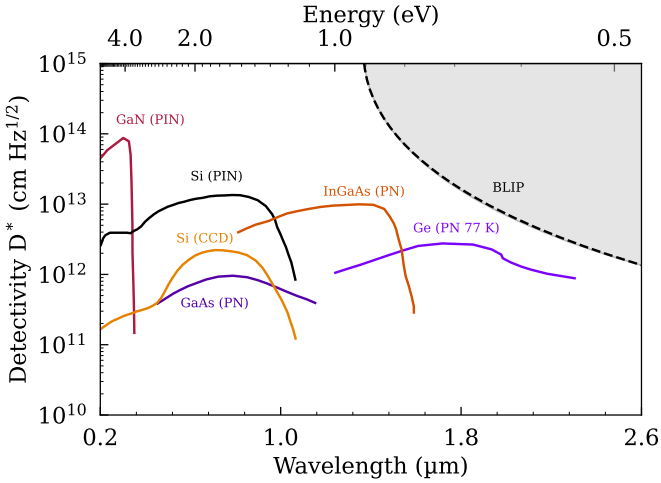


Fig. 4.10 Detectivity of typical semiconductor photodetectors at 300 K with regards to the light wavelength in visible and infrared region, adapted from [260]. The background-limited infrared photodetector (BLIP) limit is indicated in gray area. PN and PIN stand for photodiode detector while CCD stands for charge-coupled device.

In this work, we assume that the main effect of strain is the increase in sensitivity, but the effect on noise has yet to be demonstrated. A basic assumption would be that the detectivity shows the same increase as the responsivity, without considering any changes in noise level due to strain. For this reason, only the responsivity is examined in the following section.

4.3 TCAD simulation of a photodiode

This section shows the results of TCAD simulations for pin photodiodes made of strained silicon. We start by introducing the photodiode design

and the light configurations considered. The results show the responsivity improvement due to strain but also the variations in the time response. Finally a comparison is made with standard IR photodetector.

4.3.1 Photodiode design

Figure 4.11 shows the structure of the pin photodetector studied. Among the photodetector types discussed in the previous section, pin detectors show the highest responsivity and detectivity, thanks to the advantages of having an intrinsic region to absorb light over a large area, while reducing the junction capacitance for better time response.

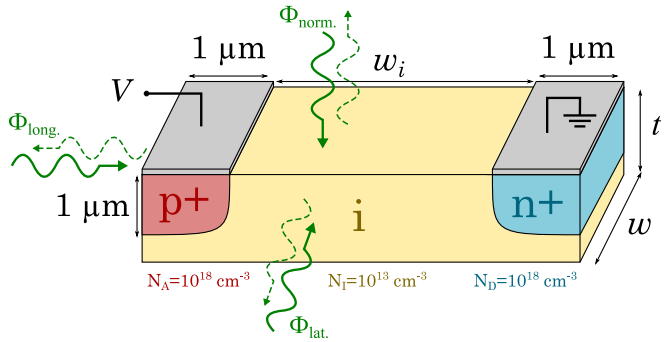
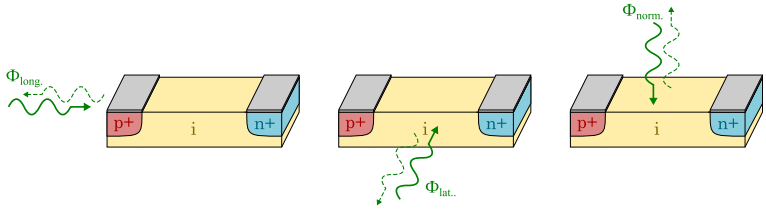


Fig. 4.11 Illustration of the pin photodiode simulated using TCAD tool. The device is formed by two doped region (p-type in red and n-type in blue) about 10^{18} cm^{-3} surrounding an n-type low-doped region (in yellow) about 10^{13} cm^{-3}, close to the intrinsic concentration in silicon. The depth of the doped junctions is of 1 µm, same as the electrode width. The length of the intrinsic region (w_i), the thickness (t) and the width (w) of the device are design parameters. The three types of light configuration, *i.e.*, longitudinal, lateral and normal, are shown by green arrows.

Three light configurations will be analysed and discussed in the following sections, namely light incident on the photodetector normally, laterally and longitudinally, as shown in Fig. 4.11. The first configuration is mainly used at low wavelengths, while the other two can be used for IR detection, but the time response would be different following lateral or longitudinal light coupling.

The simulation has been carried out using finite element TCAD simulation as implemented in *Silvaco Atlas*. The longitudinal component of the

mobility of silicon strained up to 4% in the [110] direction has been calculated using ABINIT software [108, 187], with the methodology described in chapter 2. The model of Masetti *et al.* [177] is then used to calculate the impurity dependent mobility as implemented in *Silvaco Atlas*. The absorption coefficient obtained with EPW code in chapter 3 is used to describe the change in light absorption as silicon undergoes uniaxial strain in the [110] crystal direction.



	Longitudinal	Lateral	Normal
Light coupling	*Transverse coupling needed*	*Transverse coupling needed*	*Easy*
Responsivity	*High bias for higher wavelength*	*Independent of depletion length*	*Bad at higher wavelength*
Time response	*Dependent on responsivity*	*Independent of responsivity*	*Independent of responsivity*

Fig. 4.12 Comparison between the three types of light configurations hitting a pin photodetector. The configurations are compared with respect to the ease of light coupling, the responsivity and the time response. Green, orange and red fonts are for positive, nuanced and negative behaviors.

The photodiode can be illuminated in three different directions: (i) normal to the top surface, (ii) longitudinal to the current flow in the device and along the pin structure, and (iii) lateral to the pin structure and the current flow. Figure 4.12 shows an illustration and comparison of the three configurations. The normal configuration is the simplest, both in terms of fabrication and light coupling. It works well at high absorption, when a few microns are enough to absorb most of the light power. However, the responsivity is poor at higher wavelengths because there is a limit to the depth of the depletion region when the device is biased using top electrodes. For this reason, the longitudinal configuration is preferred for IR absorption. Longitudinal photodetectors are usually fabricated vertically

with a high-doping region and electrodes on the top and bottom of a standard bulk silicon wafer. However, this fabrication scheme is incompatible with high strain techniques that require limited silicon thickness or suspended structures. For an equivalent length along the light propagation path, the longitudinal and lateral configurations have the same responsivity. However, light propagation is independent of the gap between the electrodes in the lateral configurations, making the time response of such a device independent of responsivity. In addition, the high depletion length required to absorb IR light in the longitudinal configuration results in a high bias voltage, which can be challenging. Finally, it is important to note that the light coupling and electrode contact should be compatible with the advanced fabrication scheme to strain the device. As most high-strain samples are obtained using suspended nanowires or beams, the longitudinal configuration appears to offer the most straightforward integration with the highly doped region placed at the anchor of the suspended structure.

The devices studied in this work are formed by a low n-doped region at 10^{13} cm^{-3} [268, 23], forming the so-called intrinsic region, surrounded by p-doped and n-doped regions at 10^{18} cm^{-3}. The width of the two highly doped regions is set to 1 µm, while the depth of the doped region is set to 1 µm. In fact, deep doped regions above a few microns are difficult to find due to the physical limitations of the ion implantation process [269]. The p- and n-doped regions are covered with a transparent metal layer to form a contact that is assumed to be ohmic. A negative bias is applied to the anode of the photodiode to operate in the reverse mode. The bias is set to achieve complete depletion of the intrinsic region. Theoretically, the depletion in the intrinsic (low-doped n-type) region of the p^+i junction is given by

$$l_n = \sqrt{\frac{2\varepsilon}{e}\frac{N_A}{N_I(N_A+N_I)}(\phi_0 - V)}, \tag{4.34}$$

where ε is the permittivity of silicon, N_A is the acceptor concentration of the p-doped region, N_I is the donor concentration of the intrinsic region, V is the bias voltage and $\phi_0 = k_B T/q \ln(N_A N_I/n_i^2)$ is the built-in potential. The intrinsic concentration n_i is 1.38×10^{10} cm^{-3} at 300 K [126]. When the acceptor concentration is several orders of magnitude higher than the concentration of the low-doped region, the depletion length no longer depends on the highly doped region. The voltage required for complete depletion of the intrinsic region is called the punch-through voltage V_{PT} and

is thus given by

$$V_{PT} = \phi_0 - \frac{e w_i^2}{2\varepsilon} N_I, \tag{4.35}$$

where w_i is the length of the intrinsic region.

Figure 4.13 shows the punch-through voltage as a function of the length of the intrinsic region w_i for an donor concentration N_I of 10^{12}, 10^{13} and 10^{14} cm^{-3}. The voltage to be applied is directly proportional to the doping concentration. A low value is then desired to limit the voltage to be applied, but high silicon purities leading to 10^{12} cm^{-3} are not easily achieved. For this reason we choose a value of 10^{13} cm^{-3} for the intrinsic region. At this doping level, the intrinsic region w_i is already depleted up to 10 µm without external bias, while an additional voltage up to about -75 V is required to achieve full depletion of a 100µm-thick intrinsic region w_i. The dots in Fig. 4.13 indicate the voltage required for the values of w_i studied in this work, *i.e.*, 1, 5, 10, 20, 50 and 100 µm.

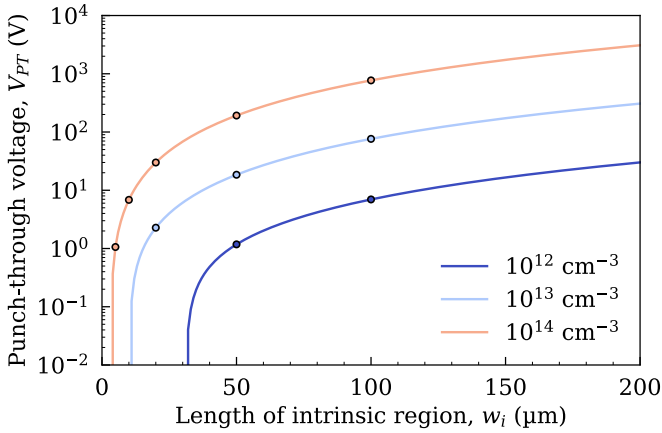


Fig. 4.13 Minimum bias voltage needed for a full depletion of the intrinsic region, called punch-through voltage V_{PT}, with regards to the length of this region w_i. The results have been computed for doping concentration of 10^{12} cm^{-3} (dark blue), 10^{13} cm^{-3} (light blue), and 10^{14} cm^{-3} (orange).

4.3.2 Strained photodiode under normal illumination

Figure 4.14 shows the calculated responsivity for a photodiode under normal illumination without ARC for several thicknesses t. The length of the

intrinsic region w_i is 20 µm and the device operates under a reverse bias of -3 V for a full depletion between the electrodes. The device has a width w of 1 µm while the thickness t varies from 1 µm to 50 µm. It is clear that the sensitivity increases with strain, showing an absorption tail up to 1.8 µm for thicker devices. However, thick devices such as the 50µm-device do not show better performance than the 20µm-device.This is due to the limited depth of the depletion region as illustrated by the inset of Fig. 4.14. In this configuration with metallic contacts on top of the device, the achievable depth of the depletion region is limited. This causes the loss of the photo-generated carriers for light at higher wavelength that penetrates deep into the material, *i.e.*, beyond the depletion region. These carriers generated outside the depletion region tend to recombine before being collected.

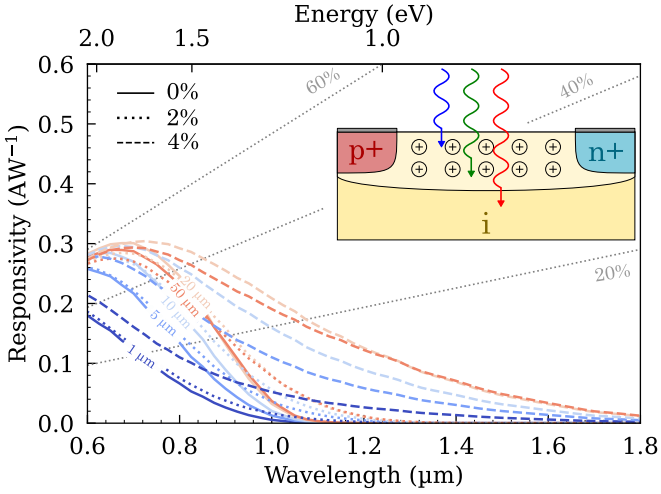


Fig. 4.14 Responsivity according to the light wavelength for a pin photodiode illuminated normally to its top surface made of silicon strained at 0% (solid), 2% (dotted) and 4% (dashed). The device is 1µm-wide and the length of its intrinsic region w_i is 20 µm. Results have been obtained for a thickness t of 1, 5, 10, 20 and 50 µm. The dotted grey lines indicate the quantum efficiency levels every 20%.

Compare to the calculation of the optical power absorbed in a silicon layer with TMM, the TCAD simulations tackle the electrical losses due to the recombination mechanisms. TMM only studies the fraction of optical power that is absorbed and the generation photocarriers, but excludes the study of the transport mechanism and the collection of the carriers at

the electrodes. For limited thickness with a full-depletion across the depth of the silicon layer, the results for the absorption power calculated using TMM in Fig. 4.2 is similar to the TCAD results of the quantum efficiency as nearly all the photogenerated carriers are collected. However, for thicker devices the quantum efficiency is significantly reduced by the recombination mechanism outside the depletion layer and differs from the TMM results.

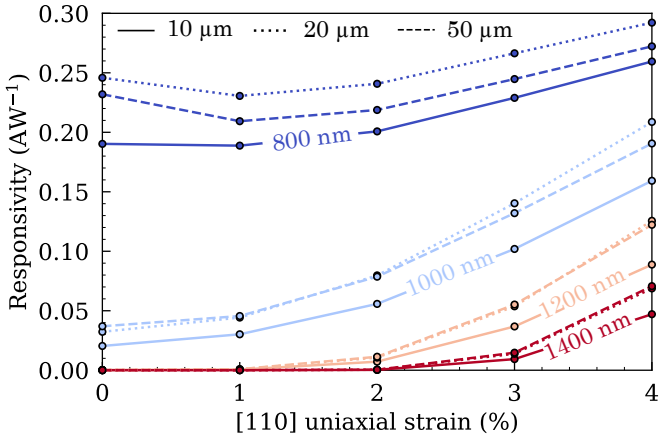


Fig. 4.15 Responsivity according to the strain for a pin photodiode illuminated normally to its top surface by a light at 800 nm, 1000 nm, 1200 nm and 1400 nm. The results are obtained for device with thickness of 10 µm (solid), 20 µm (dotted) and 50 µm (dashed).

Figure 4.15 shows the variation of responsivity with strain for light with wavelengths of 800, 1000, 1200 and 1400 nm. The figure shows the results obtained for devices with a thickness t of 10, 20 and 50 µm. As expected, strain allows higher wavelength light to be absorbed, but the responsivity of the 50µm-thick device shows limited improvement at lower wavelength such as 800 nm. It is even less sensitive at 50 µm than 20 µm due to the additional distance of the back interface which reflects part of the light reaching the end of the device. A significant improvement is made for light at 1000 nm, close to the detection limit of relaxed silicon, with the responsivity going from 0.03 AW^{-1} to 0.2 AW^{-1} for a 20µm-thick device at 4%-strain. Even in this case, this corresponds to a quantum efficiency of only 25%, far from the ideal responsivity of 0.8 AW^{-1} we might expect. However, it should be noted that the device starts to absorb 1200 nm and

1400 nm light for strains above 1% and 2%, respectively. Indeed, the absorption coefficient goes above 0.5 cm^{-1} for 1200nm-light at 1%-strain and for 1400nm-light at 2%-strain, as shown in Fig. 3.11.

In order to take advantage of the improvement in absorption coefficient due to strain in the IR region, the longitudinal and lateral configuration must be considered, as light with normal incidence on the device has been found to be unsuitable for high wavelength detection, even at 4%-strain.

4.3.3 Strained photodiode under longitudinal and lateral illumination

A longitudinally illuminated photodetector allows the full length of the depletion region w_i to be used to absorb IR light. However, complete depletion of the intrinsic region is required to absorb light to the end of the device. Figure 4.16 shows the responsivity of a photodiode with an intrinsic region of 50µm-long illuminated in the longitudinal direction. The width w and thickness t of the device are both 1 µm.

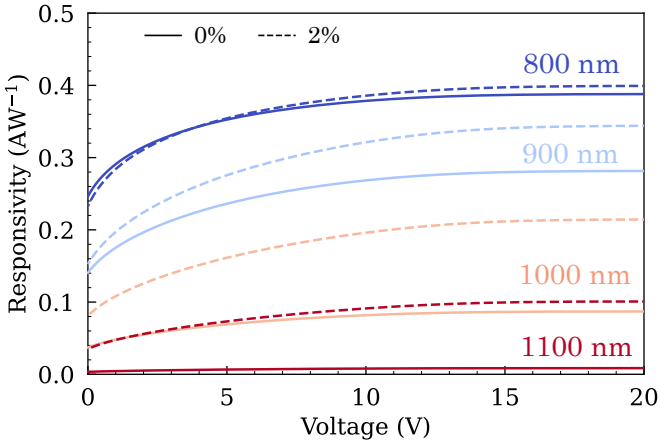


Fig. 4.16 Responsivity according to the bias voltage for a 50µm-long pin photodiode illuminated longitudinally for a strain of 0% (solid lines) and 2%-strain (dashed lines). The results are shown for light with a wavelength of 800 nm (dark blue), 900 nm (light blue), 1000 nm (orange) and 1100 nm (red).

The calculated punch-through voltage is −18.4 V but the responsivity gets close to its peaks at lower voltage thanks to the diffusion process that helps to absorb light, even outside the depletion region.For doping level

of 10^{18} cm^{-3}, the diffusion lengths for the minority carriers in the n-doped and p-doped region are about 20 µm [270] and 40 µm [271], respectively.

The strain provides a significant increase in responsivity at higher wavelengths, while lower wavelengths such as 800 nm are not better absorbed. Indeed, the responsivity is already close to its maximal value without ARC about 0.4 AW^{-1} at 0%-strain as the absorption coefficient is high enough to absorb most of the light along a length of 50 µm.

The responsivity results for the photodiode illuminated longitudinally are shown in Fig. 4.17 for a length of the intrinsic region w_i between 1 µm and 100 µm. The results for a length of 20, 50 and 100 µm have been obtained for bias voltages of −3, −20 and −75 V, respectively, while a bias voltage of −1 V has been chosen for the other values. The results were obtained without ARC, so the maximum quantum efficiency achieved is about 65%, which limits the maximum value of responsivity. The increase

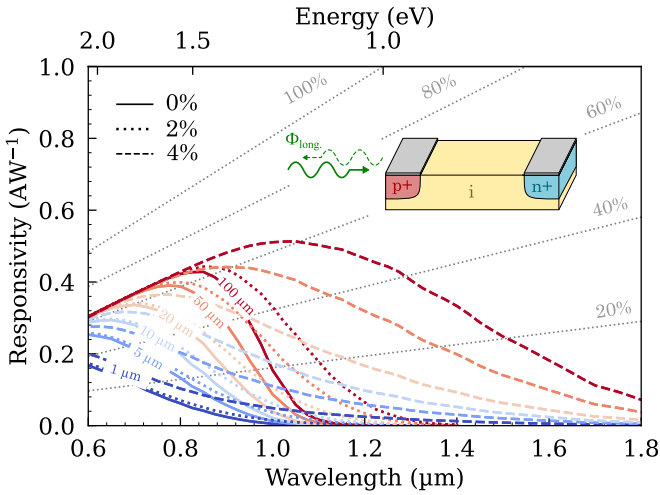


Fig. 4.17 Responsivity according to the light wavelength for a pin photodiode illuminated longitudinally, made of silicon strained at 0% (solid), 2% (dotted) and 4% (dashed). The device has a width w and a thickness t of 1 µm. Results have been obtained for a length of the intrinsic region w_i of 1, 5, 10, 20, 50 and 100 µm. The dotted grey lines indicate the quantum efficiency levels every 20%.

in absorption in the NIR with increasing thickness t is clearly visible, even in the absence of strain. In fact, a thickness of 1 µm is not sufficient to reach the maximum efficiency of 65%, whereas a 10µm-thick device starts

to reach this efficiency. For the 50µm- and 100µm-thick devices, the edges of the responsivity begin to approach the ideal limit of silicon at a wavelength of 1.1 µm. As the strain increases, this limit is pushed at higher wavelengths. This phenomenon is also visible for thinner devices, but the responsivity remains low in these cases. At 2%-strain, a 100µm-long device can absorb light up to 1.3 µm, pushing the 1.1µm-limit of relaxed silicon. At 4%-strain, the responsivity limit is pushed beyond 1.8 µm, with significant absorption in the NIR. A quantum efficiency of around 20% is even achieved at 1.5 µm, the preferred band for optical communications.

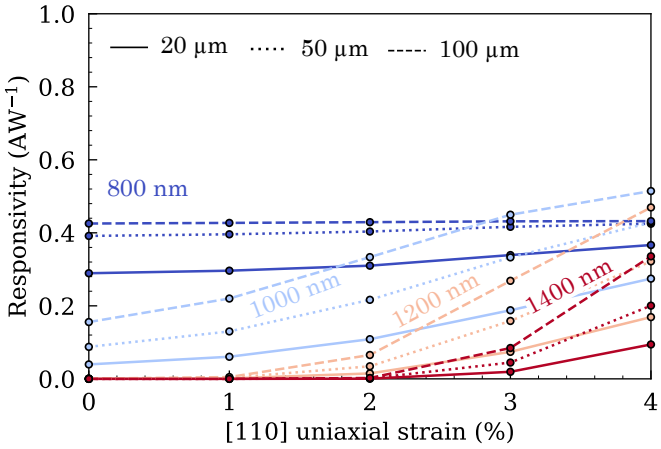


Fig. 4.18 Responsivity according to the strain for a pin photodiode illuminated longitudinally by a light at 800 nm, 1000 nm, 1200 nm and 1400 nm. The simulated results are obtained for a length of the intrinsic region of 20 µm (solid lines), 50 µm (dotted lines) and 100 µm (dashed lines).

Figure 4.18 shows the increase in responsivity with strain for wavelengths of 800, 1000, 1200 and 1400 nm and for device with intrinsic length w_i of 20, 50 and 100 µm. The responsivity increases with the length as more carriers are generated in the device. This is particularly critical at wavelengths where silicon has a low absorption coefficient. At 800 nm, the responsivity does not show a significant improvement between 50 and 100 µm, as the device is already long enough to absorb most of the light at 50 µm.

Strain also has no significant effect at 800 nm as the absorption coefficient is not significantly improved. At higher wavelengths, strain has a

significant effect, as seen for the 1000 nm wavelength, where the responsivity reaches about 0.5 AW^{-1} at 4%-strain. At 2%-strain, 1400nm-light starts to be absorbed and a responsivity of about 0.3 AW^{-1} is reached at 4%.

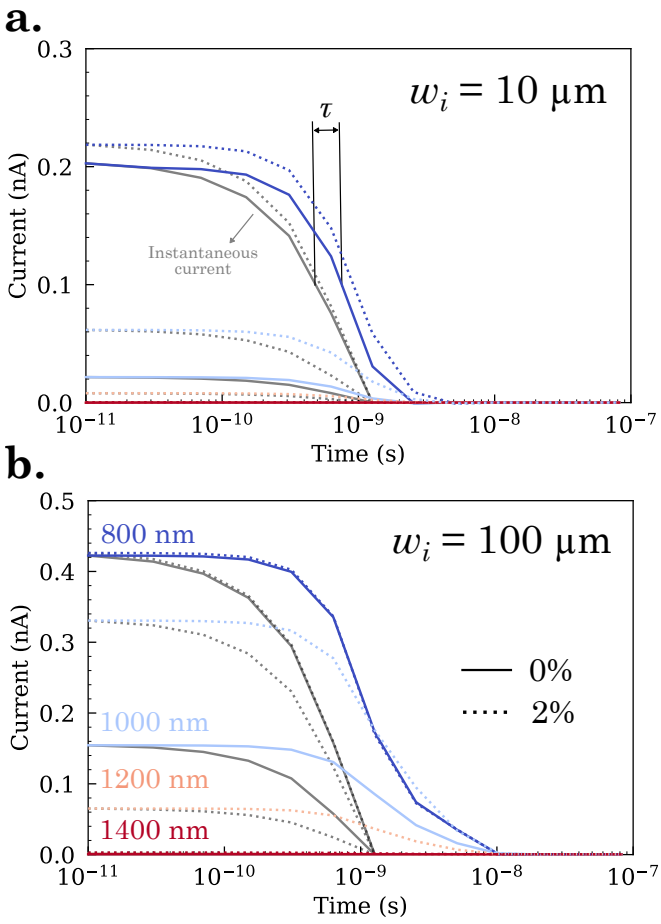


Fig. 4.19 Time response of a pin photodiode illuminated longitudinally by a light at 800 nm, 1000 nm, 1200 nm and 1400 nm for a length of the intrinsic region w_i of (a) 10 µm and (b) 100 µm. The delay τ is defined when the photocurrent reaches half its initial level. The instantaneous current, indicated in grey lines, is the current following the light ramp taking 1 ns to turn off. The results are shown for silicon undertaking uniaxial strain of 0% (solid lines) and 2% (dotted lines).

Figure 4.19 shows the time response of the longitudinal photodiode un-

der light pulses of 800, 1000, 1200 and 1400 nm, which are switched off in 1 ns. The increase in responsivity due to strain can be seen through the increase of the initial current value, while the time constant τ has been calculated at half the current amplitude. Results are given for a length of the intrinsic region w_i of 10 µm and 100 µm. As expected, the smaller the length, the lower the responsivity, especially at higher wavelengths, but the smaller the time constant. The time response increases threefold between a length of 10 µm and 100 µm, from 0.3 ns to 1 ns at 1000 nm.

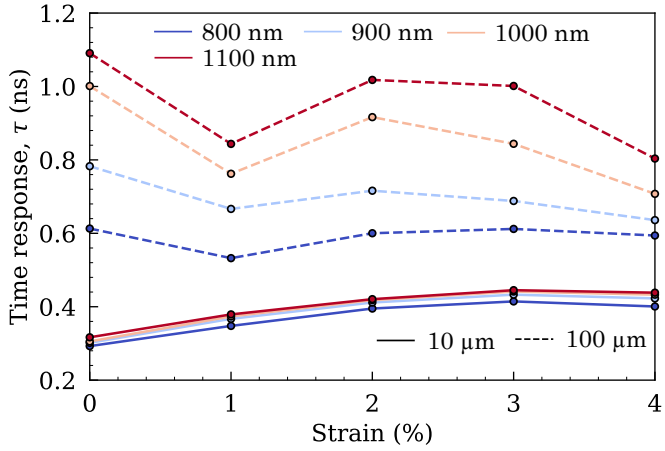


Fig. 4.20 Time response with regards to strain of a pin photodiode illuminated longitudinally by a light at 800 nm, 900 nm, 1100 nm and 1200 nm for a length of the intrinsic region of 10 µm (solid lines) and 100 µm (dashed lines). The delay τ is defined when the photocurrent reaches half its initial level.

The general trend of mobility reduction causes the time response to increase with strain, as shown in Fig. 4.20. With increasing strain, the phonon-limited hole mobility decreases monotonically from 608 $cm^2V^{-1}s^{-1}$ to 300 $cm^2V^{-1}s^{-1}$ at 4%-strain, while the electron mobility shows a sharp increase from 1366 $cm^2V^{-1}s^{-1}$ to 2071 $cm^2V^{-1}s^{-1}$ at 1%, followed by a decrease to 1204 $cm^2V^{-1}s^{-1}$ at 4%, as shown in section 2.2.6 of chapter 2. For a 10µm-thick device the time response goes from 0.3 ns to 0.4 ns for light of 1000nm-wavelength. For longer devices, the trend is less clear. Indeed, a first effect is to increase the absorption coefficient, which reduces the distance the light has to travel to generate carriers. This can be seen at high strain and at higher wavelengths, *i.e.*,

beyond 900 nm, as the time response decreases between 2%- and 4%-strain due to the absorption enhancement caused by strain. At lower strains, the enhancement of the electron mobility cause the time response to decrease at 1%-strain for 100µm-device before rising again at 2%-strain due to the non-monotonic behavior of the electron mobility. For 10µm-device, the decrease in hole mobility causes the increase of the time response.

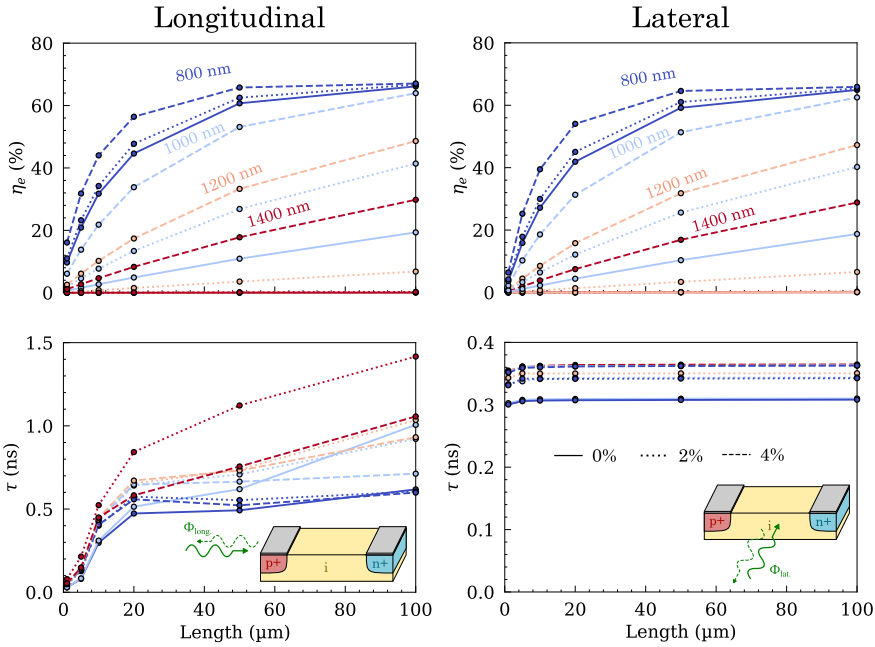


Fig. 4.21 Quantum efficiency η_e and time response τ according to the length aligned with the light propagation of a pin photodiode illuminated longitudinally and laterally by a light at 800 nm (dark blue), 1000 nm (light blue), 1200 nm (orange) and 1400 nm (red). The results are shown for silicon strained at 0% (solid lines), 2% (dotted lines) and 4% (dashed lines).

The responsivity of a photodetector with light incident laterally to the device is the same as in the longitudinal configuration, as long as the device is properly designed with complete depletion of the intrinsic region. This is shown in the quantum efficiency results in Fig. 4.21. With increasing length, the efficiency increases if the absorption wavelength limit is higher than the light wavelength. Thus, 1200nm- and 1400nm-light are not absorbed in the absence of strain, but the 100µm-long device can reach efficiencies of 30% and 48% at 4%-strain, respectively. For lower wavelengths,

such as 800 nm, there is no improvement for a length of 100 µm because the it is sufficient to absorb all the light entering the device even in the absence of strain. The 35% loss in this case is due to optical reflection at the air-silicon interface.

The main difference between the lateral and longitudinal configurations is the dependence of the time constant on the length. The time constant for the longitudinal configuration increases with the length of the device, whereas it remains constant for the lateral configuration. The results shown in this configuration are obtained for a length of 10 µm for the intrinsic region, giving a time response of about 0.3 ns in the absence of strain. Strain only slightly increased the time constant up to 0.36 ns due to the reduction in hole mobility. Furthermore, strain reduces the time constant for the longitudinal photodetector, as the increase in absorption coefficient allows carriers to be generated closer to the contact region. This is particularly evident at wavelengths of 1000 nm and above, with a reduction from 1 ns in the absence of strain to 0.7 ns.

4.3.4 Strained photodiode with antireflective coating

Figure 4.22 shows the results obtained for a photodetector illuminated longitudinally with ARC at the front interface and a metallic reflective layer at the back, allowing total reflection at the end of the device. Similar to previous calculations, devices with intrinsic region lengths w_i of 1, 5, 10, 20, 50 and 100 µm and a width w and thickness t of 1 µm are considered. The antireflective layer significantly increases the responsivity of the devices, allowing a quantum efficiency of up to 90% at 900 nm in the absence of strain for a 100µm-long device. The efficiency is even closer to 100% at 1050 nm under 4%-strain, while an efficiency of 40% is maintained at 1500 nm. 2%-strain is sufficient to extend the 20% efficiency limit from 1050 nm to 1180 nm. The effect of the reflective layer at the back is similar to increasing the length of the device, as light propagating to the end is reflected back into the device. This has a significant effect, but only at wavelengths where most of the light is not absorbed along the length.

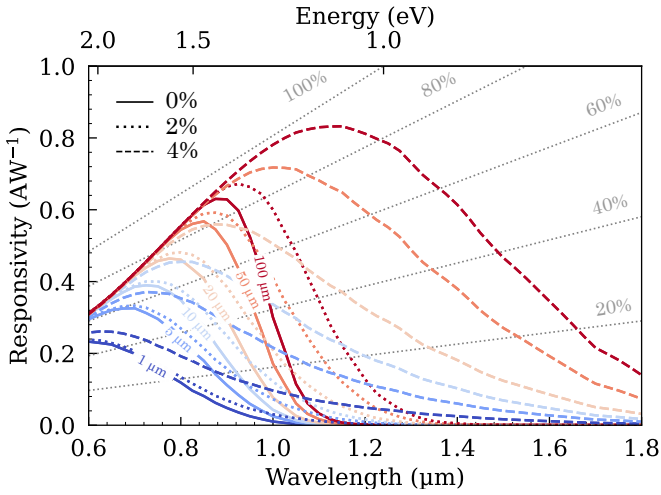


Fig. 4.22 Responsivity according to the light wavelength for a pin photodiode illuminated longitudinally with ARC at its front interface and reflective layer at its back. The results are obtained for silicon strained at 0% (solid), 2% (dotted) and 4% (dashed). The device has a width and a thickness of 1 µm. Results have been obtained for a length of the intrinsic region of 1, 5, 10, 20, 50 and 100 µm. The dotted grey lines indicate the quantum efficiency levels with steps of 20%.

The improvement in responsivity due to strain at 800, 1000, 1200 and 1400 nm is shown in Fig. 4.23. The 800 nm light does not show a clear improvement as the length is sufficient for the light to be fully absorbed. However, it can be seen that the strain can help the 20µm-device to reach a responsivity closer to that of the 50µm and longer devices. For 1000 nm, the low responsivity of 0.08 AW^{-1} (resp. 0.3 AW^{-1}) in the absence of strain reaches 0.5 AW^{-1} (resp. 0.78 AW^{-1}) under 4%-strain for a 20µm (resp. 100µm) device. The strain allows the photodiode to absorb light of 1200 nm and 1400 nm from 1% and 2%-strain respectively. Responsivities of 0.8 AW^{-1} and 0.6 AW^{-1} are even achieved at 1200 and 1400 nm respectively for 4%-strain devices with a length of 100 µm.

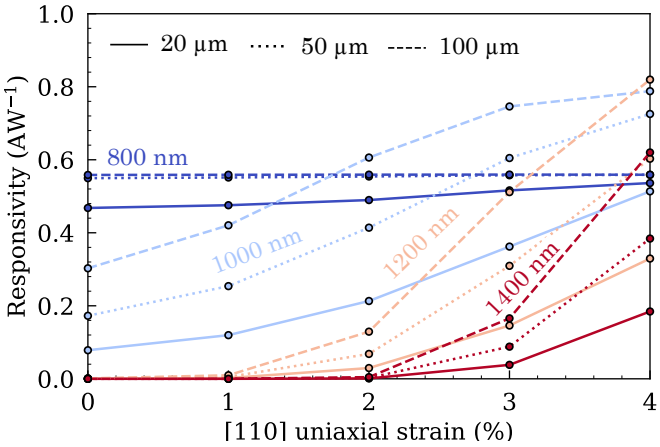


Fig. 4.23 Responsivity according to the strain for a pin photodiode illuminated longitudinally with ARC at its front interface and reflective layer at its back. The results are obtained for device with a length of the intrinsic region of 20 µm (solid lines), 50 µm (dotted lines) and 100 µm (dashed lines), illuminated by a light at 800 nm, 1000 nm, 1200 nm and 1400 nm.

The responsivity results obtained for 100µm-long devices with and without ARC are compared with typical responsivity results of other semiconductor photodetectors as shown in Fig. 4.24. At very high strains it is clear that strained silicon is a promising candidate for the NIR and even SWIR. However, it is a challenge to achieve high strain levels while producing a photodetector with the correct design, as explained in the introduction of the thesis. 2%-strain appears to be more accessible but offers only a limited increase in responsivity for 100µm-long devices. The results obtained for our photodiode in the absence of strain show a lower responsivity compared to the pin detector in the literature. A length of 100 µm already requires a bias voltage of -75 V in the longitudinal configuration for a full-depletion of the intrinsic region. In the literature, thicker devices are usually used exploiting the full thickness (up to 800 µm) of the bulk silicon wafer, for which the sharp reduction in responsivity is only limited by the band gap of the material. However, this could push the response limit down to the strain-reduced band gap, 0.93 eV at 2%-strain and 0.65 eV at 4%-strain, giving a wavelength limit of 1.33 µm and 1.90 µm respectively.

In the case of devices longer than 100 µm, we stress that the lateral

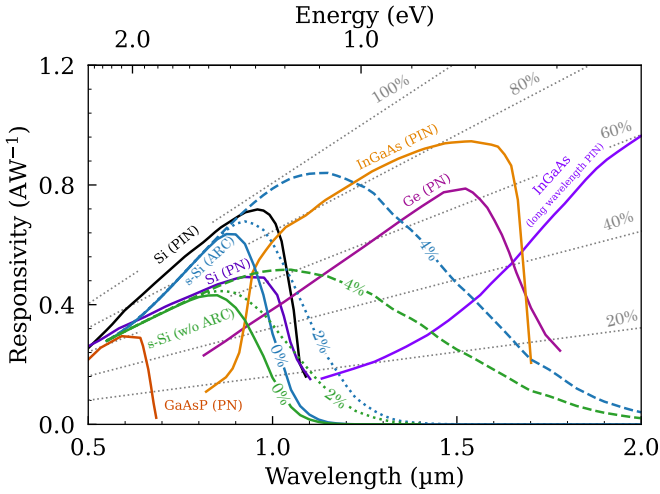


Fig. 4.24 Comparison of the responsivity of typical semiconductor photodetectors at 300 K and the results obtained for pin photodetector made of silicon strained at at 0% (solid), 2% (dotted) and 4% (dashed), with (blue) and without (green) ARC illuminated longitudinally. The curves for the results from the litterature are adapted from [260]. The dotted grey lines indicate the quantum efficiency levels with steps of 20%.

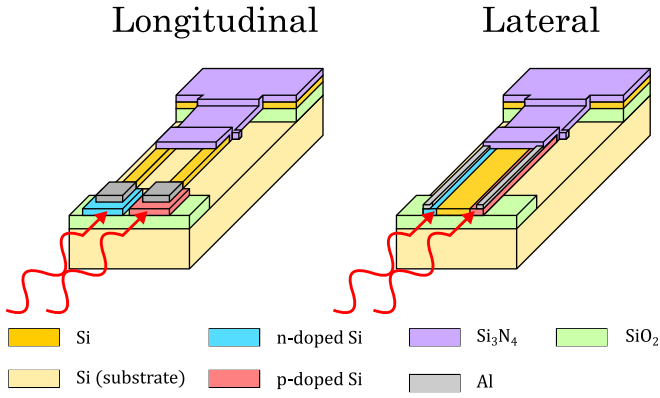


Fig. 4.25 Possible implementation for pin photodiode under lateral and longitudinal illuminations based on suspended silicon beams strained using silicon nitride actuators as developed in [147].

configuration is necessary to keep the bias voltage low enough, but the exact fabrication process of such long devices, which are strained in one

direction while maintaining contact in another along their entire length, remains unclear. Possible structures are shown in Fig. 4.25 even though the manufacturing process has yet to be established. The metallic contact for the longitudinal configuration are made at the anchor of the suspended silicon beams, while the contacts run all along the beams for the lateral configuration.

4.4 Chapter Summary

Using the mobility of strained silicon calculated in chapter 2 and the absorption coefficient calculated in chapter 3, this chapter investigates the potential of a silicon photodetector under uniaxial strain along [110] for IR light. Although strain increases silicon absorption, the transfer matrix method (TMM) has been used to determine the effective absorption that could be achieved in a silicon slab. It has been shown that a sufficient thickness, about tens of microns, is required to take advantage of the absorption enhancement in the IR region. Before examining a pin photodiode configuration in detail, the working principles of photoconductors and photodiodes have been recalled. Technology computer-aided design (TCAD) simulations have been carried out for three light couplings, normal to the photodetector surface, longitudinal to the pin structure and lateral to it. It has been shown that normal coupling works only at lower wavelengths, but fails to properly absorb IR light due to the limited depth of the depletion region. The longitudinal configuration shows high IR responsivity but reduces the time response of the photodetector for long devices. The lateral configuration allows similar responsivity without the disadvantage of increasing the time response of the photodetector. However, the need for light coupling perpendicular to the contact region increases the difficulty of integration into high strain schemes that rely on suspended structures. For a similar material length across the light propagation, both configurations show similar responsivity, with a clear increase in IR for 100µm-long devices. Efficiency of 20% is even achieved with 4%-strain at 1.5 µm, close to the typical O-band for optical communications. The responsivity can be pushed even higher by using silicon nitride antireflective coating (ARC) to achieve 35% quantum efficiency at 1.5 µm. Finally, the responsivity achieved by the strained silicon pin photodetector is compared with the typical responsivity of InGaAs and Ge photodiodes, showing its potential to compete with them.

Key messages of the chapter

- Transfer matrix method (TMM) allows the study of the dimension of a silicon layer on the absorption, essential to analyse if the increase of the absorption coefficient leads to an effective increase of the absorbed power. A thickness of at least 10 µm is needed to see a clear variation of the absorption in the IR.
- Photoconductors and photodiodes can exhibit similar responsivity if designed correctly, but the large dark current of the former configuration limits its ability to detect low light intensities. In addition, normal coupling of the light to the pin photodiode only works for lower wavelengths in the visible range, as the depth of the depletion region is limited.
- Technology computer-aided design (TCAD) simulations highlight the effect of strain on the responsivity and time response of pin photodiodes. The increase in absorption coefficient directly affects the increase in responsivity in the IR region, while the change in electron and hole mobility only affects the time response. Furthermore, in the longitudinal configuration, the increase in absorption coefficient decreases the time response as the carriers are generated closer to the first electrode.
- Lateral coupling of the light to the pin structure relaxes the trade-off between time response and responsivity in the longitudinal configuration. However, the need for contacts along the full length of the structure is difficultly compatible with high-strain fabrication schemes such as free-standing structures, as the latter have limited access to create contacts.
- A clear improvement in responsivity has been theoretically demonstrated for 100µm-long devices, although a high strain of 4% is required to compete with conventional IR photodetectors. Lower strains could give similar performance if the device length is increased even further, but careful consideration needs to be given to the fabrication scheme using highly strained structures. The performance can be further improved with antireflective coating (ARC) using silicon nitride.

Conclusion

In this work, the potential of strained silicon for infrared (IR) photodetection has been investigated. Indeed, the relatively high band gap of silicon of 1.12 eV limits its use in optical applications at wavelengths beyond 1.1 µm. These include typical near infrared (NIR) and shortwave infrared (SWIR) applications such as CO_2 monitoring or optical communications, for which germanium (Ge) or indium gallium arsenide (InGaAs) photodetectors are preferred. However, these materials involve additional extraction and environmental impacts compared to standard silicon wafer processing. They are also more expensive than large-scale silicon manufacturing processes. The motivation behind this work is therefore to find a solution for IR sensing that is compatible with the traditional silicon process. The answer we bring is based on strain engineering as a promising tool for enhancing the optoelectronic properties of semiconductors. Strain has long been known to affect the electrical mobility of semiconductors. This has been used as a standard method to improve the performance of silicon transistors in modern electronics. Although theoretical works have roughly shown that strain can affect the band structure of silicon and thus the band gap, it was not until the late 2000s that experimental works using photoluminescence (PL) demonstrated a significant reduction. At the same time, density-functional theory (DFT) was used to accurately predict the change in band structure for different strain configurations. Since then, no work has made the most of this discovery in an electronic device but recent studies by Katiyar *et al.* [56, 57]. They demonstrate experimentally the ability of silicon to absorb higher wavelengths using photoresistor or metal-silicon-metal Schottky devices, but little is known about the physical properties and their use for standard pin photodetectors. The research behind our work is therefore based on several assessments of the lack of

material and device study using strained silicon, which we have addressed in the chapters of this thesis.

- In chapter 1, we investigated the lack of exhaustive study about the band structure variations for all major strain configurations, *i.e.*, uniaxial and biaxial strain along [001], [110] and [111], allowing the band gap reduction and the variations of the effective masses to be assessed.
- In chapter 2, the lack of experimental measurements and the inaccuracy of existing theoretical models for electron mobility have been filled. Furthermore, the hole mobility for strained silicon, which was previously unattainable due to the complexity of the valence bands mechanisms, has been calculated rigorously for the first time.
- In chapter 3, we address the absence of experimental and theoretical studies for the optical properties of strained silicon, and more specifically for the absorption coefficient.
- In chapter 4, we theoretically explore the use of strain engineering in a standard pin photodiode to increase its sensitivity in the infrared (IR).

Specific findings

Chapter 1: Fundamental properties of strained silicon

In this chapter we have studied the fundamental properties of silicon for major strain configurations. Using density-functional theory (DFT) we have accurately predicted how the band structure responds to strain, particularly in terms of the band gaps and effective masses. This allows us to answer the main question of this chapter, which is to find the strain configurations that leads to the largest band gap reduction, while at the same time studying the effect of strain on effective masses and phonon energies. To the best of our knowledge, this is the first time that a detailed analysis of both biaxial and uniaxial strain along the [001], [110] and [111] directions has been carried out. In addition, this work provides detailed calculations of the effective masses for the conduction band and the three valence bands, showing how strain can significantly alter the band shapes. The effect of strain on the phonon energy is also demonstrated, with relevant

implications for Raman spectroscopy. Unlike traditional phonon deformation potential (PDP) theory, the first-principles approach captures the non-linear effects of strain and is not limited to specific strain configurations. The band gap findings show that biaxial compressive strain along [110] and tensile strain along [001] yields the most important band gap reductions of -326.5 meV and -306.6 meV at 2%-strain, respectively. As large fracture strain is more difficult to achieve using biaxial strain, uniaxial tensile configuration has been chosen as the most promising candidate for highly strained silicon. In this case, a band gap reduction of -202.9 meV at 2%-strain is found for strain along [110]. We finallly performed photoluminescence (PL) experiments on silicon beams strained up to 1% using silicon nitride stressors to confirm the theoretical predictions .

Chapter 2: Phonon-limited mobility in strained silicon

The variations in electron mobility in n-type silicon resistors have first been studied experimentally for uniaxial strain along [001] using a four-point bending scheme. The experimental results highlight the important increase in the longitudinal resistivity, showing a 50% increase at 1%-strain, while the transverse resistivity remains similar at high strain. Furthermore, a semi-empirical model allows to recover the response of undoped silicon, showing an enhancement close to 70% for the longitudinal component. These results highlight the underestimation of the existing model, in addition to the large non-linearity of the strain dependence. First-principles calculations have been performed for uniaxial strain along [001] and [110] to go into more detail behind the physical explanation and prediction of the phonon-limited mobility. The calculations, which take into account electron-phonon scattering, allow the intrinsic mobility of strained semiconductors to be studied over a wide range of temperatures or strains, bypassing the need for low-doped samples or complex experimental set-ups. It has been shown that the electron mobility is first dominated by the migration of the carriers in the lower energy valleys, causing an important increase up to 2249 $\mathrm{cm^2V^{-1}s^{-1}}$ for the longitudinal component under [001] uniaxial strain. On the contrary, uniaxial strain along [110] impact significantly the shape of the electron valleys, increasing the intravalley scattering and causing a drastic reduction in mobility at high strain down to 168 $\mathrm{cm^2V^{-1}s^{-1}}$ for the transverse component. First-principles calculations allow, for the first time, the prediction of hole mobility in strained silicon

by overcoming the difficulty of the proximity of the three valence bands. It is shown that the intraband scattering of the heavy hole (HH) band dominates the hole mobility. Furthermore, the large variations in band shape, as evidenced by the variations in effective masses, cause important changes in the hole mobility at large strains. The transverse and longitudinal components reach 1330 $cm^2V^{-1}s^{-1}$ and 1340 $cm^2V^{-1}s^{-1}$ for [001] strain of 2%, while they reach 1761 $cm^2V^{-1}s^{-1}$ and 315 $cm^2V^{-1}s^{-1}$ for [110] strain of 2%, respectively.

Chapter 3: Optical properties of strained silicon

The serious challenge of performing optical measurements on highly strained samples to observe optical properties such as refractive index and absorption coefficient has been overcome by first-principles calculations. The Bethe-Salpeter equation (BSE) method is first used within the Abinit code to calculate the dielectric function and the refractive index, taking into account the electron-hole interactions. The results show the low dependence of the zero-energy refractive index with strain, while the excitonic peak around 3.4 eV is strongly reduced. As this method does not consider electron-phonon interactions, which are essential for phonon-assisted absorption in silicon, the electron-phonon wannier (EPW) code has been employed to calculate the absorption coefficient of silicon strained along [110]. Furthermore, an analytical method is used for comparison, which showed the advantage of reduced computational cost, but based on semi-empirical parameters, which limited the accuracy of the method. Following the band gap reduction, the absorption coefficient shows a clear improvement in the IR region thanks to the strain. The effect is particularly significant in the low absorption regime, beyond the 1µm-limit of relaxed silicon. At 1.2µm-wavelength, the absorption coefficient is found to rise from 0.5×10^{-2} cm^{-1} to 168 cm^{-1} at 4%-strain.

Chapter 4: Infrared performances of strained silicon photodetector

The final chapter presents a study of the impact of strain on the infrared sensitivity of a photodiode. This is achieved through the use of TCAD simulations in conjunction with first-principles calculations of the mobility and absorption coefficient in strained silicon along [110]. We have highlighted the advantage of pin photodiode under longitudinal and lateral

light coupling to detect light at longer wavelengths. It has been shown that mobility variations mainly impact the time response of the photodetector. In contrast, the enhancement of the responsivity in the IR region is primarily attributable to the improvement of the absorption coefficient. Sufficient length along the light propagation is however needed to benefit from the absorption increase. A 20%-efficiency has been demonstrated at 1.5 µm under a strain of 4%, showing the potential for the typical O-band used in optical communications. Sensitivity can be further enhanced by using silicon nitride antireflective coating (ARC) to achieve 35% quantum efficiency at 1.5 µm. Finally, the sensitivity of the strained silicon pin photodetector is compared with the conventional sensitivity of InGaAs and Ge photodiodes, demonstrating its potential to compete with these established technologies.

Limitations and perspectives

The in-depth theoretical study carried out in this thesis highlights for the first time the potential of strained silicon for IR photodetection. Our results are largely based on advanced first-principles calculations, which allow an intrinsic understanding of the physical effects. In general, all the methodology developed in this work can be extended to most semiconductors. Indeed, the first-principles calculations, which take into account electron-phonon interactions for both optical and electrical properties, could easily be used to calculate the strain dependence of other semiconductors. The only limitation so far would be the boundary between direct absorption, which must include electron-hole interactions, and indirect absorption, which includes electron-phonon interactions. Novel methods as presented by Tiwari *et al.* [243] implement an unified theory, but this remains a recent topic . Nevertheless, the basis of any study of strain to improve detection at higher wavelengths starts with density-functional theory (DFT) to calculate the band gap variations. In addition, we have shown in this work the complementarity of using technology computer-aided design (TCAD) simulation to directly calculate the effect of the changes in material properties with strain at the device level.

We consider particularly important to emphasise the complementarity between experimental measurements and theoretical calculations. Indeed, theory is essential to understand the physical observations that can

be made, and experiments are essential to validate the theory and to bring to light unknown phenomena. We claim that this work has refined our understanding of the potential of strained silicon. However, the fabrication of a demonstrator to prove our theoretical results remains to be done. In this work, achieving strains above 1% was a major concern. Although the microfabrication scheme developed by Passi *et al.* [60] is able to reach at least 3%-strain, the thicker silicon beam of our samples compared to the thickness of the silicon nitride actuator caused premature fracture before 1%. A second way of trying to achieve high strain was the use of commercial silicon strain gauges. These gauges achieve a similar fracture strain of 1%, which is remarkable compared to the simplicity of the fabrication process of such devices. The difficulty to do optical measurements on microscopic samples or combining them with straining system was another concern. Indeed, most commercial equipment are based on large area measurements for optical transmission and reflection to study the optical absorption or the band gap variations. To solve this issue, we start to design and fabricate a homemade system to perform optical measurement through microscope objectives. However, issues remain about the sensitivity of the spectrometers and their ability to observe the small variations of the absorption coefficient due to strain.

Highly strained silicon has been shown to be achievable using uniaxial strain, but we have shown the limitation imposed by the need for lateral light coupling to detect longer wavelengths. A possible solution could be edge or grating couplers, which are widely used in photonics to collect light. In addition, silicon nitride shows the potential for multiple use as a stressor, waveguide or antireflective coating, in addition to being compatible with the standard silicon process. Even if the operating principle of the strained photodetector were to be experimentally proven, an accurate assessment of the manufacturing and its compatibility with current processes would be required. Furthermore, the strain and light coupling system would limit its use to applications where the fill factor is not a key parameter. This would therefore exclude all imaging applications, but would point to applications where a single high performance device is required, such as optical communications. An additional limitation is the indirect band gap of silicon, which will always limit the absorption coefficient of the photodetector compared to a direct band gap material such as InGaAs. Furthermore, silicon can suffer from a relatively low electron mobility that limits the maximal speed achievable by the device.

Much work remains to be done, but we hope that the results or the

methods used in this work will open up new avenues for the development of strain engineering as a powerful tool for tuning the properties of semiconductor devices.

Appendix

A Convergence study

Figure A.1 shows the convergence of the relaxation calculation to find the lattice parameter of relaxed silicon. The lattice converges at 0.5469 nm for a planewave cutoff of 20 Ha for a **k**-points grid of $8 \times 8 \times 8$.

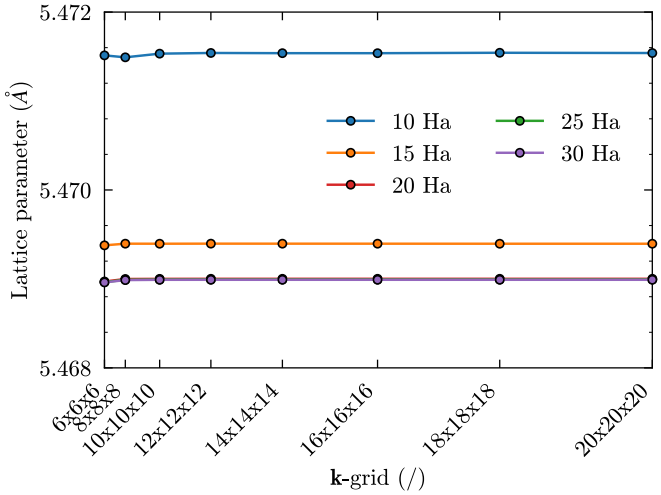


Fig. A.1 Lattice parameters with regards to the **k**-point grid and the planewave cutoff from 10 Ha (blue) to 30 Ha (purple).

The convergence study for the band gap calculation using DFT is shown in Fig. A.2 for relaxed silicon and strained at 1% along the [110] direction. The calculation are done with SOC taken into account and

under PBE GGA functional. A **k**-point grid of $10 \times 10 \times 10$ for the SCF calculation is sufficient while 20 Ha for the planewave cutoff leads to good convergence below 0.1 eV.

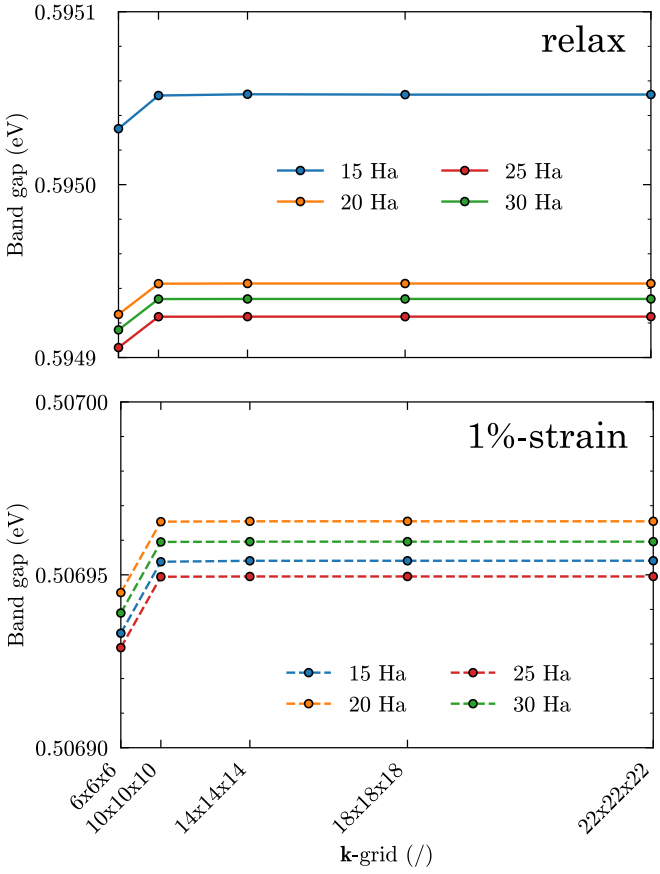


Fig. A.2 Indirect band gap calculated using DFT and PBE GGA functional with regards to the **k**-point grid and the planewave cutoff from 15 Ha (blue) to 30 Ha (green). The convergence results are shown for relaxed silicon (solid lines) and strained at 1% along the [110] direction (dashed lines).

The phonon energy are calculated using DFPT. The convergence study is performed for the energy of the optical modes at Γ. A good convergence is achieved for a **k**-point grid of $10 \times 10 \times 10$ with a planewave cutoff of 20 Ha, as shown in Fig. A.3.

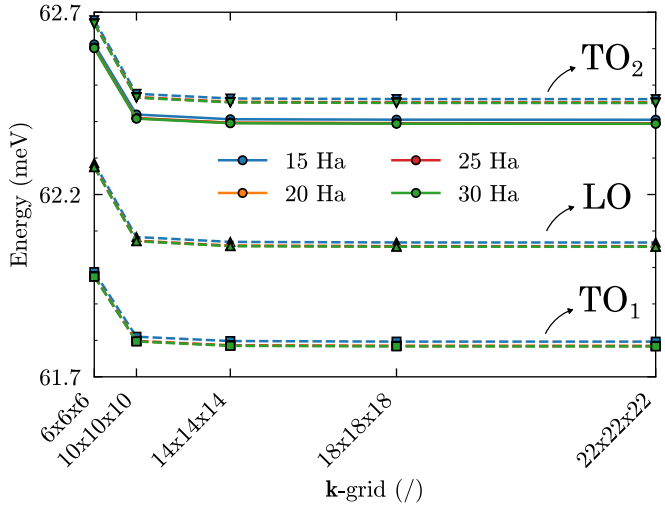


Fig. A.3 Phonon energy for the optical modes at Γ calculated using DFPT with regards to the **k**-point grid and the planewave cutoff from 15 Ha (blue) to 30 Ha (green). The convergence results are shown for the three optical modes (LO, TO_1 and TO_2) of relaxed silicon (solid lines) and strained at 1% along the [110] direction (dashed lines).

Single-shot G_0W_0 is performed to correct the band gap underestimation by taking into account the screened and coulombian many-body interactions. The calculations first include standard SCF ground-state step, followed by a NSCF run to retrieve the KS eigenvalues and eigenfunctions. Convergence for the quasi-particle correction is studied for the planewave cutoff and the **k**-point grid, as shown in Fig. A.4. Then, the screening interactions are calculated with number of bands and the cutoff for the screening interactions (dielectric matrix) as convergence parameters. Finally the quasi-particle correction is calculated based on the calculation of the self-energy matrix element Σ_x on 100 bands and a cutoff energy equal to the planewave cutoff.

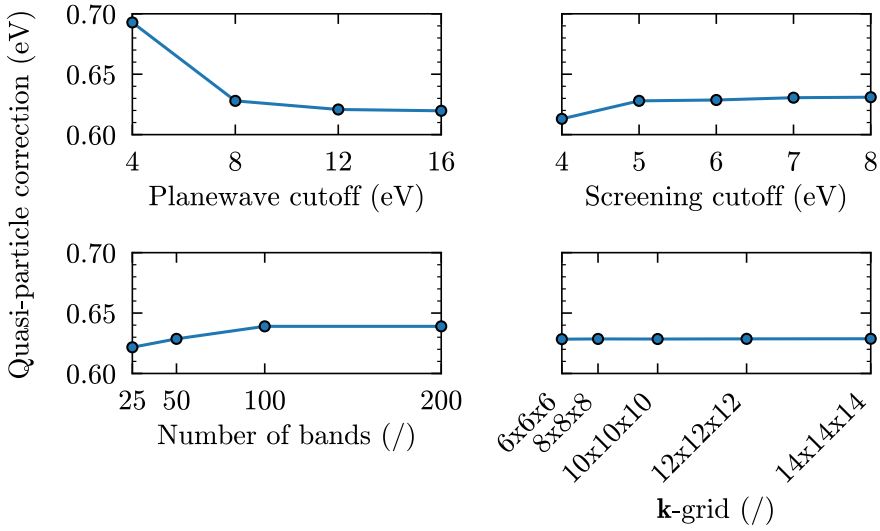


Fig. A.4 Quasi-particle correction calculated with single-shot G_0W_0 with regards to the planewave cutoff, the number of bands and cutoff energy for the calculation of the dielectric matrix (screening) and the **k**-point grid.

The first steps of the calculation to retrieve the dielectric function taking into account the electron-hole interactions within BSE framework are similar to GW. A first SCF run is performed before a NSCF step on a large range of bands. Then, the screening matrix is calculated with the same parameters found for the single-shot G_0W_0 with 6 Ha for the cutoff and 100 bands. The last steps is the BSE run with Haydock iterative method based on wavefunctions from a NSCF calculations with a shifted **k**-grid of (0.11, 0.21, 0.31) to fasten the convergence by breaking the symmetry of the **k**-grid. Figure A.5 shows the convergence study with regards to the **k**-grid on which the calculations are done, the cutoff to calculate the dielectric matrix in the screening step. Finally, the number of bands to calculate the transitions involves in the BSE run are studied along the complex shift that mimics the experimental broadening of the absorption peaks. A good convergence is achieved for a $12 \times 12 \times 12$ **k**-grid by considering seven bands for the BSE transitions (the three top valence bands and the four bottom conduction bands). A complex shift of 100 meV is chosen as broadening parameter while the dielectric cutoff of 6 Ha is kept even though BSE calculation shows faster convergence than G_0W_0 run for this parameter. The convergence results are compared to the experimental data from Green and

Keevers [236].

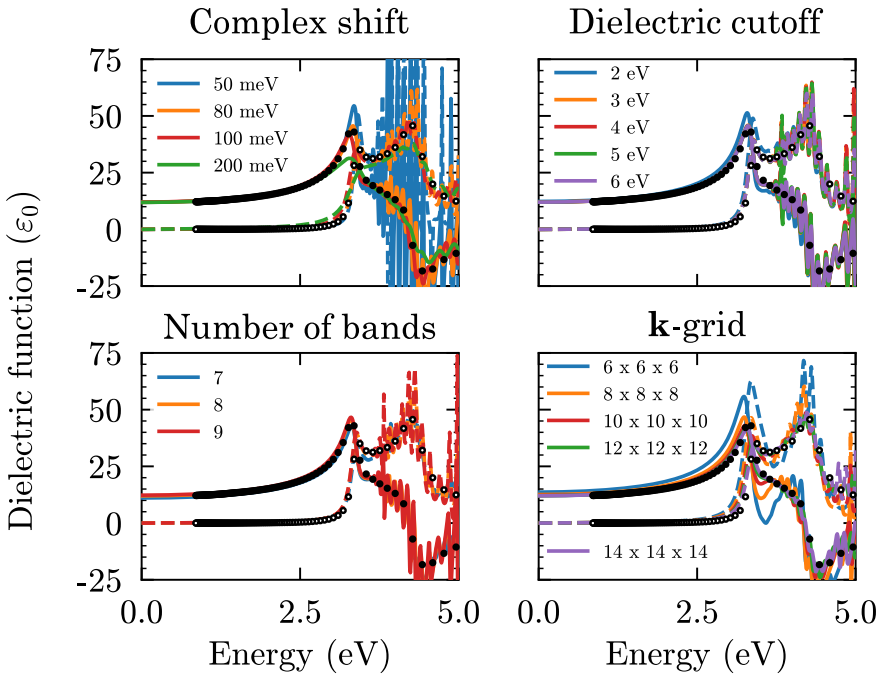


Fig. A.5 Dielectric function calculated with BSE method by varying to the number of **k** points, the energy cutoff for the screening matrix, the bands considered to calculate the possible transitions between the valence and conduction bands and the complex shift that mimics the experimental broadening of the absorption peaks. The real (solid lines) and imaginary (dashed lines) part of the dielectric function are compared to experimental results from Green and Keevers [236]. The imaginary and real parts are shown with white and black dots, respectively.

The convergence results with regards to the interpolated **k**-grid of the EPW calculation are shown in Fig. A.6. The phonon calculations were performed on a $6 \times 6 \times 6$ **q**-grid. The electron-phonon interactions are finally calculated on a $30 \times 30 \times 30$ **k**-grid using Wannier-Fourier interpolation in the EPW code.

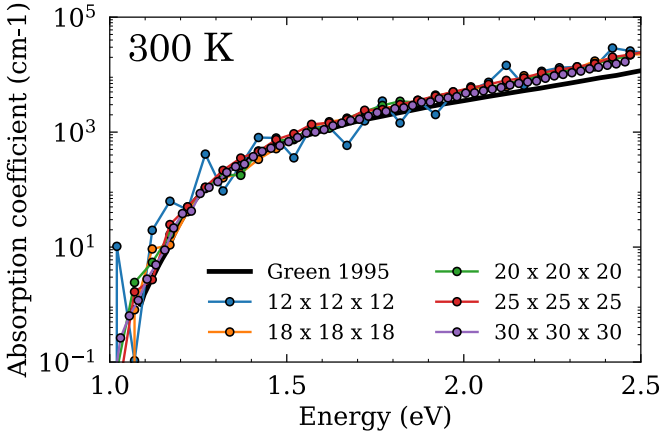


Fig. A.6 Absorption coefficient calculated with EPW method by varying to the number of **k** points. The theoretical results are compared to experimental results from Green and Keevers [236] (black solid lines).

Bibliography

[1] "Chapter 2 - Silicon MOS Technology". In: *VLSI and Computer Architecture*. Ed. by R. Shankar and E. B. Fernandez. Vol. 20. VLSI Electronics Microstructure Science. Elsevier, 1989, pp. 17–95. DOI: https://doi.org/10.1016/B978-0-12-234120-5.50007-2.

[2] Lischke, S., Peczek, A., Morgan, J. S., Sun, K., Steckler, D., Yamamoto, Y., Korndörfer, F., Mai, C., Marschmeyer, S., Fraschke, M., Krüger, A., Beling, A., Zimmermann, L. "Ultra-fast germanium photodiode with 3-dB bandwidth of 265 GHz". In: *Nature Photonics* 15 (12 2021), pp. 925–931. ISSN: 1749-4893. DOI: 10.1038/s41566-021-00893-w.

[3] Liu, Y., Li, Z., Atar, F. B., Muthuganesan, H., Corbett, B., Wang, L. "Integration of High-Performance InGaAs/GaN Photodetectors by Direct Bonding via Micro-transfer Printing". In: *ACS Applied Materials & Interfaces* 16.8 (2024), pp. 10996–11002. DOI: 10.1021/acsami.3c17663. eprint: https://doi.org/10.1021/acsami.3c17663.

[4] Yang, W., Chen, J., Zhang, Y., Zhang, Y., He, J.-H., Fang, X. "Silicon-Compatible Photodetectors: Trends to Monolithically Integrate Photosensors with Chip Technology". In: *Advanced Functional Materials* 29.18 (2019), p. 1808182. DOI: https://doi.org/10.1002/adfm.201808182. eprint: https://onlinelibrary.wiley.com/doi/pdf/10.1002/adfm.201808182.

[5] Agrawal, G. P. "Optical Communication: Its History and Recent Progress". In: *Optics in Our Time*. Ed. by M. D. Al-Amri, M. El-Gomati, and M. S. Zubairy. Cham: Springer International Publish-

ing, 2016, pp. 177–199. ISBN: 978-3-319-31903-2. DOI: 10.1007/978-3-319-31903-2_8.

[6] Wu, J., Yue, G., Chen, W., Xing, Z., Wang, J., Wong, W. R., Cheng, Z., Set, S. Y., Senthil Murugan, G., Wang, X., Liu, T. "On-Chip Optical Gas Sensors Based on Group-IV Materials". In: *ACS Photonics* 7.11 (2020), pp. 2923–2940. DOI: 10.1021/acsphotonics.0c00976. eprint: https://doi.org/10.1021/acsphotonics.0c00976.

[7] Labadie, L., Wallner, O. "Mid-infrared guided optics: a perspective for astronomical instruments". In: *Opt. Express* 17.3 (Feb. 2009), pp. 1947–1962. DOI: 10.1364/OE.17.001947.

[8] Bernal, S., Dumont, M., Berikaa, E., St-Arnault, C., Hu, Y., Castrejon, R. G., Li, W., Wei, Z., Krueger, B., Pittalà, F., Bowers, J., Plant, D. V. "12.1 terabit/second data center interconnects using O-band coherent transmission with QD-MLL frequency combs". In: *Nature Communications* 15 (1 2024), p. 7741. ISSN: 2041-1723. DOI: 10.1038/s41467-024-51682-2.

[9] MacDougal, M., Geske, J., Wang, C., Liao, S., Getty, J., Holmes, A. "Low dark current InGaAs detector arrays for night vision and astronomy". In: *Infrared Technology and Applications XXXV*. Ed. by B. F. Andresen, G. F. Fulop, and P. R. Norton. Vol. 7298. International Society for Optics and Photonics. SPIE, 2009, 72983F. DOI: 10.1117/12.820377.

[10] Li, P., Li, J., Song, S., Chen, J., Zhong, N., Xie, Q., Liu, Y., Wan, B., He, Y., Karimi-Maleh, H. "Recent advances in optical gas sensors for carbon dioxide detection". In: *Measurement* 239 (2025), p. 115445. ISSN: 0263-2241. DOI: https://doi.org/10.1016/j.measurement.2024.115445.

[11] Hu, Y., Liu, Z., Zhu, Y., Liu, Z., Song, Z., Huang, Q., Liu, X., Men, T., Zhang, G., Zheng, J., Zuo, Y., Cheng, B. "High-speed waveguide lateral Ge/Si avalanche photodetector for C-band and L-band". In: *Opt. Express* 32.15 (July 2024), pp. 25598–25606. DOI: 10.1364/OE.522133.

[12] Nath, S. "Advancements in food quality monitoring: integrating biosensors for precision detection". In: *Sustainable Food Technology* 2.4 (2024), pp. 976–992. ISSN: 2753-8095. DOI: https://doi.org/10.1039/d4fb00094c.

[13] Scafutto, R. D. M., van der Werff, H., Bakker, W. H., van der Meer, F., Souza Filho, C. R. "An evaluation of airborne SWIR imaging spectrometers for CH4 mapping: Implications of band positioning, spectral sampling and noise". In: *International Journal of Applied Earth Observation and Geoinformation* 94 (2021), p. 102233. ISSN: 1569-8432. DOI: https://doi.org/10.1016/j.jag.2020.102233.

[14] Jorge Aldave, I., Venegas Bosom, P., Vega González, L., López de Santiago, I., Vollheim, B., Krausz, L., Georges, M. "Review of thermal imaging systems in composite defect detection". In: *Infrared Physics & Technology* 61 (2013), pp. 167–175. ISSN: 1350-4495. DOI: https://doi.org/10.1016/j.infrared.2013.07.009.

[15] Breiter, R., Cabanski, W. A., Mauk, K.-H., Rode, W., Ziegler, J., Schneider, H., Walther, M. "Multicolor and dual-band IR camera for missile warning and automatic target recognition". In: *Targets and Backgrounds VIII: Characterization and Representation*. Ed. by W. R. Watkins, D. Clement, and W. R. Reynolds. Vol. 4718. International Society for Optics and Photonics. SPIE, 2002, pp. 280–288. DOI: 10.1117/12.478815.

[16] Kowalski, M., Kastek, M., Szustakowski, M. "Comparison of objects detection capabilities in LWIR and THz ranges". In: *Millimetre Wave and Terahertz Sensors and Technology VIII*. Ed. by N. A. Salmon and E. L. Jacobs. Vol. 9651. International Society for Optics and Photonics. SPIE, 2015, 96510H. DOI: 10.1117/12.2193906.

[17] Meribout, M. "Gas Leak-Detection and Measurement Systems: Prospects and Future Trends". In: *IEEE Transactions on Instrumentation and Measurement* 70 (2021), pp. 1–13. DOI: 10.1109/TIM.2021.3096596.

[18] Kwak, D., Lei, Y., Maric, R. "Ammonia gas sensors: A comprehensive review". In: *Talanta* 204 (Nov. 2019), pp. 713–730. ISSN: 0039-9140. DOI: 10.1016/j.talanta.2019.06.034.

[19] Helmich, F. P., Ivison, R. J. "FIRI—A far-infrared interferometer". In: *Experimental Astronomy* 23 (1 2009), pp. 245–276. ISSN: 1572-9508. DOI: 10.1007/s10686-008-9100-2.

[20] Walther, M., Plochocka, P., Fischer, B., Helm, H., Uhd Jepsen, P. "Collective vibrational modes in biological molecules investigated by terahertz time-domain spectroscopy". In: *Biopolymers* 67.4-5 (2002), pp. 310–313. DOI: https://doi.org/10.1002/bip.10106.

eprint: https://onlinelibrary.wiley.com/doi/pdf/10.1002/bip.10106.

[21] D'Amico, A., Natale, C. D., Castro, F. L., Iarossi, S., Catini, A., Martinelli, E. "Volatile Compounds Detection by IR Acousto-Optic Detectors". In: *Unexploded Ordnance Detection and Mitigation*. Ed. by J. Byrnes. Dordrecht: Springer Netherlands, 2009, pp. 21–59. ISBN: 978-1-4020-9253-4.

[22] Helmut Budzier, G. G. "Thermal Infrared Sensors". In: *Thermal Infrared Sensors*. John Wiley & Sons, Ltd, 2011. Chap. 6, pp. 149–251. ISBN: 9780470976913. DOI: https://doi.org/10.1002/9780470976913.ch6. eprint: https://onlinelibrary.wiley.com/doi/pdf/10.1002/9780470976913.ch6.

[23] Lee, H.-S., Sze, S. "Silicon p-i-n photodetector using internal reflection method". In: *IEEE Transactions on Electron Devices* 17.4 (1970), pp. 342–347. DOI: 10.1109/T-ED.1970.16978.

[24] Brust, D. "Band-Theoretic Model for the Photoelectric Effect in Silicon". In: *Phys. Rev.* 139 (2A July 1965), A489–A500. DOI: 10.1103/PhysRev.139.A489.

[25] Sclar, N. "Extrinsic silicon detectors for 3–5 and 8–14 μm". In: *Infrared Physics* 16.4 (1976), pp. 435–448. ISSN: 0020-0891. DOI: https://doi.org/10.1016/0020-0891(76)90084-1.

[26] Garcia, J. P., Dereniak, E. L. "Extrinsic silicon photodetector characterization". In: *Appl. Opt.* 29.4 (Feb. 1990), pp. 559–569. DOI: 10.1364/AO.29.000559.

[27] Schroder, D., Thomas, R., Swartz, J. "Free Carrier Absorption in Silicon". In: *IEEE Journal of Solid-State Circuits* 13.1 (1978), pp. 180–187. DOI: 10.1109/JSSC.1978.1051012.

[28] Tanzid, M., Ahmadivand, A., Zhang, R., Cerjan, B., Sobhani, A., Yazdi, S., Nordlander, P., Halas, N. J. "Combining Plasmonic Hot Carrier Generation with Free Carrier Absorption for High-Performance Near-Infrared Silicon-Based Photodetection". In: *ACS Photonics* 5.9 (2018), pp. 3472–3477. DOI: 10.1021/acsphotonics.8b00623.

[29] Choi, K.-K., Levine, B. F., Bethea, C. G., Walker, J., Malik, R. J. "Multiple quantum well 10 μm GaAs/AlxGa1-xAs infrared detector with improved responsivity". In: *Applied Physics Letters* 50.25 (June 1987), pp. 1814–1816. ISSN: 0003-6951. DOI: 10.1063/1.97706. eprint: https://pubs.aip.org/aip/apl/article-pdf/50/25/1814/18461757/1814_1_online.pdf.

[30] Rogalski, A. "Quantum well photoconductors in infrared detector technology". In: *Journal of Applied Physics* 93.8 (Apr. 2003), pp. 4355–4391. ISSN: 0021-8979. DOI: 10.1063/1.1558224. eprint: https://pubs.aip.org/aip/jap/article-pdf/93/8/4355/19227222/4355_1_online.pdf.

[31] Bludau, W., Onton, A., Heinke, W. "Temperature dependence of the band gap of silicon". In: *Journal of Applied Physics* 45.4 (Apr. 1974), pp. 1846–1848. ISSN: 0021-8979. DOI: 10.1063/1.1663501. eprint: https://pubs.aip.org/aip/jap/article-pdf/45/4/1846/18367322/1846_1_online.pdf.

[32] Pearsall, T. "Ga0.47In0.53As: A ternary semiconductor for photodetector applications". In: *IEEE Journal of Quantum Electronics* 16.7 (1980), pp. 709–720. DOI: 10.1109/JQE.1980.1070557.

[33] Zhou, L., Zhang, Y., Gu, Y., Chen, X., Cao, Y., Li, H. "Absorption coefficients of In0.8Ga0.2As at room temperature and 77K". In: *Journal of Alloys and Compounds* 576 (2013), pp. 336–340. ISSN: 0925-8388. DOI: https://doi.org/10.1016/j.jallcom.2013.05.224.

[34] Andreev, I. A., Serebrennikova, O. Y., Sokolovskii, G. S., Kunitsyna, E. V., Dyudelev, V. V., Gadzhiev, I. M., Deryagin, A. G., Grebenshchikova, E. A., Konovalov, G. G., Mikhailova, M. P., Il'inskaya, N. D., Kuchinskii, V. I., Yakovlev, Y. P. "Fast-response p-i-n photodiodes for 0.9–2.4 μm wavelength range". In: *Technical Physics Letters* 36 (5 2010), pp. 412–414. ISSN: 1090-6533. DOI: 10.1134/S1063785010050068.

[35] Zhong, H., Li, C., Guo, D., Cheng, K., Tang, X., Shen, K., Wu, J. "High performance InAs0.91Sb0.09 MWIR detectors with an AlAs1-ySby graded barrier". In: *Infrared Physics & Technology* 130 (2023), p. 104584. ISSN: 1350-4495. DOI: https://doi.org/10.1016/j.infrared.2023.104584.

[36] Rogalski, A., Ciupa, R., Larkowski, W. "Near room-temperature InAsSb photodiodes: Theoretical predictions and experimental data". In: *Solid-State Electronics* 39.11 (1996), pp. 1593–1600. ISSN: 0038-1101. DOI: https://doi.org/10.1016/0038-1101(96)00088-3.

[37] Kopytko, M., Rogalski, A. "New insights into the ultimate performance of HgCdTe photodiodes". In: *Sensors and Actuators A: Physical* 339 (2022), p. 113511. ISSN: 0924-4247. DOI: https://doi.org/10.1016/j.sna.2022.113511.

[38] Robertz, B., Verhelle, J., Schurmans, M. "The Primary and Secondary Production of Germanium: A Life-Cycle Assessment of Different Process Alternatives". In: *JOM* 67 (2 2015), pp. 412–424. ISSN: 1543-1851. DOI: 10.1007/s11837-014-1267-6.

[39] Fthenakis, V., Wang, W., Kim, H. C. "Life cycle inventory analysis of the production of metals used in photovoltaics". In: *Renewable and Sustainable Energy Reviews* 13.3 (2009), pp. 493–517. ISSN: 1364-0321. DOI: https://doi.org/10.1016/j.rser.2007.11.012.

[40] Zheng, K., Benedetti, M. F., van Hullebusch, E. D. "Recovery technologies for indium, gallium, and germanium from end-of-life products (electronic waste) – A review". In: *Journal of Environmental Management* 347 (2023), p. 119043. ISSN: 0301-4797. DOI: https://doi.org/10.1016/j.jenvman.2023.119043.

[41] Jiang, K., Chen, Z., Ma, W. "Research on LCA Data and Environmental Impact of Industrial Silicon Smelting and High Purity Crystal Silicon Purification". In: *Silicon* 16 (2 2024), pp. 573–583. ISSN: 1876-9918. DOI: 10.1007/s12633-023-02698-8.

[42] Schmidt, M., Hottenroth, H., Schottler, M., Fetzer, G., Schlüter, B. "Life cycle assessment of silicon wafer processing for microelectronic chips and solar cells". In: *The International Journal of Life Cycle Assessment* 17 (2 2012), pp. 126–144. ISSN: 1614-7502. DOI: 10.1007/s11367-011-0351-1.

[43] Klugmann-Radziemska, E., Kuczyńska-Łażewska, A. "The use of recycled semiconductor material in crystalline silicon photovoltaic modules production - A life cycle assessment of environmental impacts". In: *Solar Energy Materials and Solar Cells* 205 (Feb. 2020), p. 110259. ISSN: 0927-0248. DOI: 10.1016/j.solmat.2019.110259.

[44] Bridgman, P. W. "Certain Physical Properties of Single Crystals of Tungsten, Antimony, Bismuth, Tellurium, Cadmium, Zinc, and Tin". In: *Proceedings of the American Academy of Arts and Sciences* 60.6 (1925), pp. 305–383. ISSN: 01999818.

[45] Smith, C. S. "Piezoresistance Effect in Germanium and Silicon". In: *Physical Review* 94 (1 Apr. 1954), pp. 42–49. DOI: 10.1103/PhysRev.94.42.

[46] Parton, E., Verheyen, P. "Strained silicon — the key to sub-45 nm CMOS". In: *III-Vs Review* 19.3 (Apr. 2006), pp. 28–31. ISSN: 0961-1290. DOI: 10.1016/s0961-1290(06)71590-3.

[47] Yang, C., Mess, F., Skenes, K., Melkote, S., Danyluk, S. "On the residual stress and fracture strength of crystalline silicon wafers". In: *Applied Physics Letters* 102.2 (Jan. 2013). ISSN: 1077-3118. DOI: 10.1063/1.4776706.

[48] Cheng, D., Gao, Y. "A critical review on the fracture of ultra-thin photovoltaics silicon wafers". In: *Solar Energy Materials and Solar Cells* 274 (Aug. 2024), p. 112999. ISSN: 0927-0248. DOI: 10.1016/j.solmat.2024.112999.

[49] Fischetti, M. V., Laux, S. E. "Band structure, deformation potentials, and carrier mobility in strained Si, Ge, and SiGe alloys". In: *Journal of Applied Physics* 80 (4 Aug. 1996), pp. 2234–2252. ISSN: 0021-8979. DOI: 10.1063/1.363052.

[50] Hohenberg, P., Kohn, W. "Inhomogeneous Electron Gas". In: *Phys. Rev.* 136 (3B Nov. 1964), B864–B871. DOI: 10.1103/PhysRev.136.B864.

[51] Kohn, W., Becke, A. D., Parr, R. G. "Density Functional Theory of Electronic Structure". In: *The Journal of Physical Chemistry* 100.31 (1996), pp. 12974–12980. DOI: 10.1021/jp9606691. eprint: https://doi.org/10.1021/jp9606691.

[52] Bouhassoune, M., Schindlmayr, A. "Electronic structure and effective masses in strained silicon". In: *physica status solidi c* 7 (2 Feb. 2010), pp. 460–463. ISSN: 1862-6351. DOI: 10.1002/pssc.200982470.

[53] Yu, D., Zhang, Y., Liu, F. "First-principles study of electronic properties of biaxially strained silicon: Effects on charge carrier mobility". In: *Physical Review B* 78 (24 Dec. 2008), p. 245204. ISSN: 1098-0121. DOI: 10.1103/PhysRevB.78.245204.

[54] Wang, D., Nakashima, H., Morioka, J., Kitamura, T. "Microphotoluminescence evaluation of local strain for freestanding Si membranes with SiN deposition". In: *Applied Physics Letters* 91.24 (Dec. 2007), p. 241918. ISSN: 0003-6951. DOI: 10.1063/1.2825271. eprint: https://pubs.aip.org/aip/apl/article-pdf/doi/10.1063/1.2825271/13138075/241918_1_online.pdf.

[55] Wang, D., Yang, H., Morioka, J., Kitamura, T., Nakashima, H. "Local strain evaluation for freestanding Si membranes by microphotoluminescence using UV laser excitation". In: *2008 9th International Conference on Solid-State and Integrated-Circuit Technology*. IEEE, Oct. 2008, pp. 684–687. ISBN: 978-1-4244-2185-5. DOI: 10.1109/ICSICT.2008.4734646.

[56] Katiyar, A. K., Thai, K. Y., Yun, W. S., Lee, J., Ahn, J.-H. "Breaking the absorption limit of Si toward SWIR wavelength range via strain engineering". In: *Science Advances* 6 (31 July 2020), pp. 576–605. ISSN: 2375-2548. DOI: 10.1126/sciadv.abb0576.

[57] Katiyar, A. K., Kim, B. J., Lee, G., Kim, Y., Kim, J. S., Kim, J. M., Nam, S., Lee, J., Kim, H., Ahn, J.-H. "Strain modulation in crumpled Si nanomembranes: Light detection beyond the Si absorption limit". In: *Science Advances* 10.2 (2024), eadg7200. DOI: 10.1126/sciadv.adg7200. eprint: https://www.science.org/doi/pdf/10.1126/sciadv.adg7200.

[58] Munguía, J., Chouaib, H., de la Torre, J., Bremond, G., Bru-Chevallier, C., Sibai, A., Champagnon, B., Moreau, M., Bluet, J.-M. "Optical strain measurement in ultrathin sSOI wafer". In: *Nuclear Instruments and Methods in Physics Research Section B: Beam Interactions with Materials and Atoms* 253.1 (2006), pp. 18–21. ISSN: 0168-583X. DOI: https://doi.org/10.1016/j.nimb.2006.10.007.

[59] Alan, T., Hines, M. A., Zehnder, A. T. "Effect of surface morphology on the fracture strength of silicon nanobeams". In: *Applied Physics Letters* 89 (9 Aug. 2006). ISSN: 0003-6951. DOI: 10.1063/1.2338649.

[60] Passi, V., Bhaskar, U., Pardoen, T., Sodervall, U., Nilsson, B., Petersson, G., Hagberg, M., Raskin, J.-P. "High-Throughput On-Chip Large Deformation of Silicon Nanoribbons and Nanowires". In: *Journal of Microelectromechanical Systems* 21.4 (Aug. 2012), pp. 822–829. ISSN: 1057-7157. DOI: 10.1109/JMEMS.2012.2190711.

[61] Zhang, H., Tersoff, J., Xu, S., Chen, H., Zhang, Q., Zhang, K., Yang, Y., Lee, C.-S., Tu, K.-N., Li, J., Lu, Y. "Approaching the ideal elastic strain limit in silicon nanowires". In: *Science Advances* 2 (8 Aug. 2016), e1501382. ISSN: 2375-2548. DOI: 10.1126/sciadv.1501382.

[62] Pardoen, T., Colla, M.-S., Idrissi, H., Amin-Ahmadi, B., Wang, B., Schryvers, D., Bhaskar, U. K., Raskin, J.-P. "A versatile lab-on-chip test platform to characterize elementary deformation mechanisms and electromechanical couplings in nanoscopic objects". In: *Comptes Rendus Physique* 17.3 (2016), pp. 485–495. ISSN: 1631-0705. DOI: https://doi.org/10.1016/j.crhy.2015.11.005.

[63] Pesek, A., Kastler, P., Lischka, K., Palmetshofer, L. "Distribution of strain in Ge ion implanted silicon measured by high resolution X-ray diffraction". In: *Nuclear Instruments and Methods in Physics Research Section B: Beam Interactions with Materials and Atoms* 80-81 (1993), pp. 569–572. ISSN: 0168-583X. DOI: https://doi.org/10.1016/0168-583X(93)96183-D.

[64] Bisognin, G., Salvador, D. D., Napolitani, E., Carnera, A., Bruno, E., Mirabella, S., Priolo, F., Mattoni, A. "Lattice strain induced by boron clusters in crystalline silicon". In: *Semiconductor Science and Technology* 21.6 (Apr. 2006), pp. 41–44. ISSN: 1361-6641. DOI: 10.1088/0268-1242/21/6/l01.

[65] Minamisawa, R. A., Habicht, S., Buca, D., Carius, R., Trellenkamp, S., Bourdelle, K. K., Mantl, S. "Elastic strain and dopant activation in ion implanted strained Si nanowires". In: *Journal of Applied Physics* 108.12 (Dec. 2010). ISSN: 1089-7550. DOI: 10.1063/1.3520665.

[66] Jones, K. S., Prussin, S., Weber, E. R. "A systematic analysis of defects in ion-implanted silicon". In: *Applied Physics A Solids and Surfaces* 45.1 (Jan. 1988), pp. 1–34. ISSN: 1432-0630. DOI: 10.1007/bf00618760.

[67] Ratcliff, T., Shalav, A., Fong, K. C., Elliman, R., Blakers, A. "Influence of Implantation Damage on Emitter Recombination". In: *Energy Procedia* 55 (2014), pp. 272–279. ISSN: 1876-6102. DOI: 10.1016/j.egypro.2014.08.080.

[68] Kum, H., Lee, D., Kong, W., Kim, H., Park, Y., Kim, Y., Baek, Y., Bae, S.-H., Lee, K., Kim, J. "Epitaxial growth and layer-transfer techniques for heterogeneous integration of materials for electronic and photonic devices". In: *Nature Electronics* 2 (10 2019), pp. 439–450. ISSN: 2520-1131. DOI: 10.1038/s41928-019-0314-2.

[69] Li, Y. S., Nguyen, J. "Tensilely Strained Ge Films on Si Substrates Created by Physical Vapor Deposition of Solid Sources". In: *Scientific Reports* 8 (1 2018), p. 16734. ISSN: 2045-2322. DOI: 10.1038/s41598-018-35224-7.

[70] Ureña, F., Olsen, S. H., Šiller, L., Bhaskar, U., Pardoen, T., Raskin, J.-P. "Strain in silicon nanowire beams". In: *Journal of Applied Physics* 112.11 (Dec. 2012), p. 114506. ISSN: 0021-8979. DOI: 10.1063/1.4765025.

[71] Cavallo, F., Lagally, M. G. "Semiconductor nanomembranes: a platform for new properties via strain engineering". In: *Nanoscale Research Letters* 7 (1 2012), p. 628. ISSN: 1556-276X. DOI: 10.1186/1556-276X-7-628.

[72] Sun, L., Qin, G., Seo, J.-H., Celler, G. K., Zhou, W., Ma, Z. "12-GHz Thin-Film Transistors on Transferrable Silicon Nanomembranes for High-Performance Flexible Electronics". In: *Small* 6 (22 Nov. 2010), pp. 2553–2557. ISSN: 1613-6810. DOI: https://doi.org/10.1002/smll.201000522.

[73] Zhu, Y., Xu, F., Qin, Q., Fung, W. Y., Lu, W. "Mechanical Properties of Vapor-Liquid-Solid Synthesized Silicon Nanowires". In: *Nano Letters* 9 (11 Nov. 2009), pp. 3934–3939. ISSN: 1530-6984. DOI: 10.1021/nl902132w.

[74] Gordon, M. J., Baron, T., Dhalluin, F., Gentile, P., Ferret, P. "Size Effects in Mechanical Deformation and Fracture of Cantilevered Silicon Nanowires". In: *Nano Letters* 9 (2 Feb. 2009), pp. 525–529. ISSN: 1530-6984. DOI: 10.1021/nl802556d.

[75] Zhang, H., Fung, K.-Y., Zhuang, Y., Cao, K., Song, J., Hu, A., Lu, Y. "Fracture of a silicon nanowire at ultra-large elastic strain". In: *Acta Mechanica* 230 (4 Apr. 2019), pp. 1441–1449. ISSN: 0001-5970. DOI: 10.1007/s00707-017-2015-0.

[76] Dubois, S. M.-M., Rignanese, G.-M., Pardoen, T., Charlier, J.-C. "Ideal strength of silicon: An ab initio study". In: *Phys. Rev. B* 74 (23 Dec. 2006), p. 235203. DOI: 10.1103/PhysRevB.74.235203.

[77] Ang, K.-W., Chui, K.-J., Chin, H.-C., Foo, Y.-L., Du, A., Deng, W., Li, M.-F., Samudra, G., Balasubramanian, N., Yeo, Y.-C. "50 nm Silicon-On-Insulator N-MOSFET Featuring Multiple Stressors: Silicon-Carbon Source/Drain Regions and Tensile Stress Silicon Nitride Liner". In: *2006 Symposium on VLSI Technology, 2006. Digest of Technical Papers.* 2006, pp. 66–67. DOI: 10.1109/VLSIT.2006.1705219.

[78] Raymond, G., Morin, P., Devos, A., Hess, D. A., Braccini, M., Volpi, F. "Characterisation of silicon nitride thin films used as stressor liners on CMOS FETs". In: *2008 9th International Conference on Ultimate Integration of Silicon*. 2008, pp. 199–202. DOI: 10.1109/ULIS.2008.4527173.

[79] Reboh, S., Morin, P., Hÿtch, M. J., Houdellier, F., Claverie, A. "Mechanics of silicon nitride thin-film stressors on a transistor-like geometry". In: *APL Materials* 1.4 (Oct. 2013). ISSN: 2166-532X. DOI: 10.1063/1.4826545.

[80] Ericson, F., Schweitz, J.-Å. "Micromechanical fracture strength of silicon". In: *Journal of Applied Physics* 68.11 (Dec. 1990), pp. 5840–5844. ISSN: 0021-8979. DOI: 10.1063/1.346957. eprint: https://pubs.aip.org/aip/jap/article-pdf/68/11/5840/18638100/5840_1_online.pdf.

[81] Fan, D., Sigg, H., Spolenak, R., Ekinci, Y. "Strain and thermal conductivity in ultrathin suspended silicon nanowires". In: *Physical Review B* 96 (11 Sept. 2017), p. 115307. ISSN: 2469-9950. DOI: 10.1103/PhysRevB.96.115307.

[82] Chen, M., Pethö, L., Sologubenko, A. S., Ma, H., Michler, J., Spolenak, R., Wheeler, J. M. "Achieving micron-scale plasticity and theoretical strength in Silicon". In: *Nature Communications* 11 (1 May 2020), p. 2681. ISSN: 2041-1723. DOI: 10.1038/s41467-020-16384-5.

[83] Xia, X., Zhang, B., Shi, Y., Qin, J., Yu, J., Zhang, X. "Elastic Stretch Limit Exceeding 10% for Silicon Wires with Submicron to Micron Diameters". In: *Advanced Engineering Materials* (June 2024). ISSN: 1438-1656. DOI: 10.1002/adem.202302187.

[84] Roundy, D., Cohen, M. L. "Ideal strength of diamond, Si, and Ge". In: *Phys. Rev. B* 64 (21 Nov. 2001), p. 212103. DOI: 10.1103/PhysRevB.64.212103.

[85] Yi, T., Li, L., Kim, C.-J. "Microscale material testing of single crystalline silicon: process effects on surface morphology and tensile strength". In: *Sensors and Actuators A: Physical* 83 (1-3 May 2000), pp. 172–178. ISSN: 09244247. DOI: 10.1016/S0924-4247(00)00350-2.

[86] Nakao, S., Ando, T., Shikida, M., Sato, K. "Changes in mechanical properties of micron-sized single-crystal-silicon film at high temperature". In: *The 13th International Conference on Solid-State Sensors, Actuators and Microsystems*. Vol. 2. IEEE, 2005, pp. 1961–1964. ISBN: 0-7803-8994-8. DOI: 10.1109/SENSOR.2005.1497484.

[87] Tsuchiya, T., Hirata, M., Chiba, N., Udo, R., Yoshitomi, Y., Ando, T., Sato, K., Takashima, K., Higo, Y., Saotome, Y., Ogawa, H., Ozaki, K. "Cross comparison of thin-film tensile-testing methods examined using single-crystal silicon, polysilicon, nickel, and titanium films". In: *Journal of Microelectromechanical Systems* 14.5 (2005), pp. 1178–1186. DOI: 10.1109/JMEMS.2005.851820.

[88] Gaither, M. S., DelRio, F. W., Gates, R. S., Cook, R. F. "Deformation and fracture of single-crystal silicon theta-like specimens". In: *Journal of Materials Research* 26 (20 Oct. 2011), pp. 2575–2589. ISSN: 0884-2914. DOI: 10.1557/jmr.2011.319.

[89] Pollak, F. H., Cardona, M. "Energy band structure of germanium and gallium arsenide: The k.p method". In: *Journal of Physics and Chemistry of Solids* 27.2 (1966), pp. 423–425. ISSN: 0022-3697. DOI: https://doi.org/10.1016/0022-3697(66)90049-7.

[90] Dresselhaus, G., Kip, A. F., Kittel, C. "Plasma resonance in crystals: Observations and theory". In: *Physical Review* 100 (2 1955), pp. 618–625. DOI: 10.1103/PhysRev.100.618.

[91] Dexter, R. N., Lax, B. "Effective Masses of Holes in Silicon". In: *Physical Review* 96 (1 Oct. 1954), pp. 223–224. ISSN: 0031-899X. DOI: 10.1103/PhysRev.96.223.

[92] Okada, Y., Tokumaru, Y. "Precise determination of lattice parameter and thermal expansion coefficient of silicon between 300 and 1500 K". In: *Journal of Applied Physics* 56 (2 1984), pp. 314–320. DOI: 10.1063/1.333965.

[93] Rideau, D., Feraille, M., Ciampolini, L., Minondo, M., Tavernier, C., Jaouen, H., Ghetti, A. "Strained Si, Ge, and Si1-x Gex alloys modeled with a first-principles- optimized full-zone kp method". In: *Physical Review B - Condensed Matter and Materials Physics* 74 (19 2006). DOI: 10.1103/PhysRevB.74.195208.

[94] Chelikowsky, J. R., Cohen, M. L. "Nonlocal pseudopotential calculations for the electronic structure of eleven diamond and zincblende semiconductors". In: *Physical Review B* 14 (2 1976), pp. 556–582. DOI: 10.1103/PhysRevB.14.556.

[95] Slater, J. C., Koster, G. F. "Simplified LCAO method for the periodic potential problem". In: *Physical Review* 94 (6 1954), pp. 1498–1524. DOI: 10.1103/PhysRev.94.1498.

[96] Chadi, D. J., Cohen, M. L. "Tight-binding calculations of the valence bands of diamond and zincblende crystals". In: *physica status solidi (b)* 68.1 (1975), pp. 405–419. DOI: https://doi.org/10.1002/pssb.2220680140. eprint: https://onlinelibrary.wiley.com/doi/pdf/10.1002/pssb.2220680140.

[97] Kohn, W., Sham, L. J. "Self-Consistent Equations Including Exchange and Correlation Effects". In: *Phys. Rev.* 140 (4A Nov. 1965), A1133–A1138. DOI: 10.1103/PhysRev.140.A1133.

[98] Perdew, J. P., Chevary, J. A., Vosko, S. H., Jackson, K. A., Pederson, M. R., Singh, D. J., Fiolhais, C. "Atoms, molecules, solids, and surfaces: Applications of the generalized gradient approximation for exchange and correlation". In: *Phys. Rev. B* 46 (11 Sept. 1992), pp. 6671–6687. DOI: 10.1103/PhysRevB.46.6671.

[99] Cohen, A. J., Mori-Sánchez, P., Yang, W. "Insights into Current Limitations of Density Functional Theory". In: *Science* 321.5890 (Aug. 2008), pp. 792–794. ISSN: 1095-9203. DOI: 10.1126/science.1158722.

[100] Vogl, P., Hjalmarson, H. P., Dow, J. D. "A Semi-empirical tight-binding theory of the electronic structure of semiconductors†". In: *Journal of Physics and Chemistry of Solids* 44.5 (1983), pp. 365–378. ISSN: 0022-3697. DOI: https://doi.org/10.1016/0022-3697(83)90064-1.

[101] Jancu, J.-M., Scholz, R., Beltram, F., Bassani, F. "Empirical spds* tight-binding calculation for cubic semiconductors: General method and material parameters". In: *Phys. Rev. B* 57 (11 Mar. 1998), pp. 6493–6507. DOI: 10.1103/PhysRevB.57.6493.

[102] Niquet, Y. M., Rideau, D., Tavernier, C., Jaouen, H., Blase, X. "Onsite matrix elements of the tight-binding Hamiltonian of a strained crystal: Application to silicon, germanium, and their alloys". In: *Physical Review B - Condensed Matter and Materials Physics* 79 (24 2009). DOI: 10.1103/PhysRevB.79.245201.

[103] Perdew, J. P., Levy, M. "Physical Content of the Exact Kohn-Sham Orbital Energies: Band Gaps and Derivative Discontinuities". In: *Phys. Rev. Lett.* 51 (20 Nov. 1983), pp. 1884–1887. DOI: 10.1103/PhysRevLett.51.1884.

[104] Faleev, S. V., Schilfgaarde, M. V., Kotani, T. "All-electron self-consistent GW approximation: Application to Si, MnO, and NiO". In: *Physical Review Letters* 93 (12 2004), pp. 126406-1-126406–4. DOI: 10.1103/PhysRevLett.93.126406.

[105] Onida, G., Reining, L., Rubio, A. "Electronic excitations: Density-functional versus many-body Green's-function approaches". In: *Reviews of Modern Physics* 74 (2 2002), pp. 601–659. DOI: 10.1103/RevModPhys.74.601.

[106] Schilfgaarde, M., Kotani, T., Faleev, S. "Quasiparticle Self-Consistent *GW* Theory". In: *Phys. Rev. Lett.* 96 (22 June 2006), p. 226402. DOI: 10.1103/PhysRevLett.96.226402.

[107] Kane, E. O. "Band Structure of Silicon from an Adjusted Heine-Abarenkov Calculation". In: *Physical Review* 146 (2 June 1966), pp. 558–567. ISSN: 0031-899X. DOI: 10.1103/PhysRev.146.558.

[108] Gonze, X., Amadon, B., Antonius, G., Arnardi, F., Baguet, L., Beuken, J.-M., Bieder, J., Bottin, F., Bouchet, J., Bousquet, E., Brouwer, N., Bruneval, F., Brunin, G., Cavignac, T., Charraud, J.-B., Chen, W., Côté, M., Cottenier, S., Denier, J., Geneste, G., Ghosez, P., Giantomassi, M., Gillet, Y., Gingras, O., Hamann, D. R., Hautier, G., He, X., Helbig, N., Holzwarth, N., Jia, Y., Jollet, F., Lafargue-Dit-Hauret, W., Lejaeghere, K., Marques, M. A. L., Martin, A., Martins, C., Miranda, H. P. C., Naccarato, F., Persson, K., Petretto, G., Planes, V., Pouillon, Y., Prokhorenko, S., Ricci, F., Rignanese, G.-M., Romero, A. H., Schmitt, M. M.,

Torrent, M., Setten, M. J., Troeye, B. V., Verstraete, M. J., Zérah, G., Zwanziger, J. W. "The ABINITproject: Impact, environment and recent developments". In: *Computer Physics Communications* 248 (2020). DOI: 10.1016/j.cpc.2019.107042.

[109] Romero, A. H., Allan, D. C., Amadon, B., Antonius, G., Applencourt, T., Baguet, L., Bieder, J., Bottin, F., Bouchet, J., Bousquet, E., Bruneval, F., Brunin, G., Caliste, D., Côté, M., Denier, J., Dreyer, C., Ghosez, P., Giantomassi, M., Gillet, Y., Gingras, O., Hamann, D. R., Hautier, G., Jollet, F., Jomard, G., Martin, A., Miranda, H. P. C., Naccarato, F., Petretto, G., Pike, N. A., Planes, V., Prokhorenko, S., Rangel, T., Ricci, F., Rignanese, G.-M., Royo, M., Stengel, M., Torrent, M., Setten, M. J. V., Troeye, B. V., Verstraete, M. J., Wiktor, J., Zwanziger, J. W., Gonze, X. "ABINIT: Overview and focus on selected capabilities". In: *Journal of Chemical Physics* 152 (12 2020). DOI: 10.1063/1.5144261.

[110] Setten, M. J., Giantomassi, M., Bousquet, E., Verstraete, M. J., Hamann, D. R., Gonze, X., Rignanese, G.-M. "The PSEUDODOJO: Training and grading a 85 element optimized norm-conserving pseudopotential table". In: *Computer Physics Communications* 226 (2018), pp. 39–54. DOI: 10.1016/j.cpc.2018.01.012.

[111] Perdew, J. P., Burke, K., Ernzerhof, M. "Generalized gradient approximation made simple". In: *Physical Review Letters* 77 (18 1996), pp. 3865–3868. DOI: 10.1103/PhysRevLett.77.3865.

[112] Monkhorst, H. J., Pack, J. D. "Special points for Brillouin-zone integrations". In: *Physical Review B* 13 (12 June 1976), pp. 5188–5192. ISSN: 0556-2805. DOI: 10.1103/PhysRevB.13.5188.

[113] Nye, J. F. "Physical properties of crystals: their representation by tensors and matrices". In: *Acta Crystallographica Section A* 41.6 (1985), pp. 624–624. DOI: https://doi.org/10.1107/S0108767385001477. eprint: https://onlinelibrary.wiley.com/doi/pdf/10.1107/S0108767385001477.

[114] Madelung, O. *Semiconductors*. Ed. by O. Madelung. Data in Science and Technology. Berlin, Heidelberg: Springer Berlin Heidelberg, 1991. ISBN: 978-3-540-53150-0. DOI: 10.1007/978-3-642-45681-7.

[115] Hopcroft, M. A., Nix, W. D., Kenny, T. W. "What is the Young's Modulus of Silicon?" In: *Journal of Microelectromechanical Systems* 19.2 (2010), pp. 229–238. DOI: 10.1109/JMEMS.2009.2039697.

[116] Priester, C., Allan, G., Lannoo, M. "Band-edge deformation potentials in a tight-binding framework". In: *Phys. Rev. B* 37 (14 May 1988), pp. 8519–8522. DOI: 10.1103/PhysRevB.37.8519.

[117] Bouhassoune, M., Schindlmayr, A. "Ab Initio Study of Strain Effects on the Quasiparticle Bands and Effective Masses in Silicon". In: *Advances in Condensed Matter Physics* 2015 (2015), pp. 1–8. ISSN: 1687-8108. DOI: 10.1155/2015/453125.

[118] Bogumilowicz, Y., Hartmann, J., Cherkashin, N., Claverie, A., Rolland, G., Billon, T. "SiGe virtual substrates growth up to 50% Ge concentration for Si/Ge dual channel epitaxy". In: *Materials Science and Engineering: B* 124-125 (2005), pp. 113–117. ISSN: 0921-5107. DOI: https://doi.org/10.1016/j.mseb.2005.08.052.

[119] Spry, R. J., Compton, W. D. "Recombination Luminescence in Irradiated Silicon". In: *Phys. Rev.* 175 (3 Nov. 1968), pp. 1010–1020. DOI: 10.1103/PhysRev.175.1010.

[120] Munguía, J., Bremond, G., Torre, J., Bluet, J.-M. "Photoluminescence study of an ultrathin strained silicon on insulator layer". In: *Applied Physics Letters* 90.4 (Jan. 2007), p. 042110. ISSN: 0003-6951. DOI: 10.1063/1.2432290. eprint: https://pubs.aip.org/aip/apl/article-pdf/doi/10.1063/1.2432290/14364961/042110_1_online.pdf.

[121] Munguía, J., Bluet, J.-M., Baira, M., Marty, O., Bremond, G., Hartmann, J. M., Mermoux, M. "Thickness dependence of photoluminescence for tensely strained silicon layer on insulator". In: *Applied Physics Letters* 93.19 (Nov. 2008). ISSN: 0003-6951. DOI: 10.1063/1.3023058.

[122] Munguía, J., Bluet, J.-M., Marty, O., Bremond, G., Mermoux, M., Rouchon, D. "Temperature dependence of the indirect bandgap in ultrathin strained silicon on insulator layer". In: *Applied Physics Letters* 100.10 (Mar. 2012), p. 102107. ISSN: 0003-6951. DOI: 10.1063/1.3691955. eprint: https://pubs.aip.org/aip/apl/article-pdf/doi/10.1063/1.3691955/14244507/102107_1_online.pdf.

[123] Wang, D., Yang, H., Kitamura, T., Nakashima, H. "Influence of freely diffusing excitons on the photoluminescence spectrum of Si thick films with depth distribution of strain". In: *Journal of Applied Physics* 107.3 (Feb. 2010). ISSN: 0021-8979. DOI: 10.1063/1.3305463.

[124] Gioia, G., Ortiz, M. "Delamination of Compressed Thin Films". In: ed. by J. W. Hutchinson and T. Y. Wu. Vol. 33. Advances in Applied Mechanics. Elsevier, 1997, pp. 119–192. DOI: https://doi.org/10.1016/S0065-2156(08)70386-7.

[125] Tran, F., Blaha, P. "Accurate Band Gaps of Semiconductors and Insulators with a Semilocal Exchange-Correlation Potential". In: *Phys. Rev. Lett.* 102 (22 June 2009), p. 226401. DOI: 10.1103/PhysRevLett.102.226401.

[126] Barber, H. "Effective mass and intrinsic concentration in silicon". In: *Solid-State Electronics* 10.11 (1967), pp. 1039–1051. ISSN: 0038-1101. DOI: https://doi.org/10.1016/0038-1101(67)90122-0.

[127] Hensel, J. C., Hasegawa, H., Nakayama, M. "Cyclotron Resonance in Uniaxially Stressed Silicon. II. Nature of the Covalent Bond". In: *Physical Review* 138 (1A Apr. 1965), A225–A238. ISSN: 0031-899X. DOI: 10.1103/PhysRev.138.A225.

[128] Stradling, R. A., Zhukov, V. V. "Cyclotron resonance of electrons in silicon at temperatures up to 200 K". In: *Proceedings of the Physical Society* 87 (1 Jan. 1966), pp. 263–271. ISSN: 0370-1328. DOI: 10.1088/0370-1328/87/1/329.

[129] Ohyama, T., Yoshihara, T., Murase, K., Otsuka, E. "Observation of cyclotron resonance at the split-off valence band in silicon". In: *Physics Letters A* 33 (1 Sept. 1970), pp. 55–56. ISSN: 03759601. DOI: 10.1016/0375-9601(70)90646-8.

[130] Ramos, L. E., Teles, L. K., Scolfaro, L. M., Castineira, J. L., Rosa, A. L., Leite, J. R. "Structural, electronic, and effective-mass properties of silicon and zinc-blende group-III nitride semiconductor compounds". In: *Physical Review B - Condensed Matter and Materials Physics* 63 (16 Apr. 2001). ISSN: 1550235X.

[131] Inaoka, T., Kinjyo, Y., Yanagisawa, S., Tomori, K. "Anisotropy of the silicon valence band induced by strain with various orientations". In: *Journal of Applied Physics* 113 (18 May 2013). ISSN: 0021-8979.

[132] Janssen, J. L., Gillet, Y., Poncé, S., Martin, A., Torrent, M., Gonze, X. "Precise effective masses from density functional perturbation theory". In: *Physical Review B* 93 (20 May 2016), p. 205147. ISSN: 2469-9950. DOI: 10.1103/PhysRevB.93.205147.

[133] Poncé, S., Margine, E. R., Giustino, F. "Towards predictive many-body calculations of phonon-limited carrier mobilities in semiconductors". In: *Physical Review B* 97 (12 Mar. 2018), p. 121201. DOI: 10.1103/PhysRevB.97.121201.

[134] Ma, J., Zhang, H., Song, J., Wang, G., Wang, X., Xu, X. "Impact of [110]/(001) uniaxial stress on valence band structure and hole effective mass of silicon". In: *Journal of Semiconductors* 32 (2 Feb. 2011), p. 022002. ISSN: 1674-4926. DOI: 10.1088/1674-4926/32/2/022002.

[135] Zhang, C. "Directional, averaged and density of states effective masses of hole in (001), (101) and (111) biaxially strained Si and strained Si1-xGex materials". In: *Materials Research Innovations* 18 (sup2 May 2014), S2-753-S2–758. ISSN: 1432-8917. DOI: 10.1179/1432891714Z.000000000469.

[136] Hu, H., Zhang, H., Song, J., Xuan, R., Dai, X. "Hole effective mass in strained Si (111)". In: *Science China Physics, Mechanics and Astronomy* 54 (3 Mar. 2011), pp. 450–452. ISSN: 1674-7348. DOI: 10.1007/s11433-010-4229-1.

[137] Born, M., Huang, K. *Dynamical theory of crystal lattices*. Oxford University Press, USA, 1954, p. 432. ISBN: 9780198503699.

[138] Pick, R. M., Cohen, M. H., Martin, R. M. "Microscopic Theory of Force Constants in the Adiabatic Approximation". In: *Phys. Rev. B* 1 (2 Jan. 1970), pp. 910–920. DOI: 10.1103/PhysRevB.1.910.

[139] Ganesan, S., Maradudin, A. A., Oitmaa, J. "A lattice theory of morphic effects in crystals of the diamond structure". In: *Annals of Physics* 56.2 (1970), pp. 556–594. ISSN: 0003-4916. DOI: https://doi.org/10.1016/0003-4916(70)90029-1.

[140] Anastassakis, E., Pinczuk, A., Burstein, E., Pollak, F., Cardona, M. "Effect of static uniaxial stress on the Raman spectrum of silicon". In: *Solid State Communications* 8.2 (Jan. 1970), pp. 133–138. ISSN: 00381098. DOI: 10.1016/0038-1098(70)90588-0.

[141] Chandrasekhar, M., Renucci, J. B., Cardona, M. "Effects of interband excitations on Raman phonons in heavily doped n-Si". In: *Physical Review B* 17.4 (Feb. 1978), pp. 1623–1633. ISSN: 0163-1829. DOI: 10.1103/PhysRevB.17.1623.

[142] Nielsen, O. H., Martin, R. M. "Stresses in semiconductors: Ab initio calculations on Si, Ge, and GaAs". In: *Physical Review B* 32.6 (1985), pp. 3792–3805. ISSN: 01631829. DOI: 10.1103/PhysRevB.32.3792.

[143] Anastassakis, E., Cantarero, A., Cardona, M. "Piezo-Raman measurements and anharmonic parameters in silicon and diamond". In: *Physical Review B* 41.11 (Apr. 1990), pp. 7529–7535. ISSN: 0163-1829. DOI: 10.1103/PhysRevB.41.7529.

[144] Peng, C. Y., Huang, C. F., Fu, Y. C., Yang, Y. H., Lai, C. Y., Chang, S. T., Liu, C. W. "Comprehensive study of the Raman shifts of strained silicon and germanium". In: *Journal of Applied Physics* 105.8 (2009). ISSN: 00218979. DOI: 10.1063/1.3110184.

[145] Gravier, S., Coulombier, M., Safi, A., Andre, N., Boe, A., Raskin, J.-P., Pardoen, T. "New On-Chip Nanomechanical Testing Laboratory - Applications to Aluminum and Polysilicon Thin Films". In: *Journal of Microelectromechanical Systems* 18.3 (June 2009), pp. 555–569. ISSN: 1057-7157. DOI: 10.1109/JMEMS.2009.2020380.

[146] Kumar Bhaskar, U., Pardoen, T., Passi, V., Raskin, J.-P. "Piezoresistance of nano-scale silicon up to 2 GPa in tension". In: *Applied Physics Letters* 102.3 (Jan. 2013), p. 031911. ISSN: 0003-6951. DOI: 10.1063/1.4788919.

[147] Bhaskar, U., Passi, V., Houri, S., Escobedo-Cousin, E., Olsen, S. H., Pardoen, T., Raskin, J.-P. "On-chip tensile testing of nanoscale silicon free-standing beams". In: *Journal of Materials Research* 27.3 (Feb. 2012), pp. 571–579. ISSN: 0884-2914. DOI: 10.1557/jmr.2011.340.

[148] Escobedo-Cousin, E., Olsen, S. H., Pardoen, T., Bhaskar, U., Raskin, J.-P. "Experimental observations of surface roughness in uniaxially loaded strained Si microelectromechanical systems-based structures". In: *Applied Physics Letters* 99.24 (Dec. 2011), p. 241906. ISSN: 0003-6951. DOI: 10.1063/1.3669413.

[149] Colla, M. S., Amin-Ahmadi, B., Idrissi, H., Malet, L., Godet, S., Raskin, J. P., Schryvers, D., Pardoen, T. "Dislocation-mediated relaxation in nanograined columnar palladium films revealed by on-chip time-resolved HRTEM testing". In: *Nature Communications* 6.1 (Jan. 2015), p. 5922. ISSN: 2041-1723.

[150] Ayón, A. A., Braff, R., Lin, C. C., Sawin, H. H., Schmidt, M. A. "Characterization of a Time Multiplexed Inductively Coupled Plasma Etcher". In: *Journal of The Electrochemical Society* 146.1 (Jan. 1999), p. 339. DOI: 10.1149/1.1391611.

[151] De Wolf, I. "Micro-Raman spectroscopy to study local mechanical stress in silicon integrated circuits". In: *Semiconductor Science and Technology* 11.2 (1996), pp. 139–154. ISSN: 02681242. DOI: 10.1088/0268-1242/11/2/001.

[152] Loudon, R. "The Raman effect in crystals". In: *Advances in Physics* 13.52 (Oct. 1964), pp. 423–482. ISSN: 0001-8732. DOI: 10.1080/00018736400101051.

[153] Pelikán, P., Čeppan, M., Liška, M. *Applications of Numerical Methods in Molecular Spectroscopy*. CRC Press, Nov. 2020, p. 368. ISBN: 9781003068686. DOI: 10.1201/9781003068686.

[154] Ureña, F., Olsen, S. H., Raskin, J. P. "Raman measurements of uniaxial strain in silicon nanostructures". In: *Journal of Applied Physics* 114.14 (2013). ISSN: 00218979. DOI: 10.1063/1.4824291.

[155] Zanatta, A. R. "Revisiting the optical bandgap of semiconductors and the proposal of a unified methodology to its determination". In: *Scientific Reports* 9.1 (Aug. 2019). ISSN: 2045-2322. DOI: 10.1038/s41598-019-47670-y.

[156] Rau, U., Werner, J. H. "Radiative efficiency limits of solar cells with lateral band-gap fluctuations". In: *Applied Physics Letters* 84.19 (Apr. 2004), pp. 3735–3737. ISSN: 0003-6951. DOI: 10.1063/1.1737071. eprint: https://pubs.aip.org/aip/apl/article-pdf/84/19/3735/10203398/3735_1_online.pdf.

[157] Mattheis, J., Rau, U., Werner, J. H. "Light absorption and emission in semiconductors with band gap fluctuations—A study on Cu(In,Ga)Se2 thin films". In: *Journal of Applied Physics* 101 (June 2007). ISSN: 0021-8979. DOI: 10.1063/1.2721768.

[158] Dunstan, D. J. "Evidence for a common origin of the Urbach tails in amorphous and crystalline semiconductors". In: *Journal of Physics C: Solid State Physics* 15.13 (May 1982), pp. L419–L424. ISSN: 0022-3719. DOI: 10.1088/0022-3719/15/13/008.

[159] Jia, W., He, Y., Cao, Y., Wang, X., Lin, Z., Li, W., Xu, M., Li, E. "Strain-tunable carrier mobility of Fe-doped GaN: A first-principles study". In: *Micro and Nanostructures* 168 (Aug. 2022), p. 207300. ISSN: 2773-0123. DOI: 10.1016/J.MICRNA.2022.207300.

[160] Fletcher, A. S., Nirmal, D. "A survey of Gallium Nitride HEMT for RF and high power applications". In: *Superlattices and Microstructures* 109 (Sept. 2017), pp. 519–537. ISSN: 0749-6036. DOI: 10.1016/J.SPMI.2017.05.042.

[161] Egard, M., Ohlsson, L., Ärlelid, M., Persson, K.-M., Borg, B. M., Lenrick, F., Wallenberg, R., Lind, E., Wernersson, L.-E. "High-frequency performance of self-aligned gate-last surface channel In 0.53Ga 0.47as MOSFET". In: *IEEE Electron Device Letters* 33 (3 2012), pp. 369–371. DOI: 10.1109/LED.2011.2181323.

[162] Rodrigues, I. H., Vorobiev, A. "Low-Field Mobility and High-Field Velocity of Charge Carriers in InGaAs/InP High-Electron-Mobility Transistors". In: *IEEE Transactions on Electron Devices* 69 (4 2022), pp. 1786–1791. ISSN: 1557-9646. DOI: 10.1109/TED.2022.3147733.

[163] Yeo, Y.-C., Gong, X., Dal, M. J. H., Vellianitis, G., Passlack, M. "Germanium-based transistors for future high performance and low power logic applications". In: *2015 IEEE International Electron Devices Meeting (IEDM)*. 2015. DOI: 10.1109/IEDM.2015.7409613.

[164] Du, C., Huang, X., Jiang, C., Pu, X., Zhao, Z., Jing, L., Hu, W., Wang, Z. L. "Tuning carrier lifetime in InGaN/GaN LEDs via strain compensation for high-speed visible light communication". In: *Scientific Reports* 6 (1 2016), p. 37132. ISSN: 2045-2322. DOI: 10.1038/srep37132.

[165] Ochiai, T., Akazawa, T., Miyatake, Y., Sumita, K., Ohno, S., Monfray, S., Boeuf, F., Toprasertpong, K., Takagi, S., Takenaka, M. "Ultrahigh-responsivity waveguide-coupled optical power monitor for Si photonic circuits operating at near-infrared wavelengths". In: *Nature Communications* 13 (1 2022), p. 7443. ISSN: 2041-1723. DOI: 10.1038/s41467-022-35206-4.

[166] Raghuveera, E., Rao, G. P., Lenka, T. R. "Prospects of III–V Semiconductor-Based High Electron Mobility Transistors (HEMTs) Towards Emerging Applications". In: ed. by T. R. Lenka, S. K. Saha, and L. Fu. Springer Nature Singapore, 2024, pp. 123–137. ISBN: 978-981-99-4495-8.

[167] Sun, R., Lai, J., Chen, W., Zhang, B. "GaN Power Integration for High Frequency and High Efficiency Power Applications: A Review". In: *IEEE Access* 8 (2020), pp. 15529–15542. DOI: 10.1109/ACCESS.2020.2967027.

[168] Thompson, S. E., Suthram, S., Sun, Y., Sun, G., Parthasarathy, S., Chu, M., Nishida, T. "Future of Strained Si/Semiconductors in Nanoscale MOSFETs". In: 2006, pp. 1–4. ISBN: 2156-017X. DOI: 10.1109/IEDM.2006.346877.

[169] Thompson, S., Armstrong, M., Auth, C., Alavi, M., Buehler, M., Chau, R., Cea, S., Ghani, T., Glass, G., Hoffman, T., Jan, C.-H., Kenyon, C., Klaus, J., Kuhn, K., Ma, Z., Mcintyre, B., Mistry, K., Murthy, A., Obradovic, B., Nagisetty, R., Nguyen, P., Sivakumar, S., Shaheed, R., Shifren, L., Tufts, B., Tyagi, S., Bohr, M., El-Mansy, Y. "A 90-nm logic technology featuring strained-silicon". In: *IEEE Transactions on Electron Devices* 51.11 (2004), pp. 1790–1797. DOI: 10.1109/TED.2004.836648.

[170] Jaeger, R., Suhling, J., Ramani, R., Bradley, A., Xu, J. "CMOS stress sensors on [100] silicon". In: *IEEE Journal of Solid-State Circuits* 35.1 (2000), pp. 85–95. DOI: 10.1109/4.818923.

[171] Dhar, S., Kosina, H., Palankovski, V., Ungersboeck, S., Selberherr, S. "Electron Mobility Model for Strained-Si Devices". In: *IEEE Transactions on Electron Devices* 52 (4 Apr. 2005), pp. 527–533. ISSN: 0018-9383. DOI: 10.1109/TED.2005.844788.

[172] Ma, J. L., Fu, Z. F., Wei, Q., Zhang, H. M. "Uniaxial Stress Induced Electron Mobility Enhancement in Silicon". In: *Silicon* 5 (3 July 2013), pp. 219–224. ISSN: 1876-990X. DOI: 10.1007/s12633-013-9144-4.

[173] Zheng, K., Shao, R., Deng, Q., Zhang, Y., Li, Y., Han, X., Zhang, Z., Zou, J. "Observation of enhanced carrier transport properties of Si ⟨100⟩-oriented whiskers under uniaxial strains". In: *Applied Physics Letters* 104 (1 Jan. 2014). ISSN: 0003-6951. DOI: 10.1063/1.4861425.

[174] Feste, S. F., Schäpers, T., Buca, D., Zhao, Q. T., Knoch, J., Bouhassoune, M., Schindlmayr, A., Mantl, S. "Measurement of effective electron mass in biaxial tensile strained silicon on insulator". In: *Applied Physics Letters* 95 (18 Nov. 2009). ISSN: 0003-6951. DOI: 10.1063/1.3254330.

[175] Ungersboeck, E., Dhar, S., Karlowatz, G., Sverdlov, V., Kosina, H., Selberherr, S. "The Effect of General Strain on the Band Structure and Electron Mobility of Silicon". In: *IEEE Transactions on Electron Devices* 54 (9 2007), pp. 2183–2190. ISSN: 1557-9646. DOI: 10.1109/TED.2007.902880.

[176] Drude, P. "Zur Elektronentheorie der Metalle". In: *Annalen der Physik* 306.3 (Jan. 1900), pp. 566–613. ISSN: 1521-3889. DOI: 10.1002/andp.19003060312.

[177] Masetti, G., Severi, M., Solmi, S. "Modeling of carrier mobility against carrier concentration in arsenic-, phosphorus-, and boron-doped silicon". In: *IEEE Transactions on Electron Devices* 30 (7 July 1983), pp. 764–769. ISSN: 0018-9383. DOI: 10.1109/T-ED.1983.21207.

[178] Li, S. S., Thurber, W. R. "The dopant density and temperature dependence of electron mobility and resistivity in n-type silicon". In: *Solid-State Electronics* 20.7 (1977), pp. 609–616. ISSN: 0038-1101. DOI: https://doi.org/10.1016/0038-1101(77)90100-9.

[179] Kanda, Y. "A graphical representation of the piezoresistance coefficients in silicon". In: *IEEE Transactions on Electron Devices* 29 (1 Jan. 1982), pp. 64–70. ISSN: 0018-9383. DOI: 10.1109/T-ED.1982.20659.

[180] Thurber, W. R., Mattis, R. L., Liu, Y. M., Filliben, J. J. "Resistivity-Dopant Density Relationship for Phosphorus-Doped Silicon". In: *Journal of The Electrochemical Society* 127.8 (Aug. 1980), p. 1807. DOI: 10.1149/1.2130006.

[181] Thurber, W. R., Mattis, R. L., Liu, Y. M., Filliben, J. J. "Resistivity-Dopant Density Relationship for Boron-Doped Silicon". In: *Journal of The Electrochemical Society* 127.10 (Oct. 1980), p. 2291. DOI: 10.1149/1.2129394.

[182] Ismail, K., Nelson, S. F., Chu, J. O., Meyerson, B. S. "Electron transport properties of Si/SiGe heterostructures: Measurements and device implications". In: *Applied Physics Letters* 63 (5 Aug. 1993), pp. 660–662. ISSN: 0003-6951. DOI: 10.1063/1.109949.

[183] Poncé, S., Margine, E. R., Verdi, C., Giustino, F. "EPW: Electron–phonon coupling, transport and superconducting properties using maximally localized Wannier functions". In: *Computer Physics Communications* 209 (2016), pp. 116–133. ISSN: 0010-4655. DOI: https://doi.org/10.1016/j.cpc.2016.07.028.

[184] Lee, H., Poncé, S., Bushick, K., Hajinazar, S., Lafuente-Bartolome, J., Leveillee, J., Lian, C., Lihm, J.-M., Macheda, F., Mori, H., Paudyal, H., Sio, W. H., Tiwari, S., Zacharias, M., Zhang, X., Bonini, N., Kioupakis, E., Margine, E. R., Giustino, F. "Electron–phonon physics from first principles using the EPW code". In: *npj Computational Materials* 9 (1 Aug. 2023), p. 156. ISSN: 2057-3960. DOI: 10.1038/s41524-023-01107-3.

[185] Zhou, J.-J., Park, J., Lu, I.-T., Maliyov, I., Tong, X., Bernardi, M. "Perturbo: A software package for ab initio electron–phonon interactions, charge transport and ultrafast dynamics". In: *Computer Physics Communications* 264 (2021), p. 107970. ISSN: 0010-4655. DOI: https://doi.org/10.1016/j.cpc.2021.107970.

[186] Cepellotti, A., Coulter, J., Johansson, A., Fedorova, N. S., Kozinsky, B. "Phoebe: a high-performance framework for solving phonon and electron Boltzmann transport equations". In: *Journal of Physics: Materials* 5.3 (July 2022), p. 035003. ISSN: 2515-7639. DOI: 10.1088/2515-7639/ac86f6.

[187] Brunin, G., Miranda, H. P. C., Giantomassi, M., Royo, M., Stengel, M., Verstraete, M. J., Gonze, X., Rignanese, G.-M., Hautier, G. "Phonon-limited electron mobility in Si, GaAs, and GaP with exact treatment of dynamical quadrupoles". In: *Physical Review B* 102 (9 Sept. 2020), p. 94308. DOI: 10.1103/PhysRevB.102.094308.

[188] Poncé, S., Li, W., Reichardt, S., Giustino, F. "First-principles calculations of charge carrier mobility and conductivity in bulk semiconductors and two-dimensional materials". In: *Reports on Progress in Physics* 83.3 (Feb. 2020), p. 036501. ISSN: 1361-6633. DOI: 10.1088/1361-6633/ab6a43.

[189] Beaty, R., Jaeger, R., Suhling, J., Johnson, R., Butler, R. "Evaluation of piezoresistive coefficient variation in silicon stress sensors using a four-point bending test fixture". In: *IEEE Transactions on Components, Hybrids, and Manufacturing Technology* 15.5 (1992), pp. 904–914. DOI: 10.1109/33.180057.

[190] Sze, S., Ng, K. K. *Physics of Semiconductor Devices*. Wiley, Oct. 2006. ISBN: 9780471143239. DOI: 10.1002/0470068329.

[191] Ziman, J. *Electrons and Phonons*. Oxford University Press, Feb. 1960. ISBN: 9780198507796. DOI: 10.1093/acprof:oso/9780198507796.001.0001.

[192] Giustino, F., Cohen, M. L., Louie, S. G. "Electron-phonon interaction using Wannier functions". In: *Physical Review B* 76 (16 Oct. 2007), p. 165108. DOI: 10.1103/PhysRevB.76.165108.

[193] Poncé, S., Royo, M., Stengel, M., Marzari, N., Gibertini, M. "Long-range electrostatic contribution to electron-phonon couplings and mobilities of two-dimensional and bulk materials". In: *Physical Review B* 107 (15 Apr. 2023), p. 155424. ISSN: 2469-9950. DOI: 10.1103/PhysRevB.107.155424.

[194] Li, W. "Electrical transport limited by electron-phonon coupling from Boltzmann transport equation: Anab initiostudy of Si, Al, and MoS_2". In: *Physical Review B* 92.7 (Aug. 2015). ISSN: 1550-235X. DOI: 10.1103/physrevb.92.075405.

[195] Gonze, X., Lee, C. "Dynamical matrices, Born effective charges, dielectric permittivity tensors, and interatomic force constants from density-functional perturbation theory". In: *Phys. Rev. B* 55.16 (Apr. 1997), pp. 10355–10368. ISSN: 0163-1829, 1095-3795. DOI: 10.1103/physrevb.55.10355.

[196] Royo, M., Stengel, M. "First-Principles Theory of Spatial Dispersion: Dynamical Quadrupoles and Flexoelectricity". In: *Phys. Rev. X* 9 (2 June 2019), p. 021050. DOI: 10.1103/PhysRevX.9.021050.

[197] Zhou, J., Poncé, S., Charlier, J.-C. "Guidelines for accurate and efficient calculations of mobilities in two-dimensional semiconductors". In: *Physical Review B* 110.12 (Sept. 2024). ISSN: 2469-9969. DOI: 10.1103/physrevb.110.125304.

[198] Trimarchi, G., Peng, H., Im, J., Freeman, A. J., Cloet, V., Raw, A., Poeppelmeier, K. R., Biswas, K., Lany, S., Zunger, A. "Using design principles to systematically plan the synthesis of hole-conducting transparent oxides: Cu3VO4 and Ag 3VO4 as a case study". In: *Physical Review B - Condensed Matter and Materials Physics* 84 (16 2011).

[199] Grosso, G., Pastori Parravicini, G. *Solid State Physics*. 1st ed. New York: Academic Press, 2000.

[200] Green, M. A. "Intrinsic concentration, effective densities of states, and effective mass in silicon". In: *Journal of Applied Physics* 67.6 (1990), pp. 2944–2954. DOI: https://doi.org/10.1063/1.345414.

[201] Blöchl, P. E., Jepsen, O., Andersen, O. K. "Improved tetrahedron method for Brillouin-zone integrations". In: *Phys. Rev. B* 49 (23 June 1994), pp. 16223–16233. DOI: 10.1103/PhysRevB.49.16223.

[202] Leveillee, J., Zhang, X., Kioupakis, E., Giustino, F. "Ab initio calculation of carrier mobility in semiconductors including ionized-impurity scattering". In: *Physical Review B* 107.12 (Mar. 2023). ISSN: 2469-9969.

[203] Poncé, S., Macheda, F., Margine, E. R., Marzari, N., Bonini, N., Giustino, F. "First-principles predictions of Hall and drift mobilities in semiconductors". In: *Physical Review Research* 3 (4 Oct. 2021), p. 043022. ISSN: 2643-1564. DOI: 10.1103/PhysRevResearch.3.043022.

[204] Morin, F. J. "Lattice-Scattering Mobility in Germanium". In: *Phys. Rev.* 93 (1 Jan. 1954), pp. 62–63. DOI: 10.1103/PhysRev.93.62.

[205] Oliver, J. D., Eastman, L. F., Kirchner, P. D., Schaff, W. J. "Electrical characterization and alloy scattering measurements of LPE GaxIn1-xAs/InP for high frequency device applications". In: *Journal of Crystal Growth* 54.1 (1981), pp. 64–68. ISSN: 0022-0248. DOI: https://doi.org/10.1016/0022-0248(81)90250-5.

[206] Novák, J., Kuliffayová, M., Morvic, M., Kordoš, P. "Growth and properties of low-doped In0.53Ga0.47As LPE layers using rare-earth oxides". In: *Journal of Crystal Growth* 96.3 (1989), pp. 645–648. ISSN: 0022-0248. DOI: https://doi.org/10.1016/0022-0248(89)90062-6.

[207] Toriyama, T., Sugiyama, S. "Analysis of piezoresistance in p-type silicon for mechanical sensors". In: *Journal of Microelectromechanical Systems* 11 (5 Oct. 2002), pp. 598–604. ISSN: 10577157. DOI: 10.1109/JMEMS.2002.802904.

[208] Kozlovskiy, S., Boiko, I. "First-order piezoresistance coefficients in silicon crystals". In: *Sensors and Actuators A: Physical* 118 (1 Jan. 2005), pp. 33–43. ISSN: 09244247. DOI: 10.1016/j.sna.2004.07.003.

[209] Giustino, F. "Electron-phonon interactions from first principles". In: *Reviews of Modern Physics* 89 (1 Feb. 2017), p. 15003. DOI: 10.1103/RevModPhys.89.015003.

[210] Claes, R., Brunin, G., Giantomassi, M., Rignanese, G.-M., Hautier, G. "Assessing the quality of relaxation-time approximations with fully automated computations of phonon-limited mobilities". In: *Phys. Rev. B* 106 (9 Sept. 2022), p. 094302. DOI: 10.1103/PhysRevB.106.094302.

[211] Morin, F. J., Geballe, T. H., Herring, C. "Temperature Dependence of the Piezoresistance of High-Purity Silicon and Germanium". In: *Physical Review* 105 (2 Jan. 1957), pp. 525–539. DOI: 10.1103/PhysRev.105.525.

[212] Colman, D., Bate, R. T., Mize, J. P. "Mobility Anisotropy and Piezoresistance in Silicon p-Type Inversion Layers". In: *Journal of Applied Physics* 39 (4 Mar. 1968), pp. 1923–1931. ISSN: 0021-8979. DOI: 10.1063/1.1656464.

[213] Matsuda, K., Suzuki, K., Yamamura, K., Kanda, Y. "Nonlinear piezoresistance effects in silicon". In: *Journal of Applied Physics* 73 (4 Feb. 1993), pp. 1838–1847. ISSN: 0021-8979. DOI: 10.1063/1.353169.

[214] Lenkkeri, J. T. "Nonlinear Effects in the Piezoresistivity of p-Type Silicon". In: *physica status solidi (b)* 136 (1 July 1986), pp. 373–385. ISSN: 0370-1972. DOI: 10.1002/pssb.2221360141.

[215] Tufte, O. N., Stelzer, E. L. "Piezoresistive properties of heavily doped n-type silicon". In: *Physical Review* 133 (6A Mar. 1964), A1705–A1716. ISSN: 0031-899X. DOI: 10.1103/PhysRev.133.A1705.

[216] Cho, C. H., Jaeger, R. C., Suhling, J. C. "Characterization of the temperature dependence of the piezoresistive coefficients of silicon from -150°C to +125°C". In: *IEEE Sensors Journal* 8 (8 Aug. 2008), pp. 1455–1468. ISSN: 1530437X. DOI: 10.1109/JSEN.2008.923575.

[217] Dorey, A., Maddern, T. "The effect of strain on MOS transistors". In: *Solid-State Electronics* 12 (3 Mar. 1969), pp. 185–189. ISSN: 00381101. DOI: 10.1016/0038-1101(69)90030-6.

[218] Beaty, R., Jaeger, R., Suhling, J., Johnson, R., Butler, R. "Evaluation of piezoresistive coefficient variation in silicon stress sensors using a four-point bending test fixture". In: *IEEE Transactions on Components, Hybrids, and Manufacturing Technology* 15 (5 1992), pp. 904–914. ISSN: 01486411. DOI: 10.1109/33.180057.

[219] Jaeger, R., Suhling, J., Ramani, R. "Errors associated with the design, calibration and application of piezoresistive stress sensors in (100) silicon". In: *IEEE Transactions on Components, Packaging, and Manufacturing Technology: Part B* 17 (1 1994), pp. 97–107. ISSN: 10709894. DOI: 10.1109/96.296437.

[220] Caughey, D., Thomas, R. "Carrier mobilities in silicon empirically related to doping and field". In: *Proceedings of the IEEE* 55.12 (1967), pp. 2192–2193. DOI: 10.1109/PROC.1967.6123.

[221] Irvin, J. C. "Resistivity of Bulk Silicon and of Diffused Layers in Silicon". In: *Bell System Technical Journal* 41.2 (Mar. 1962), pp. 387–410. ISSN: 0005-8580. DOI: 10.1002/j.1538-7305.1962.tb02415.x.

[222] Mousty, F., Ostoja, P., Passari, L. "Relationship between resistivity and phosphorus concentration in silicon". In: *Journal of Applied Physics* 45.10 (Oct. 1974), pp. 4576–4580. ISSN: 1089-7550. DOI: 10.1063/1.1663091.

[223] Benedict, L. X., Shirley, E. L., Bohn, R. B. "Theory of optical absorption in diamond, Si, Ge, and GaAs". In: *Phys. Rev. B* 57 (16 Apr. 1998), R9385–R9387. DOI: 10.1103/PhysRevB.57.R9385.

[224] Rajkanan, K., Singh, R., Shewchun, J. "Absorption coefficient of silicon for solar cell calculations". In: *Solid-State Electronics* 22.9 (1979), pp. 793–795. ISSN: 0038-1101. DOI: https://doi.org/10.1016/0038-1101(79)90128-X.

[225] Noffsinger, J., Kioupakis, E., Van de Walle, C. G., Louie, S. G., Cohen, M. L. "Phonon-assisted optical absorption in silicon from first principles". In: *Physical Review Letters* 108.16 (2012), p. 167402. DOI: https://doi.org/10.1103/PhysRevLett.108.167402.

[226] Zacharias, M., Patrick, C. E., Giustino, F. "Stochastic approach to phonon-assisted optical absorption". In: *Physical Review Letters* 115.17 (2015), p. 177401. DOI: https://doi.org/10.1103/PhysRevLett.115.177401.

[227] Fan, H. Y. "Infra-red Absorption in Semiconductors". In: *Reports on Progress in Physics* 19.1 (Jan. 1956), pp. 107–155. DOI: 10.1088/0034-4885/19/1/304.

[228] Falk, R. A. "Near IR Absorption in Heavily Doped Silicon - An Empirical Approach". In: *Conference Proceedings from the International Symposium for Testing and Failure Analysis* 09.2 (2000), pp. 121–127.

[229] Sturm, J. C., Reaves, C. M. "Silicon temperature measurement by infrared absorption: Fundamental processes and doping effects". In: *IEEE Transactions on Electron Devices* 39.1 (1992), pp. 81–88. ISSN: 15579646. DOI: 10.1109/16.108215.

[230] Tsai, C.-Y. "Absorption coefficients of silicon: A theoretical treatment". In: *Journal of Applied Physics* 123.18 (2018), p. 183103. DOI: https://doi.org/10.1063/1.5028053.

[231] Adler, S. L. "Quantum Theory of the Dielectric Constant in Real Solids". In: *Phys. Rev.* 126 (2 Apr. 1962), pp. 413–420. DOI: 10.1103/PhysRev.126.413.

[232] Ehrenreich, H., Cohen, M. H. "Self-Consistent Field Approach to the Many-Electron Problem". In: *Phys. Rev.* 115 (4 Aug. 1959), pp. 786–790. DOI: 10.1103/PhysRev.115.786.

[233] Hartree, D. R. "The Propagation of Electromagnetic Waves in a Refracting Medium in a Magnetic Field". In: *Mathematical Proceedings of the Cambridge Philosophical Society* 27.1 (1931), pp. 143–162. DOI: 10.1017/S0305004100009440.

[234] CastilloMussot, M., Sham, L. J. "Excitonic effect in the optical spectrum of semiconductors". In: *Phys. Rev. B* 31 (4 Feb. 1985), pp. 2092–2098. DOI: 10.1103/PhysRevB.31.2092.

[235] Hedin, L. "New Method for Calculating the One-Particle Green's Function with Application to the Electron-Gas Problem". In: *Phys. Rev.* 139.3A (Aug. 1965), A796–A823. ISSN: 0031-899X. DOI: 10.1103/physrev.139.a796.

[236] Green, M. A., Keevers, M. J. "Optical properties of intrinsic silicon at 300 K". In: *Progress in Photovoltaics: Research and Applications* 3.3 (1995), pp. 189–192. DOI: https://doi.org/10.1002/pip.4670030303.

[237] Albrecht, S., Reining, L., Del Sole, R., Onida, G. "Excitonic Effects in the Optical Properties". In: *physica status solidi (a)* 170.2 (1998), pp. 189–197. DOI: https://doi.org/10.1002/(SICI)1521-396X(199812)170:2<189::AID-PSSA189>3.0.CO;2-3. eprint: https://onlinelibrary.wiley.com/doi/pdf/10.1002/%28SICI%291521-396X%28199812%29170%3A2%3C189%3A%3AAID-PSSA189%3E3.0.CO%3B2-3.

[238] Lin, H., Luo, Z., Gu, T., Kimerling, L. C., Wada, K., Agarwal, A., Hu, J. "Mid-infrared integrated photonics on silicon: a perspective". In: *Nanophotonics* 7.2 (2017), pp. 393–420. DOI: https://doi.org/10.1515/nanoph-2017-0085.

[239] Patrick, C. E., Giustino, F. "Unified theory of electron-phonon renormalization and phonon-assisted optical absorption". In: *Journal of Physics: Condensed Matter* 26.36 (2014), p. 365503. DOI: https://doi.org/10.1088/0953-8984/26/36/365503.

[240] Noffsinger, J., Giustino, F., Malone, B. D., Park, C.-H., Louie, S. G., Cohen, M. L. "EPW: A program for calculating the electron–phonon coupling using maximally localized Wannier functions". In: *Computer Physics Communications* 181.12 (2010), pp. 2140–2148. ISSN: 0010-4655. DOI: https://doi.org/10.1016/j.cpc.2010.08.027.

[241] Marzari, N., Vanderbilt, D. "Maximally localized generalized Wannier functions for composite energy bands". In: *Phys. Rev. B* 56 (20 Nov. 1997), pp. 12847–12865. DOI: 10.1103/PhysRevB.56.12847.

[242] Marzari, N., Mostofi, A. A., Yates, J. R., Souza, I., Vanderbilt, D. "Maximally localized Wannier functions: Theory and applications". In: *Rev. Mod. Phys.* 84 (4 Oct. 2012), pp. 1419–1475. DOI: 10.1103/RevModPhys.84.1419.

[243] Tiwari, S., Kioupakis, E., Menendez, J., Giustino, F. "Unified theory of optical absorption and luminescence including both direct and phonon-assisted processes". In: *Physical Review B* 109.19 (May 2024). ISSN: 2469-9969. DOI: 10.1103/physrevb.109.195127.

[244] Ridley, B. K. *Quantum processes in semiconductors*. 4th ed. Oxford University Press, 1990.

[245] Vandenberghe, W. G., Fischetti, M. V. "Deformation potentials for band-to-band tunneling in silicon and germanium from first principles". In: *Applied Physics Letters* 106.1 (2015), p. 013505. DOI: https://doi.org/10.1063/1.4905591.

[246] Dunlap, W. C., Watters, R. L. "Direct Measurement of the Dielectric Constants of Silicon and Germanium". In: *Phys. Rev.* 92 (6 Dec. 1953), pp. 1396–1397. DOI: 10.1103/PhysRev.92.1396.

[247] Nunley, T. N., Fernando, N. S., Samarasingha, N., Moya, J. M., Nelson, C. M., Medina, A. A., Zollner, S. "Optical constants of germanium and thermally grown germanium dioxide from 0.5 to 6.6eV via a multisample ellipsometry investigation". In: *Journal of Vacuum Science & Technology B* 34.6 (Sept. 2016), p. 061205. ISSN: 2166-2746. DOI: 10.1116/1.4963075. eprint: https://pubs.aip.org/avs/jvb/article-pdf/doi/10.1116/1.4963075/13552602/061205_1_online.pdf.

[248] Borrego, J., Zierak, M., Charache, G. "Parameter extraction for TPV cell development". In: *AIP Conference Proceedings* 321.1 (Jan. 1995), pp. 371–378. ISSN: 0094-243X. DOI: 10.1063/1.47046. eprint: https://pubs.aip.org/aip/acp/article-pdf/321/1/371/12064006/371_1_online.pdf.

[249] Humlíček, J. "Silicon-Germanium Alloys (SixGe1-x) Revisited". In: *Handbook of Optical Constants of Solids*. Ed. by E. D. Palik. Burlington: Academic Press, 1997, pp. 537–552. ISBN: 978-0-12-544415-6. DOI: https://doi.org/10.1016/B978-012544415-6.50118-7.

[250] Gavoret, J., Nozières, P., Roulet, B., Combescot, M. "Optical absorption in degenerate semiconductors". In: *Journal de Physique* 30 (11-12 1969), pp. 987–997. ISSN: 0302-0738. DOI: 10.1051/jphys:019690030011-12098700.

[251] Howell, H. B., Jacobowitz, H. "Matrix Method Applied to the Multiple Scattering of Polarized Light". In: *Journal of the Atmospheric Sciences* 27.8 (Nov. 1970), pp. 1195–1206. ISSN: 1520-0469. DOI: 10.1175/1520-0469(1970)027<1195:mmattm>2.0.co;2.

[252] Katsidis, C. C., Siapkas, D. I. "General transfer-matrix method for optical multilayer systems with coherent, partially coherent, and incoherent interference". In: *Appl. Opt.* 41.19 (July 2002), pp. 3978–3987. DOI: 10.1364/AO.41.003978.

[253] Luque-Raigon, J. M., Halme, J., Miguez, H., Lozano, G. "Symmetry analysis of the numerical instabilities in the transfer matrix method". In: *Journal of Optics* 15.12 (Nov. 2013), p. 125719. DOI: 10.1088/2040-8978/15/12/125719.

[254] Harbecke, B. "Coherent and incoherent reflection and transmission of multilayer structures". In: *Applied Physics B Photophysics and Laser Chemistry* 39.3 (Mar. 1986), pp. 165–170. ISSN: 1432-0649. DOI: 10.1007/bf00697414.

[255] Laff, R. A. "Silicon Nitride as an Antireflection Coating for Semiconductor Optics". In: *Appl. Opt.* 10.4 (Apr. 1971), pp. 968–969. DOI: 10.1364/AO.10.000968.

[256] Tao, Y., Rajapakse, A., Erickson, A. "Advanced antireflection for back-illuminated silicon photomultipliers to detect faint light". In: *Scientific Reports* 12.1 (Aug. 2022). ISSN: 2045-2322. DOI: 10.1038/s41598-022-18280-y.

[257] Bauer, G. "Absolutwerte der optischen Absorptionskonstanten von Alkalihalogenidkristallen im Gebiet ihrer ultravioletten Eigenfrequenzen". In: *Annalen der Physik* 411 (Jan. 1934), pp. 434–464. ISSN: 00033804. DOI: 10.1002/(ISSN)1521-388910.1002/andp.v411:410.1002/andp.19344110405.

[258] Philipp, H. R. "Optical Properties of Silicon Nitride". In: *Journal of The Electrochemical Society* 120.2 (1973), p. 295. ISSN: 0013-4651. DOI: 10.1149/1.2403440.

[259] DiDomenico, M., Svelto, O. "Solid-state photodetection: A comparison between photodiodes and photoconductors". In: *Proceedings of the IEEE* 52.2 (1964), pp. 136–144. DOI: 10.1109/PROC.1964.2802.

[260] Rogalski, A. *Infrared detectors*. 2nd ed. London, England: CRC Press, Nov. 2010.

[261] Rose, A. "Performance of Photoconductors". In: *Proceedings of the IRE* 43.12 (1955), pp. 1850–1869. DOI: 10.1109/JRPROC.1955.278047.

[262] Bemski, G. "Recombination in Semiconductors". In: *Proceedings of the IRE* 46.6 (1958), pp. 990–1004. DOI: 10.1109/JRPROC.1958.286838.

[263] Gerlach, W., Schlangenotto, H., Maeder, H. "On the radiative recombination rate in silicon". In: *Physica Status Solidi (a)* 13.1 (Sept. 1972), pp. 277–283. ISSN: 1521-396X. DOI: 10.1002/pssa.2210130129.

[264] Gärtner, W. W. "Depletion-Layer Photoeffects in Semiconductors". In: *Phys. Rev.* 116 (1 Oct. 1959), pp. 84–87. DOI: 10.1103/PhysRev.116.84.

[265] Gwyn, C. W., Scharfetter, D. L., Wirth, J. L. "The Analysis of Radiation Effects in Semiconductor Junction Devices". In: *IEEE Transactions on Nuclear Science* 14.6 (1967), pp. 153–169. DOI: 10.1109/TNS.1967.4324787.

[266] Wiele, F. "Photodiode Quantum Efficiency". In: *Solid State Imaging*. Springer Netherlands, 1976, pp. 47–90. ISBN: 9789401015349. DOI: 10.1007/978-94-010-1534-9_4.

[267] Vliet, K. M. "Noise Limitations in Solid State Photodetectors". In: *Applied Optics* 6.7 (July 1967), p. 1145. ISSN: 1539-4522. DOI: 10.1364/ao.6.001145.

[268] Shi, C., Dong, Y., Li, Q. "High-Performance Nonequilibrium InSb PIN Infrared Photodetectors". In: *IEEE Transactions on Electron Devices* 66.3 (Mar. 2019), pp. 1361–1367. ISSN: 1557-9646. DOI: 10.1109/ted.2019.2895032.

[269] Lee, D., Mayer, J. "Ion-implanted semiconductor devices". In: *Proceedings of the IEEE* 62.9 (1974), pp. 1241–1255. DOI: 10.1109/PROC.1974.9603.

[270] Wang, C., Misiakos, K., Neugroschel, A. "Minority-carrier transport parameters in n-type silicon". In: *IEEE Transactions on Electron Devices* 37.5 (May 1990), pp. 1314–1322. ISSN: 0018-9383. DOI: 10.1109/16.108194.

[271] Swirhun, S., Kwark, Y.-H., Swanson, R. "Measurement of electron lifetime, electron mobility and band-gap narrowing in heavily doped p-type silicon". In: *1986 International Electron Devices Meeting*. IRE, 1986, pp. 24–27. DOI: 10.1109/iedm.1986.191101.